A Measurement of the Antiproton and Proton Charge-to-Mass Ratios Using Two Simultaneously Trapped Ions

A thesis presented

by

Anton Nabil Khabbaz

to

The Department of Physics

in partial fulfillment of the requirements

for the degree of

Doctor of Philosophy

in the subject of

Physics

Harvard University

Cambridge, Massachusetts

June 2, 1998

Abstract

We measured that the ratio of the antiproton charge-to-mass ratio to that of the proton is $-1.000\,000\,000\,01(7)$, fifteen times more accurately than in past studies [1, 2]. This comparison is the most accurate limit for CPT violation in a baryon system and is among the most precise mass spectroscopy measurements made to date [3].

A negative hydrogen ion was used to eliminate the biggest systematic error of the previous work: comparing particles of opposite charge. Measuring the charge-to-mass ratio of the negative hydrogen ion accurately determines the charge-to-mass ratio of the proton since the proton-to-electron mass ratio and the binding energy of the negative hydrogen ion are accurately known.

An antiproton and a negative hydrogen ion were confined in a Penning trap at the same time: the first time that simultaneously trapped species were used for a precise measurement. We determined charge-to-mass ratios by measuring cyclotron frequencies. While the antiproton cyclotron frequency was measured in the trap center, the negative hydrogen ion was kept in a large enough cyclotron orbit to avoid influencing the measurement. The particle's locations were then reversed.

The largest uncertainty in this work was due to a very small drift in the magnetic field as measured by the particle. We reduced this uncertainty by doubling the signal-to-noise ratio in the most important tuned circuit used for detection, and increasing the cyclotron damping by a factor of two.

Contents

Acknowledgments

I would like to thank my advisor, Professor Gerald Gabrielse, for his support and encouragement while completing this experiment at CERN in Geneva, Switzerland. I would also like to thank Christoph Heimann, David Hall and David Phillips for their roles in this measurement and Professor Richard Wilson, Professor Jene Golovchenko, and Dr. Hartmut Kalinowsky for their counsel. Michael Doser and the LEAR staff delivered antiprotons to us with a smile when we needed it. I also would like to thank fellow graduate students and post-doctoral fellows Daphna Enzer, John Estrada, Lisa Lapidus, Carla Levy, Paul Oxley, Steve Peil, Timothy Roach, and Peter Yesley. Best of luck to you all.

Most of all, I would like to thank my family and Sana' Odeh. They supported me, often daily. they believed in me, and they gave me perspective.

Publications

1. "Q/M for the Antiproton and Proton Have the Same Magnitude to 9 Parts in 10^{11}," G. Gabrielse, A. Khabbaz, D. S. Hall, C. Heimann, H. Kalinowsky, W. Jhe, (to be published).

2. "Comparing the Antiproton and Proton and Progress toward Cold Antihydrogen," B. Brown, G. Gabrielse, D. S. Hall, C. Heimann, W. Jhe, H. Kalinowsky, A. Khabbaz, T. Roach, and P. Yesley, Nuclear Physics B (Proceedings Supplements) **56A**, 326 (1997).

3. "Comparing the Antiproton and Proton and Progress toward Cold Antihydrogen," G. Gabrielse, D. S. Hall, A. Khabbaz, T. Roach, P. Yesley, C. Heimann, H. Kalinowsky, W. Jhe, and B. Brown, in *Proceedings of the Fifteenth International Conference on Atomic Physics,* University of Amsterdam, August 5–9, 1996.

4. "Neutron Yields for Muon Irradiated PdD: Implications for Cold Fusion," A. Khabbaz, J.A. Golovchenko, R. Wilson, M. Burns, M. Chen, M. Bloomer, S. G. Steadman, D. Albagli, V. Cammarata, M. Schloh, M.S. Wrighton, K.S. Kwok, M. Gaudreau, S. Luckhardt, R. Parker, R. Debbe, D. Lowenstein, Brookhaven National Laboratory Report(1989).

List of Tables

List of Figures

Chapter 1

Introduction

We used a new technique to measure the ratio of the proton (p) and antiproton ($\bar{p}$) charge-to-mass ratios. The cyclotron frequencies of two charged particles orbiting in the magnetic field of a Penning trap determined their charge-to-mass ratios, allowing us to complete the most precise test of charge conjugation, parity and time reversal invariance for a baryon system made to date.

1.1 CPT Invariance

Charge conjugation (C), parity (P), and time reversal (T) invariance require that a proton and an antiproton have the same charge-to-mass ratio except for an opposite sign. When a proton scatters off a photon, a PT transformation changes the proton's position and time according to:

$$\begin{aligned} x &\rightarrow -x \\ t &\rightarrow -t. \end{aligned}$$

This transformation reverses the particle's spin and leaves its velocity alone. C turns the proton into an antiproton. The CPT transformation takes an incoming spin-up proton and turns it into an outgoing spin-down antiproton. The scattering amplitude should thus be the same when an incoming proton is transformed under CPT to an outgoing antiproton. A consequence of CPT invariance is that each matter particle has an anti-matter counterpart equal in mass and opposite in charge. CPT invariance is a prediction of quantum field theories.

A measured difference in the proton and antiproton cyclotron frequencies could only be explained with new physics. One of the postulates used to prove the CPT theorem could be violated. These postulates are basic to quantum field theory: the theory has a vacuum state, it is Lorentz invariant, it has local fields, and it has a positive definite space-time metric [4]. Some string theories which postulate CPT violation could be valid. Colladay and coworkers [5] propose adding a term to the Lagrangian in the standard model that violates CPT invariance at a precision of 1 part in 10^{17}. Another possibility is that the weak equivalence principle does not hold for antimatter. If gravity accelerates an antiproton at a different rate than a proton the two particles are subject to different gravitational red shifts [6]. When measured at the same height the proton and the antiproton would have different cyclotron frequencies. According to this test, we could measure a difference in the gravitational constant between matter and antimatter to 1 part in 10^6. Some reasons such as these must be offered if we had measured a difference in the antiproton and proton charge-to-mass ratios.

A few tests of CPT invariance at a comparable or higher precision to our measurement have been completed. A summary of all the CPT measurements is shown in Fig. 1.1. The most precise test of CPT invariance relies on a small number of experiments and a phenomenological model. R. Carosi et. al. [7] measured the mass difference between two mesons, the neutral kaon (K^0) and its antiparticle ($\bar{K}^0$) (Top of Fig. 1.1). They measured the probability amplitudes for both the long lived kaon (K_L) and the short lived kaon (K_S) to decay into two charged pions or two neutral pions. They measured the K_S and K_L lifetimes to 1 part in 10^3 and they used the small mass difference between K_S and K_L. This determined the mixture of the CP eigenstates, K^0 and $\bar{K}^0$, that is in each of the physical particles, K_L and K_S. Carosi added a CPT violating term to their phenomenological model and looked for an additional contribution that could not be explained with CP violation alone. From the size of this contribution, they deduced that the K^0 and $\bar{K}^0$ masses differ by less than 5 parts in 10^{18}. More recent measurements determine that the kaon mass difference is zero to 7 parts in 10^{19} [8], without the theoretical assumptions of the earlier kaon measurement. Although widely accepted as a valid test of the CPT theorem, some have claimed that since the test is for exponentially decaying particles, the model used is incapable of describing CPT violation effects correctly [9]. Since CPT invariance is such a fundamental assumption, other precise tests are desirable.

Other precise CPT tests are more direct. Van Dyck and coworkers [10] measured the electron and positron magnetic moments [10] (middle of Fig. 1.1). They compared the energy needed to flip the electron's spin with the energy needed to increase its cyclotron orbit in a strong magnetic field. The ratio of the corresponding frequencies determined the magnetic moment of the electron. They confirmed that for leptons CPT invariance holds to 2 parts in 10^{12}.

In the measurement (second from the top of Fig. 1.1) described in this thesis, we compared the proton and antiproton cyclotron frequencies. This comparison directly measured the ratio of their charge-to-mass ratios, confirming that for baryons CPT invariance holds to 7 parts in 10^{11}.

Finally, this thesis and that of C. Heimann [11] should be regarded as preliminary

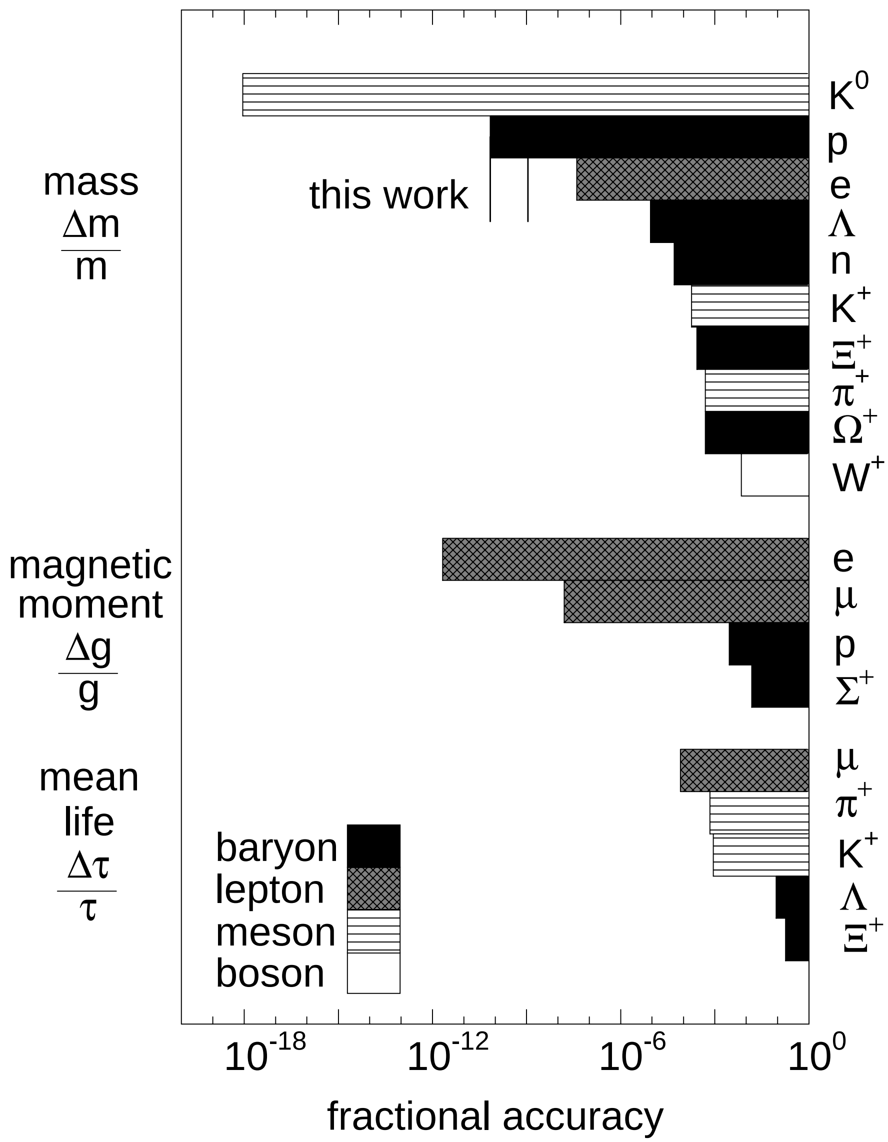

Figure 1.1: Precise tests of CPT invariance.

analyses of the TRAP data. The differences are briefly mentioned in Sec. 6.1. The official TRAP value for the comparison of the charge-to-mass ratios of the antiproton and the proton has yet to be determined.

1.2 History

Measurement of the properties of the antiproton ($\bar{p}$) has a long tradition. Fig. 1.2a shows the results of all the antiproton mass and charge-to-mass measurements made to date. The $\bar{p}$ was discovered in 1955 at the Bevatron laboratory. O. Chamberlain et. al. [12] identified it by measuring its momentum using a bending magnet and measuring its velocity using a Čerenkov counter. In the 1970's, $\bar{p}$ mass measurements were performed at the European Center for Nuclear Research (CERN) [13] and at the Brookhaven National Laboratory (BNL) [14, 15, 16]. A $\bar{p}$ was captured on various target materials, such as lithium, silicon, and lead. The $\bar{p}$ entered into an orbit with a target atom much smaller than that of the most tightly bound electron, yet it was still large enough that nuclear forces did not dominate. The energy levels in this regime are hydrogen-like. While cascading to its ground state just prior to annihilation, the $\bar{p}$ emitted X-rays. Roberson [15] measured the energy of these X-rays and determined the $\bar{p}$ mass by assuming that the antiproton and the electron have the same charge. Ultimately, relativistic and other corrections limited their precision. They attained an accuracy of 5 parts in 10^5.

The availability of low energy antiprotons at the Low Energy Antiproton Ring (LEAR) at CERN and the techniques of precision frequency measurements using Penning traps [17] made possible precise comparisons of the proton and antiproton charge-to-mass ratios. In 1986, antiprotons were trapped [18] and in 1989 cooled [19, 20] from 6 MeV beam energies to 0.4 meV, about 10 orders of magnitude. In 1990, an

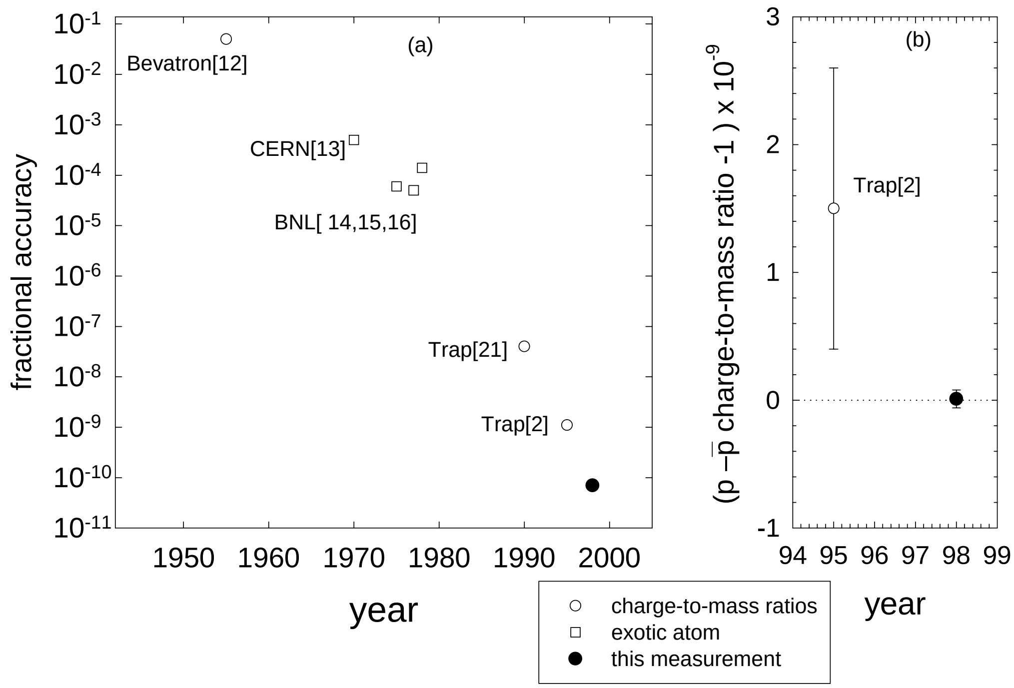

Figure 1.2: The numbers attached are the references to the measurements. (a) The accuracy of the antiproton charge-to-mass ratio measurements and the exotic atom measurements since the antiproton discovery. (b) A comparison of the present result and the 1995 published result [2].

initial measurement of the ratio of the antiproton and proton charge-to-mass ratios was made using hundreds of trapped antiprotons. The measurement was accurate to 4×10^{-8} [21]. In 1995, by comparing a single $\bar{p}$ with a single p, the ratio was measured to 1×10^{-9}[2]. By simultaneously trapping a single H^- and a single $\bar{p}$, we recently measured the ratio to 7×10^{-11}. This latest Penning trap experiment (dark circle in Figs. 1.2) is more accurate than measurements made with earlier techniques by six orders of magnitude.

1.3 Improving the Measurement

We improved the ratio of the $\bar{p}$ to p charge-to-mass ratios by measuring the cyclotron frequency of an H^- instead of a proton and by confining an H^- and a $\bar{p}$ in a Penning trap at the same time. This approach eliminated the systematic errors that occur when comparing particles of opposite charge. In this measurement the large magnetic field drift limited our accuracy. To minimize this error, we made faster and more accurate cyclotron frequency measurements.

The proton and the antiproton cyclotron frequencies were compared in a uniform magnetic field. The cyclotron frequency (ω_c) is the orbit frequency of a particle of charge (e) in such a field (Fig. 1.3a). It is called "cyclotron" after the particle accelerator that uses a strong, nearly uniform magnetic field. It is proportional to the magnetic ($\mathbf{B}$) field strength and the charge-to-mass ratio. It is given by:

$$\omega_c = \frac{|e\mathbf{B}|}{m}. \tag{1.1}$$

We used a reference charged particle such as a proton or an H^- ion to measure the $\mathbf{B}$ field strength. The difference between antiproton and proton cyclotron frequencies determines the ratio of their charge-to-mass ratios,

$$\frac{\omega_c(p) - \omega_c(\bar{p})}{\omega_c(p)} = 1 - \left|\frac{e/m(\bar{p})}{e/m(p)}\right|. \tag{1.2}$$

Since the $\mathbf{B}$ field drifted in time, we alternately measured $\omega_c(\bar{p})$ then $\omega_c(p)$.

Measuring the cyclotron frequency in just a $\mathbf{B}$ field is not practical since along the $\mathbf{B}$ field axis no force exists and the charged particle drifts freely out of the measurement region. We measured the antiproton's cyclotron frequency in a Penning Trap [22, 23]. A Penning trap is made from a uniform magnetic ($\mathbf{B}$) field superim-

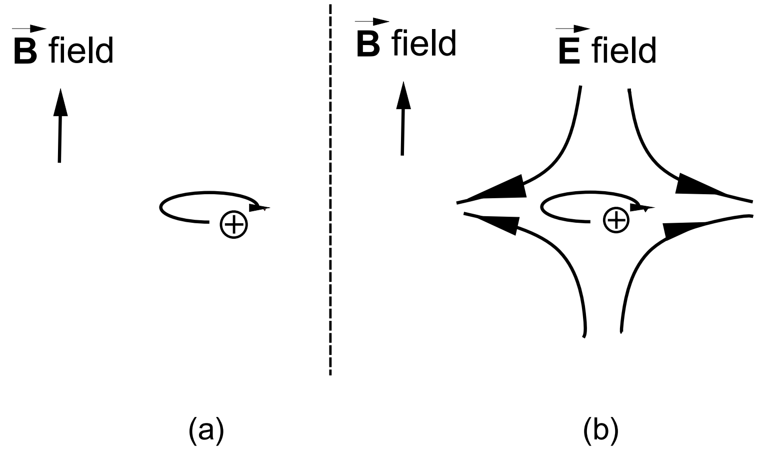

Figure 1.3: (a) In a uniform magnetic field a charged particle orbits at the cyclotron frequency ($\omega_c = eB/m$). (b) A superimposed electric quadrupole confines the particle along the magnetic field axis. Perpendicular to the **B** field, the electric force slightly reduces the cyclotron frequency.

posed upon an electric quadrupole (**E**) field. The electric field confines the particle along the **B** field axis (Fig. 1.3b). The quadrupole field is made by applying voltages to cylindrical electrodes. This field causes the particle to oscillate in simple harmonic motion along the field axis at the "axial" frequency (ω_z). Perpendicular to the **B** field axis the particle orbits in a superposition of two circular motions. These motions result from the inward magnetic force and the outward electric force. At a frequency slightly below the original cyclotron frequency the particle orbits at the "modified" cyclotron frequency (ω_c'). The modified cyclotron frequency (ω_c'), is the largest and most important frequency to measure. At a much lower frequency the particle also orbits at the "magnetron" frequency (ω_m). It is called "magnetron," after the electron tube which uses electrons orbiting in a strong magnetic field to produce microwaves. The three Penning trap frequencies are further described in Eq. 2.5 and Eq. 2.7. They measure the strength of the **B** field and the **E** field.

Combined in quadrature using an invariance theorem [24],

$$\omega_c^2 = (\omega_c')^2 + \omega_z^2 + \omega_m^2, \tag{1.3}$$

the three frequencies determine the original cyclotron frequency ($\omega_c = eB/m$).

Instead of measuring the proton cyclotron frequency ($\omega_c(p)$) directly, we measured the H^- cyclotron frequency ($\omega_c(H^-)$). The H^- to p mass ratio is accurately known (Sec. 4.1). By far the largest error is due to uncertainty in proton-to-electron mass ratio, yet this is still 50 times smaller than we require for an antiproton charge-to-mass ratio measurement accurate to 1 part in 10^{10},

$$\begin{aligned} M_{H^-}/M_p &= 1.001\ 089\ 218\ 750(2) \\ \omega_c(p) &= \omega_c(H^-)M_{H^-}/M_p. \end{aligned} \tag{1.4}$$

Since the mass ratio is accurately known, so is the ratio of the H^- and proton's cyclotron frequencies. Converting $\omega_c(H^-)$ to $\omega_c(p)$ with Eq. 1.4 adds no appreciable error to our measurement.

Using an H^- instead of a p eliminated the largest error in the previous work [1, 2]. A systematic error resulted from comparing particles of opposite charge because the equilibrium position of the particle in a Penning trap is set by the total electric field. Trapping particles of opposite charge in a Penning trap requires reversing the total electric field, and this cannot be done precisely. The largest part of the electric field comes from the voltage applied to the ring electrode, which is the central electrode making up a Penning trap (Fig. 1.4). When the voltage is switched, this electric field is reversed almost exactly. However, charges on non-conducting patches of the electrode surfaces produce a stray electric field which does not reverse. As shown

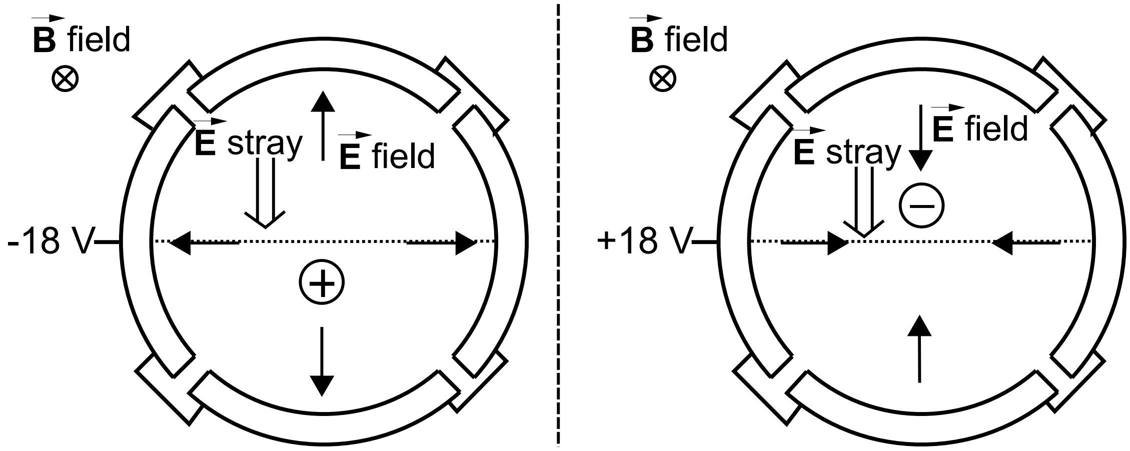

Figure 1.4: Illustrations of the 1 part in 10^9 systematic error of comparing particles of opposite charge(1995 published measurement [1, 2]). The ring electrode of a Penning trap and the different equilibrium positions of a proton (left) and an antiproton (right). The equilibrium position of a charged particle in a Penning is determined by the total **E** field. The electric field has a large component set by the applied voltage and also a small stray component set by charges on insulating surfaces inside the trap. The drawing is not to scale.

in Fig. 1.4, the $\bar{p}$ and a p then have different equilibrium positions in the trap. Insofar as the magnetic field is not quite perfectly uniform, the particles at different locations orbit at different cyclotron frequencies.

The 1995 published $\bar{p}$ to p result was limited by this systematic error. The cyclotron frequency of the antiproton was directly compared with the cyclotron frequency of the proton. Due to the non-conducting patches, the p and the $\bar{p}$ differed in position up to 20 μm (Fig. 1.4). A small magnetic field gradient (2 mGauss/mm [1] out of a 60 kGauss **B** field) caused the $\bar{p}$ and p cyclotron frequencies to differ by 1 part in 10^9, essentially the measurement uncertainty. Improving the direct $\bar{p}$ and p mass comparison required even better control of the electric field and an even more uniform magnetic field. Both were very difficult to obtain.

Comparing the H^- and the $\bar{p}$ cyclotron frequencies eliminated this systematic error. The size of the difference in equilibrium positions between the two charged particles is proportional to the difference in the applied electric field. In the direct proton/antiproton cyclotron frequency comparison described above, the applied **E** field made by applying 20 Volts to the ring electrode switched signs. This caused a 1 part in 10^9 systematic error. When we compared the cyclotron frequency of an H^- to that of an antiproton, the applied electric field only changed by a small amount (20 mV out of 20 V). The applied electric field was essentially the same at both the equilibrium positions of the H^- and antiproton. If the **B** field was stable in time, the H^- and $\bar{p}$ cyclotron frequencies would be measured in the same strength **B** field.

While $\omega_c(p)$ or $\omega_c(\bar{p})$ might shift due to a systematic error, to the lowest order the difference frequency ($\omega_c(p)$ - $\omega_c(\bar{p})$) does not shift. This is because the $\bar{p}$ and H^- are close in charge-to-mass and are measured under similar circumstances. Some examples of frequency shifts discussed in this thesis are: the influence of the outer particle on the inner one (Sec. 4.2.3); measuring the axial frequency when its orbit is too large (Sec. 2.4); not fully reducing the magnetron orbit (Sec. 2.5); and approximating the magnetic field as a constant when it drifts significantly (Sec. 4.4.1). Even though the difference frequency was not susceptible to shifts, we still insured that the measurement procedure did not shift either $\omega_c(\bar{p})$ or $\omega_c(H^-)$.

We trapped a single $\bar{p}$ and a single H^- ion at the same time. When measuring the H^- cyclotron frequency, we kept the $\bar{p}$ in a large enough cyclotron orbit so that it did not change the H^- cyclotron frequency. (This is discussed in Sec. 4.2.3.) We used a radio-frequency drive applied to one segment of the ring electrode. The drive made an oscillating electric field across the ring at the precise frequency needed to increase the orbit of the antiproton's cyclotron motion. Since the charge-to-mass ratio of the H^- and the $\bar{p}$ differ by 1 part in 10^3, their cyclotron frequencies also

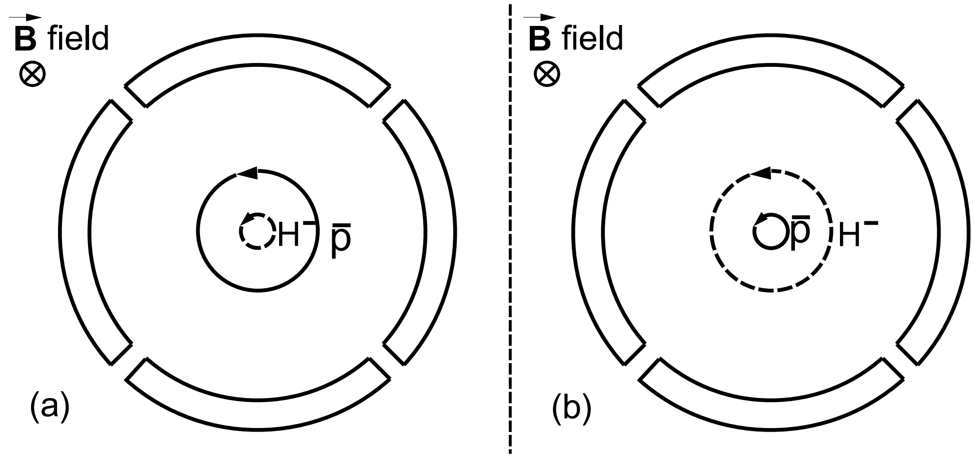

Figure 1.5: The modified cyclotron orbits of H^- and $\bar{p}$ and the ring trap electrode during the measurement. (left) First, the H^- was measured in the trap center while the $\bar{p}$ was kept in a cyclotron orbit large enough not to influence the H^- (1 mm). (right) Next, the $\bar{p}$ was measured in the trap center while the H^- was kept in a large orbit. The drawing is not to scale.

differ by 1 part in 10^3. When the antiproton's radio frequency drive strength was low enough it did not affect the H^-. With the $\bar{p}$ in a 1 mm orbit, we measured the Penning trap frequencies of the H^-. Following this we reversed the position of the $\bar{p}$ and the H^- and measured the Penning trap frequencies of the $\bar{p}$ (Fig. 1.5). We alternated between measuring an antiproton and an H^- four to six times.

Simultaneously trapping the H^- and the $\bar{p}$ simplified the measurement and allowed more alternate proton and antiproton cyclotron frequency measurements compared with the procedure used in the direct proton/antiproton comparison [1, 2]. In that work, the proton was first trapped and its cyclotron frequency measured. Then the trapping voltage was reversed and an antiproton was loaded and its cyclotron frequency measured. To load an antiproton, millions of cooling electrons were first loaded, high voltages were switched, and then the electrons were removed. The stray electric fields sometimes changed after loading, and it could take hours before the cyclotron frequency of the antiproton was ready to be measured again. In this comparison of the $\bar{p}$ and $H^-$the particles were loaded together. During the measurement cycle more alternate H^- and $\bar{p}$ cyclotron frequency measurements were made since we had eliminated the need for loading electrons and switching high voltages during the measurement. Each of the eight measurements made in 1995 by simultaneously trapping an antiproton and an H^- is accurate to 3 parts in 10^{10}.

The major source of error in the $\bar{p} - H^-$ comparison was caused by the large $\mathbf{B}$ field drift between the $\bar{p}$ and H^- measurements. This occurred when the center of the Penning trap mechanically drifted compared to the coils which make the $\mathbf{B}$ field. Unlike the systematic error of comparing oppositely charged particles, this error did not systematically cause $\omega_c(\bar{p})$ to be greater than $\omega_c(p)$ or vice-versa. Instead it increased the scatter between measurements. To keep the $\mathbf{B}$ field drift low enough to make any accurate measurement a regulation system (Sec. 4.3.1) controlled the pressure over each of the cryogenic dewars in the magnet and in the apparatus. After improving this circuit, the system reliably regulated during all the $\bar{p} - H^-$ measurements made in 1995 and 1996. Even with this circuit working, the $\mathbf{B}$ field drifted up to 2 parts in 10^9 between $\bar{p}$ and H^- cyclotron measurements, about thirty times the final measurement accuracy.

In 1996, we halved the time between $\bar{p}$ and H^- cyclotron measurements compared with those made in 1995. This minimized the effect of the drifting $\mathbf{B}$ field. To accomplish this we doubled the signal-to-noise ratio for the most important motion, the modified cyclotron motion (Sec. 2.3.2). We reduced the trap capacitance, improved the tuning of the RLC circuit used for detection (Sec. 2.3.3), and increased the coupling between the tuned circuit and the particle. This allowed more accurate and quicker cyclotron frequency measurements. Because of the large $\mathbf{B}$ field drift, we fit the data consistently allowing the $\mathbf{B}$ field to drift in time. We fit for the frequency difference ($\omega_c(p) - \omega_c(\bar{p})$ in Eq. 1.2) by fitting hundreds of data points in one fitting step. As a result of these improvements we measured in one night in 1996 the ratio of the proton and antiproton charge-to-mass ratios accurately to 1 part in 10^{10}.

The major challenge of the measurement was to keep the H^- trapped for over a day, the time required to complete a measurement. Initially the H^- stayed trapped for less than 3 hours. To keep it for days, the trap vacuum had to be better than 4×10^{-16} Torr (page 98). All the electrons used initially for loading $\bar{p}$ and H^- had to be removed. While we cycled a cleaning routine to remove the electrons, we kept the H^- and $\bar{p}$ trapped. To keep the H^-, the axial motion and the magnetron motion of the H^- had to remain small. After months of trials, we developed a procedure to keep the H^- trapped for days. Still, our method was not highly consistent; we gathered only nine nights of $\bar{p} - H^-$ comparisons.

In this work, we show that size of the antiproton and the proton charge-to-mass ratios are the same to 7 parts in 10^{11} (Fig. 1.2). This measurement sets the most accurate limit for CPT violation in protons and is among the most precise mass spectroscopy measurement made to date [3]. For the first time, two ions are simultaneously trapped for a precise mass spectroscopy measurement.

The remainder of this work describes how we compared the proton and antiproton charge-to-mass ratios. Chapter 2 describes how we measured the three motions in a Penning trap. Chapter 3 describes loading and keeping a single H^- and antiproton in the trap. Chapter 4 describes the steps necessary to alternately measure the $\bar{p}$ and H^-, and how the data determines the $\bar{p} - p$ charge-to-mass ratios. It also describes the influence of the outer particle and the changing **B** field. Chapter 5 describes the measurement data and shows how we achieved our accuracy. Finally, Chapter 6 describes how the measurement could be improved in the future.

In this thesis, angular frequencies (ω) are referred to in units of radians/second and cyclical frequencies (ν) in units of cycles/second. They are related by $\omega = 2\pi\nu$.

Chapter 2

Measuring the Penning Trap Frequencies

A charged particle in a Penning trap oscillates at three frequencies: the modified cyclotron frequency (ω_c'), the axial frequency (ω_z) and the magnetron frequency (ω_m). The three frequencies together determine the cyclotron frequency (ω_c) of a charged particle orbiting in a magnetic field. The trap motions are well described in Ref. [25], and details of the trap used for this measurement are well described in Ref. [1].

In this experiment, the measurement of the modified cyclotron frequency limited the accuracy. We more than doubled the accuracy by improving the signal-to-noise ratio in the cyclotron detection circuit and by increasing the cyclotron damping. The results of this study are relevant to other Penning trap measurements that use a high frequency RLC tuned circuit for particle detection.

Ideally, we want to measure the three Penning trap frequencies in the smallest possible orbits, so that frequency shifts due to electric and magnetic field inhomogeneities are as small as possible. Furthermore, frequency shifts due to special relativity are also smaller. On the other hand, orbits must be large enough to get enough signal to measure the cyclotron and axial motions. In the following sections the motions in the Penning trap are reviewed, and the precision that each frequency must be measured is discussed. The detection of the particle motions is described. Next, we show how we measure each Penning trap frequency and how frequency shifts that cause errors in the cyclotron frequency measurement are prevented.

2.1 The Penning Trap

A spatially uniform 59 kGauss **B** field was used to perform the experiment (Table 2.1). It was made from a superconducting solenoid, wound with wire made from a single filament of niobium titanium (NbTi). When the **B** field gradient is low a change in the relative positions of the trap center and the solenoid does not affect **B** field in the trap center (Sec. 4.3.1). When the **B** field curvature is low, a particle experiences the same **B** field independent of its magnetron radius (Fig. 2.32). The curvature in the magnetic field is characterized by the second order Legendre coefficient for an azimuthally symmetric spherical expansion. This coefficient is called a "bottle" in the ion trap literature. The **B** field uniformity during the $\bar{p}$ − H^- comparison was the same as the **B** field uniformity used in the $\bar{p} - p$ comparison completed in 1995 [2]. The **B** field gradients and curvatures in all three directions were carefully measured and tuned to be as small as possible. It was uniform enough in space so that the **B** field at the equilibrium position of the $\bar{p}$ and H^- was the same to 1 part in 10^{10}. Still, the **B** field drifted in time, differing between alternate cyclotron measurements. While the **B** field gradient and bottle were low, even lower values would have improved the measurement.

An open-endcap Penning trap [26] produced the electric field in the trap center.

Gradient (Gauss/cm)	Bottle (B_2) (Gauss/cm^2)
0.02	0.5

Table 2.1: The typical gradient and bottle for the 59 kGauss **B** field used in this experiment [1]. The bottle is the second order coefficient for an azimuthally symmetric spherical expansion of the magnetic field.

We used an open-endcap Penning trap rather than a more typical hyperbolic Penning trap [17] because antiprotons could be easily loaded into its trap center through the large openings. The open-endcap Penning trap consisted of a ring electrode, two compensation electrodes and two endcaps made of stacked hollow cylinders (Fig. 2.1). The ring and compensation electrodes were divided to allow particle detection. The electrodes were made of oxygen free high conductivity (OFE) copper.

Ideally the electrostatic potential is a quadrupole. When a voltage is applied to the ring electrode (-V_0) and another voltage is applied to the compensation electrode (V_c), the electrostatic potential near the trap center is given by the expansion,

$$V(r,\theta,\phi) = \frac{V_0}{2}\left[C_2\left(\frac{r}{d}\right)^2 P_2\left(\cos(\theta)\right) + C_4\left(\frac{r}{d}\right)^4 P_4\left(\cos(\theta)\right) + \cdots\right] \quad (2.1)$$

$$d^2 = \frac{1}{2}\left(z_0^2 + \frac{\rho_0^2}{2}\right), \quad (2.2)$$

where (r,θ,ϕ) are the spherical coordinates from the trap center and $P_n(\cos(\theta))$ are the Legendre polynomials. The characteristic trap dimension (d) is related to the trap radius ($\rho_0 = 0.600$ cm) and the trap's axial length ($z_0 = 0.586$ cm) as shown in Fig. 2.1. The applied voltages are symmetric around the trap axis so the electrostatic potential does not depend on ϕ. The odd coefficients $(C_1, C_3, C_5\cdots)$ are zero insofar as the potential below the ring electrode is identical to the potential above it ($\theta \rightarrow \pi - \theta$). When the compensation voltage (V_c) is adjusted properly, the

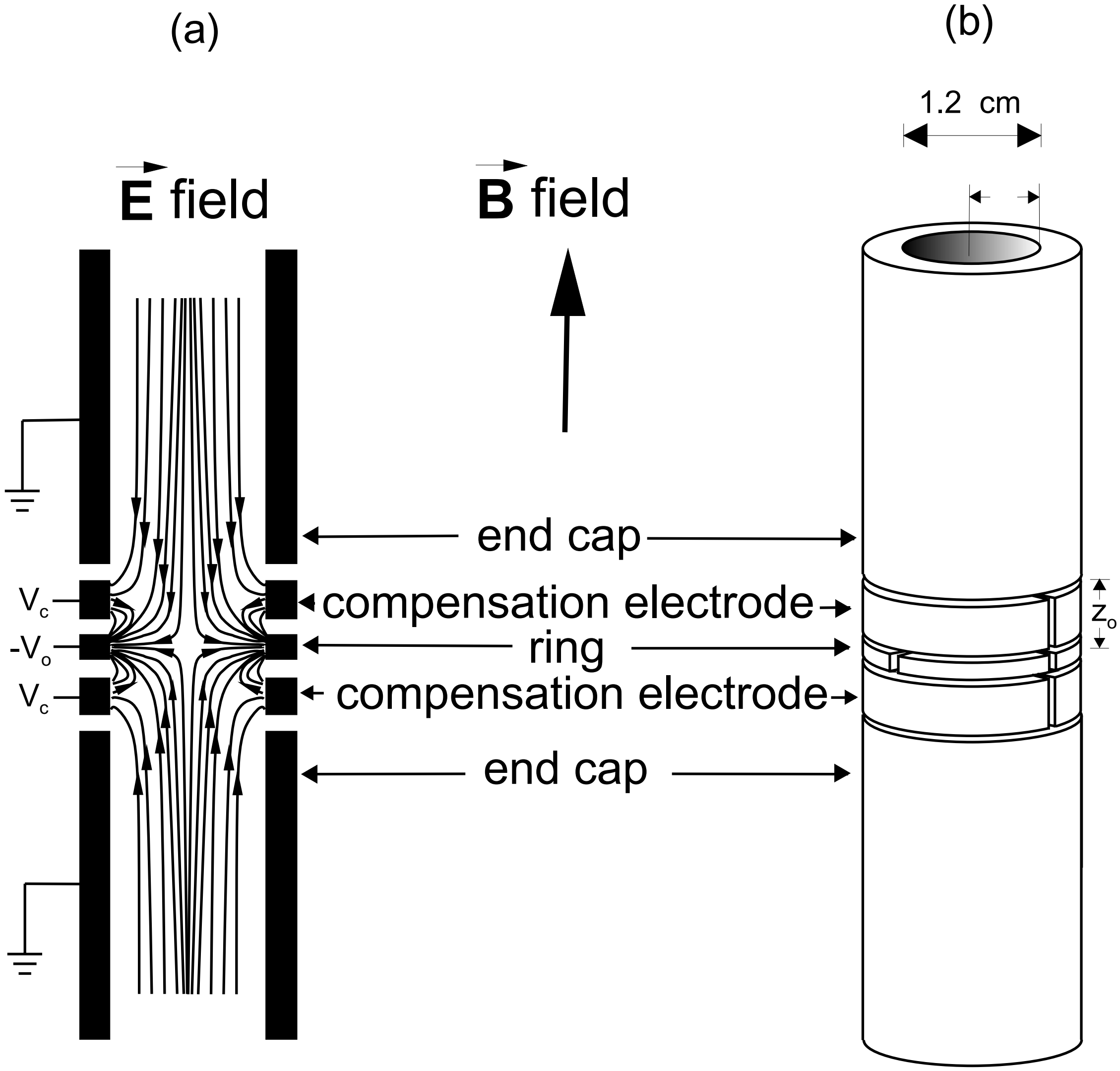

Figure 2.1: Open-endcap Penning trap. (a) When the proper ratio of $-V_c/V_0$ is applied to the trap, the potential in the trap center is well approximated by a quadrupole. Shown are the **E** field lines to trap a positively charged particle. V_0 is positive. (b) ρ_0 is the trap radius and z_0 is the trap length. The ring electrode is divided into quadrants and the compensation electrode is split into halves. This allows us to detect the three particle motions.

higher order even coefficients, C_4 and C_6, are also zero. The coefficient C_2 relates the strength of the electric field to the ring voltage (-V_0). For a hyperbolic trap the coefficient C_2 is approximately 1, and for the open-endcap trap C_2 is calculated to be 0.545 [26]. Expressed in cylindrical coordinates (ρ, z), the potential is:

$$V(\rho, z) = C_2 V_0 \left(\frac{z^2 - \rho^2/2}{2d^2} \right). \tag{2.3}$$

This potential causes the particle to exhibit simple harmonic motion along the **B** field axis. As a particle of charge (e) moves along the **B** field axis, it feels an electric restoring force, $F = -m\omega_z^2 z$ (Eq. 2.3), where ω_z^2 is:

$$\omega_z^2 = \frac{eV_0 C_2}{md^2}. \tag{2.4}$$

For the force to be restoring, the axial electric field must point toward the trap center. For a positively charged particle V_0 is positive $(eV_0 > 0)$. The equation of motion is:

$$m\ddot{z} = -m\omega_z^2 z. \tag{2.5}$$

The particle oscillates at the axial frequency, ω_z. This frequency measures the static electric field strength.

The open-endcap Penning trap makes a precise quadrupole potential over a large region [26]. This is important since the particle is measured in a large axial orbit. To avoid shifts in the measured axial frequency, the potential should be the quadrupole of Eq. 2.3. The coefficient C_4 measures the degree to which the potential is not harmonic or "anharmonic" and is directly proportional to the voltage ratio $-V_c/V_0$. To make C_4 zero for the open-endcap trap, $-V_c/V_0$ should ideally be 0.8811 [26]. By measuring the axial frequency shift when the axial orbit was large, we adjusted V_c

and tuned C_4 to zero (Sec. 2.4). A careful choice of compensation electrode lengths sets C_6 to zero when C_4 is tuned to zero. This maximizes the quadratic region of the trap. In comparison to a hyperbolic Penning trap of a comparable size, the disadvantage of the open-endcap Penning trap is that it produces a smaller quadratic region. The choice of electrode lengths keeps the axial frequency independent of V_c to the first order. The electrode length keeps the coefficient C_2 of Eq. 2.4 independent of V_c. While V_c is optimally adjusted, the axial frequency is stable, making tuning much easier.

The Lorentz equation describes the motion in the plane perpendicular to the **B** field axis,

$$m\ddot{\vec{\rho}} = e(\vec{E} + \dot{\vec{\rho}} \times \vec{B}). \tag{2.6}$$

The electric force is radially outward (Fig. 1.3b). It is measured by the axial frequency, $eE/m = \omega_z^2\rho/2$ (Eq. 2.3 and Eq. 2.4). The magnetic force is in the plane. When the particle orbits in a circle, the force is radially inward. It is measured by the cyclotron frequency, $e\dot{\vec{\rho}} \times \vec{B}/m = -\omega_c|\dot{\rho}|$. In this case $|\dot{\rho}| = \omega\rho$ and $\ddot{\rho} = -\omega^2\rho$, where ω is the particle's angular frequency. The Lorentz force equation becomes:

$$-\omega^2\rho = \frac{1}{2}\omega_z^2\rho - \omega_c\omega\rho. \tag{2.7}$$

In the plane, the particle orbits in a superposition of two circular motions. The frequencies are given by the two solutions to Eq. 2.7, called the modified cyclotron frequency (ω_c') and the magnetron frequency (ω_m),

$$\begin{pmatrix} \omega_c' \\ \omega_m \end{pmatrix} = \frac{\omega_c}{2} \pm \frac{\sqrt{\omega_c^2 - 2\omega_z^2}}{2}. \tag{2.8}$$

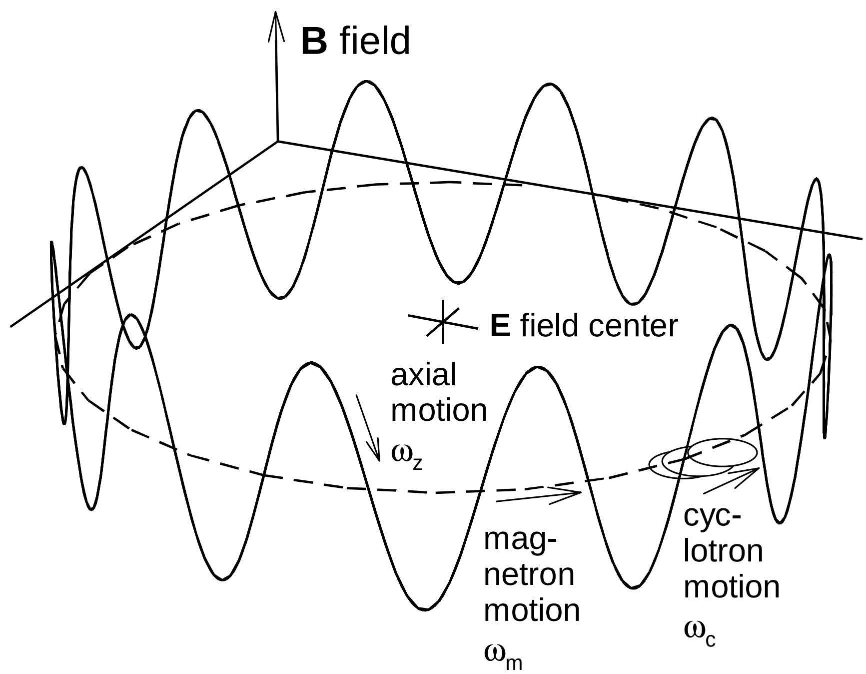

Figure 2.2: The three independent motions in an ideal Penning trap. Parallel to the **B** field axis, the particle oscillates at the axial frequency (ω_z). In the perpendicular plane the electric and magnetic forces cause the particle to orbit slowly at the magnetron frequency (ω_m), and quickly at the modified cyclotron frequency (ω_c').

The modified cyclotron frequency (ω_c') occurs at a high frequency when the electric force is small compared with the magnetic force. This frequency is slightly below the original cyclotron frequency since $\omega_z \ll \omega_c$. For this reason it is called "modified." The magnetron frequency (ω_m) occurs at a much lower frequency when the electric and magnetic forces are nearly equal in magnitude. The magnetron velocity is $\vec{v} \approx \vec{E} \times \vec{B}$, just as for a mass filter. The axial, cyclotron, and magnetron motions are shown together in Fig. 2.2.

The motion in the plane depends on the relative size of the magnetron and cyclotron radii. When the magnetron radius is large compared with the cyclotron radius, the particle never enters the trap center (Fig. 2.3a). Cornell and cowork-

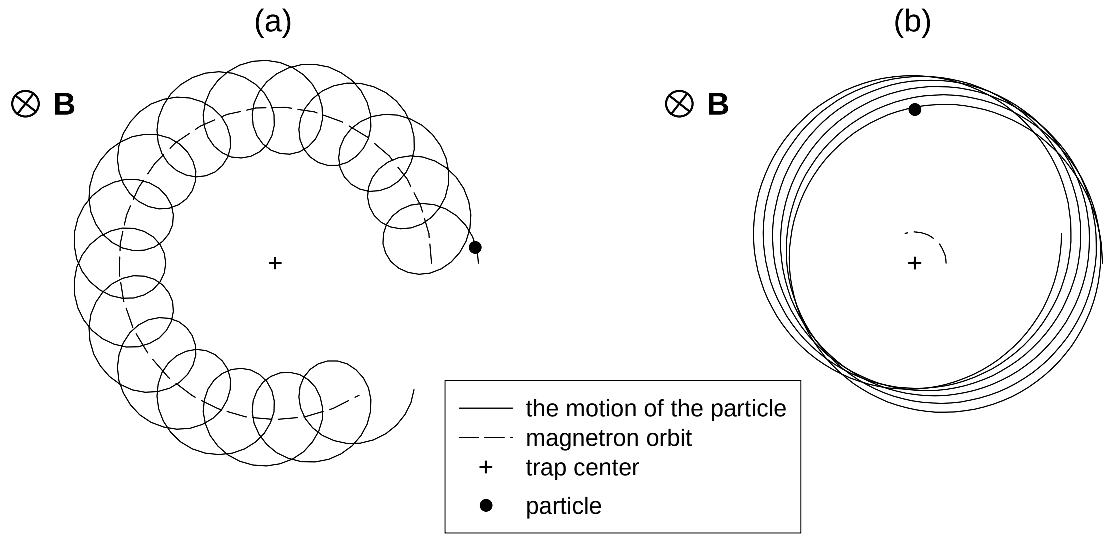

Figure 2.3: The motion of a charged particle perpendicular to the **B** field in a Penning trap: (a) The motion of the particle when the magnetron orbit is larger than the cyclotron orbit; (b) The motion of the particle when the magnetron orbit is smaller than the cyclotron orbit.

ers [27] propose measuring two simultaneously trapped ions in this limit. When two particles have the same magnetron orbit, they sample the same electric and magnetic field so, in principal, the measurement is free from systematic errors. The difficulty is that when the magnetron orbit is large, neither the electric field nor the magnetic field is as pure as it is in the trap center. We worked in the limit where the magnetron orbit was small compared with the cyclotron orbit (Fig. 2.3b). The magnetron radius needed to be reduced to less than 50 μm. Afterwards the cyclotron orbit was measured when its radius varied between 360 μm and 24 μm.

An invariance theorem [24] relates the modified cyclotron frequency (ω_c'), the axial frequency (ω_z), and the magnetron frequency (ω_m) to the cyclotron frequency (ω_c),

$$\omega_c^2 = (\omega_c')^2 + \omega_z^2 + \omega_m^2, \tag{2.9}$$

Motion	Frequency	Precision required	
	(MHz)	(Hz)	fractional precision
ν_c	89.251	0.01	1×10^{-10}
ν_c'	89.244	0.01	1×10^{-10}
ν_z	1.149	0.8	7×10^{-7}
ν_m	0.007	120	2×10^{-2}

Table 2.2: The precision required of each Penning trap frequency to measure ν_c precisely to 1 part in 10^{10}. $\omega = 2\pi\nu$. $\mathbf{B} = 59$ kGauss, V_0= -26 V.

which is more general than Eq. 2.8. It holds when there is an angle between the electric field and magnetic field axes. It also holds when the trap has an additional quadratic electrostatic potential that is not proportional to the second order Legendre Polynomial, P_2. To use the invariance theorem, we kept the electric field quadratic, and kept the magnetic field as spatially uniform. We also measured the modified cyclotron frequency with no shift due to special relativity.

The modified cyclotron, the axial and the magnetron frequencies each require a different precision (Table 2.1). Since ω_c' is the dominant contribution to ω_c, it is the most accurate and the most difficult to measure. The axial and magnetron frequencies contribute much less to ω_c, so they do not need to be measured as accurately.

2.2 Particle Detection

The modified cyclotron motion of the antiproton, the axial motion of the antiproton and the electron axial motion are all detected the same way. A resistor is attached across the appropriate trap electrodes dissipating the energy in the motion and reducing the particle's orbit. The resistor also provides a measurable signal. Differences in the frequency, the trap capacitance and the mass make detection of the three motions much different. For concreteness the proton axial motion is taken as an example. How the motion is both damped and detected is described here.

The resistor is made by attaching an inductor (L) across the trap. At the particle's oscillation frequency the reactance of the inductor (L) cancels out the reactance of the trap capacitance (C). The tuned circuit acts like a pure resistor to ground. The value of the resistor is related to the quality factor (Q) of this circuit,

$$R = \frac{Q}{\omega_z C}. \tag{2.10}$$

For the greatest signal-to-noise ratio, this resistor should be as large as possible, and the RLC tuned circuit should be low loss. At high frequencies (above 10 MHz) the inductor is made out of silver plated copper, at the proton axial frequency (1.2 MHz) it is made out of the superconductor, NbTi [1]. Losses in the circuit are kept to a minimum by having a very well defined path for the current return. An example of the current path is shown in Fig. 2.15.

A particle with charge (e), mass (m), and position relative to the trap center (z) feels a damping force (Fig. 2.4). The particle's oscillating motion induces an image current (I) to pass through the resistor (R). This creates a voltage across the trap (V_s) and an electric force:

$$f_e = -\frac{e\alpha V_s}{2z_0}, \tag{2.11}$$

which opposes the particle's motion. Here $2z_0$ is the spacing between the trap electrodes and α is a geometric constant which relates the strength of the electric field to the induced voltage (V_s). If the particles were trapped between infinite parallel plates α would be 1. In the open-endcap Penning trap α depends on which electrodes are coupled to the particle and varies between 0.25 and 0.45. The geometrical

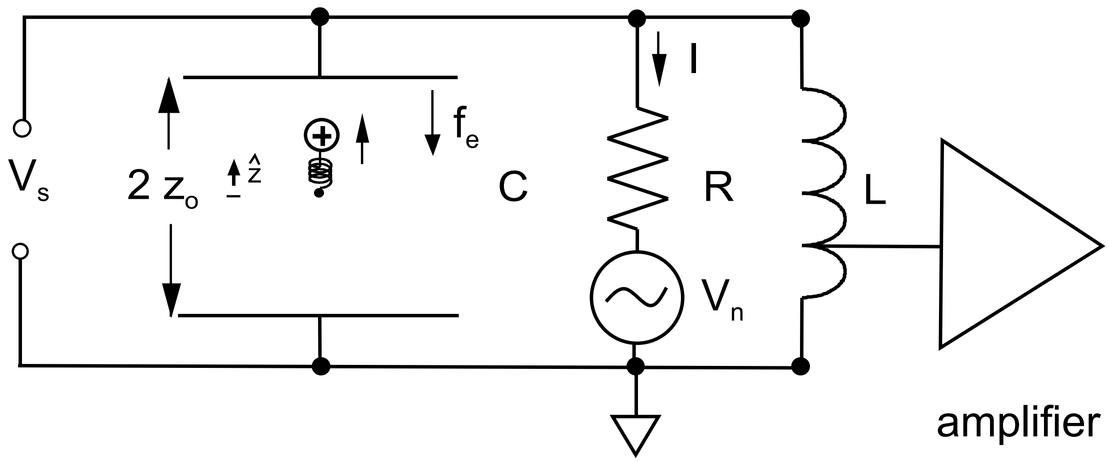

Figure 2.4: Detecting the particle motion. We attach a low loss inductor (L) across the trap electrodes. At the axial frequency, the inductor (L) tunes out the trap capacitance (C) and the circuit behaves like a pure resistor (R). The particle's motion induces a current to flow (I) through the resistor (R). This current both dissipates the energy of the particle and produces a detected signal.

constant (α) has been calculated for the split compensation electrode [26] used to detect the axial motion. By expanding the trapping potential allowing asymmetric solutions, we also calculated α for the cyclotron motion[1]. The calculation agrees with the experiment to at least 8% [1].

The resistor dissipates the particle's energy. The rate at which the particle loses energy, $-f_e\dot{z}$, equals the rate that the resistor dissipates energy, V_sI. This equality determines the induced current [28],

$$I = \frac{e\alpha}{2z_0}\dot{z}. \tag{2.12}$$

The particle produces a current which depends on the particle's velocity and is independent of the resistance the current goes through.

[1] I solved this problem for the 1995 published charge-to-mass comparison. It is written up in the thesis of David Phillips [1].

The opposing electric force is also proportional to the velocity. This force adds a damping term to axial equation of motion (Eq. 2.5),

$$m\ddot{z} + m\omega_z^2 z = -m\frac{\dot{z}}{\tau_z}, \tag{2.13}$$

where τ_z is given by:

$$\tau_z = \left(\frac{2z_0}{e\alpha}\right)^2 \frac{m}{R}. \tag{2.14}$$

In the equivalent formula for the cyclotron motion, the trap's axial height is replaced by the trap radius ($z_0 \rightarrow \rho_0$). Since $1/\tau_z \ll \omega_z$, the motion is very weakly damped; the equation's quality factor, $Q = \omega_z \tau_z$, is about 4×10^7. Solving this equation shows that the axial energy (E_z) decreases in time with a time constant, τ_z.

$$E_z(t) = E_z(0)e^{-t/\tau_z}. \tag{2.15}$$

The opposing damping force exponentially dissipates the particle's axial energy. When τ_z is short, the energy dissipates faster.

The voltage across the resistor (V_s) is set by the noise in the circuit. The Johnson noise of the resistor (R) contributes to the input noise. It is given by:

$$V_n^2 = 4\kappa_B T R \Delta\nu, \tag{2.16}$$

where κ_B is the Boltzmann constant, T is the temperature of the resistor, and $\Delta\nu$ is the frequency bin width that the signal is measured in. The input resistance of the GaAs FET used to amplify the signal also contributes to the input noise. This is kept at a minimum by coupling as small a signal to the FET as possible, a signal not much larger than the amplifier's input noise. Typically we couple 1/3 of the

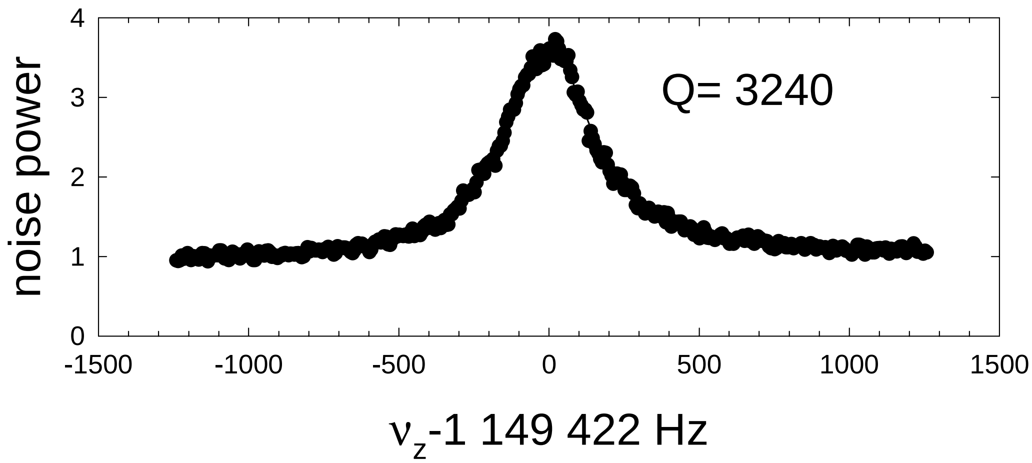

Figure 2.5: The noise power of the input RLC circuit for the proton axial amplifier. The amplifier can detect a single $\bar{p}$ or H^-.

inductor to the input of the FET. This noise adds to the Johnson noise and increases the effective temperature of the RLC tuned circuit.

The output signal measures the voltage across the input RLC circuit (V_s). On resonance the reactance of the capacitor (C) and inductor (L) cancel. The input signal (V_s) is then the noise voltage (V_n). Off resonance the input voltage (V_s) decreases. The reactance of the capacitor (C) and the inductor (L) add a reactance to ground. In series with the resistor (R), this divides down the noise voltage (V_n). Because of this divider, V_s is proportional to the input impedance. It has a Lorentzian profile in frequency. This noise profile is amplified near the trap at 4 K, further amplified at room temperature and viewed on a frequency spectrum analyzer (Fig. 2.5). The width the lorentzian of the noise profile measures the circuit quality factor (Q) and thus the input resistance using Eq. 2.10.

The particle is most easily measured in a large orbit, with higher kinetic energy (E_z). The square of voltage induced ($V_s^2 = (IR)^2$) is proportional to the particle's energy (Eq. 2.12). When the frequency bin width ($\Delta\nu$) is larger than $1/(2\pi\tau_z)$, all the signal is deposited in one bin. In this case, the signal-to-noise ratio is given by:

$$\frac{V_s^2}{V_n^2} = \frac{E_z}{2\kappa_B T \Delta\nu \tau_z}. \tag{2.17}$$

A shorter τ_z makes it possible to detect a particle with less energy. By cooling the apparatus to 4 K we maximize the signal-to-noise ratio. This reduces the effective temperature of the input circuit and reduces the Johnson noise and FET input noise. It also minimizes losses in the tuned circuit which makes Q higher and the damping time (τ) shorter. Cooling to 4 K also allows us to attain the low vacuum necessary to measure single particles.

The cyclotron motion of a single particle places us in the rare position to estimate the noise temperature of the amplifier. The measured cyclotron frequencies were fitted and determined the cyclotron energy (E_c) and the cyclotron time constant (τ). This is described on page 35. The signal-to-noise ratio shown in Fig. 2.6a occurred for a 10 eV cyclotron excited particle with a frequency bin width of 0.02 Hz, and with a time constant of 7.2 minutes. This signal-to-noise ratio indicated that the noise temperature was 60 K (Eq. 2.17), much larger than 4 K, the temperature of the thermal bath. Perhaps the amplifier was not well enough heat sunk. It was heat sunk through OFHC copper supports in contact with a 4 K liquid helium dewar. The amplifier, a Mitsubishi GaAs FET model 1100, dissipated 10 mWatts when operating.

The method to detect the motion depends on the time constant (Table 2.3). The cyclotron motion had the longest time constant. The long time constant gave a narrow signal but also gave lower signal-to-noise. An oscillating electric field was first used to increase the particle's cyclotron energy and orbit radius. The cyclotron frequency was measured while the particle spiraled into the trap center. Over the

Motion	α	Resistor				τ		
		ν (MHz)	Q	C (pF)	R (MΩ)	τ (sec)	$\delta\nu$ (Hz)	accuracy (%)
$\bar{p}$ cyclotron	0.356	89.244	900	7.5	0.20	350	0.0005	5
$\bar{p}$ axial	0.450	1.149	3240	22	20	2.2	0.07	10
e^- axial	0.450	63.5	800	14	0.14	0.17	0.94	40

Table 2.3: The time constant (τ) measured in 1996 for the antiproton ($\bar{p}$) cyclotron motion, the antiproton ($\bar{p}$) axial motion and electron (e^-) axial motion. $\omega = 2\pi\nu$. The $\bar{p}$ cyclotron time constant is measured and the others are estimated based on Q and capacitance measurements. For the $\bar{p}$ cyclotron motion α is calculated using two quarter ring segments as in the 1996 configuration. The damping width in Hz is $\delta\nu = 1/(2\pi\tau)$.

span of 3 to 4 time constants, some 20 minutes, the particle decayed down to an orbit too small to measure (Fig. 2.6a). The details of this are described on page 36. This same method can work for detecting the axial motion but since the time constant is much shorter, the measurement must be completed within 10 seconds (Table 2.3). Instead, we used two oscillating electric fields to put energy into the axial orbit which then dissipated in the external resistor (R). The motion is that of a driven harmonic oscillator with damping. While the electric fields were on, the particle remained in a large orbit. We performed a Fourier transform to measure the proton axial frequency (Fig. 2.6b). This is further discussed in Sec. 2.4.

For short time constants the motion can be detected by driving the particle with the input noise. Near the resonant frequency the reactance of L and C cancel. The circuit behaves as the resistor (R) coupled to the particle. Since the particle's velocity is proportional to the induced current (I in Eq. 2.12) the equation of motion (Eq. 2.13) is also an equation for the current. When the noise term is added, it can be rewritten as [29]:

$$-L_c\dot{I} - \frac{1}{C_p}\int^t I(\varepsilon)\,d\varepsilon = RI + V_n, \tag{2.18}$$

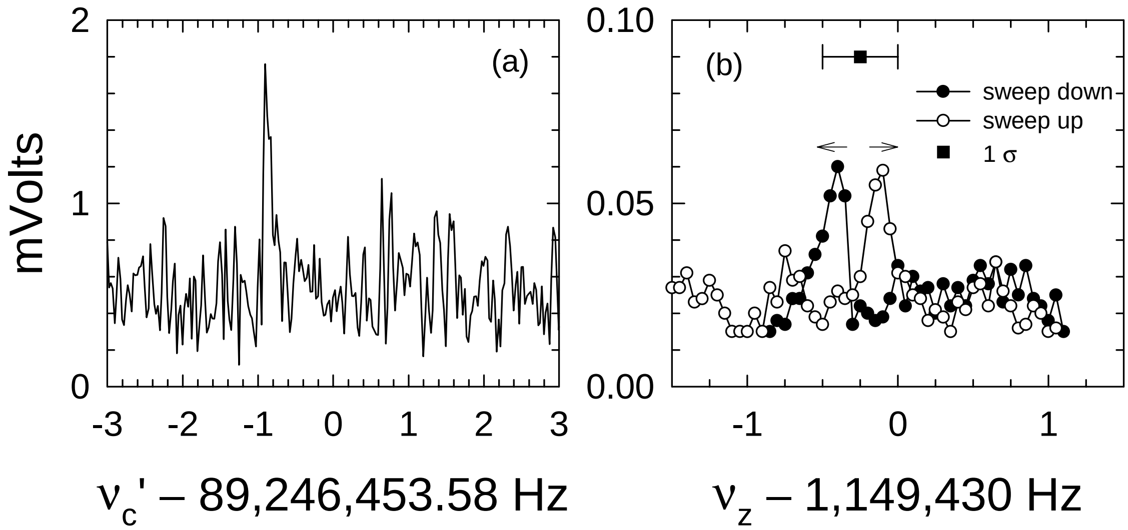

Figure 2.6: (a) A signal from a single $\bar{p}$ excited in a 9.5 eV cyclotron orbit. Since τ was 7.2 minutes, and the frequency bin width was $\Delta\nu$= 0.02 Hz, the circuits effective temperature was about 60 K (Eq. 2.17). (b) The response from the driven axial motion. This signal is discussed on page 62.

where $L_c = \tau_z R$ and $C_p^{-1} = \omega_z^2 \tau_z R$. This is the equation for a series RLC circuit with noise. The particle adds a series inductor and capacitor to the tuned circuit as shown in Fig. 2.7. For frequencies (ω) close to the particle's resonant frequency (ω_z) the current through the circuit is:

$$|I|^2 \propto \frac{1}{(2\tau_z(\omega - \omega_z))^2 + 1}. \tag{2.19}$$

On resonance ($\omega = \omega_z$) the current is maximum. The series inductor (L_p) and capacitor (C_p) short out the noise, and the measured signal V_s dramatically goes to zero. At this frequency the particle gains $\frac{1}{2}\kappa_B T$ of axial energy. Off resonance, the noise level returns to the background set by the input noise. We call the signal seen when the noise is shorted a "dip." In terms of the measured frequency ($\nu = \omega/(2\pi)$) the width of the "dip" is $\delta\nu = 1/(2\pi\tau_z)$. The width of the "dip" increases with the

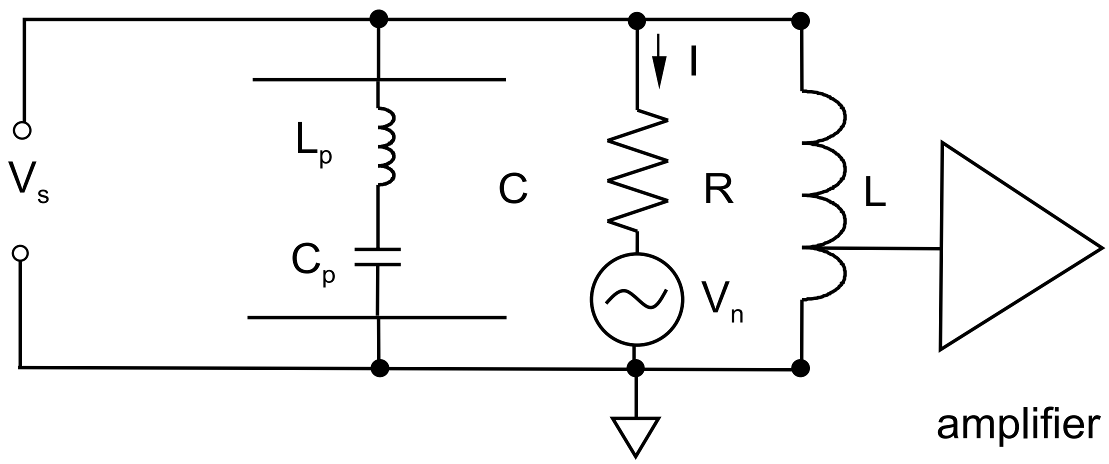

Figure 2.7: The effect of the particle is to add series inductor (L_p) and capacitor (C_p) across the resistor (R). Shown here is an equivalent circuit.

number of particles. Two examples of electron "dips" are shown in Fig. 2.8.

Since the time constant was too long we did not detect cyclotron "dips" nor proton axial "dips." With a cyclotron time constant of 350 sec., detecting a cyclotron "dip" was impossible. Because the "dip" width per particle was 0.4 mHz, it took nearly one hour to perform the Fourier transform. In that time the "dip" center frequency drifted by 200 linewidths. Were the cyclotron time constant 20 times shorter, detecting a "dip" would be conceivable. Detecting a proton axial "dip" is possible, but difficult. In order to see the axial proton "dip" the amplified signal was averaged for at least 15 minutes [1, 30]. It was easier to measure the proton axial motion using applied oscillating electric fields as described above instead of measuring a "dip."

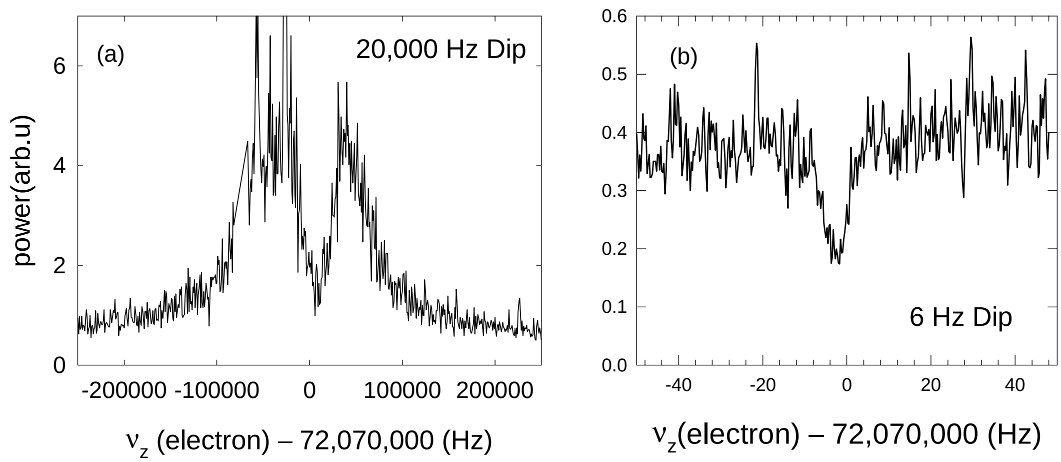

Figure 2.8: Electron "dips" in the noise profile show how the width varies with the number of electrons. (a) The noise profile of the electron amplifier with 20,000 electrons in the trap. When the frequency is much different than the axial frequency L or C of the tuned circuit short out the noise. At the resonant frequency of the particles, the series inductor (L_p) and capacitor (C_p) short out the noise. (b) The noise profile with an expanded frequency axis from only 6 electrons. The width per electron is 1 Hz.

2.3 The Modified Cyclotron Motion

The modified cyclotron frequency (ν_c') was the largest and most important frequency to measure. Its accuracy limits the accuracy of the charge-to-mass ratio. Due to special relativity, the modified cyclotron frequency depends on the particle's kinetic energy. The modified cyclotron motion is coupled to another RLC tuned circuit, which exponentially damped the energy. While the particle damped, we measured the modified cyclotron frequency (ν_c'), then we performed an initial nonlinear fit to determine the modified cyclotron frequency for a particle with no kinetic energy (ν_{c0}'). The initial fit assumed that the $\mathbf{B}$ field was constant over the one hour required to attain an accuracy of 1 part in 10^{10}.

A very small drift in the magnetic field was nonetheless significant given our high precision. In the time required to measure $\nu'_{c\,0}$ its value drifted by 10 times the error bar (σ'_{c0}) produced by the initial fit. This drift meant that the error bar (σ'_{c0}) was too small. To make the $\nu'_{c\,0}$ measurement less susceptible to the **B** field drift, we reduced the time required to measure $\nu'_{c\,0}$, by reducing the cyclotron damping time. Because of the drift, some $\nu'_{c\,0}$ measurements were not accurate enough, and were discarded. The real error bar was determined by a more complex fit, called the simultaneous fit. It fitted successive sets of ν'_c measurements at once and determined the **B** field drift over hours as described in Chapter 4.

In the following sections the initial fit is used to study the accuracy of the modified cyclotron frequency. This is the simplest case of the simultaneous fit which we will discuss later (Sec. 4.4.2), when the **B** field is constant and when only one set of ν'_c measurements is considered. It also has the essential nonlinear qualities of the simultaneous fit. It allows us to study parts of the ν'_c measurement that do not depend on the **B** field drift. Here the question is: When the magnetic field drift is constant, under what circumstances do the ν'_c measurements determine $\nu'_{c\,0}$ accurately to 0.01 Hz, the required accuracy for a 1 part in 10^{10} measurement? Based on the signal-to-noise ratio and on the fit residuals, error bars were assigned to each ν'_c measurement. When the **B** field was constant, the error bar on $\nu'_{c\,0}$ predicted by the initial nonlinear fit (σ'_{c0}) was a good estimate of the error bar. Fitting the ν'_c data to the initial fit was a good way to identify ν'_c data sets that did not reliably determine $\nu'_{c\,0}$.

2.3.1 The Relativistic Shift of the Cyclotron Frequency

A relativistic charged particle experiences a cyclotron frequency shift. The cyclotron frequency is (compare with Eq. 1.1)

$$\begin{aligned} \omega_c &= \frac{eB}{\gamma m} \\ \gamma &= \frac{1}{\sqrt{1-(v/c)^2}}, \end{aligned} \tag{2.20}$$

where m is the rest mass and γ is the special relativistic factor, v is the particle's velocity, and c is the speed of light. When the particle is in a large orbit, it moves faster, it appears heavier in the laboratory frame, and the particle's cyclotron frequency shifts downward. When $v \ll c$, the cyclotron frequency shifts in proportion to the particle's cyclotron kinetic energy (E_c),

$$\delta\nu_c = -\nu_c \frac{E_c}{mc^2}, \tag{2.21}$$

where $2\pi\nu_c = \omega_c$.

In a Penning trap, the modified cyclotron frequency similarly shifts due to special relativity as [25]:

$$\delta\nu_c' = -\nu_{c\,0}' \frac{E_c'}{mc^2}, \tag{2.22}$$

where $2\pi\nu_c' = \omega_c'$, E_c' is the kinetic energy in the modified cyclotron motion, and $\nu_{c\,0}'$ is the modified cyclotron frequency with no kinetic energy. Both the cyclotron frequency and the modified cyclotron frequency are mostly determined by the **B** field, so both shift in the same way. The modified cyclotron relativistic shift ($\delta\nu_c'$) can be accurately measured (Fig. 2.9); this allows us to accurately determine the modified cyclotron kinetic energy (E_c'). The relativistic shift also makes it possible to count

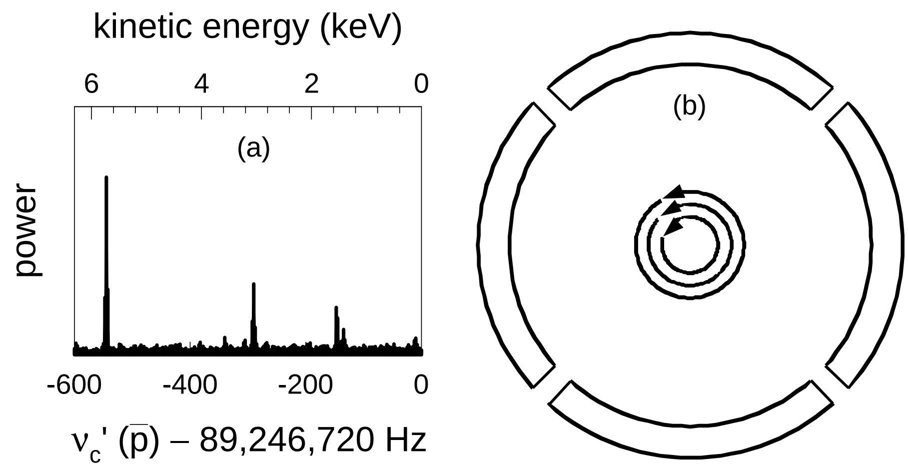

Figure 2.9: Special relativity shifts the modified cyclotron frequency for energetic antiprotons down. $2\pi\nu'_c = \omega'_c$. (a) Three simultaneously trapped antiprotons have different kinetic energies. (b) Their orbits are large relative to the trap's ring electrode ($\rho_0 = 0.6$ cm). The drawing is to scale.

small numbers of protons, antiprotons, and H^- in the trap. When trapped particles have different kinetic energies, the difference in cyclotron frequencies is easily measured, and the trapped particles can be distinguished.

The relativistic shift complicates the modified cyclotron frequency measurement. In order to get a high enough signal-to-noise ratio, we found that the cyclotron energy needed to be at least 1 eV. Relativity shifts the cyclotron frequency for such a particle by 0.1 Hz. This is 10 times larger than the cyclotron frequency accuracy needed to complete a charge-to-mass measurement of 1 part in 10^{10}.

2.3.2 Measuring the Modified Cyclotron Frequency

With an antiproton in a large cyclotron orbit, we measured the cyclotron frequency repeatedly while the particle lost energy. This determined the modified cyclotron frequency for a particle with negligible kinetic energy (ν'_{c0}).

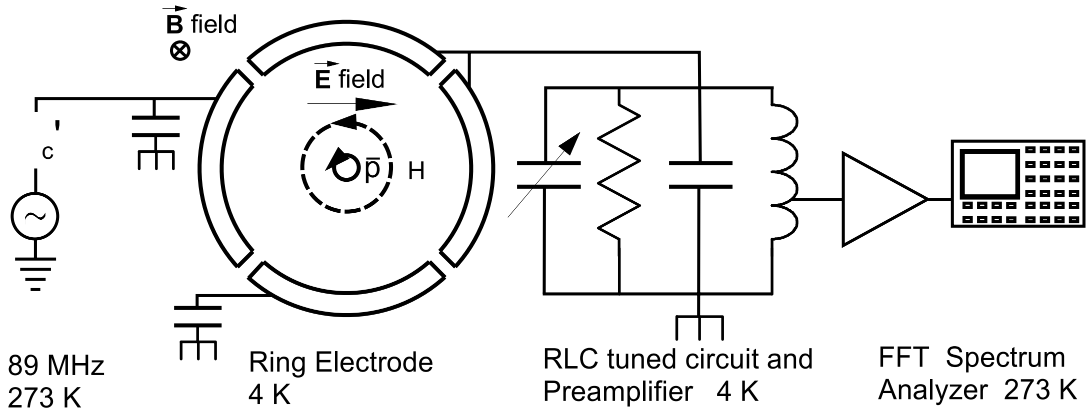

Figure 2.10: An oscillating electric field across the ring initially increases the cyclotron orbit of the $\bar{p}$. The H^-, previously in a large orbit, is not resonant with this electric field. A tunable *RLC* circuit attached to half the ring electrode damps the $\bar{p}$ motion and produces a detectable signal. This signal was amplified at 4 Kelvin, further amplified at room temperature, and its frequency spectrum measured.

An oscillating electric field increased the cyclotron kinetic energy of an antiproton. The field was made by a phase continuous frequency synthesizer which applied a voltage to one segment of the ring electrode (Fig. 2.10). The electric field across the ring electrode oscillated at the same frequency and phase of the antiproton. The cyclotron motion was that of a driven harmonic oscillator. The electric field increased the orbit of the antiproton. Since special relativity shifted the cyclotron frequency of the $\bar{p}$ downward as its kinetic energy increased, the frequency of the synthesizer was swept downward as well. In most cases, the particle's frequency followed the frequency of the synthesizer. By controlling the electric field strength and the range over which the frequency of the synthesizer swept, one can control the antiproton's kinetic energy. After increasing the antiproton's cyclotron kinetic energy, the radio frequency **E** field was turned off.

A tunable *RLC* circuit detected the modified cyclotron motion. A low loss inductor made out of silver plated copper and a small varactor [30] was attached

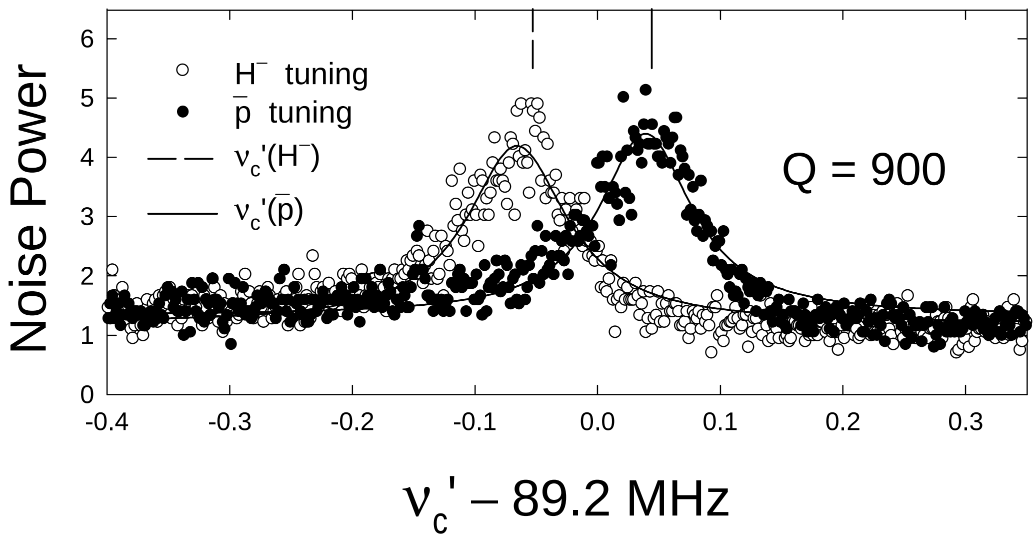

Figure 2.11: The cyclotron noise profile the H^- (open circles) and the antiproton (dark circles). This profile measures the impedance of the RLC tuned circuit. By changing the applied voltage on the tuning capacitor, the RLC circuit can most sensitively detect either $\nu_c'(\bar{p})$ or $\nu_c'(H^-)$.

to half of the ring electrode (Fig. 2.10). At ν_c' half of the ring electrode had a high impedance, while the other trap electrodes were at ground potential. The trap capacitor and tuned circuit is precisely analogous to that used for detecting the axial motion described on page 24. The signal-to-noise ratio (Eq. 2.17) is determined by the time constant (τ in Eq. 2.14). By adjusting a D.C. bias voltage, the varactor was tuned so that the cyclotron detector was most sensitive at the measured frequency. Between measuring $\nu_c'(\bar{p})$ and $\nu_c'(H^-)$ the RLC circuit was tuned by 100 kHz. The noise profile of the cyclotron amplifier measures the impedance of the RLC circuit for the different cyclotron tuning (Fig. 2.11).

The cyclotron motion is described by a damped harmonic oscillator equation [25]. This is very similar to the axial motion (Eq. 2.13). The resistor (R) dissipates the particle's cyclotron kinetic energy (E_c') with a characteristic time constant (τ in

Eq. 2.15). The energy and particle orbit decrease exponentially. Special relativity shifts ν_c' in proportion to its kinetic energy; as the $\bar{p}$ loses energy, ν_c' approaches an endpoint value ($\nu_{c\,0}'$),

$$\nu_c'(t) = \nu_{c\,0}' - \delta\nu_c'(0)e^{-t/\tau}, \tag{2.23}$$

where t is time, $\nu_{c\,0}'$ is the modified cyclotron frequency for a particle with zero kinetic energy, and $\delta\nu_c'(0)$ is the particle's initial relativistic shift, a measure of the particle's initial kinetic energy.

We fit the modified cyclotron frequencies to one time constant (τ). In principle the parallel resistor (R) and the time constant (τ) are functions of frequency. As $\nu_c'(t)$ shifts so should τ. However, the shifts are small enough to make the effect negligible. To measure $\nu_{c\,0}'$, the relativistic shift ($\delta\nu_c'$) is initially 20 Hz, which is small compared with the width of the cyclotron tuned circuit, 50 kHz. As the cyclotron frequency shifted, the circuit impedance and τ were stable to 4 parts in 10^4, much smaller than the fit uncertainty of τ.

We measured a single antiproton's modified cyclotron frequencies as the particle decayed, mixed the amplified noise signal down to audio frequencies, then used the HP 3561A dynamic signal analyzer to perform a fast Fourier transform. After increasing the cyclotron orbit with the radio frequency field, the cyclotron kinetic energy and signal were large. The Fourier transform was performed with a large frequency bin width (Fig. 2.12a). The bin width was kept large enough so that in the time required to Fourier transform, the particle's frequency remained in one frequency bin. The measured modified cyclotron frequency was the center frequency of the bin with the largest signal. The initial error assigned ($\sigma_{\rm bin}$) was one half of one bin width. This assignment means that the measured frequency was 68% likely within the bin with the largest signal. On page 51, we justify and improve this error

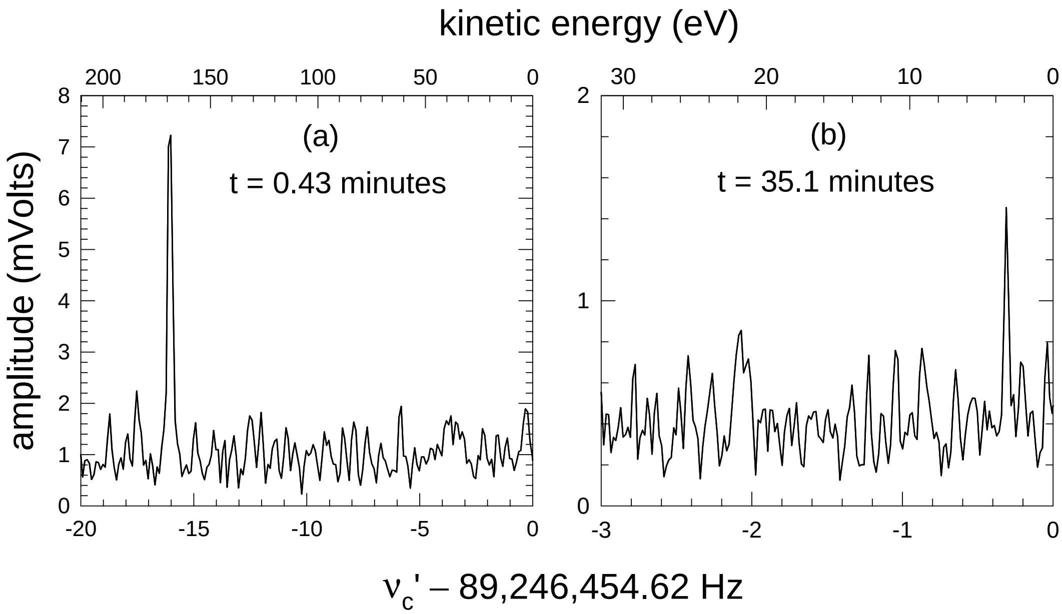

Figure 2.12: The cyclotron signals at the start (initial) and end (final) of a measurement. (a) The initial modified cyclotron kinetic energy (E_c') is large and the Fourier transform bin width ($\Delta\nu$) is 0.1 Hz. (b) The final modified cyclotron kinetic energy is small and the bin width is 0.016 Hz.

assignment. As the $\bar{p}$ lost its kinetic energy, the signal decreased. To measure it, a smaller frequency bandwidth was used (Fig. 2.12b). The measurement ended when the signal was too small and required too long an averaging time to be measured. Typical initial and final cyclotron kinetic energies are shown in Table 2.4.

A nonlinear fit determined the endpoint modified cyclotron frequency (ν_{c0}'). We fitted the measured ν_c' data to Eq. 2.23 and determined the three fit parameters, ν_{c0}', τ, and $\delta\nu_c'(0)$ (Fig. 2.13a). This equation assumed the $\mathbf{B}$ field was constant. We found the best fit parameters by making an initial estimate and then minimized the weighted sum of squares of the fit residuals, χ^2. The fit residuals are the difference between the measured ν_c' and the prediction of the fit. Each residual was weighted by $1/\sigma_{\rm bin}^2$, where $\sigma_{\rm bin}$ was the error bar. Usually nonlinear fits have many χ^2 minima.

Year	Initial measured state			Final measured state		
	$\delta\nu_c'$ (Hz)	E_c' (eV)	ρ (μm)	$\delta\nu_c'$ (Hz)	E_c' (eV)	ρ (μm)
1995	-20	210	360	-0.30	3	43
1996	-6	63	200	-0.09	1	24
extrapolation to:				-0.01	0.1	8

Table 2.4: The antiproton's modified cyclotron initial and final measured state in 1995 and in 1996. $\delta\nu_c'$ is the relativistic frequency shift, E_c' is the antiproton's kinetic energy, and ρ is the antiproton's cyclotron radius.

When the ν_c' data fitted well to an exponential as in Fig 2.13a, we found only one χ^2 minimum for a τ varying over a wide range, from 3 to 20 minutes. In this fit we assumed that the background **B** field was stable in time, which was not strictly true. In Chapter 4 a more complex fit is performed which allows the **B** field to drift in time.

Figures 2.13b, 2.13c, 2.13d and 2.13f describe the quality of the fit. Fig. 2.13b shows the relativistic shift, $|\delta\nu_c'(t)|$, the difference between the measured ν_c' and the fitted endpoint ν_{c0}'. It shows how close in frequency the last measured ν_c' points approach the endpoint (ν_{c0}'). Frequency measurements with smaller relativistic shifts determine the endpoint frequency (ν_{c0}') more accurately. The slope of the line in Fig. 2.13b measures the time constant (τ). To fit the ν_{c0}' to 0.01 Hz, the fit was extrapolated past the last measured ν_c', to the time where the relativistic shift was 0.01 Hz. The extrapolation time is also shown (Fig. 2.13b). Fig. 2.13c shows the fit residuals measured in Hz, and Fig. 2.13d shows the residuals measured relative to the error bar assigned ($\sigma_{\rm bin}$ in Fig. 2.13f). When the fit is good and the error bars are assigned correctly, 68% of the fit residuals should fall within ±1 on Fig. 2.13d. The last points are the most critical to determine the endpoint modified cyclotron frequency (ν_{c0}'). They have by far the largest weights, and they have the smallest

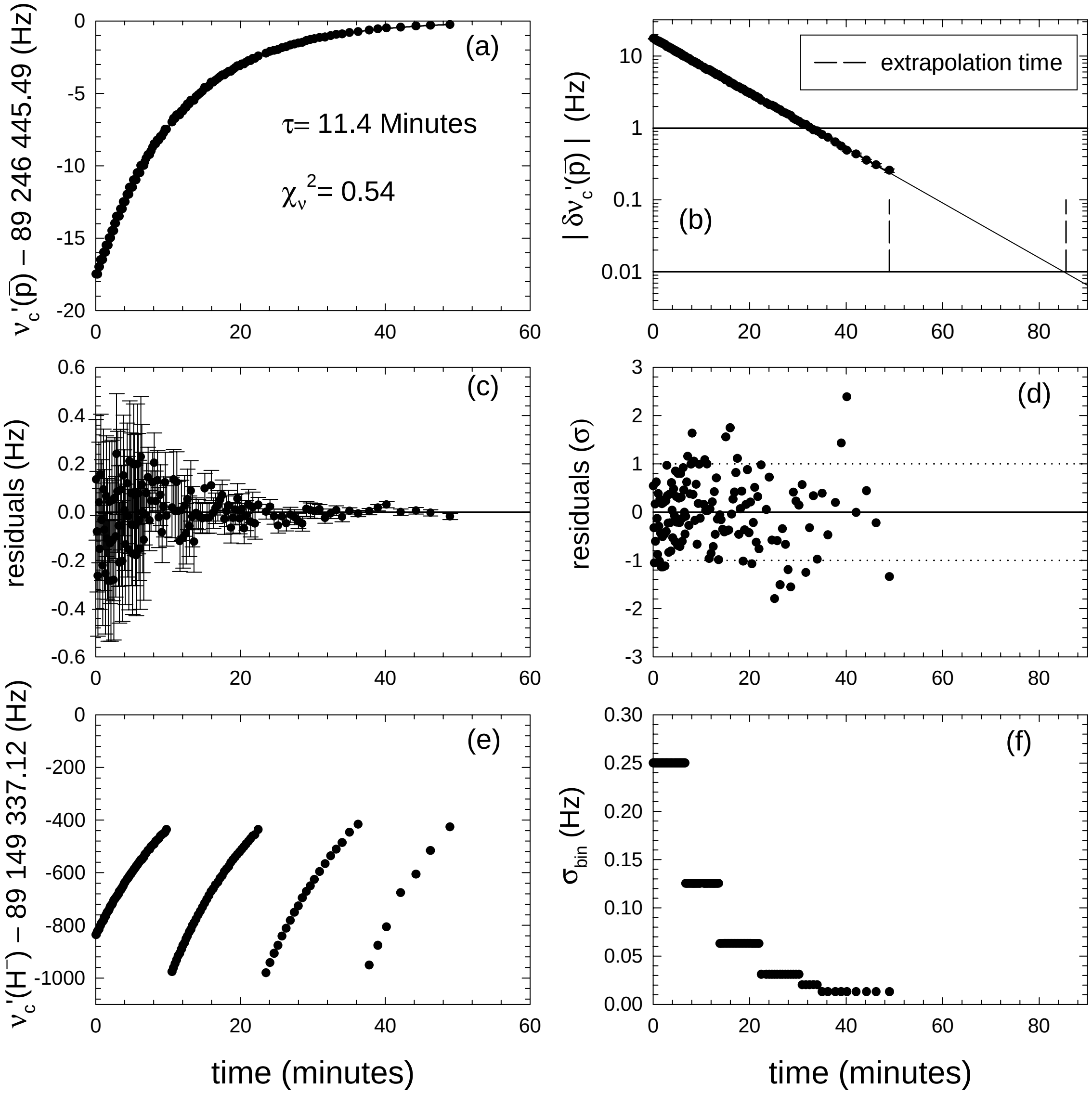

Figure 2.13: The change in the modified cyclotron frequency with time. (a) The measured values of $\nu_c'(\bar{p})$ are fit to Eq. 2.23 to determine the modified cyclotron frequency for a $\bar{p}$ with no kinetic energy (ν_{c0}'). (b) $|\delta\nu_c'|$ is the relativistic shift, the difference between each ν_c' measurement and ν_{c0}'. The slope measures the time constant (τ). The fit is extrapolated by 40 minutes to determine ν_{c0}' to 0.01 Hz. (c) The fit residuals are the difference between the measured ν_c', and the fit prediction. (d) The residuals measured relative to the error bar, $\sigma_{\rm bin}$. (e) $\nu_c'(\mathrm{H}^-)$ relative to its endpoint. (f) $\sigma_{\rm bin}$ is the error bar.

relativistic shifts ($\delta\nu_c'$). In this case χ^2 per degree of freedom (χ_ν^2) was 0.54, much smaller than the expected value, 1. Also the fit predicted that ν_{c0}' was accurate to better than 1 part in 10^{10}.

We took data for times encompassing three to four time constants. This was necessary to measure the cyclotron damping time (τ) well enough and the endpoint modified cyclotron frequency (ν_{c0}') to 1 part in 10^{10}. This step slowed down the measurement.

The **B** field was kept stable and the H^- was kept in a large orbit during the ν_c' measurements. The H^- was also coupled to the tuned circuit so its energy also decayed. When its orbit decreased enough to influence the measured particle, the radio frequency **E** field drove it into a large orbit, causing the frequency shifts seen in Fig. 2.13e. This is further discussed on page 123. During the measurement we kept the **B** field at the particle stable. When the pressures above the magnet helium and apparatus helium dewars were stable, the trap center drifted least with respect to the solenoid coils. We only took measurements when the experiment and magnet cryogenic dewars had been stable for hours. We recorded the ambient magnetic field, the magnet temperature, the pressure and flow above the helium dewars, and the state of a regulation system meant to stabilize the **B** field. Regulation is discussed on page 134.

The fits and plots for large parts of the analysis in this thesis were performed with software written in Mathematica. The hundreds of modified cyclotron (ν_{c0}') endpoint measurements, the ambient variables that describe the **B** field stability, the axial measurements and the resulting cyclotron measurements were all plotted and analyzed with this software.

2.3.3 Reducing the Cyclotron Damping Time

The accuracy of the endpoint modified cyclotron frequency ($\nu'_{c\,0}$) improved when τ was short. When τ was shorter it took less time to extrapolate the fit so the $\nu'_{c\,0}$ measurements were less susceptible to $\mathbf{B}$ field drift. In 1996, we reduced τ by 2.4 times compared with measurements made in 1995; this reduced the extrapolation time (Fig. 2.14). Reducing τ also increased the signal-to-noise ratio (Eq. 2.17). This allowed us to measure ν'_c when the cyclotron orbit and the relativistic shift were smaller (Fig. 2.14d). The increased signal-to-noise ratio in 1996 also led to smaller errors on individual ν'_c measurements (page 51). The result was that the 1996 charge-to-mass measurement was three times more accurate than each charge-to-mass measurement made in 1995 (Chapter 5).

We reduced the time constant (τ in Eq. 2.14) by increasing the coupling between the trap and the charged particle (α in Eq. 2.14). We increased the parallel resistor (R in Eq. 2.10) by adding a varactor increased to tune of the RLC circuit and by reducing the trap capacitance (Eq. 2.10).

In 1996, we reduced τ by adding the varactor [30] allowing us to make the RLC detector maximally sensitive either at $\nu'_c(\mathrm{H}^-)$ or $\nu'_c(\bar{p})$ (Fig. 2.11). Without a reliable tuning capacitor in 1995, we set the center frequency of the RLC circuit half way between $\nu'_c(\bar{p})$ and $\nu'_c(\mathrm{H}^-)$. Because the RLC circuit was mistuned, when measuring either $\nu'_c(\mathrm{H}^-)$ or $\nu'_c(\bar{p})$ the parallel resistor (R in Eq. 2.14) was 2/3 of its optimal value. This meant that during the measurement τ was 1.5 times longer than if the tuned circuit were optimally tuned (Eq. 2.10). Adding the varactor clearly reduced τ but also introduced some losses in the tuned circuit. Because of the varactor, the Q of the RLC circuit decreased by 10%.

In 1996, we also increased the coupling between the particle and the tuned

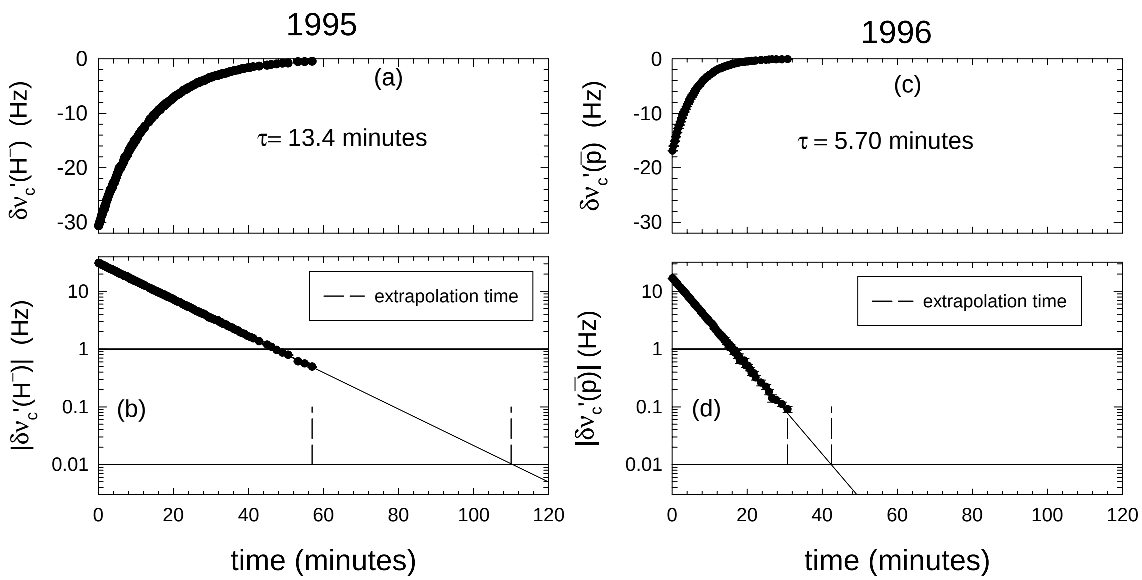

Figure 2.14: A comparison of the measurement accuracy between 1995 and 1996. (a) The relativistic shift($\delta\nu'_c$) in 1995. It is the difference between the measured modified cyclotron frequency (ν'_c) and the fitted endpoint (ν'_{c0}). (b) The relativistic shift ($\delta\nu'_c$) in 1995 plotted on a log scale. The time constant (τ) is measured by the slope. The most important points for determining the cyclotron endpoint (ν'_{c0}) are those with $|\delta\nu'_c| < 1$ Hz. (c) The relativistic shift in 1996. (d) The shorter time constant (τ) in 1996 reduced the extrapolation time, and so allowed the **B** field less time to drift during the ν'_{c0} fit. It also increased the signal-to-noise ratio (Eq. 2.17) and allowed more accurate measurements when $|\delta\nu'_c| < 1$ Hz.

circuit (α in Eq. 2.14). Instead of placing the high impedance resistor on one of the quarter ring electrode segments, we placed the high impedance resistor on two of the quarter ring electrode segments as in Fig. 2.10. For the same size induced current, this creates a larger opposing electric force (Eq. 2.11). This change increased α by $\sqrt{2}$ and should have reduced τ by half. In practice using two one quarter ring electrode segments also increased the trap capacitance.

The shortest τ was achieved by keeping the tuned circuit capacitor (Fig. 2.10) low. This made the parallel resistor largest. The capacitor to use in Eq. 2.14 is not obvious since many components make up the input RLC circuit. At high frequencies, the value of the circuit capacitance depends on where it is measured and at what frequency. This is especially true in our case since long inductive straps connect the trap to the main inductor underneath the amplifier used to tune out the total capacitance (Fig. 2.15). We found that at high frequencies not all the capacitance in the RLC circuit contributes in determining the equivalent resistance (Eq. 2.10). Only the capacitance of the trap, which is about half of the total capacitance, contributes.

The circuit components used to compute the particle's time constant (τ) are the inductor and capacitor as measured from the half ring electrode segment (Fig. 2.15C) to ground. The inductor starts at the half ring electrode segment (Fig. 2.15C). It is composed of the 12 cm long inductive strap, a ceramic feedthrough (Fig. 2.15B) and the amplifier coil to ground. At 90 MHz the 10 pF of stray capacitance in this path does not add to the trap capacitance because the coil shorts out much of it, and the impedance of the 0.07 μH copper strap is large. The trap capacitance starts at the half ring electrode segment (Fig. 2.15C), goes to the two split compensation electrodes (D, D$'$), through the two 12 cm long copper straps, through the two ceramic feedthroughs (A, A$'$) and through two capacitors (c1, c2) to ground.

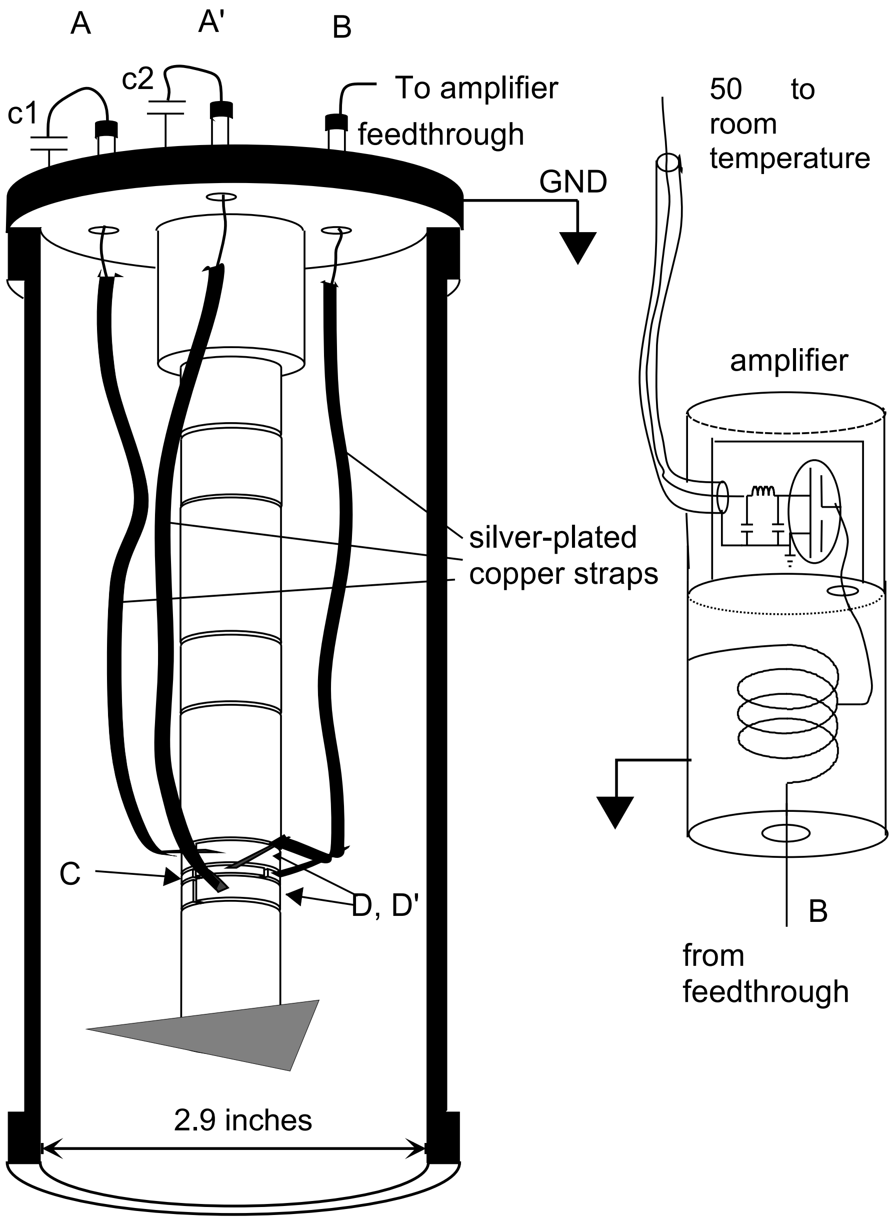

Figure 2.15: The inductor as seen from the trap starts from the ring (C) goes through a silver-plated OFHC copper strap to the feedthrough (B), then to the amplifier and ground. The trap capacitance starts at the ring (C), goes to the compensation electrodes (D, D′), through their straps and feedthroughs (A and A′), then through the the capacitors (c1,c2) to ground.

We reduced the trap capacitance by a factor of 4 by floating the compensation electrodes. The trap capacitance is set by two series capacitors, the capacitor between the half ring electrode and one compensation electrode, and the capacitor between the compensation electrode and ground (Fig. 2.16a). Initially the compensation electrodes were grounded at high frequencies. A 1000 pF capacitor was placed at A and A$'$ in Fig. 2.15. This arrangement maximized the trap capacitance. Using an optimally tuned circuit with a Q of 900, we measured a long time constant, 24 minutes (right of Fig. 2.16). Next we floated the compensation electrodes, connecting them to ground with a 1 pF capacitor and the capacitance of the feedthrough. With an optimally tuned circuit with a Q of 900, we measured a four times shorter time constant (left of Fig. 2.16). This change dramatically reduced the trap capacitance as measured by the particle (Fig. 2.15C); however, the capacitance in parallel to the radio frequency coil (Fig. 2.15B) only changed by 10%.

We changed the electronics located above the trap at 4 K (Fig. 2.17) to reduce the time constant. We changed capacitors and inductors attached to the compensation electrodes that were allowed to float. The DC lines that provided the trapping potentials, -V_0 and V_c in Fig. 2.1 were filtered. Lossy components in the tuned circuits used for particle detection were eliminated. Components were chosen to allow a large enough radio frequency voltage to be applied to each electrode through its "drive" line. This voltage increased the energy in various motions such as the $\bar{p}$ modified cyclotron motion. Lossy components between two halves of each compensation electrode and resistors between the segments of the ring electrode were eliminated. This reduced losses in the magnetron motion and helped prevent cyclotron frequency shifts (this is discussed on page 81).

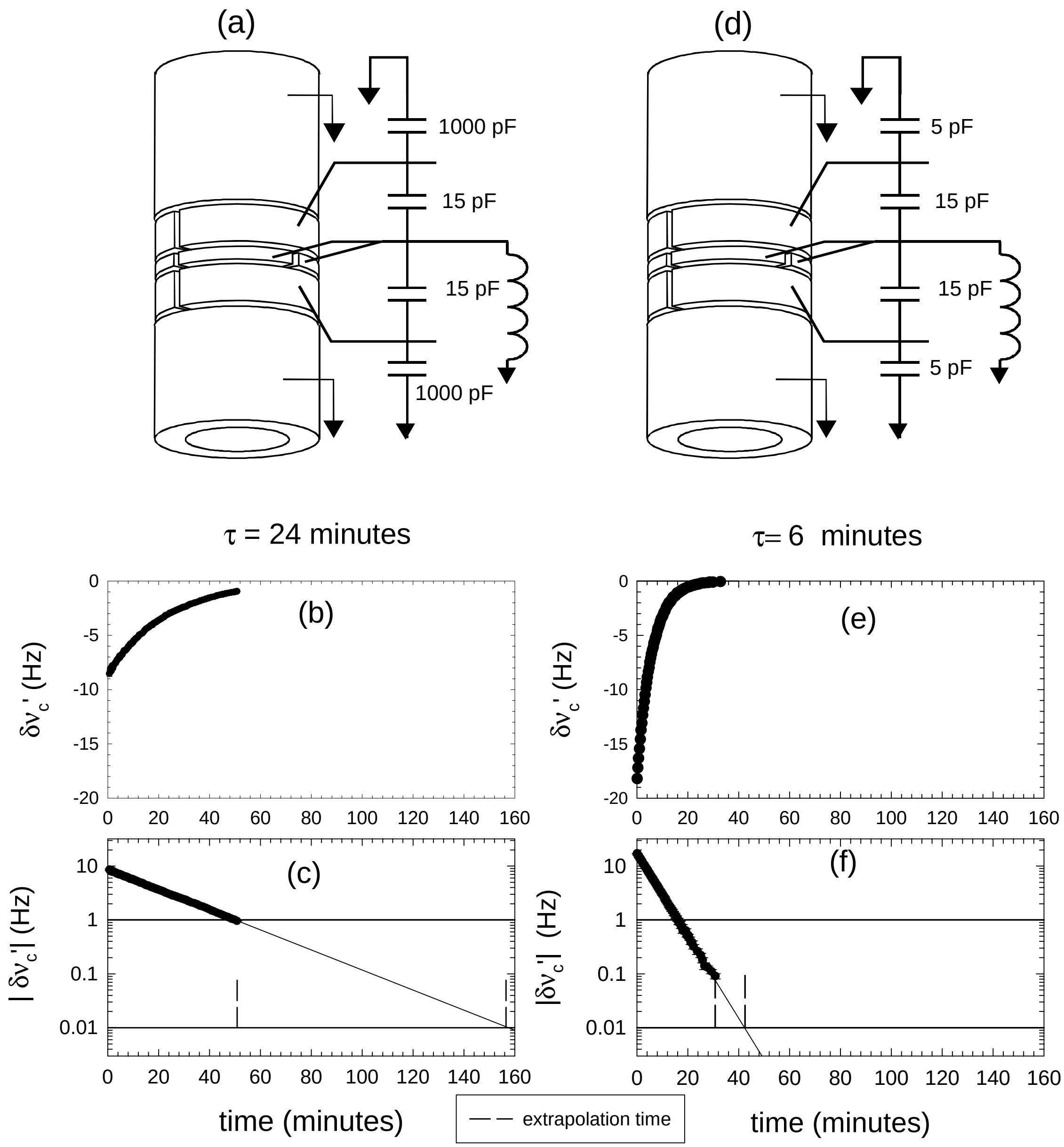

Figure 2.16: Reduction of the time constant by floating the compensation electrodes. (a,b,c) When the split compensation electrodes were grounded through a 1000 pF capacitor, the measured time constant (τ) was 24 minutes. (d,e,f) When the split compensation electrodes were floated by being connected to ground through a 5 pF capacitor, the time constant (τ) was reduced by a factor of 4 to 6 minutes. Other factors which influence τ, such as the Q of the RLC circuit and the coupling between the particle and the trap (α in Eq. 2.11), were the same in both cases. The capacitance values are measured by the particle using the measured τ and Eq. 2.14.

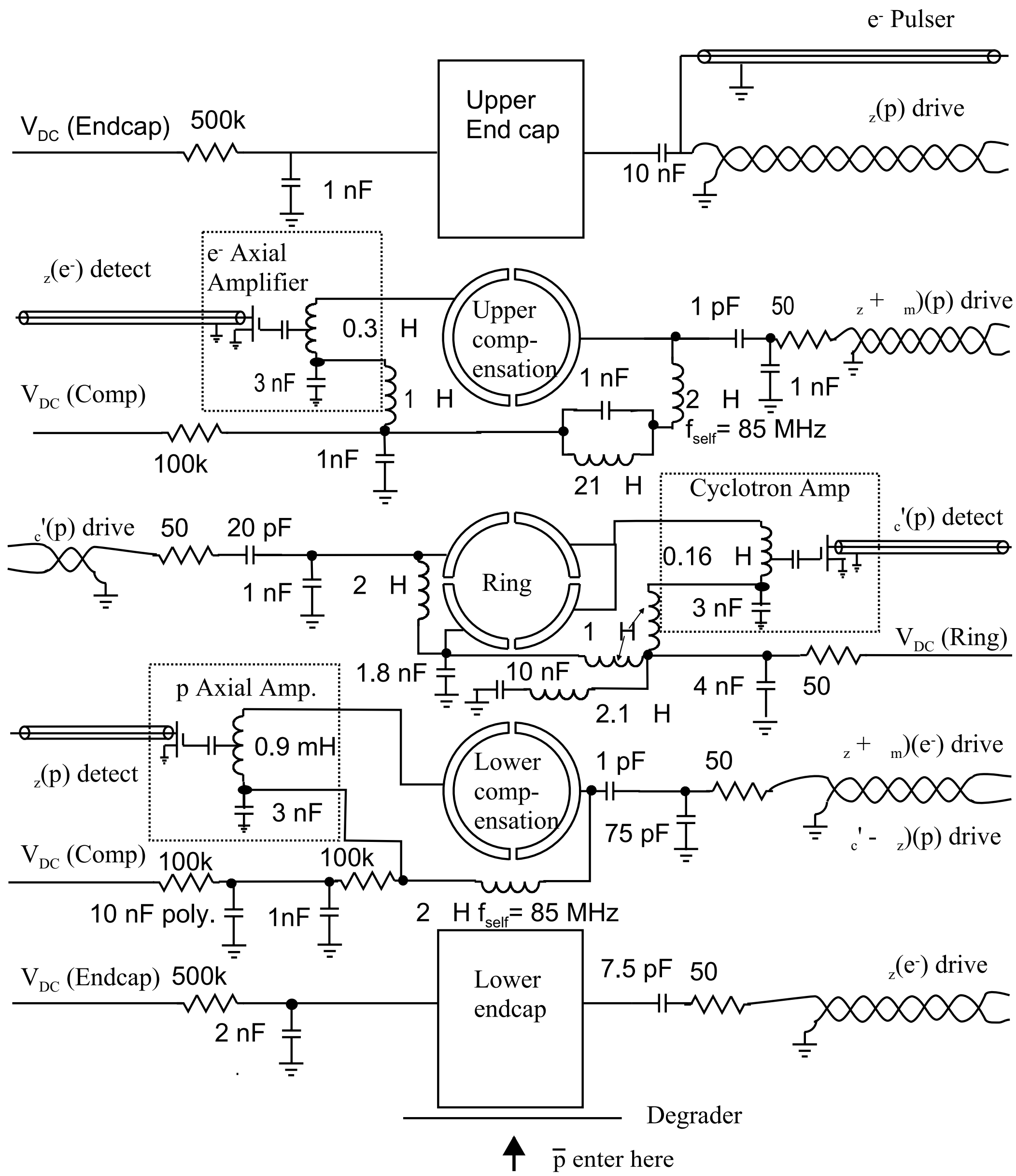

Figure 2.17: The trap electronics used for the 1996 measurement. All capacitors are ceramic except where noted.

2.3.4 The ν_c' Measurement Errors

To have confidence in the endpoint cyclotron frequency ($\nu_{c\,0}'$) prediction, we checked the distribution of the fit residuals. For a good fit to our model, the residuals should scatter randomly over a width equal to the error bar assigned to each cyclotron measurement. Since the final cyclotron measurements were much more heavily weighted than the initial ones it was important that the relative weights were correct. Weighting the cyclotron measurements correctly produced the most accurate cyclotron endpoint prediction. We found that the ν_c' fit residuals followed a Gaussian distribution as they should with a width which depended on the signal-to-noise ratios.

We grouped the fit residuals by year and by the frequency bandwidth of the spectrum analyzer used in the ν_c' measurement. In 1996, we used two nights of ν_c' measurements. In 1995, we used the eight nights included in the $\bar{p}$ − H^- charge-to-mass measurement. In each year ν_c' measurements were taken with six different frequency bin widths. The nominal error bar (σ_{bin}) assigned to each measurement was 1/2 of the bin width. For the initial ν_c' measurements σ_{bin} was 0.25 Hz and for the final measurements it was 0.01 Hz as in Fig. 2.13e. We fitted each group of residuals to a Gaussian. Half of the Gaussian half width determined the real error bar ($\sigma_{\mathrm{scatter}}$). We compared the frequency bin width ($2\sigma_{\mathrm{bin}}$) with the Gaussian half width ($2\sigma_{\mathrm{scatter}}$).

When the signal-to-noise ratio was high (as in Fig. 2.12a) the distribution of fit residuals followed a narrow Gaussian. The real error bar was less than the nominal error bar ($\sigma_{\mathrm{scatter}} = 0.75\sigma_{\mathrm{bin}}$). This was the case for the initial 1995 ν_c' measurements (Fig. 2.18a) and for all the 1996 ν_c' measurements (Figures 2.18c, 2.18d, 2.19c, and 2.19d). In this case 80% of the ν_c' measurements fell in the nearest frequency bin to the fit and 20% fell one frequency bin over. Some residuals missed by one bin width because the Fourier transform windowing function, the Hanning window, spread the signal's power in the three central frequency bins. Residuals also missed by one bin because 10% of the time the particle decayed across frequency bins and deposited some of its power in two neighboring bins.

When the signal-to-noise ratio was low (as in Fig. 2.12b), the residuals were distributed in a wider Gaussian compared with the frequency bin width. This was the case for the most important and accurate ν_c' measurements in 1995 (Figures 2.18b, 2.19a, and 2.19b). More frequently the ν_c' measurements missed the fit by one bin width. The signal was so low that noise and signal in the neighboring frequency bin sometimes produced a larger signal than was in the frequency bin closest to the fit.

The distribution of fit residuals demonstrated that in 1996 we improved the signal-to-noise ratio compared with measurements made in 1995. In 1995, as the signal-to-noise ratio and σ_{bin} decreased, the residuals deviated more significantly compared with the bin width. In this case, the real error bar (σ_{scatter}) increased relative to the nominal error bar (Fig. 2.20). In 1996, even for the ν_c' measurements made with a low signal-to-noise ratio, $\sigma_{\text{scatter}} = 0.75\sigma_{\text{bin}}$. This improvement in signal-to-noise ratio is a result of reducing the cyclotron damping time constant.

For all the modified cyclotron frequency (ν_{c0}') fits we replaced the nominal error bar with the real error bar ($\sigma_{\text{bin}} \rightarrow \sigma_{\text{scatter}}$). This increased χ_ν^2 toward 1, since this based the error bar on the scatter of the residuals (Fig. 2.21a). For the 1996 charge-to-mass measurement, this replacement preserved the relative weights of the measurements and had no effect on ν_{c0}'. In 1995 this replacement had a only small effect on ν_{c0}' (Fig. 2.21b).

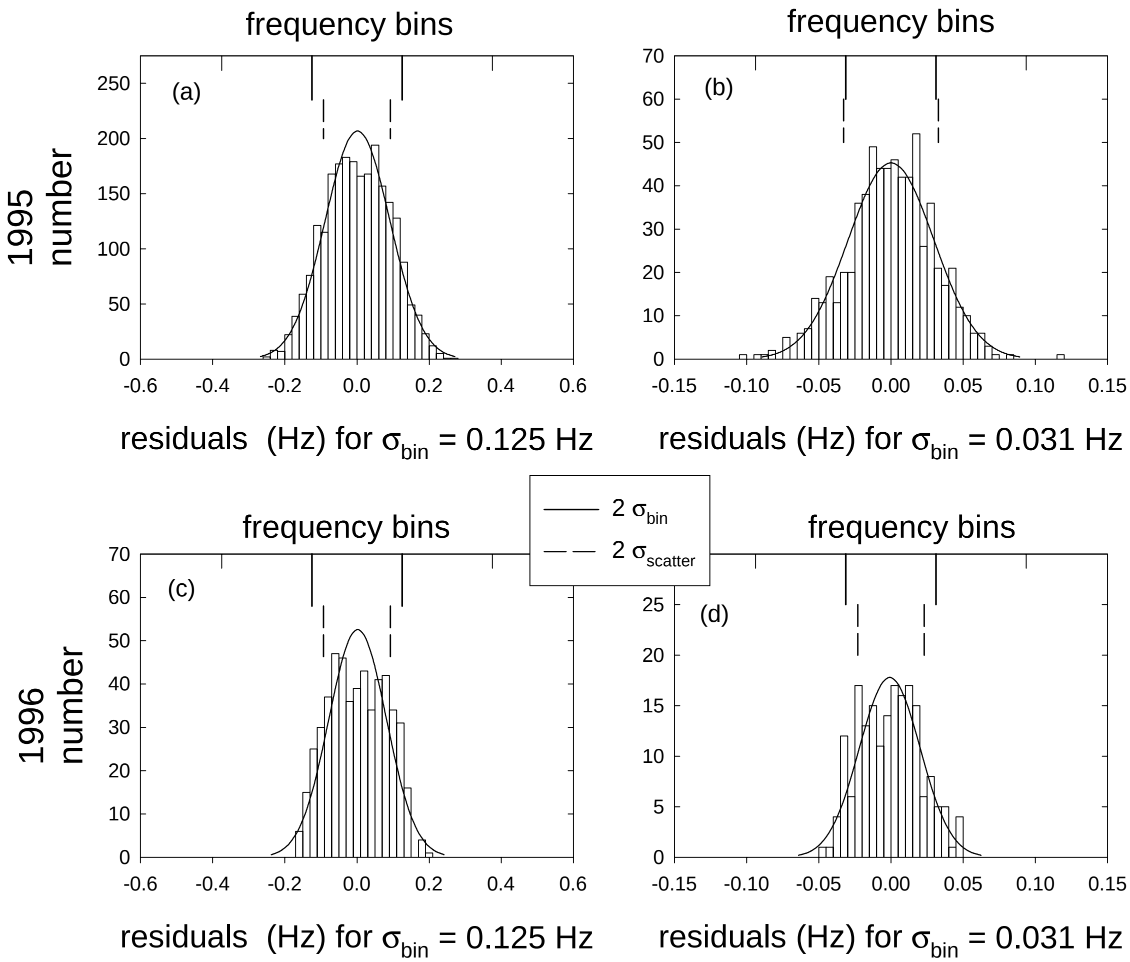

Figure 2.18: Residuals for the initial ν_c' measurements when fit to Eq. 2.23. The residuals are grouped by year and by the bin width of the spectrum analyzer used to measure ν_c'. Each distribution of residuals fits well to a Gaussian. $\sigma_{\rm bin}$ is half of the frequency bandwidth. $\sigma_{\rm scatter}$ is half of the Gaussian half width. (a,c,d) When the signal-to-noise ratio is large $\sigma_{\rm scatter} = 0.75\sigma_{\rm bin}$. (b) When the signal-to-noise ratio is smaller, the residuals are distributed in a wider Gaussian compared with the frequency bin width.

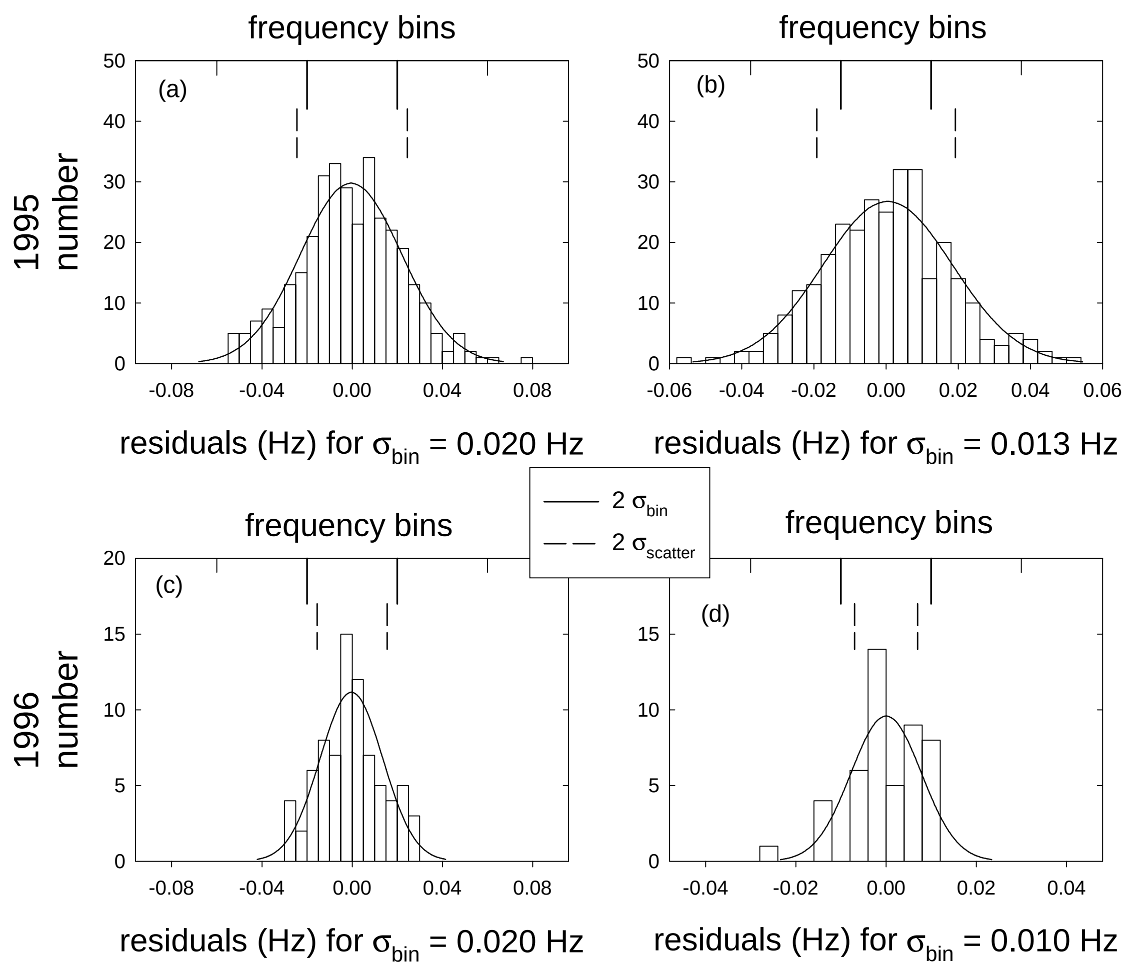

Figure 2.19: The residuals from the most accurate and important ν_c' measurements still fit well to a Gaussian. $\sigma_{\rm bin}$ is half of the frequency bin width. $\sigma_{\rm scatter}$ is half of the Gaussian half width. (c,d) For the accurate measurements made in 1996, $\sigma_{\rm scatter}$ is still $0.75\sigma_{\rm bin}$. (a, b) For measurements made in 1995 the latest ν_c' residuals are distributed in a wider Gaussian compared with the frequency bin width.

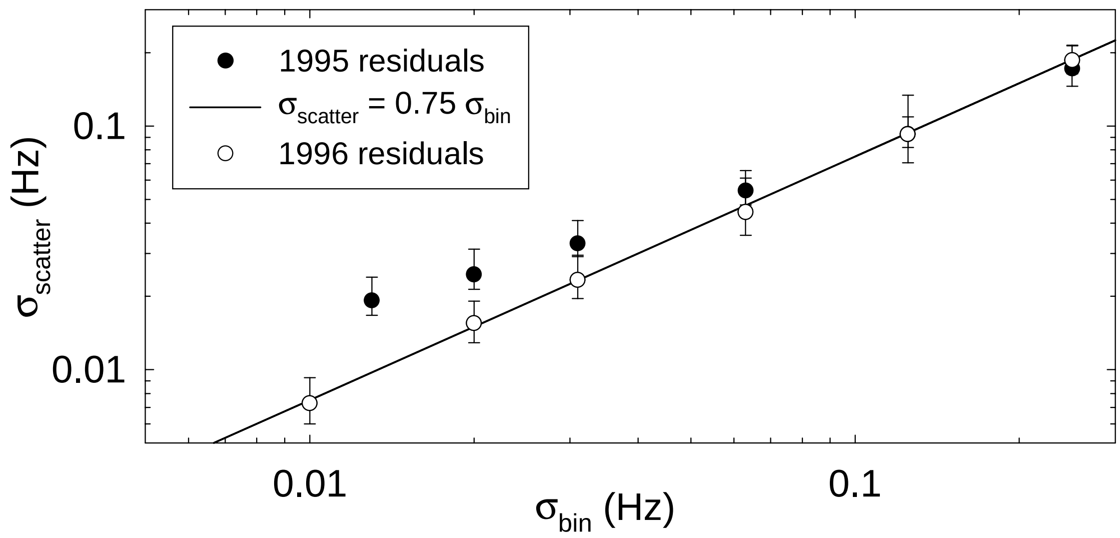

Figure 2.20: The scatter error bar (σ_{scatter}) plotted against the bin width error bar (σ_{bin}). The reduced scatter in the accurate measurements shows the improvement in the signal-to-noise ratio in 1996. The real error bar (σ_{scatter}) measures the scatter in the fit residuals. The accurate modified cyclotron measurements made in 1995 scattered significantly compared with the nominal error bar (σ_{bin}). $\sigma_{\text{scatter}} > \sigma_{\text{bin}}$. The accurate modified cyclotron measurements made in 1996 still scattered less than the nominal error bar. $\sigma_{\text{scatter}} = 0.75\sigma_{\text{bin}}$. This is a result of reducing the cyclotron damping time (τ). The scatter of the residuals for σ_{bin}=0.010 Hz, 0.013 Hz, 0.020 Hz, 0.031 Hz, and 0.125 Hz are shown in Figures 2.18 and 2.19.

2.3.5 The Accuracy of the Cyclotron Endpoint Frequency

We used a Monte Carlo simulation to determine if the endpoint frequency of the modified cyclotron motion ($\nu'_{c\,0}$) was accurate. A nonlinear fit (Eq. 2.23) to a set of ν'_c measurements produced an endpoint cyclotron frequency ($\nu'_{c\,0}$) and its uncertainty (σ'_{c0}). This fit assumed that the **B** field is stable in time. The ν'_c measurements were weighted by different error bars and residuals followed a Gaussian distribution (page 51). When the ν'_c measurements scatter within their error bars, the resulting endpoint frequency ($\nu'_{c\,0}$) also scatters. The endpoint uncertainty resulting from the fit (σ'_{c0}) is reliable when it accurately estimates the scatter in the endpoint frequency

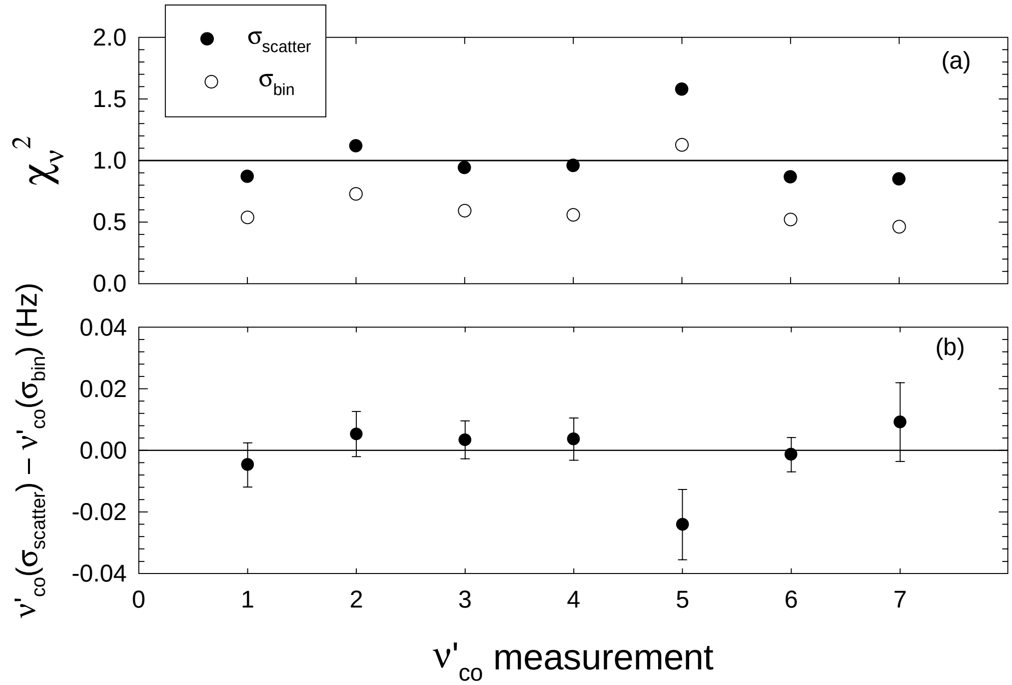

Figure 2.21: The effect of adjusting the error bars. (a) When we replaced $\sigma_{\rm bin}$ with $\sigma_{\rm scatter}$ the fit's χ^2_ν increased toward 1. The measurements are for the 7 sequential ν'_{c0} measurements made the night of 1 August 1995. (b) Adjusting the error bars did not change the ν'_{c0} fit result.

(ν'_{c0}). Were the fit linear with Gaussian residuals, one could prove that the fit error bar accurately determines the scatter in the endpoint frequencies. The simulation described here confirmed that this nonlinear fit accurately determines the endpoint frequency (ν'_{c0}) and its uncertainty (σ'_{c0}).

We simulated one thousand data sets, then we fit them. We fit a real data set to Eq. 2.23. This determined the true fit parameters, ν'_{c0}(true), τ(true), and $\delta\nu'_c$(0,true). Each simulated data set had the same ν'_c measurement times and error bars as the real set. We replaced the measured frequency (ν'_c(t)) with a simulated frequency made by adding a random frequency to the frequency predicted by evaluating Eq. 2.23 using the true fit parameters. The random frequency came from a

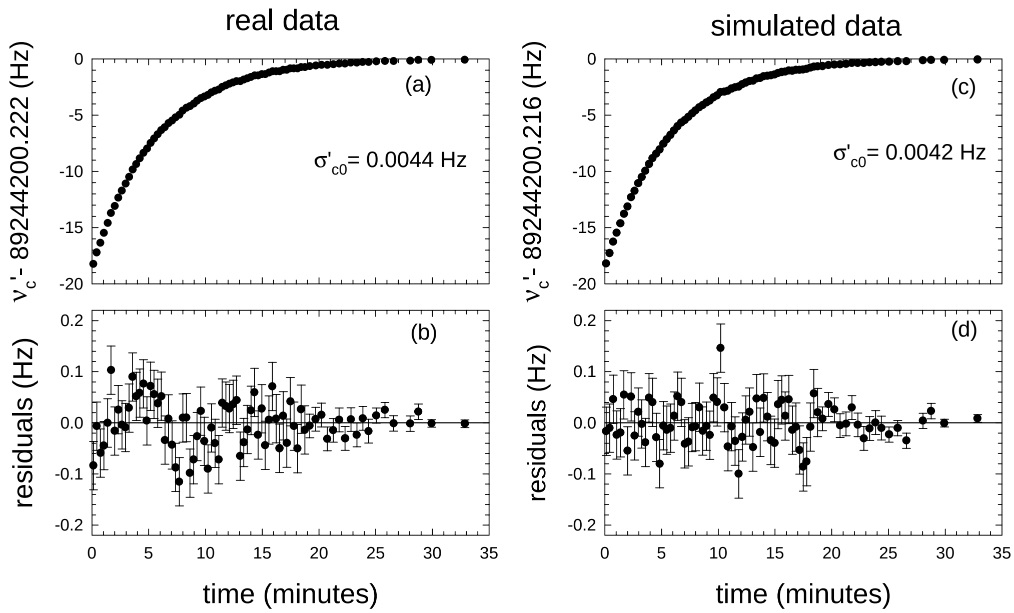

Figure 2.22: A real and simulated set of ν_c' measurements produce the same endpoint frequency ($\nu_{c\,0}'$) and error bar (σ_{c0}'). (a) The real data. (b) The fit residuals of the real data. (c) Simulated data generated by adding Gaussian noise to the prediction of the fit to the real data. It was then fit to produce an endpoint cyclotron frequency ($\nu_{c\,0}'$(simulated)) and its error bar (σ_{c0}'). (d) The fit residuals of the simulated data.

Gaussian distribution with a width equal to the ν_c' error bar. We then fit the ν_c' simulated data to Eq. 2.23 just as for the real data. The fit produced an endpoint frequency ($\nu_{c\,0}'$(simulated)) and its error bar (σ_{c0}'). Most simulated data sets fit to the same endpoint as the real data set (Fig. 2.22).

The simulation shows that the fit correctly predicts the endpoint modified cyclotron frequency ($\nu_{c\,0}'$). The simulated endpoint frequencies ($\nu_{c\,0}'$(simulated)) should scatter with a width given by the fit error bar (σ_{c0}'). From one simulation to the next σ_{c0}' differed by 10%. The best estimate of the fit error bar is the average of the fit error bars ($\bar{\sigma}_{c0}'$). The distribution of simulated endpoint frequencies follows a Gaussian distribution. Half of the half-width is given by σ in Fig. 2.23. The error bar produced by the fit ($\bar{\sigma}_{c0}'$) correctly estimates the scatter of ν_c' (σ of Fig. 2.23),

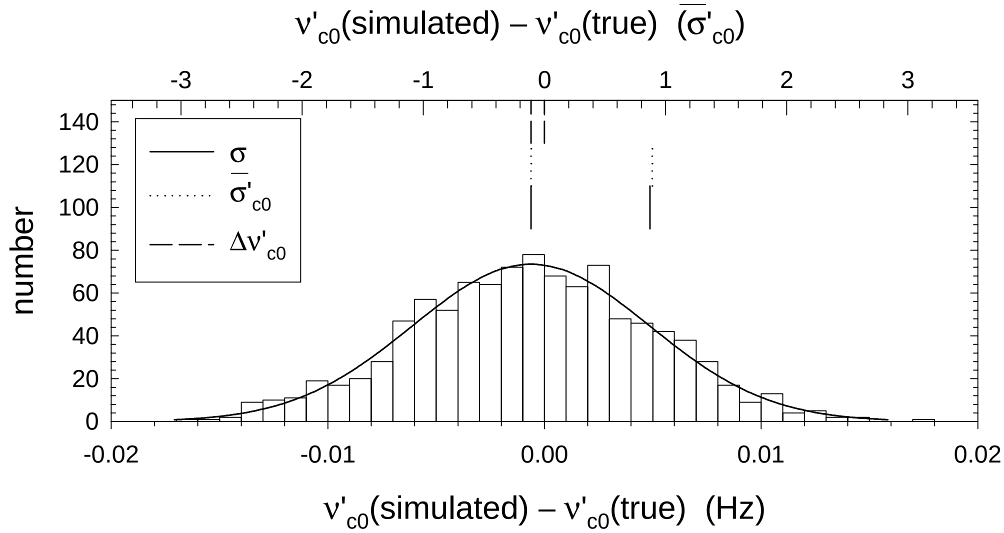

Figure 2.23: The average of the error bars ($\bar{\sigma}'_{c0}$) produced by the ν'_{c0} fit is a good estimate of the scatter in ν'_{c0}. Plotted is a histogram of the simulated endpoints (ν'_{c0}(simulated)) compared with ν'_{c0}(true). The histogram is fit to a Gaussian to get its center frequency and its half-width (2σ). $\bar{\sigma}'_{c0}$ is a good estimate of σ. $\Delta\nu'_{c0}$ is the difference between the center frequency of the Gaussian and ν'_{c0}(true). It is small compared with the error bar ($\bar{\sigma}'_{c0}$).

and is a good estimate of the error. The expected center frequency is ν'_{c0}(true), determined by fitting the real data to Eq. 2.23. ν'_{c0}(true) differs by only a small amount from the center frequency of the Gaussian.

When the **B** field was a constant and when ν'_c measurements were distributed in a Gaussian fashion, the ν'_{c0} prediction was correct. The error bar means that with 68% certainty the true ν'_{c0} endpoint is within σ'_{c0} of the fitted ν'_{c0} endpoint. Under these circumstances, the error bar is small enough for a 1 part in 10^{10} measurement.

2.3.6 Accurate ν'_{c0} Measurements in Practice

The best measurements of the modified cyclotron frequency endpoint (ν'_{c0}) produced an χ^2_ν about equal to 1 and had some modified cyclotron (ν'_c) measurements with small relativistic shifts ($|\delta\nu_c'| < 1$).

When contaminant electrons or ions were trapped the modified cyclotron measurements deviated from an exponential. In both examples in Fig. 2.24 the residuals from the most accurate cyclotron measurements deviated from the fit by much more than the error bar (Fig. 2.24c and 2.24f). These residuals are the most important in determining the endpoint cyclotron frequency ($\nu'_{c\,0}$). The residuals show a nonrandom pattern, much different from the random residuals in Fig. 2.22b. In order for χ^2_ν to be about 1, larger error bars than the carefully assigned ones (Sec. 2.3.4) need to be used and these are not justified. Even a few contaminant particles in the trap center cause these deviations. Deviations as these illustrated the need to remove all contaminants prior to measuring the cyclotron frequency. Our best judgment for when the cyclotron measurement was free from contaminants was when χ^2_ν was less than 2. Measurements with χ^2_ν less than 2 were included in the measurement set.

The fit determines the cyclotron endpoint frequency ($\nu'_{c\,0}$) reliably only when the relativistic shifts ($\delta\nu_c'$) of the latest ν_c' measurements are small enough. It took over 1 hour to extrapolate the fit in Fig. 2.25a and Fig. 2.25b past the last measurement to determine $\nu'_{c\,0}$ to 0.01 Hz. During this extrapolation time the $\mathbf{B}$ field and $\nu'_{c\,0}$ drifted by 0.1 Hz (shown in Fig. 4.15). The $\nu'_{c\,0}$ drift is 10 times larger than the $\nu'_{c\,0}$ error bar (σ'_{c0}) and is also 10 times larger than the $\nu'_{c\,0}$ accuracy required for a charge-to-mass ratio measurement of 1 part in 10^{10}. The large drift is contrary to the fit assumption that $\nu'_{c\,0}$ is constant (Eq. 2.23). When ν_c' measurements are made with smaller relativistic shifts ($\delta\nu_c'$) the extrapolation is also much smaller (Fig. 2.25c and Fig. 2.25d); this minimizes the effect of the drifting $\mathbf{B}$ field.

The relativistic shift ($\delta\nu_c'$) of the last ν_c' measurement should be less than 1 Hz for a reliable endpoint frequency ($\nu'_{c\,0}$). We looked for a change in the fitted $\nu'_{c\,0}$ endpoint when the most accurate ν_c' measurements were excluded. We first included

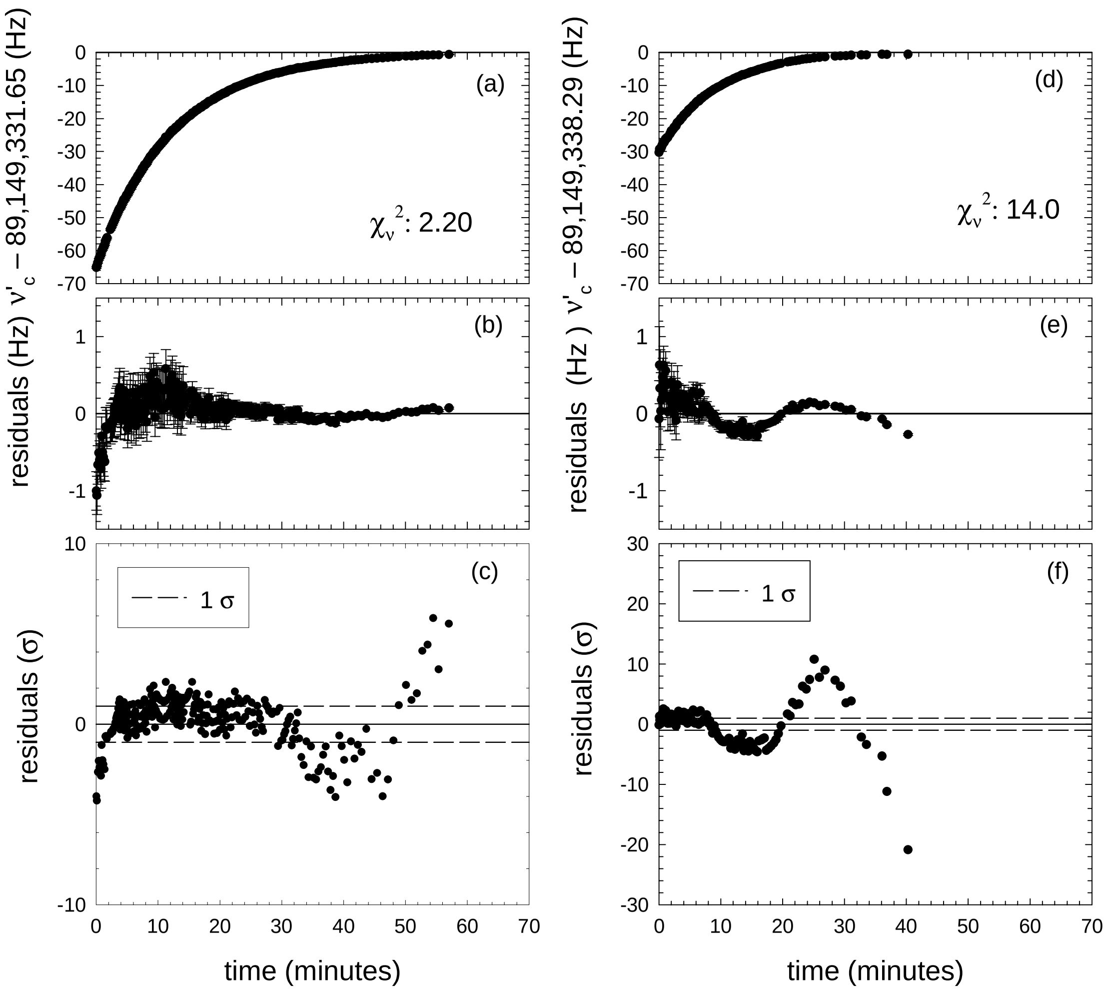

Figure 2.24: Two examples of ν_c' measurements that produce a bad fit. (a) A ν_{c0}' measurement, its fit to Eq. 2.23, and its χ_ν^2. (b,c) The fit residuals in Hz and in units of the error bar (σ). The most important residuals deviate from the fit by much more than the error bar (σ), and are not randomly distributed. (d,e,f) Another more dramatic example of a bad fit to Eq. 2.23.

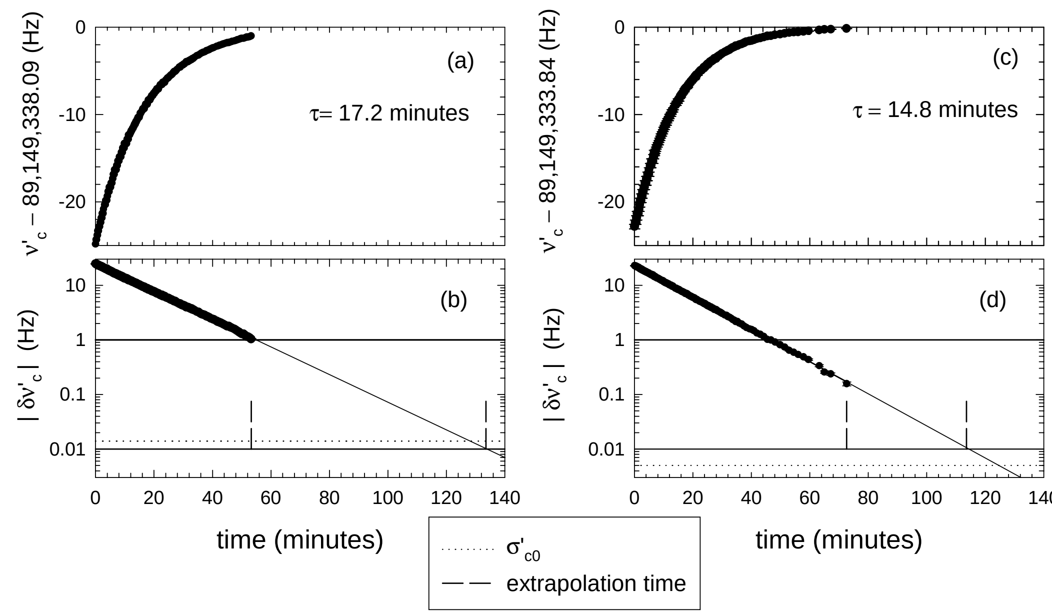

Figure 2.25: (a) A ν'_{c0} measurement with too large of a fit extrapolation. (b) The relativistic shift ($\delta\nu'_c$). In the time required to extrapolate the fit to 0.01 Hz, ν'_{c0} drifts considerably compared with the error bar produced by the fit (σ'_{c0}). This measurement was discarded. (c,d) A ν'_{c0} measurement with a fit extrapolation half as big. The last ν'_c measurement has a 10 times smaller relativistic shift ($\delta\nu'_c$) compared with (b). This measurement was included.

all the ν'_c measurements and computed the endpoint frequency (ν'_{c0}(all)). We then excluded the most accurate ν'_c measurements and computed ν'_{c0}(subset). The fit process worked very nicely at the desired accuracy as long as the relativistic shift of the last ν'_c measurement was larger than 1 Hz (Fig. 2.26).

2.3.7 Conclusion

In the absence of the large **B** field drift, our tests show that the fit to Eq. 2.23 accurately determines the endpoint cyclotron frequency (ν'_{c0}). The fit residuals are randomly distributed with a width equal to the error bar. The nonlinear fit accurately determined the endpoint frequency (ν'_{c0}) and its error bar since we had

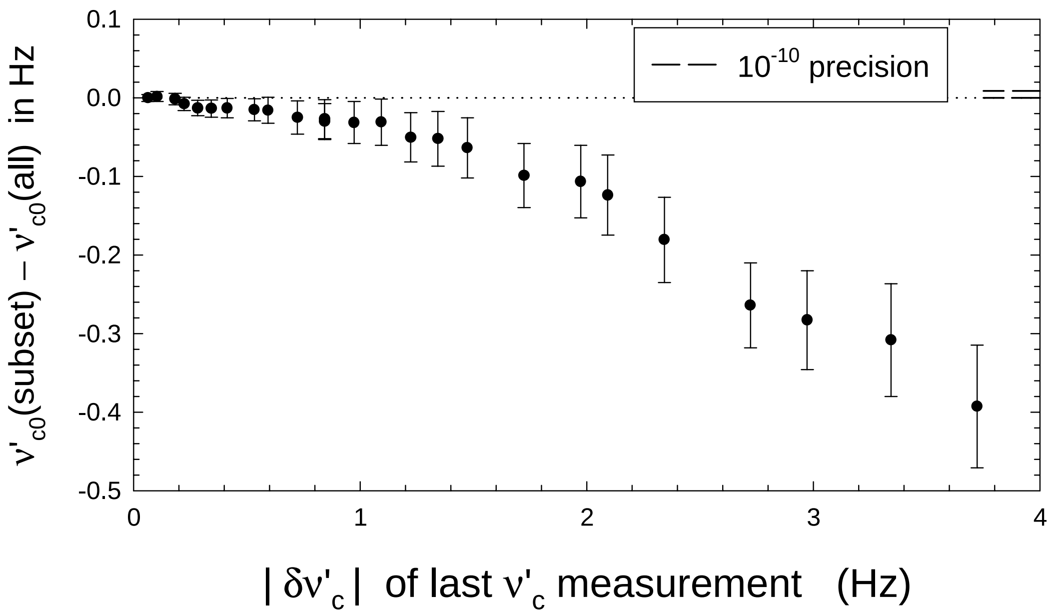

Figure 2.26: ν'_{c0} is not accurate when the relativistic shift ($\delta\nu'_c$) of the last measured ν'_c is too large. ν'_{c0}(all) is the fit result from including all the ν'_c measurements. ν'_{c0}(subset) is the fit result from excluding the accurate ν'_c measurements with the smallest relativistic shifts. When the relativistic shift of the last ν'_c measurement was greater than 1 Hz, the endpoint (ν'_{c0}) was not accurate.

randomly distributed residuals. The modified endpoint frequency (ν'_{c0}) is most accurate when χ^2_ν is reasonably close to 1 and the relativistic shifts ($\delta\nu'_c$) for the most accurate ν'_c measurements are less than 1 Hz.

2.4 The Axial Motion

As with the cyclotron orbit, the axial frequency was most accurately measured for a small orbit. In order to measure it in a small orbit, the trapping potential had to be a quadrupole (Eq. 2.3). Here the method to detect the axial motion is described along with how the electrostatic potential was tuned to be nearest to the ideal quadrupole. Finally, how the axial frequency was measured accurately overnight is described.

2.4.1 Detecting the Axial Motion

The axial motion was that of a driven harmonic oscillator with damping. We used two oscillating **E** fields to increase the axial energy. The **E** fields increased the particle's kinetic energy, inducing a larger, more easily measurable signal. The motion was detected with an RLC circuit.

The signals used to increase the particle's energy were at a lower frequency than the detected frequency [17, 25]. When a large signal was measured at the axial frequency (ν_z) it was due to the particle and not due directly to the applied signals. A low frequency signal (ν_{mod}) was applied to the ring electrode (Fig. 2.27). This modulated the DC trapping potential (-V_0) and the resulting axial frequency (Eq. 2.4). The axial frequency (ν_z) was analogous to the carrier frequency in radio frequency modulation (FM). A small component of the particle's axial energy was at two sideband frequencies ($\nu_z \pm \nu_{\mathrm{mod}}$). When another drive was applied to the endcap at one sideband, $\nu_z - \nu_{\mathrm{mod}}$, the axial energy increased, allowing a large signal to be detected at ν_z.

The RLC circuit used for detection was made with a superconducting inductor and a reduced capacitor. The inductor, built by David Phillips [1] out of niobium titanium (NbTi), was superconducting even in the 59 kGauss **B** field. Using NbTi instead of oxygen free high conductivity copper improved the Q and the signal-to-noise ratio by 4 times. The low frequency (1.15 MHz) of the RLC tuned circuit made the circuit capacitance independent of the lead inductance; this is much simpler than the complicated circuit capacitance for the cyclotron case (Sec. 2.3.3). By removing 11 pF from the input RLC circuit in 1996, we reduced the axial damping time (τ_z)

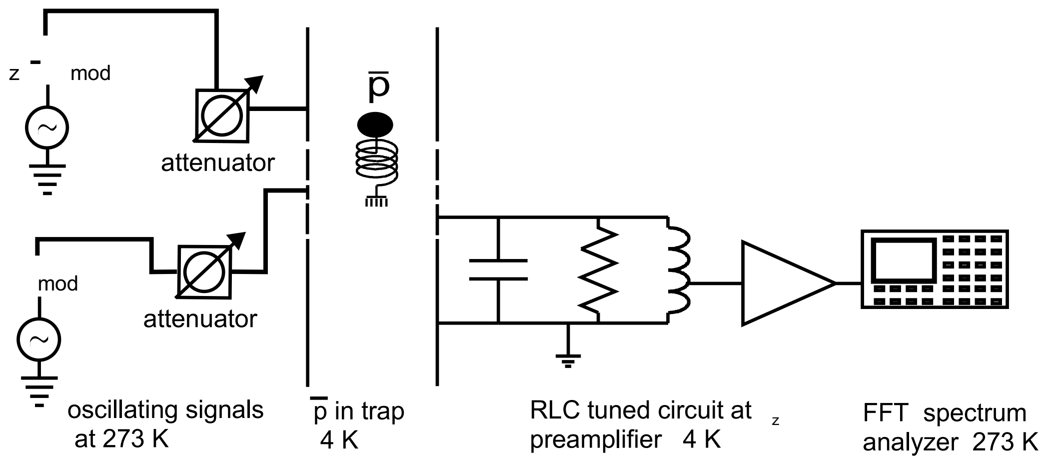

Figure 2.27: Two oscillating signals increase the axial energy. The ring is modulated at $\nu_{\text{mod}} = 91$ kHz, and this modulates the axial frequency of the particle (ν_z). When the endcap is driven with a signal at $\nu_z - \nu_{\text{mod}} = 1,058$ kHz, the $\bar{p}$ responds at ν_z. An RLC circuit detects the motion.

and improved the signal-to-noise ratio by 20%. This allowed us to detect the particle in smaller orbits where the axial frequency was more precise. The axial amplifier noise profile is shown in Fig. 2.5 and the time constant is given in Table 2.3 on page 30.

To measure the axial frequency the frequency applied to the endcap was swept through resonance. The trapping voltage (-V_0) was first adjusted to make the axial frequency resonant with the tuned circuit. The compensation voltage (V_c) was also tuned. The signal applied to the endcap was set below $\nu_z - \nu_{\text{mod}}$ and the frequency was swept upward. At each frequency we recorded the detected signal power in a small bandwidth (0.25 Hz) at the sum of the endcap frequency and the modulation frequency (ν_{mod}). When the endcap frequency equaled $\nu_z - \nu_{\text{mod}}$ a large response at ν_z was seen (Fig. 2.6b). Next, we started the endcap sweep signal above $\nu_z - \nu_{\text{mod}}$ and swept it down. When the trap compensation voltage was optimally tuned (see below) the signal appeared as in Fig. 2.6b. While measuring, another fixed frequency signal was applied to one section of a compensation electrode to keep the magnetron orbit small (Sec. 2.5.1).

2.4.2 Measuring ν_z

Optimally adjusting the compensation voltage (V_c of Fig. 2.1) was necessary to measure the axial frequency precisely. When this was done the region over which the potential was a good quadrupole (as in Eq. 2.3) was largest. Then signals from small axial orbits which determine the axial frequency more precisely could be measured.

When the potential is not a quadrupole, the axial equation of motion changes from being harmonic (Eq. 2.13) to being anharmonic. The solution to the anharmonic equation is presented in Ref. [25, 31]. The size of the anharmonic contribution is measured by the coefficient C_4 of the fourth order Legendre polynomial (Eq. 2.1). C_4 is proportional to the the ratio of the compensation voltage to the ring voltage (Vc/Vo). Unlike harmonic motion, the axial frequency changes for anharmonic motion as the axial excursion increases. This makes it necessary to measure ν_z with small enough applied signals. Unlike the harmonic solution, the axial excursion measured depends not only on the size of the applied signals, but also on how the axial frequency is reached.

The axial response seen experimentally differs depending on the voltage applied to the compensation electrode and on the direction that the endcap frequency approached $\nu_z - \nu_{\mathrm{mod}}$. When -$V_c/V_0$ and C_4 are too high, sweeping the endcap frequency upward gives the bigger response (Fig. 2.28a). In principle the axial frequency is where the large response first begins. It is also centered around the smaller response. When -V_c/V_0 and C_4 are too low, the downward sweep gives the larger

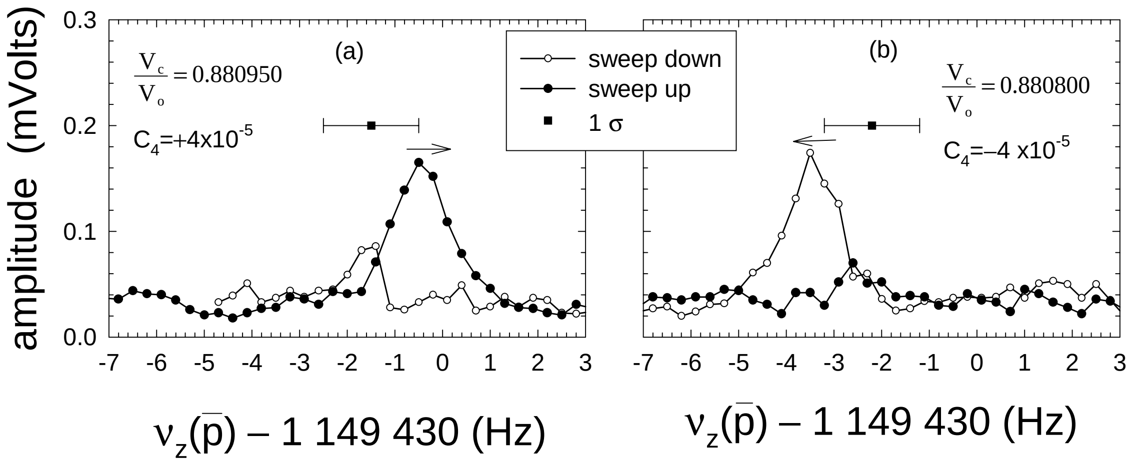

Figure 2.28: Two successive axial responses show the effect of changing the compensation voltage. The points and uncertainties indicate the axial frequency and error bar that is deduced from these examples. (a) The axial response when C_4 was slightly positive. The axial frequency is centered around the smaller peak, and occurs at the onset of the large signal. (b) The axial response when C_4 is slightly negative.

response (Fig. 2.28b).

The qualitatively different responses were used to tune C_4 to zero. With a fixed strength axial drive we changed the compensation voltage until the sweep direction of the large axial response changed. This defined the optimal compensation voltage to a certain accuracy. As C_4 approached zero, the measured signal grew bigger and occurred at a more precise frequency. The strength of the axial applied signals was then lowered and the process repeated. Eventually C_4 was tuned to less than 1×10^{-5}. At that stage, the axial frequency could be measured to 0.25 Hz (Fig. 2.6b) which is better than we required.

Once the compensation voltage (V_c) was set correctly, the axial frequency did not shift as the drive power changed. The axial response was measured by applying signals of -25 dBm on both the ring electrode and the endcap electrode. As we low-

Particle	ν_z(Hz)	-V_0 (V)	-V_c/V_0 (%)
$\bar{p}$	1 149 437	26.063 70	88.082
H^-	1 149 431	26.035 80	88.082

Table 2.5: The 1996 axial trapping parameters for the $\bar{p}$ and the H^-. ν_z is the axial frequency, V_0 is the ring trapping voltage, and V_c/V_0 is the ratio of the compensation to the ring voltage.

ered the drive power the measured axial signal did not shift appreciably (Fig. 2.29). The lower drive power measured the axial frequency more accurately but took longer to complete. For a 1 part in 10^{10} measurement, -25 dBm drive power measured the axial response accurately.

Since the time of the 1995 published $\bar{p}$ to p charge-to-mass measurement [2], two developments made finding the optimal ring voltage (-V_0) and compensation voltage (V_c) easier. First, we more completely removed the cooling electrons which were required initially to load antiprotons. This kept the electrons from changing the stray electric field and kept V_0 and V_c stable for days. Once the -V_0 and V_c were initially tuned, only a minor adjustment needed to be made to complete a measurement. This improved electron removal eliminated the large voltage shifts that occasionally took place after loading antiprotons. To find the optimal -V_0 and V_c again took several hours at times, slowing down the measurement (page 129 of Ref. [1]). Second, since the H^- and the $\bar{p}$ had nearly identical charge-to-mass ratios, once V_0 and the ratio V_c/V_0 were measured for the H^- they could be accurately predicted for the $\bar{p}$. In practice, both particles were compensated for the same ratio of V_c/V_0 to within 1 part in 10^5. Furthermore, once $V_0(H^-)$ was measured, predicting $V_0(\bar{p})$ was accurate to within 1 mV. This provided a good starting estimate and made optimizing the trapping parameters much easier (Table 2.5).

During each night of $\bar{p}$ to H^- comparisons, we measured $\nu_z(H^-)$ and $\nu_z(\bar{p})$ regu-

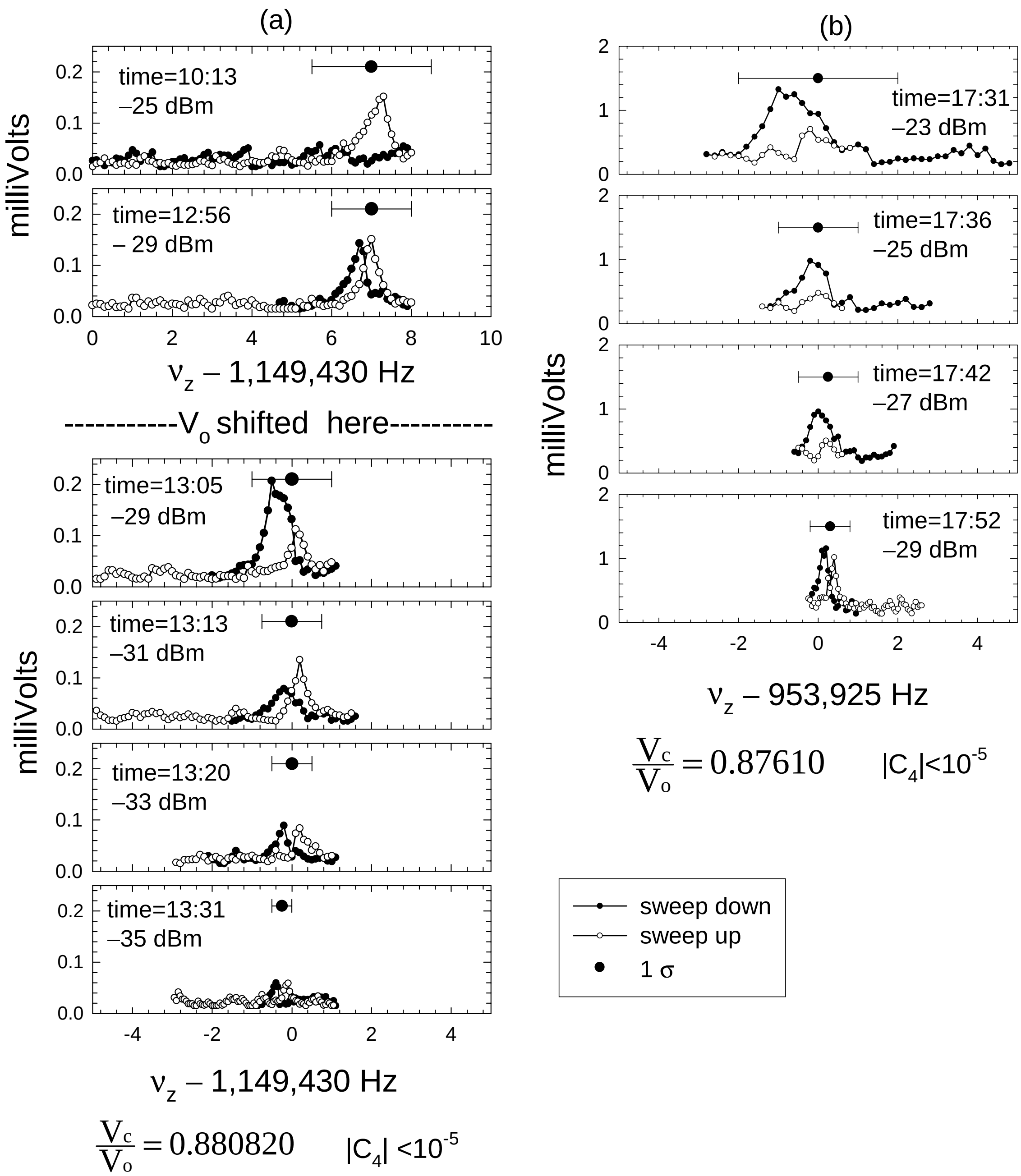

Figure 2.29: The axial frequency measured at high drive powers (−25 dBm) was the same as measured at lower drive powers. The power written in each figure was applied to both the endcap and the ring electrodes. As the power decreased, the axial frequency did not shift. In both series (a) and (b) the ratio $-V_c/V_0$ was held fixed.

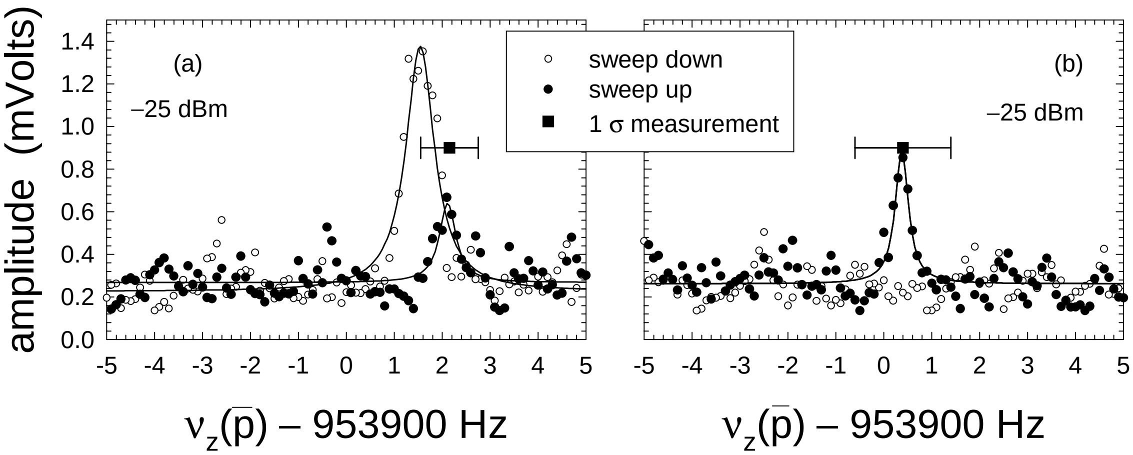

Figure 2.30: During the charge-to-mass measurement the radio frequency drive is swept upward then downward through the antiproton's resonant frequency. The endcap and ring driving signals were at -25 dBm. (a) When a response is seen in both directions the true response is centered around the smaller peak. (b) When a response is seen in only one direction the error bar was increased.

larly in a well compensated trap. Prior to beginning the measurement the compensation voltage was tuned to set C_4 to within 1×10^{-5} of the optimal value. During each measurement the power applied to each oscillating drive was set consistently to either -25 dBm or -27 dBm, low enough not to cause a power dependent frequency shift. The axial frequency was measured while both sweeping the endcap signal upward and downward. Most often we measured a response from the particle in both directions. In this case the error bars were smaller and were centered around the smaller peak (Fig. 2.30a, Fig. 2.29 and Fig. 2.28). Occasionally the particle only responded in one direction. In this case, the axial error bar was increased (Fig. 2.30b).

All the night's $\bar{p}$ and H^- axial responses were fitted for the difference frequency, $\nu_z(\bar{p}) - \nu_z(H^-)$. In the simultaneous fit described by Eq. 4.8 the difference frequency needed to be measured to 0.8 Hz. The sum frequency, $\nu_z(\bar{p}) + \nu_z(H^-)$, needed to be measured much less precisely. The night's axial responses were fitted at once and assumed a constant difference frequency (Fig. 2.31). This assumed that a slow voltage drift changed the axial frequency of both particles equally. All the axial data points were fit to a parabola with one constant term for the $\bar{p}$ data points and another for the H^- data points. The total voltage drift overnight was about equal to the axial error bar on individual measurements, so whether the data was fit to a linear drift or a parabola, the difference frequency was the same. The fit in Fig. 2.31 had 11 degrees of freedom and a χ^2_ν of 0.57, indicating that the fit was good. The fit predicted the difference frequency, $\nu_z(\bar{p}) - \nu_z(\mathrm{H}^-)$, accurately to 0.5 Hz which was slightly better than required to complete the 1 part in 10^{10} measurement.

To the first order, systematic shifts did not effect the difference frequency, $\nu_z(\bar{p}) - \nu_z(\mathrm{H}^-)$. The charge-to-mass ratios were very close for the $\bar{p}$ and the H^-; thus the ratio V_c/V_0 was about the same for both (Table 2.5). They both were measured with nearly the same electrostatic **E** field profile and were driven with the same strength oscillating signals. If C_4 were not zero, both particles would experience the same power dependent axial frequency shift. Even in this case, the frequency $\nu_z(\bar{p}) - \nu_z(\mathrm{H}^-)$ would still be accurate to the first order. By properly compensating and by measuring ν_z with low enough powers, we nevertheless insured that these shifts did not occur.

2.5 The Magnetron Motion

The magnetron motion is the slow circular motion perpendicular to the **B** field (Fig. 2.2). It results from a radially outward electric force and a radially inward magnetic force (Eq. 2.8).

The magnetron radius (ρ) tends to increase in time since lower energy orbits are

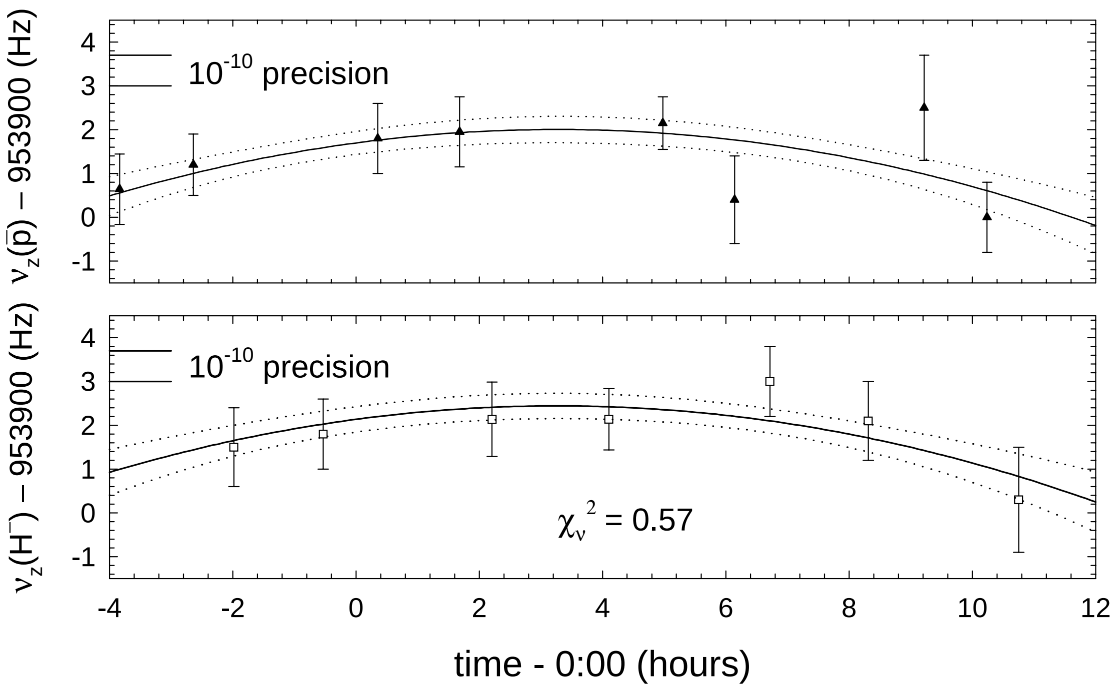

Figure 2.31: The H^- and $\bar{p}$ axial frequency measurements from midnight on 2 August 1995. The axial measurements were allows to drift as a parabola, where the difference between $\nu_z(\bar{p})$ and $\nu_z(\mathrm{H}^-)$ was held fixed. The difference frequency, $\nu_z(\bar{p}) - \nu_z(\mathrm{H}^-)$ was measured more accurately than we required for a 1 part in 10^{10} measurement.

larger. The magnetron potential energy (E_m) is given by the quadrupole potential (Eq. 2.3) when $z = 0$,

$$E_m = -\frac{m\omega_z^2\rho^2}{4}, \tag{2.24}$$

where ω_z is the angular axial frequency (Eq. 2.4), and m is the mass. The potential energy decreases when the radius increases (Fig. 2.32). To reach its highest potential, an oscillating electric field moves the particle inward against the radially outward electric force and pulls it up the potential hill (Fig. 2.32). This process is called "magnetron cooling [25]." The magnetron energy is mostly potential. Because $\omega_m \ll \omega_z$, the magnetron kinetic energy ($m\omega_m^2\rho^2/2$) is a negligible fraction (1 part in

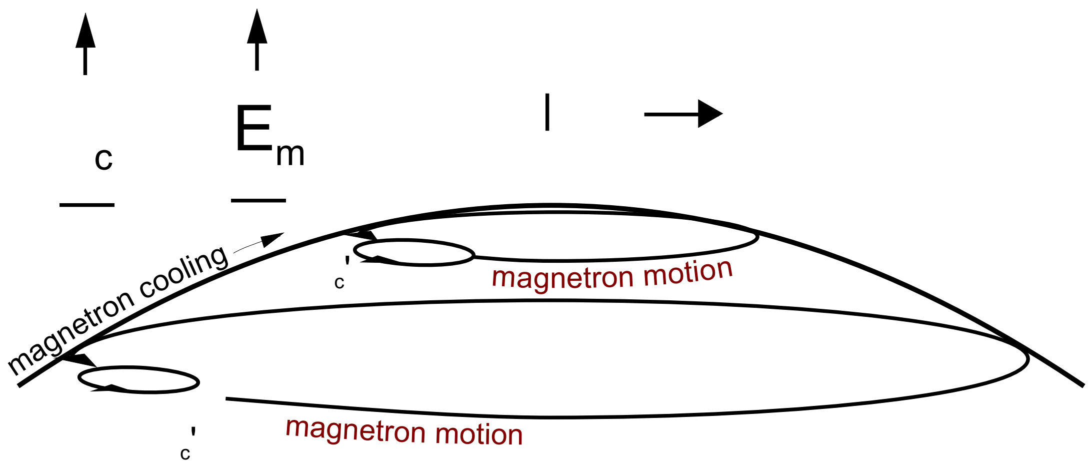

Figure 2.32: Small radius (ρ) magnetron orbits are highest in magnetron energy (E_m). Because of the **B** field bottle (Table 2.1), the cyclotron frequency (ν_c) shifts downward when the magnetron orbit is large.

10^4) of the total energy. The quantum picture (Fig. 2.33) shows a harmonic oscillator with negative energy levels and a highest energy state. The levels are separated by $\hbar\omega_m$ and the highest level also has the smallest radius. Any process that dissipates magnetron energy increases its orbit. Because ω_m is so low, the radiation field couples weakly to the magnetron motion and dissipates the magnetron energy over years. However steps in the $\bar{p}$ − H^- measurement and cleaning sequence dissipate the magnetron energy in minutes.

To avoid errors, it was important that measurements of ν_c take place in a small magnetron radius. In a large radius the **B** field was weaker (Table 2.1) and the measured ν_c shifted downward (Fig. 2.32). If the $\bar{p}$ was measured in a large magnetron orbit while the H^- was measured in a small magnetron orbit, the difference frequency, $\Delta\nu_c = \nu_c(p) - \nu_c(\bar{p})$, was not zero. $\Delta\nu_c$ may have been of either sign since either particle could have been in the large magnetron orbit. To be sure that we measured a difference in the charge-to-mass ratios and not a difference in the magnetron radius, we carefully reduced the magnetron radius of each particle.

In the following sections we describe how to reduce the magnetron orbit, how to measure its frequency accurately, and how to insure that the magnetron orbit is small enough to avoid frequency shifts.

2.5.1 Reducing the Magnetron Orbit

To magnetron cool, an oscillating electric field couples the magnetron and axial equations of motion. This electric field is applied to the split compensation electrode (Fig. 2.1) at a frequency $\nu_z + \nu_m$. It creates an inhomogeneous potential that depends on the particle's position as:

$$V \propto zx \cos\left[(\omega_z + \omega_m)t\right], \tag{2.25}$$

where z is the axial displacement, x one of the radial directions and $\omega = 2\pi\nu$. Classically this potential exerts an electric force both radially inward and along the axial direction. Quantum mechanically, photons couple the axial and magnetron motions. The three Penning trap motions are all essentially harmonic oscillators and can be quantized [32]. The axial energy levels are separated by $\hbar\omega_z$, the cyclotron energy levels are separated by $\hbar\omega_c'$, and the magnetron energy levels are separated by $\hbar\omega_m$. A photon $\hbar(\omega_m + \omega_z)$ gets absorbed by the particle (Fig. 2.33). This increases both the axial energy and magnetron energy [33]. The axial energy then damps since the motion is coupled to an RLC circuit. This damping leads to large measurable signal (Fig. 2.35) at ν_z and indicates that the electric field is resonant. The magnetron motion gains energy $\hbar\omega_m$; its potential energy increases and its orbit decreases or "cools." At a slower rate the drive also stimulates emission of the photon $\hbar(\omega_m + \omega_z)$ (Fig. 2.33), and this process increases or "heats" the magnetron

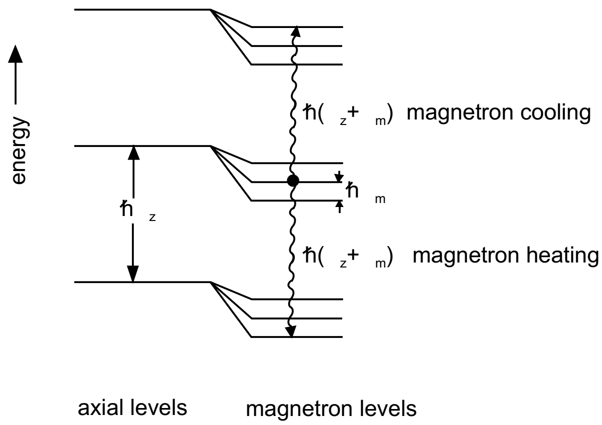

Figure 2.33: Two processes lead to reducing the magnetron radius. More frequently the particle absorbs a photon of energy $\hbar(\omega_m + \omega_z)$, and both the axial and the magnetron energy levels increase. This reduces the magnetron orbit and "cools" the motion. Also sometimes the drive can stimulate emission of a photon of energy $\hbar(\omega_m + \omega_z)$ and both the axial and magnetron energy decrease. This increases the magnetron orbit or "heats" the motion.

orbit. When the magnetron orbit is large, the magnetron cooling drive decreases the magnetron orbit.

Magnetron cooling in this way can reduce the magnetron orbit sufficiently to prevent cyclotron frequency shifts. Magnetron cooling reduces the magnetron energy (E_m) to a limit related to the equilibrium axial energy (E_z) [25],

$$E_m = -\frac{\nu_m}{\nu_z} E_z. \tag{2.26}$$

When the magnetron energy is greater than this limit, the cooling rate is larger than the heating rate, and the magnetron orbit decreases. To keep the axial energy small, the axial motion stays coupled to the *RLC* tuned circuit. This is done by adjusting the trapping potential (V_0) to keep the axial frequency (ν_z) fixed on the tuned circuit. The circuit acts as a thermal bath and keeps the axial energy at 4 K.

Magnetron Motion		
State	Radius (μm)	Energy (μeV)
cooling limit	4	-2
For $\nu_c(\bar{p})$ to be accurate to 0.01 Hz	51	-361

Table 2.6: When we reached the cooling limit, the magnetron orbit was small enough not to shift the measured cyclotron frequency (ν_c).

When the cooling limit is reached, the magnetron orbit is small enough not to cause any shift in the cyclotron frequency (Table 2.6).

To reach the cooling limit, both the cooling drive must be resonant, and the axial motion must remain coupled to the thermal bath (the *RLC* circuit). When the axial frequency is not tuned to the *RLC* circuit, its motion is undamped; the magnetron-cooling drive increases the axial energy well above the 4 K temperature of the bath, and the magnetron energy remains large. To magnetron cool a particle we left the magnetron-cooling drive at a frequency ν_m above the axial amplifier. We then varied the trapping potential (V_0) and this varied the axial frequency (Eq. 2.4). When the axial frequency (ν_z) was tuned to the frequency of the *RLC* circuit, both the magnetron-cooling drive was resonant and the axial motion was damped. This reduced the magnetron orbit enough that further cooling made no cyclotron frequency change.

2.5.2 Measuring ν_m

We measured the magnetron frequency (ν_m) by first applying the endcap and the ring signals to increase the particle's axial energy. While they were resonant, we monitored the resulting large axial frequency at ν_z. We then applied another signal which swept around the magnetron-cooling frequency, $\nu_z + \nu_m$. When this signal resonated, it also put energy into the axial motion. At that point the driven axial signal decreased [1, 25]. The width of this signature set the accuracy limit of this measurement. We compared this measurement with the prediction of Eq. 2.8:

$$\nu_m = \frac{\nu_z^2}{2\nu_c'}, \tag{2.27}$$

and we found that the two differed by -0.8 ± 0.1 Hz [1]. Using Eq. 2.27 predicted the magnetron frequency well within the 120 Hz accuracy that we required so determined the magnetron frequency sufficiently accurately.

2.5.3 Voltage Sweeps to Efficiently Magnetron Cool

The strength of the electric restoring force for the axial motion (Eq. 2.4) depends on the magnetron radius. In a small radius the trapping potential is very close to the ideal quadrupole making the electric restoring force independent of magnetron radius. In a larger radius C_4 of Eq. 2.1 is not zero, and the restoring force is proportional to C_4. For a still larger radius in our open-endcap Penning trap, the force always increases with the radius. The axial frequency increases as this force increases. To keep ν_z fixed in resonance with the RLC tuned circuit, we decreased the magnitude of the voltage (V_0) applied to the ring electrode (Fig. 2.34). One H^- in a large magnetron orbit (Fig. 3.17) required a trapping voltage (V_0) reduced by 700 mV out of 26 V. Some magnetron heated electrons required reducing the trapping voltage (V_0) by 70 mV out of 43 V (Fig. 3.16).

The magnetron radius dependent trapping voltage makes reducing the magnetron orbit difficult. In order for the magnetron-cooling applied signal (Eq. 2.25) to be resonant, the trapping voltage (V_0) must be correct to within 2 mV. Most often a fixed trapping voltage (V_0) does not place the particle in resonance with the

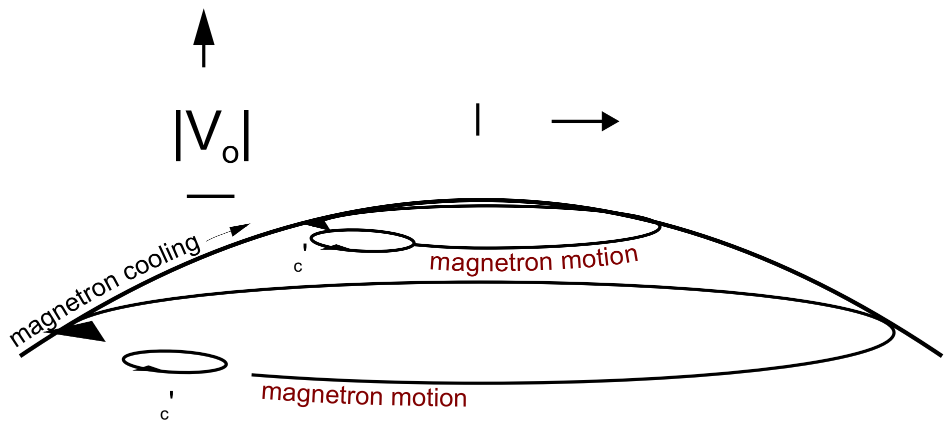

Figure 2.34: The trapping voltage (V_0) required to keep the axial frequency constant decreases for particles in large magnetron orbits. ρ is the magnetron radius and V_0 is the ring voltage necessary to keep the particle's axial frequency fixed on the axial amplifier.

applied magnetron-cooling signal. We found sweeping the trapping voltage critical for reducing the magnetron radius sufficiently.

The best way to reduce large magnetron orbits is with a fast voltage sweep (Table 2.7). When the particle is in a big magnetron orbit, the electric field is not as precise as when it is in the trap center. The particle samples a range of different strength electric restoring forces and oscillates in a range of axial frequencies. The

Type of Sweep	Rate (mV/sec)	Rate (Hz/sec)	Drive Time (seconds)	Purpose
fast voltage sweep	0.50	11.0	0.007	magnetron cool
slow voltage sweep	0.05	1.1	0.072	magnetron cool
frequency sweep	—	0.1	0.720	measure ν_z

Table 2.7: Different sweeps have much different rates. A voltage sweep changes the particle's axial resonance frequency (ν_z). A frequency sweep changes the driving signal applied to the endcap electrode at $\nu_z - \nu_{\mathrm{mod}}$. The rate that ν_z and the endcap applied signal approach each other is shown. The drive time is the length of time that the driving signal is resonant with the particle.

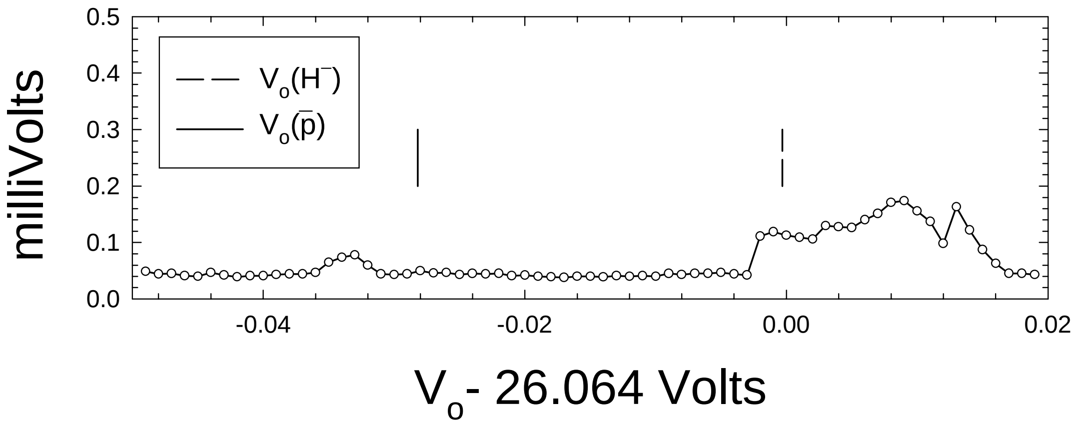

Figure 2.35: The $\bar{p}$ and H^- magnetron cooled over a wide voltage range. We applied the magnetron-cooling signal at ν_m above the axial amplifier, and swept the ring voltage (V_0). The response seen was at ν_z and showed the voltage where the $\bar{p}$ magnetron cooled (small bump) and where the H^- magnetron cooled (broad larger signal). The legend shows the trapping voltages used once the particles fully magnetron cooled.

axial frequency is not restricted to any 0.25 Hz frequency bin and cannot be detected with the axial frequency sweeps (Fig. 2.30). To see the axial response the magnetron orbit was first reduced. A magnetron-cooling signal was applied at a frequency ν_m above the axial amplifier, and the ring voltage was swept. Sweeping the voltage guarantees that all axial frequency components will be resonant with the magnetron-cooling signal and that the magnetron orbit will decrease. Fig. 2.35 shows the measured response seen when a $\bar{p}$ and H^- both were magnetron cooling. At the lower voltage $\nu_z(\bar{p})$ was resonant with the amplifier and the $\bar{p}$ magnetron cooled; at the higher voltage $\nu_z(H^-)$ was resonant and the H^- magnetron cooled. Since the H^- showed magnetron cooling over a 20 mV range, its axial frequency was 440 Hz wide, much wider than the 1 Hz axial frequencies. After repeated sweeps this magnetron-cooling response narrowed and eventually stopped. This indicated that the magnetron orbit had decreased.

The magnetron orbit was further reduced by sweeping the trapping voltage (-V_0) at a 10 times slower rate (Table 2.7). Repeating at a slower rate gives the particle much longer to interact resonantly with the magnetron-cooling drive and cools more efficiently. The amplitude of the driven axial signal indicates when the particle is magnetron cooled. As the particle magnetron cools, the axial frequency becomes narrower and the driven response gets bigger. In addition to the magnetron-cooling signal we kept fixed the endcap ($\nu_z - \nu_{\rm mod}$) and the ring ($\nu_{\rm mod}$) axial signals. The endcap and ring axial signals applied together drive the axial motion at ν_z. The trapping voltage (V_0) is swept and at some point the axial frequency (ν_z) resonates with the axial driving signals and with the magnetron-cooling signal. At first (Fig. 2.36a), no driven response was seen at any voltage. The particle had too large a magnetron orbit and too wide an axial frequency to give any response. After repeating, a large driven response was seen in 20 minutes (Fig. 2.36c). The magnetron orbit had been reduced sufficiently to produce a narrow driven signal.

These slow voltage sweeps should fully magnetron cool the particle. Once the particle is in a small magnetron orbit, the trapping potential is very nearly a pure quadrupole. The electric restoring force no longer depends on magnetron radius and the trapping voltage (V_0) and the axial frequency no longer shifts. When the voltage is correct, the magnetron-cooling drive remains resonant and efficient. This cools the magnetron motion to the cooling limit in about 20 minutes. We found that once an axial response such as in Fig. 2.36c was seen, repeated slow voltage sweeps did not further increase the response amplitude. Furthermore, after seeing such a response, we could measure a narrow axial signal at the lowest powers such as in Fig. 2.6b.

The axial frequency sweeps did not reduce the magnetron orbit. They held the trapping voltage (V_0) and the axial frequency (ν_z) fixed at a point which may not

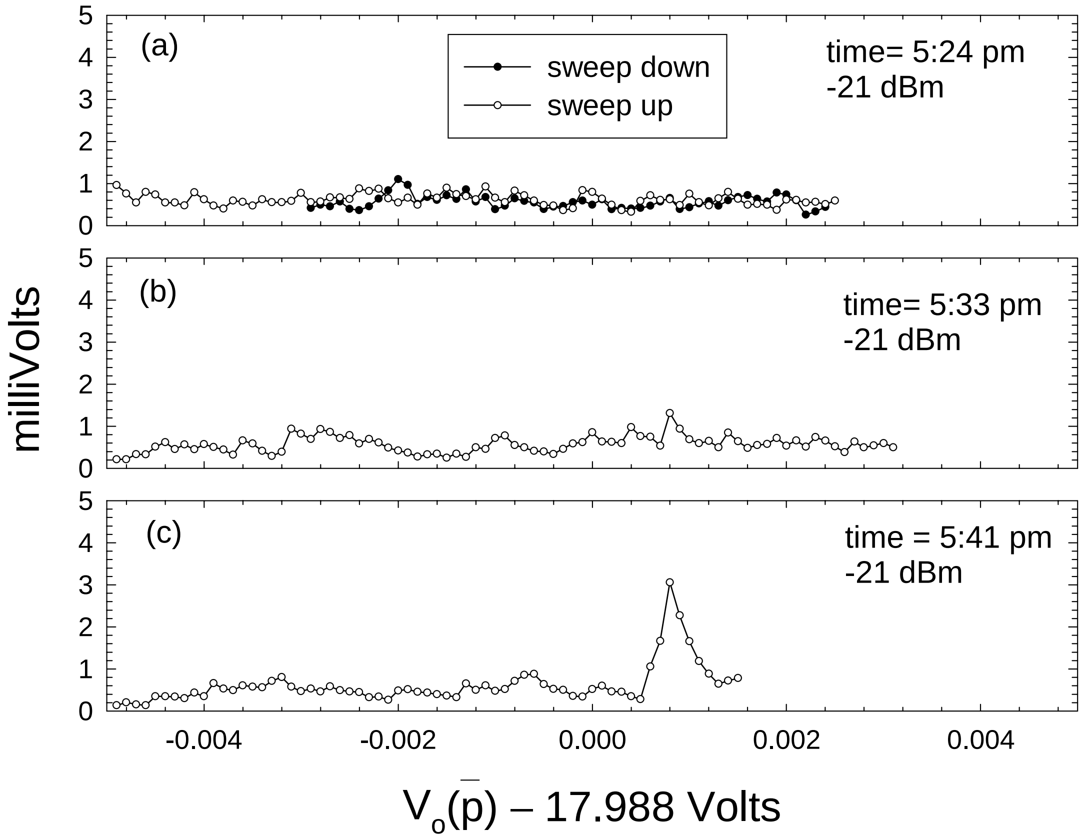

Figure 2.36: Slowly sweeping the ring voltage (V_0) cools the magnetron motion. Plotted is the driven response at ν_z versus the trapping potential. The magnetron-cooling drive at $\nu_m + \nu_z$, the ring electrode drive at $\nu_{\rm mod}$, and the endcap drive at $\nu_z - \nu_{\rm mod}$ are applied at fixed frequencies. The power of the $\nu_{\rm mod}$ and the $\nu_z - \nu_{\rm mod}$ drives is recorded in each figure. Once the motion is cooled a large driven axial response at ν_z is seen. (a) No response after two voltage sweeps. (b) A small barely detectable response. (c) After the particle magnetron cooled we see a large response.

be in precise resonance with the magnetron-cooling drive. The magnetron-cooling may not be efficient and the magnetron orbit may not reach the cooling limit. In contrast, the slow voltage sweeps are guaranteed to be resonant and efficient at some point.

Even if a large signal is seen during an axial frequency sweep, the particle may still be in a large magnetron orbit. In a frequency sweep, the endcap signal ($\nu_z - \nu_{\mathrm{mod}}$) is resonant with the particle for much longer than for a slow voltage sweep (Drive Time in Table 2.7) and drives it into a larger orbit. Even if the particle is slightly magnetron heated, it still may give a large signal. In Fig. 2.37a a signal was seen during an axial frequency sweep, but the signal size was smaller than expected. Afterwards, when a voltage sweep was tried, no driven axial signal was seen (Fig. 2.37b). This indicated that the particle was not magnetron cooled fully. Twenty minutes of slow voltage sweeps led to large signals (Figures 2.37d and 2.37e) and indicated that the $\bar{p}$ had fully magnetron cooled. In the final frequency sweep the endcap signal drove the $\bar{p}$ with less power than used initially (Fig. 2.37a) and produced a larger signal (Fig. 2.37f). A driven axial response during a slow voltage sweep is a better test of magnetron cooling than a driven axial response during a frequency sweep.

When the trapping voltage is fixed, magnetron cooling can take hours (Fig. 2.38). For a particle initially in a large magnetron orbit, we repeatedly measured the modified cyclotron frequency. For each measurement in Fig. 2.38 the magnetron-cooling drive was on and the trapping voltage was held fixed. The $\mathbf{B}$ field bottle (Table 2.1) makes the cyclotron and the modified cyclotron frequencies shift downward when the magnetron radius is large. Magnetron cooling takes much longer than when the voltage is swept, because the magnetron-cooling drive is nonresonant and less efficient.

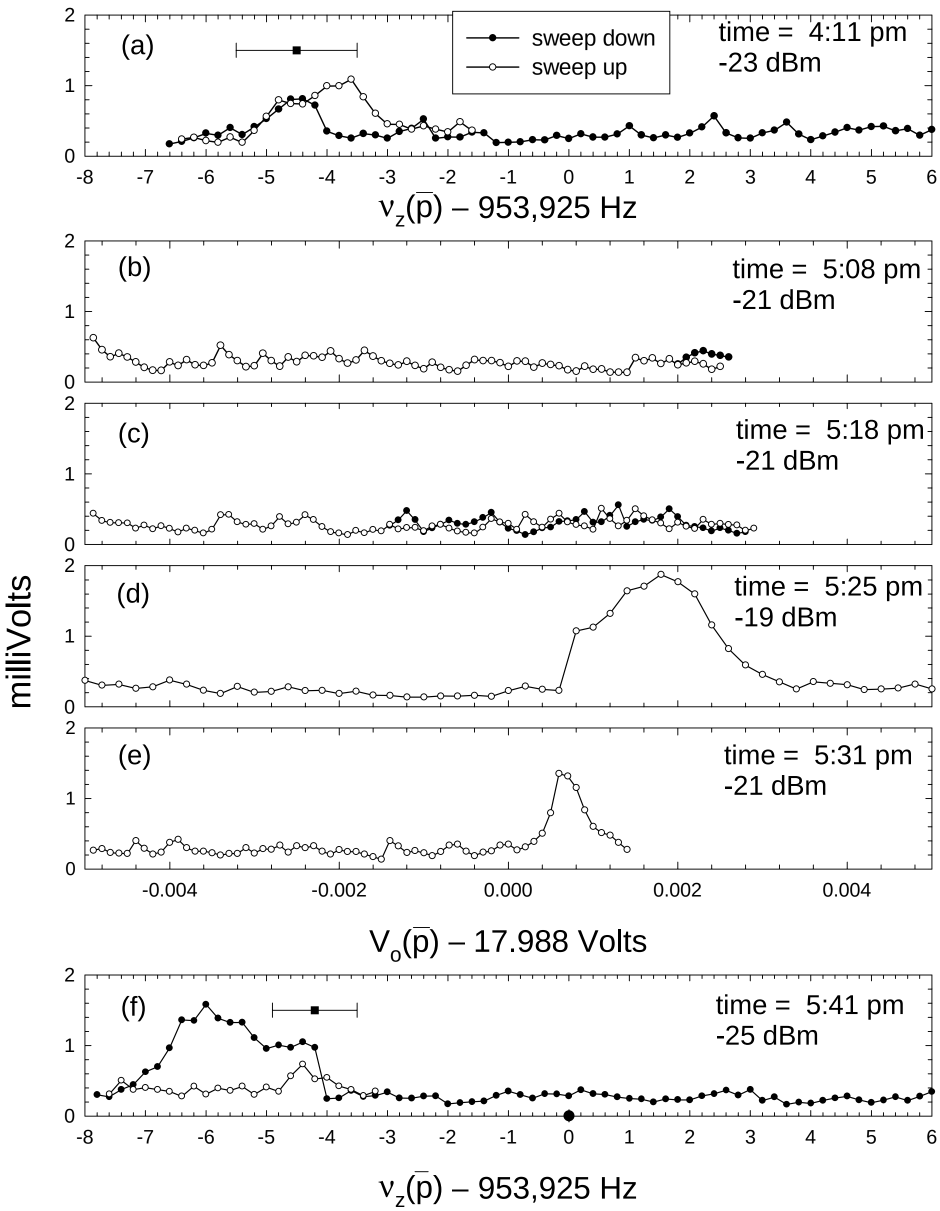

Figure 2.37: A driven axial response during a frequency sweep does not indicate that the $\bar{p}$ is magnetron cooled. The drive power of the endcap ($\nu_z - \nu_{\rm mod}$) and ring ($\nu_{\rm mod}$) signals is shown in each figure. (a) A frequency sweep showed an axial signal, but the driven response was smaller than expected. (b) No response during a slow voltage sweep showed that the $\bar{p}$ was magnetron heated. (c,d,e) After repeating the slow voltage sweeps for 20 minutes, the particle magnetron cooled and gave a large axial response. (f) A final frequency sweep gave a bigger signal than measured initially even though the axial drive power was lower.

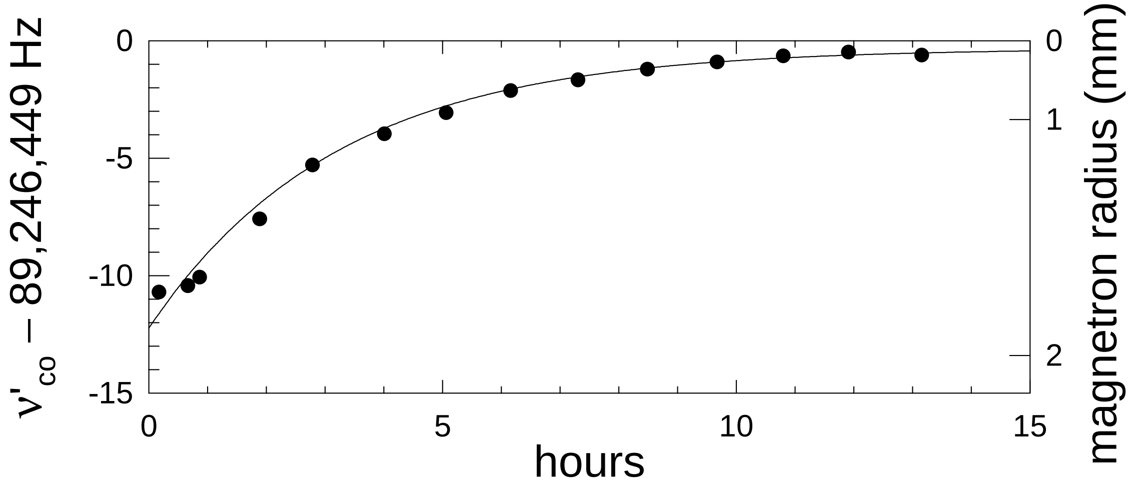

Figure 2.38: Magnetron cooling when V_0 is fixed can take hours. Plotted is the modified cyclotron frequency with no kinetic energy (ν'_{c0}) in time. The trapping voltage (V_0) and the magnetron-cooling drive ($\nu_z + \nu_m$) are held constant. The particle initially had a large magnetron radius and because of the **B** field bottle ν'_{c0} shifted downward. The particle inefficiently magnetron cooled since the magnetron-cooling drive was not resonant. For the first 5 hours no axial response was seen.

During the $\bar{p}$ to H^- comparison, steps in the measurement cycle heated the magnetron motion. We repeated a sequence three times a day to remove electrons from the trap. This process increased the magnetron orbit of the $\bar{p}$ and the H^-. Initially, a slow voltage sweep showed that the $\bar{p}$ was magnetron cooled (Fig. 2.39a). Immediately after cleaning the trap, the $\bar{p}$ was in a large magnetron orbit and gave no axial response during the slow voltage sweep (Fig. 2.39b). Repeated slow voltage sweeps over 20 minutes cooled the magnetron motion (Figures 2.39c and 2.39d). Finally at low powers the $\bar{p}$ was measured precisely during an axial frequency sweep (Fig. 2.39e).

One reason why removing electrons heats the magnetron motion is that we lowered the trapping voltage to 1 V in the process; at a low voltage, resistors placed around the ring electrode dissipated the magnetron energy. At low voltage the

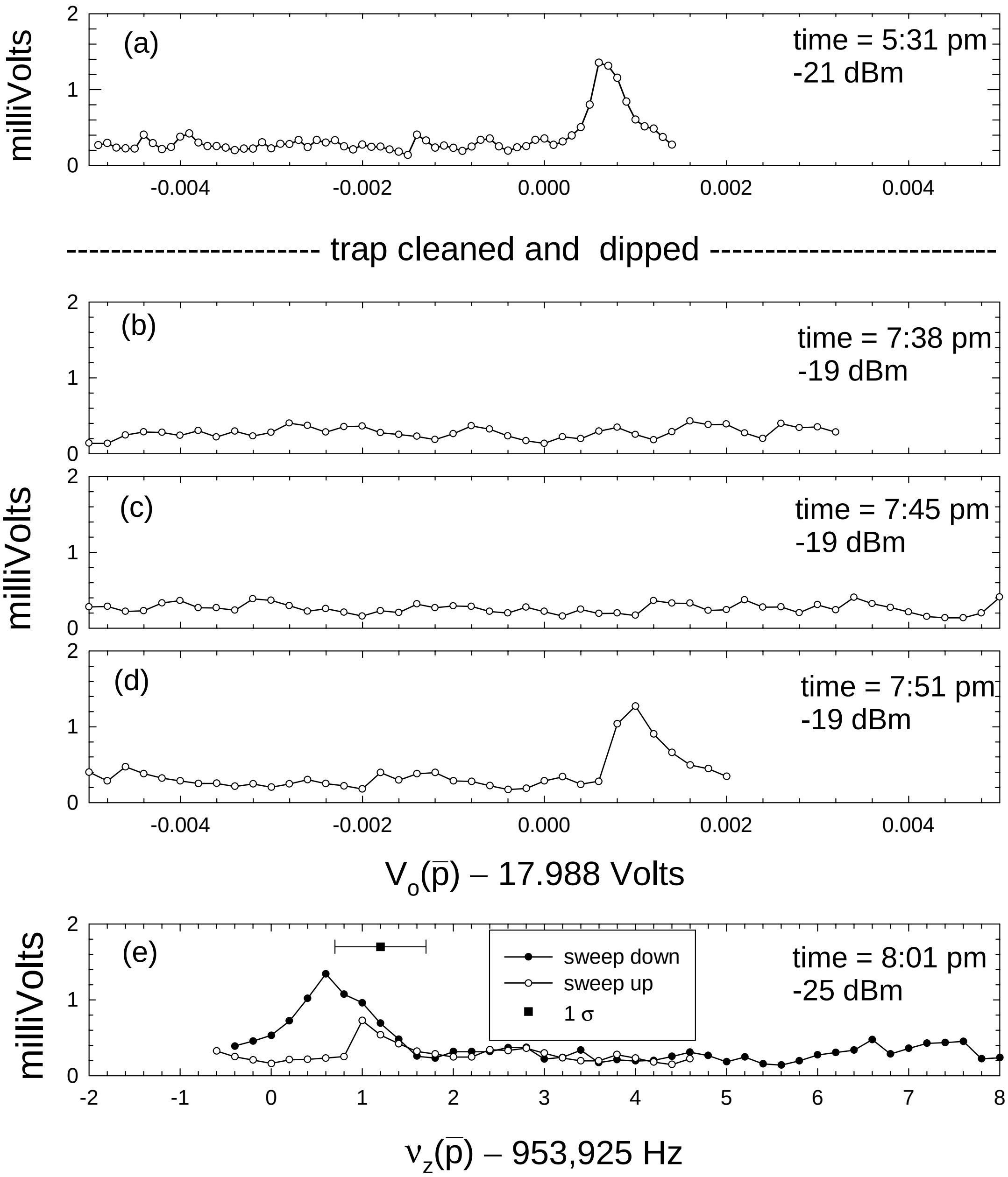

Figure 2.39: The process used to remove electrons increased the magnetron orbit of the $\bar{p}$. (a) A slow voltage sweep indicated that the $\bar{p}$ was magnetron cooled. We then removed electrons. (b) After removing electrons, the slow voltage sweep showed that the $\bar{p}$ became magnetron heated. No response was seen. (c,d) Repeated slow voltage sweeps magnetron cooled the $\bar{p}$, and led to a large driven axial signal. (e) Immediately afterwards, a low power frequency sweep measured the axial frequency accurately.

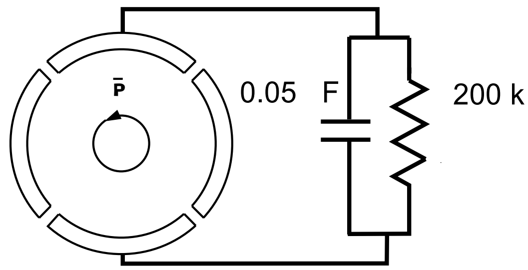

Figure 2.40: Resistors across the ring electrode increase the magnetron orbit. At 1 V, the magnetron frequency is 280 Hz, and at least 5% of the induced current passes through the resistors. This dissipates magnetron energy and increases the magnetron radius. In 1996 we removed these resistors.

magnetron frequency is much lower than at high voltage. As the particle orbits, more of the induced current passes through the resistor rather than the capacitor in Fig. 2.40. This dissipates magnetron energy and increases the magnetron orbit. In 1996, we removed these resistors, but still the electron cleaning procedure heated the magnetron motion. This made it critical to perform the slow voltage sweeps on each particle before each $\bar{p}$ to H^- charge-to-mass measurement.

Not reducing the magnetron orbit sufficiently in the $\bar{p}$ to H^- measurement caused a large cyclotron difference frequency ($\nu_c(p) - \nu_c(\bar{p}) = \Delta\nu_c$) between the p and the $\bar{p}$. When one particle was not magnetron cooled, it was measured in a smaller **B** field compared with the other particle. This caused a measurement error in the difference frequency ($\Delta\nu_c$). Since either the $\bar{p}$ or the H^- could have ended up in the larger magnetron orbit, the frequency difference ($\Delta\nu_c$) could have been of either sign. To measure the size of the effect, we plotted the frequency difference ($\Delta\nu_c$) on nights where we did not magnetron cool the motion sufficiently (Fig. 2.41). Fig. 2.41 shows all the measurements that were made on two successive nights, where before the second night no slow voltage sweeps were performed. We still cycled the electron removal procedure three times, heating the magnetron motion. The

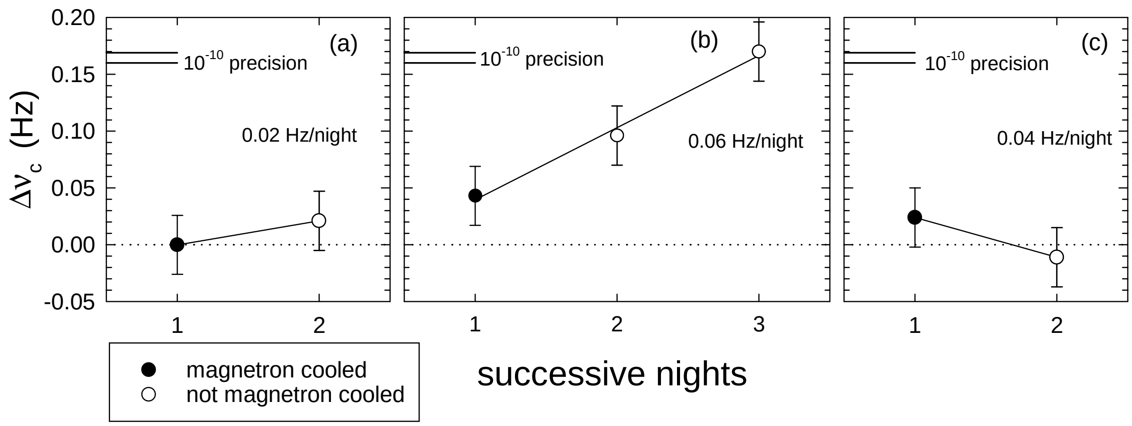

Figure 2.41: On a day when slow voltage sweeps to cool the magnetron motion were not performed, the frequency difference, $\nu_c(p) - \nu_c(\bar{p}) = \Delta\nu_c$, increased compared with the previous day. The increase was either positive or negative, and its magnitude was about 0.04 Hz on average. (a,c) no measurable magnetron cooling effect is seen. (b) A measurable increase is seen due to magnetron heating. This measurement was made before realizing the importance of the slow voltage sweeps.

difference between the measurements of $\Delta\nu_c$ on the first and second night measured the effect of increasing the magnetron radius prior to the second night. In Fig. 2.41a and 2.41c no measurable effect is seen due to magnetron heating. In Fig. 2.41b not magnetron cooling caused a frequency shift. We found that not performing the necessary voltage sweeps led to an increase in $\Delta\nu_c$ measurements of 0.04 Hz. This was about twice the error bar for each measurement. For this reason we excluded those measurements made without first performing the slow voltage sweeps.

2.6 Conclusion

We showed how to measure ν_c', ν_z, and ν_m accurately enough for a 10^{-10} measurement. The relativistic shift in the modified cyclotron frequency was accounted for. A fit determined the modified cyclotron endpoint frequency (ν_{c0}'), the modified cyclotron frequency with no relativistic shift. When the **B** field was stable, this was accurate. In Chapter 4 the affect of the **B** field drift and the affect of the second particle are taken into account. When the electrostatic potential was tuned to be a quadrupole, the axial frequency could be measured to the accuracy we required. In a large magnetron radius, both ν_c' and ν_z shift. However, repeatedly sweeping the trapping potential (V_0) while magnetron cooling eliminated these shifts.

Chapter 3

Preparing a Single $\bar{p}$ and H^- for Measurement

Soon after first observing a single H^- ion in the trap[1], we began using a single H^- ion to measure the $\bar{p}$ to p charge-to-mass ratio. Measuring the H^- cyclotron frequency instead of the proton's eliminated the systematic error of the previous work [1]: comparing particles of opposite charge. The H^- ions were consistently loaded along with antiprotons. The number of trapped particles was reduced to a single $\bar{p}$ and a single H^-. A single $\bar{p}$ and H^- must remain trapped together for at least one day to complete a charge-to-mass ratio measurement; keeping an H^- this long turned out to be more difficult than first expected. At first, we could only keep the H^- trapped for a few hours. The procedure was then improved: the axial energy of the H^- was consistently kept low, electrons were more efficiently eliminated, and the trap vacuum was restored to its previous value. This procedure increased the

[1]On June 9, 1994, Wolfgang Quint and David Phillips discovered an H^- trapped along with a $\bar{p}$ while completing the direct proton and antiproton measurements of the charge-to-mass ratios published in 1995. The hope to use an H^- had been mentioned in the first proposal to CERN in 1984.

H^- hold time to up to 5 days. How antiprotons and H^- ions were loaded and how a single one of each was kept trapped for days is discussed here.

3.1 Loading H^- and Antiprotons

At the European Center for Nuclear Research (CERN), in Geneva, Switzerland, the Low Energy Antiproton Ring (LEAR) facility provided $\bar{p}$ for the trap experiment. When the antiprotons entered the trap, the H^- were also formed. This was the main way we loaded H^-. The H^- could also be loaded using an internal electron beam.

Antiprotons were produced when a 26 GeV proton beam from the CERN Proton Synchrotron (PS) collided with an iridium target [34, 35]. (The PS accelerator complex is shown in Fig. 3.1.) They emerged with a wide angular distribution and with a large momentum spread. The Antiproton Collector ring (AC) and the Antiproton Accumulator (AA) [34] gathered these antiprotons and produced a monoenergetic beam of up to 10^{12} $\bar{p}$ of momentum 1 GeV/c. The antiprotons were subsequently slowed to 600 MeV/c in the PS. The $\bar{p}$ entered LEAR where they were accelerated, decelerated or stored. LEAR provided $\bar{p}$ to experiments, either continuously or in bunches. To load $\bar{p}$ in our experiment the $\bar{p}$ were decelerated to 105 MeV/c and extracted in a pulse of 250 nanoseconds.

The antiprotons entered the trap vacuum enclosure through a 10 μm titanium window and passed through a 116 μm gold-plated aluminum degrader (Fig. 3.2a). The degrader stopped about half of the antiprotons and approximately 1 in 10^4 emerged into the trapping region with kinetic energy below 3 keV [18]. The magnetic field confined the antiprotons perpendicular to its axis. The antiprotons traveled along the magnetic field axis until they reached the upper high voltage electrode (UPHV), which was held at -3 kV (Fig. 3.2b). Antiprotons with kinetic energy

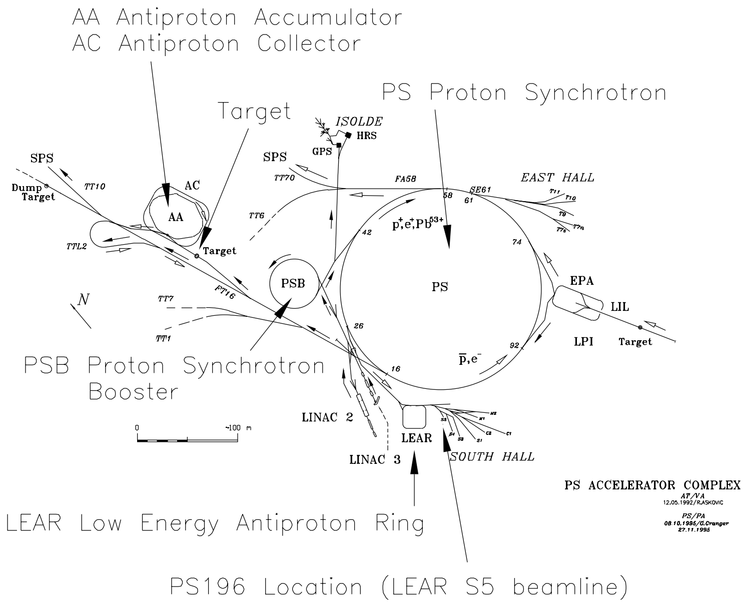

Figure 3.1: The CERN antiproton complex. Antiprotons were formed at the target, collected in the AC, stored in the AA, and transferred to LEAR for further cooling before extraction to our experiment, the PS196 site.

less than 3 keV reversed directions. Before the antiprotons reached the degrader, its voltage was suddenly switched to −3 kV (Fig. 3.2c). The antiprotons were trapped between the UPHV electrode and the degrader [18, 36]. Most of the antiprotons trapped initially had initially less than 1 keV of kinetic energy (Fig. 3.3). In some earlier experiments more antiprotons with kinetic energy between 1 to 2 keV were seen than in Fig. 3.3.

Electrons were used to dissipate the energy of the $\bar{p}$. Prior to loading antiprotons, electrons were loaded in the measurement trap. We applied −1.2 kV to a very sharp tungsten field emission point (FEP) (Fig. 3.2a). This created an electric field strong enough at the FEP tip to eject electrons. The FEP emitted a 30 nA electron beam. The ring electrode was also biased to 43 Volts (Fig. 3.2a). Some electrons collided with background gas atoms or with other electrons, lost their energy near the ring

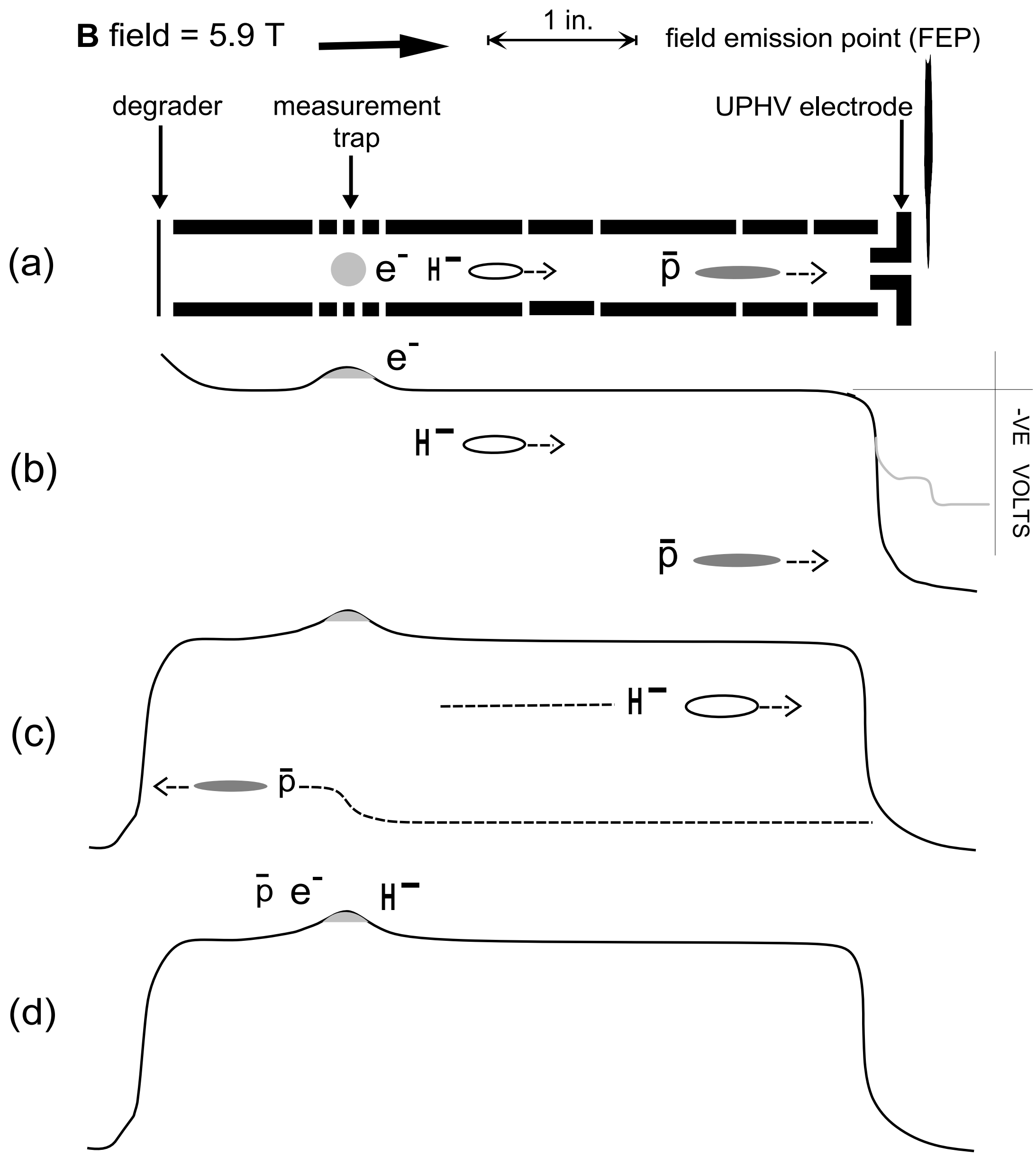

Figure 3.2: The steps followed to load antiprotons and H^-. (a) The trap electrodes are shown. Within 100 nanoseconds after the antiprotons pass through the degrader H^- was formed. (b) (solid line) The initial arrangement of voltages used to load the $\bar{p}$ and H^-. (dotted line) To form H^- using the field emission point (FEP), the FEP and the upper high voltage electrode (UPHV) were also negatively biased. (c) 250 nanoseconds after the $\bar{p}$ enter, the potential on the degrader changed from 100 V to -3 kV. This completed the trap. (d) 60 seconds later the $\bar{p}$ and H^- lost all their energy through repeated collisions with the trapped electrons.

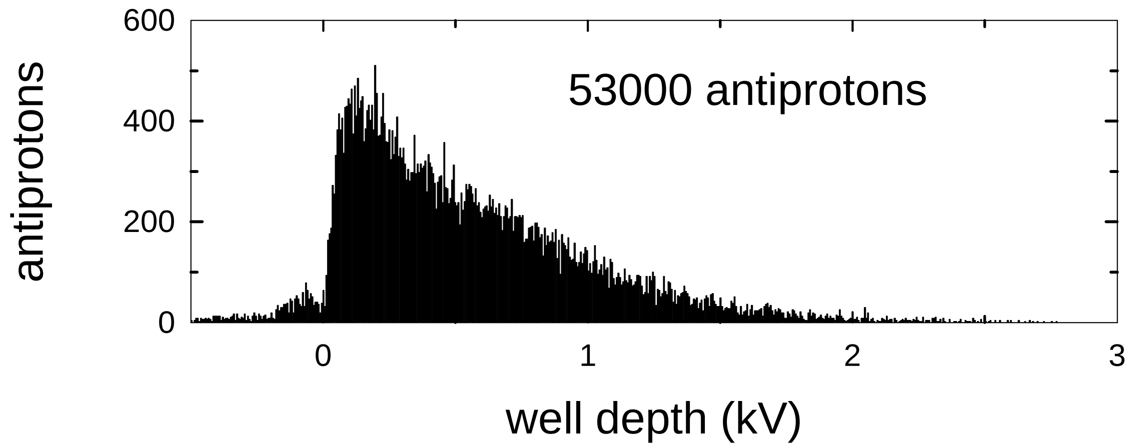

Figure 3.3: The energy spectrum of the antiprotons indicated that the $\bar{p}$ emerged from the degrader with typically 1 keV of energy. The antiprotons were loaded without being cooled with electrons. They were held for 100 seconds prior to being counted.

electrode and were trapped. An RLC circuit was used to damp and detect the electron axial motion. After reducing their magnetron orbit, an electron "dip" as in Fig. 2.8 was seen (Fig. 3.4). Initially $500,000$ e^- with an axial temperature near 4 K were loaded.

The antiprotons lost their kinetic energy when they collided with electrons. Every collision transferred a small fraction of the antiproton's axial energy to the electrons. With a time constant of 0.2 seconds (Table 2.3), electrons then dissipated the energy in the RLC circuit. In 10^8 passes and 100 seconds, the axial kinetic energy of the antiprotons decreased to the temperature of the electrons, to about 4 K. The antiprotons were then confined in the measurement trap [19, 35].

Loading antiprotons also liberated hydrogen and electrons. When the antiprotons crashed through the degrader, they dislodged hydrogen atoms from the degrader surface. The mechanism is probably similar to the way the electron beam created from the FEP dislodged hydrogen for loading protons in the trap. The

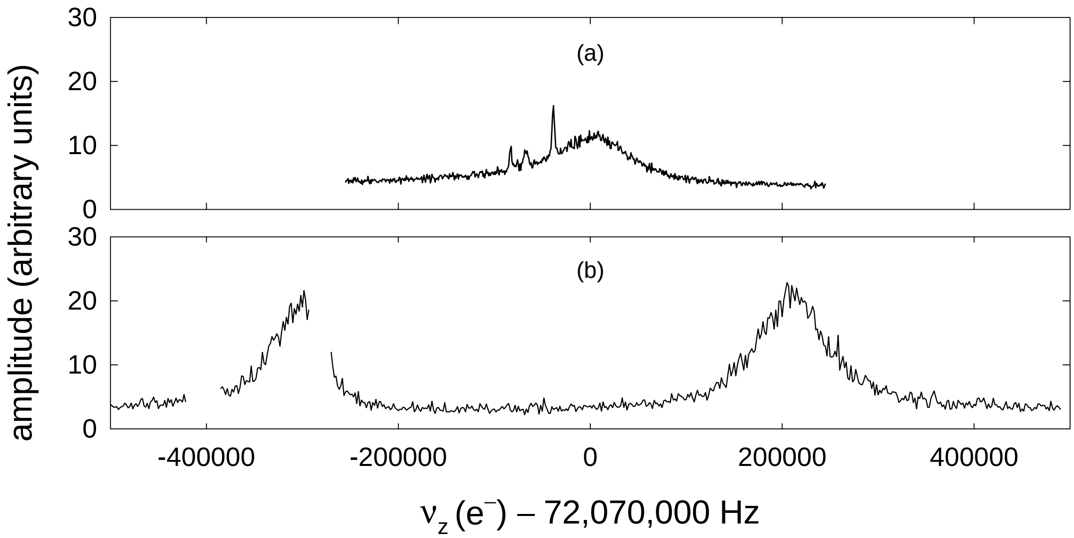

Figure 3.4: 500,000 e^- in the trap prior to $\bar{p}$ and H^- loading. (a) The noise profile of the input *RLC* circuit of the electron amplifier when no electrons are present. (b) Electrons in the trap short out the input noise of the *RLC* circuit. The width of this "dip" measures the number of electrons trapped.

antiproton entry also liberated electrons of less than 100 eV from the degrader. Initially biasing the degrader to 100 Volts prevented those electrons from entering the trap.

Electrons and neutral hydrogen (H) recombined in the trap to form H^-. The H may recombine with the electrons cooled in the trap center. This is most likely for neutral H with a kinetic energy less than 1 eV. Another possibility is that when the electrons and the hydrogen emerged from the degrader with the correct energy and momentum they recombined at the degrader surface. However, the H^- formed in this way must have more than 100 eV to escape from the degrader potential.

After the high voltage on the degrader switched [36], the H^- ions were trapped between the degrader and the UPHV endcap. The H^- collided with the electrons multiple times, dissipating their axial energy, just as for the antiprotons. Within

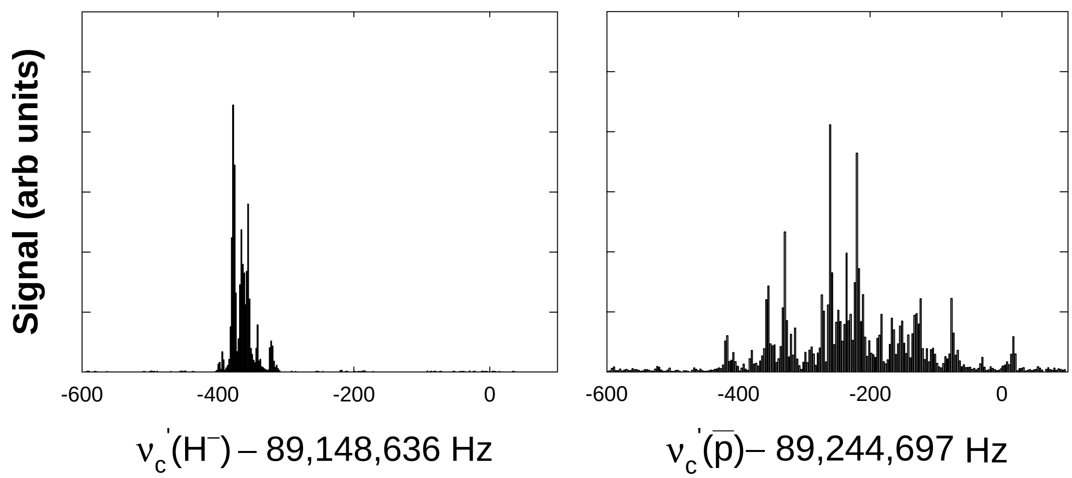

Figure 3.5: 5 minutes after loading $\bar{p}$ from LEAR, 20 H^- and about 100 $\bar{p}$ are trapped.

5 minutes after antiprotons entered the trap, we counted the number of trapped $\bar{p}$ and H^-. After the H^- and the $\bar{p}$ lost their initial kinetic energy, we removed most of the electrons. We then removed many of the antiprotons and measured the cyclotron frequency of the remaining trapped $\bar{p}$ and H^-. The number of trapped particles was estimated by counting the individual frequency peaks (Fig. 3.5).

H^- ions were also loaded using the field emission point. We used a similar arrangement of voltages as was used when the H^- was formed during antiproton loading (Fig. 3.2b). First, 300,000 electrons were loaded and formed a "dip" (Fig. 3.4b). Afterwards, the field emission point (FEP) was turned on again, to liberate H from the degrader. With the FEP still firing, the degrader potential was switched from +70 V to −150 V within 20 nsec to confine the H^-. The H^- cooled by passing through the trapped electrons many times. When the trapped electrons were removed, about 10 H^- were trapped (Fig. 3.6). Based on the degrader voltage, these H^- initially had less 150 eV of kinetic energy. Loading the H^- in this way can be

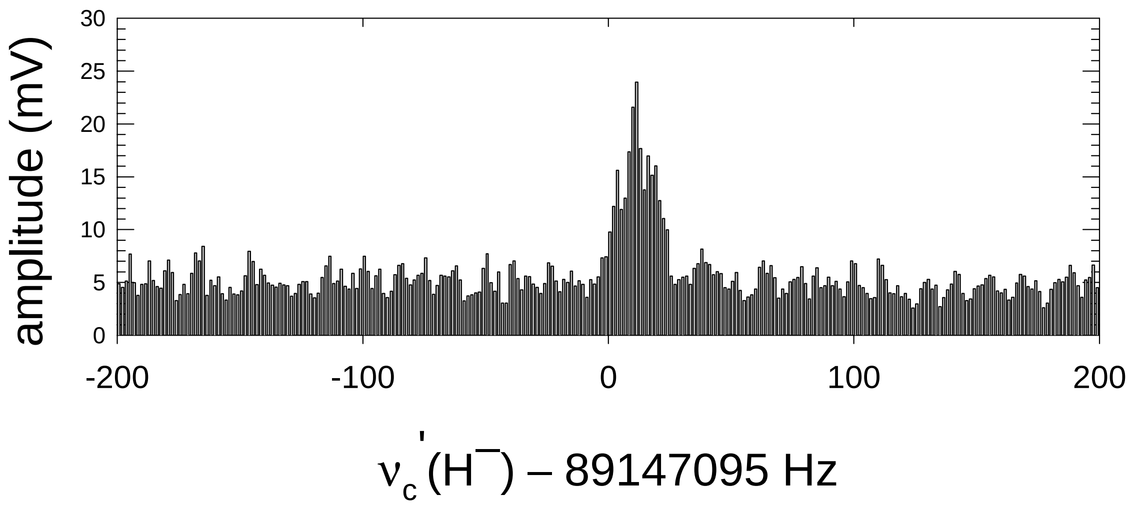

Figure 3.6: H$^-$ loaded independently of loading $\bar{p}$. We used the FEP to heat the degrader and to form H$^-$. We let the ions cool through many electron collisions. Pictured here is the modified cyclotron frequency from about 10 H$^-$.

done without antiproton beamtime; this would allow more time to study how to keep the H$^-$, one of the most difficult parts of the experiment.

Some limits on the initial kinetic energy of the H$^-$ can be set based on our observations. One measure of the initial H$^-$ kinetic energy is the number of trapped electrons and to the time needed to efficiently cool them. We found that we accumulated the maximum number of H$^-$ ions with fewer cooling electrons and with a shorter interaction time (Table 3.1) than required to cool the $\bar{p}$. For this reason we expect that the H$^-$ originally had much less kinetic energy than the antiprotons did. The H$^-$ also had some initial kinetic energy. The H$^-$ only accumulated after colliding several times with electrons over 20 seconds. When the H$^-$ passed through the trap once, we only trapped one or two single H$^-$ ions. Based on these observations we suspect that the initial H$^-$ kinetic energy was between $10 - 150$ eV.

In 1996, we added a filter to the circuit used to switch the degrader voltage quickly to -3 kV. This circuit was essential for trapping both H$^-$ and $\bar{p}$. Over many

Particle	Number of Trapped e^-	Interaction Time (seconds)	Initial Energy (eV)
$\bar{p}$	800,000	100	1000
H^-	500,000	20	$10 - 150$

Table 3.1: The H^- are formed with less kinetic energy than the $\bar{p}$ have. To lose their initial energy, the H^- require fewer electrons and a shorter interaction time than the $\bar{p}$ require. The $\bar{p}$ initial kinetic energy is from Fig. 3.3 while the H^- kinetic energy is only an estimate based on the reduced number of trapped electrons and the reduced interaction time.

years of operation it had deteriorated and had begun to "ring" when it switched (unfiltered response of Fig. 3.7) sending large high frequency components to the trap (Fig. 3.8). The ringing became so bad that after each hour of loading antiprotons, the FETs that amplify the small detected signals needed to be replaced. We installed a 30 MHz low pass filter, eliminating the ringing (filtered response of Fig. 3.7). The filter was a three element Butterworth low pass with a 50 Ω resistor to terminate the reflected wave. After installing this filter, the high voltage switch both trapped $\bar{p}$ and left intact the FETs.

3.2 Keeping a Single H^- and Antiproton

In order to measure the charge-to-mass ratio it was important to keep a single H^- ion and an antiproton together in the trap for at least one day. This allowed us sufficient time to remove the extra ions, magnetron cool the $\bar{p}$ and H^- and complete at least one night's measurement. Within three to eight hours the H^- often left the trap. Contrary to our initial expectations, the $\bar{p}$ usually remained trapped long after the H^- was lost. Although the antiproton and the H^- have similar charge-to-mass ratios, some process dissociated the H^- and did not annihilate the $\bar{p}$. Exciting one

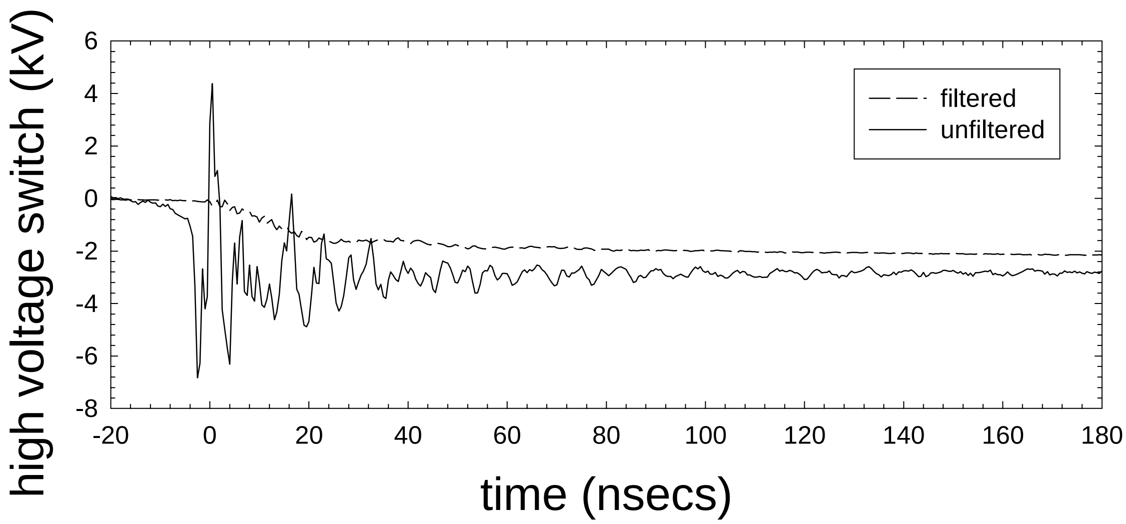

Figure 3.7: The potential applied to the degrader electrode in time both filtered and unfiltered. It steps from 0 to -3 kV. The filter removed the high frequency "ringing".

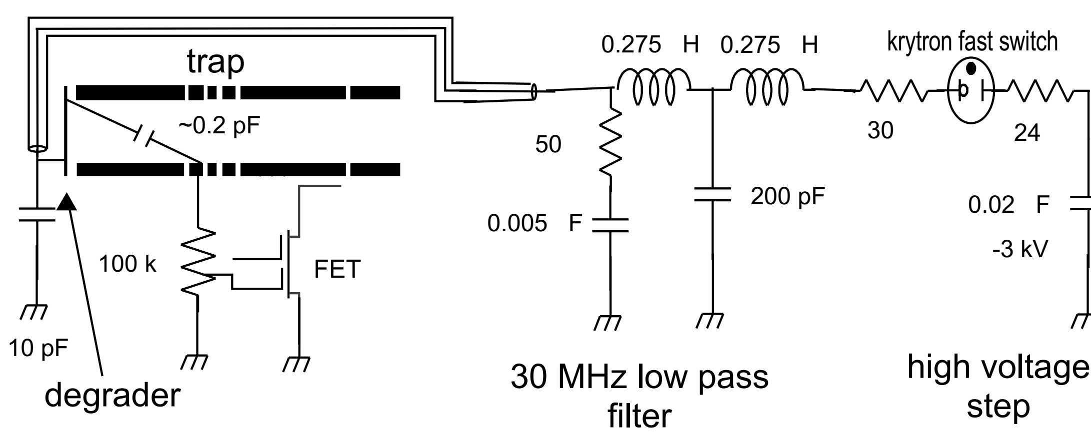

Figure 3.8: The circuit of the high voltage pulser. When the krytron switch closed a capacitor charged to -3 kV quickly applied a potential to the degrader. With no filter installed, the circuit rang, blowing the FETs connected to the trap. A low pass filter terminated with 50 Ω eliminated the ringing.

of the electrons of the H^- by more than 0.75 eV dissociated it. Since the trap was in a sealed dark container at 4 K, photons were not responsible. When an energetic H^- collided with a background He atom or with a charged particle, the H^- dissociated. To keep the H^- beyond one hour, the bulk of the electrons and the extra $\bar{p}$ had to be removed within minutes. We also found that unless the axial and magnetron orbit of the H^- remained small, the H^- also easily left the trap. We knew immediately when the H^- left, for we kept it in a large cyclotron orbit and measured ν_c' as in Fig. 2.12a. To keep the H^- trapped, the trap vacuum was kept low, extra charged particles were removed, and the H^- was kept in small axial and magnetron orbits.

3.2.1 The Trap Vacuum

The method used to complete the $\bar{p}$ to H^- comparison required a low vacuum. The vacuum within our trap was measured to be 5×10^{-17} Torr some time ago, using antiprotons as a vacuum gauge [21, 35]. The method used to measure an H^- and a $\bar{p}$ simultaneously required keeping an H^- in a large orbit with high kinetic energy for many hours. Keeping an H^- in a large orbit required a vacuum about as good as achieved above.

The Langevin cross section determined the rate that antiprotons annihilate. When an antiproton approaches a nearby gas atom, the $\bar{p}$ polarized and attracts the atom. The $\bar{p}$ enters an orbit with the nucleus much smaller than the nearest electron and ultimately annihilates. Any background gas would be predominantly helium since the trap was in a sealed can kept at 4.2 K. The $\bar{p}$ to He cross section is [37]:

$$\sigma = \frac{2\pi e}{v_{\rm rel}}\sqrt{\frac{\alpha}{\mu}} = \frac{8.4 \times 10^{-16}\,\mathrm{cm}^2}{\sqrt{E_c(\mathrm{eV})}}, \tag{3.1}$$

where e is the electron charge in e.s.u., α is the polarizability in cm^3, μ is the reduced mass in grams, v_{rel} is the relative velocity in cm/sec and E_c is the antiproton's kinetic energy.

This cross section can be used to estimate the helium density (ρ_{He}) in the trap,

$$\rho_{\mathrm{He}} = \frac{1}{v_{\mathrm{rel}}\sigma\tau}, \tag{3.2}$$

where τ is the antiproton lifetime. When the cyclotron kinetic energy of the $\bar{p}$ is below 100 eV, the Langevin cross section is larger than the geometric cross section of He. In this energy range, the $\bar{p}$ lifetime only depends on the He density and is independent of the relative velocity (v_{rel}). Now that we can use radiofrequency detection to measure the number of $\bar{p}$, we could set a more stringent limit on the trap vacuum than we set some time ago. The width of an antiproton "dip" could be measured accurately to about 1%. This measures the number of antiprotons trapped. By trapping 1000 antiprotons for 7 days, an upper limit on the trap vacuum better than 6×10^{-18} Torr could be established. In 1990, hundreds of trapped antiprotons were held for 60 days [35]. The number held was measured by estimating the initial number of antiprotons and by counting antiproton annihilations. This test led to an antiproton lifetime estimate of 103 days, giving a He density of 95 atoms/cm^3 and a background pressure of 5×10^{-17} Torr [21, 35]. In this work, we used the same apparatus to achieve this same low pressure.

At low kinetic energies the H^- should survive in the trap better than the $\bar{p}$. Low energy H^- have a much smaller cross section than given by the Langevin cross section (Fig. 3.9). In the range of 1 eV to 1 keV, a H^- and a He atom form a molecule H He^- and then the extra electron detaches [38, 39].

At high cyclotron energies the H^- dissociates more readily than the $\bar{p}$ annihilates. At 4 keV, the electron detachment cross section for a collision between an H^- ion

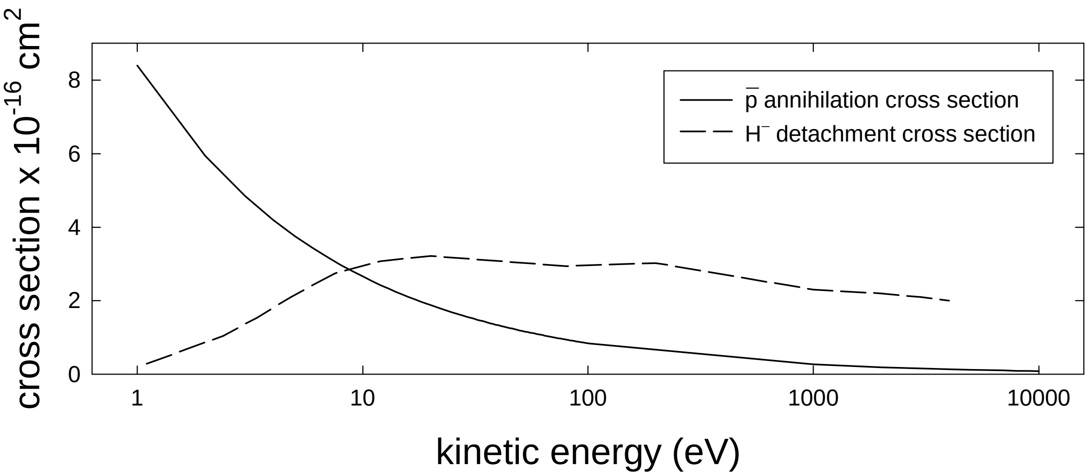

Figure 3.9: The cross section for $\bar{p}$ annihilation and H^- dissociation as a function of energy. The $\bar{p}$ annihilation cross section is based on the Langevin cross section with He atoms. The cross section for electron detachment between a He atom and an H^- is based on References [38, 39]. At high velocities the H^- is more likely to dissociate than the $\bar{p}$ is to annihilate.

with He is 2×10^{-16} cm^2 [38, 39], about equal to the geometric cross section. This process dissociates the trapped H^-. In contrast, a 4 keV $\bar{p}$ is much less likely to annihilate, since the He $-\ \bar{p}$ Langevin cross section at this energy is much smaller. Because of the relatively large cross section for H^- dissociation, we often lost high velocity H^- in the trap but rarely lost high velocity $\bar{p}$.

The H^- loss rate allowed us to estimate the pressure in the apparatus. In 1995 we often kept a single 4 keV H^- for many hours. On two occasions we kept a 4 keV H^- for 25 hours, and on a few other occasions we kept a 4 keV H^- for 12 hours. Based on these lifetime measurements, a 4 keV H^- ion very likely collided with a background He atom with a time constant of 15 hours. This time constant and the electron detachment cross section above indicated that the density of He atoms (Eq. 3.2) in the trap was about 1000 atoms/cm^3 and that the pressure at 4.2 K was about 4×10^{-16} Torr.

Our clearest sign of a worse vacuum was a mass scan. When we had a vacuum leak, He^{++} was the most abundant ion trapped. We fired the field emission point at the degrader and loaded positive ions. This process loaded ions of H, C, N, O and possibly He, all with large axial kinetic energies. Immediately after loading, the trapping potential (V_0) was swept over a large voltage range. This sweep placed the axial frequency of different ions in resonance with the axial amplifier, allowing the RLC circuit to damp their axial energy. The damping ions produced a large signal. When we had a vacuum leak, He^{++} dominated the mass scan (Fig. 3.10a). This occurred in 1995, three months after the trap can pressure was measured to be 4×10^{-16} Torr. The vacuum was not low enough to complete the $\bar{p}$ to H^- comparison. In 1996 after restoring the good vacuum, no He^{++} signal was observed (Fig. 3.10b).

As the vacuum became worse, the measurement became more difficult to complete. We more often lost the H^- and the $\bar{p}$; we lost the H^- over hours, while we lost the $\bar{p}$ over days. When the background He pressure became large, an energetic $\bar{p}$ ionized He atoms and electrons became trapped. This continually loaded electrons and disturbed the measurement. In a poor vacuum it also became increasingly difficult to measure the axial frequency.

We achieved the low vacuum by cryopumping and having a vacuum enclosure within a vacuum enclosure. The trap was housed in an oxygen free high conductivity (OFHC) copper trap can. This was a soft copper tube sealed at both ends with removable copper caps. The trap can was in thermal contact with a He dewar kept at 4.2 K. The trap can inner surfaces rapidly cryopumped all gases and initially cryopumped helium. Surrounding the can was a pressure of approximately 10^{-6} Torr. This made it very difficult for gas atoms at atmosphere to enter the trap can. Eight joints consisting of indium squeezed between copper surfaces sealed the trap can. To get the seals leak tight, the sealing surfaces were all sanded flat. The leak (Fig. 3.10a)

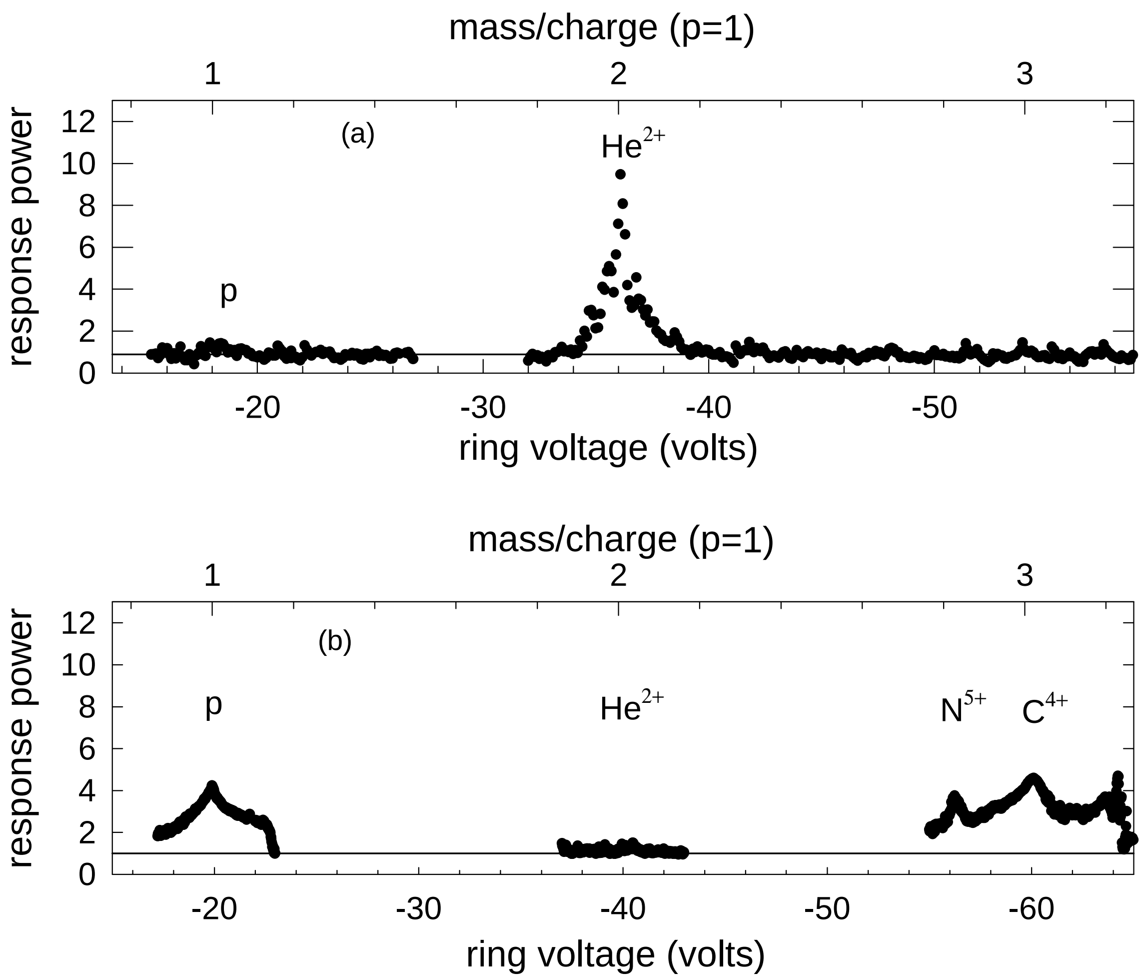

Figure 3.10: An ion scan shows when the vacuum had degraded. Sweeping the trapping voltage (V_0) places elements with different mass/charge in resonance with the axial detector. (a) When He gas fills the trap, He^{++} dominates any other signal. (b) After restoring the good vacuum, no He^{++} peak is seen.

was caused by one surface being warped by 0.3 mm. Once fixed in 1996, we found the total leak rate at room temperature was less than 2×10^{-9} mbar l/sec.

3.2.2 Removing Extra Antiprotons

To keep the H^-, we removed the extra antiprotons from the trap. After initially loading $\bar{p}$ and H^-, thousands of antiprotons were trapped. We increased their cyclotron energy to measure them. When we left the energetic $\bar{p}$ trapped for more than a few minutes they stripped the H^- and soon no H^- were left trapped. To keep the H^-, these initial $\bar{p}$ had to be eliminated. Once we had removed the bulk of the $\bar{p}$ we often had left a few trapped $\bar{p}$ and a single H^- ion. To complete a $\bar{p}$ to H^- measurement, we had to remove all but one $\bar{p}$.

It was not obvious at first how to remove all but 1 $\bar{p}$ while keeping the H^-. The most obvious way to eliminate the charged particles was to eject them along the magnetic field axis. Simply reducing the trapping potential and the axial restoring force did not work. The H^- often left the trap before the $\bar{p}$ did. It was difficult to apply a signal to remove just one $\bar{p}$ since, to the first order, all the $\bar{p}$ had the same axial frequency. We removed the extra antiprotons by selectively increasing the cyclotron kinetic energy of a single $\bar{p}$.

The oscillating electric field drive described on page 36 can increase the cyclotron kinetic energy of one particular antiproton. Antiprotons with different cyclotron kinetic energies have much different relativistically shifted cyclotron frequencies. When the drive frequency is swept over the modified cyclotron frequency of one $\bar{p}$, its orbit increases (Fig. 3.11). The drive does not change the orbits of the other antiprotons since their cyclotron frequencies are not resonant. The H^- is not influenced by this drive either, since $\nu_c'(H^-)$ is about 100 kHz nonresonant. Once this

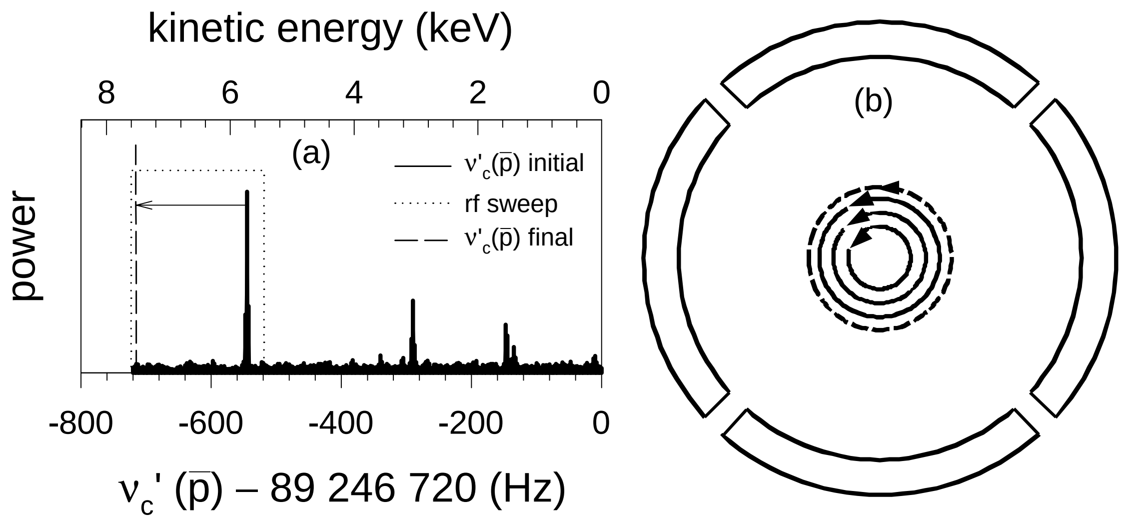

Figure 3.11: A radio frequency electric field increases the kinetic energy of only one $\bar{p}$. (a) Three antiprotons have different modified cyclotron frequencies. The electric field frequency is swept over the cyclotron frequency of just the most energetic $\bar{p}$. The kinetic energy of this $\bar{p}$ increases while the others are not effected. (b) The cross section of the ring electrode and the 3 antiproton orbits. The drawing is to scale.

drive places the antiproton in much different orbits, the orbits remain different for minutes.

We used the relativistic shift to remove the extra antiprotons, one at a time. Once the antiprotons had different kinetic energies, we reduced the trapping potential to 0.7 Volts. We then repeatedly allowed the drive to increase the kinetic energy of the most energetic $\bar{p}$. After a few sweeps, this $\bar{p}$ left the trap. Following this we removed the next most energetic $\bar{p}$. We chose the electric field strength and the reduced trapping potential experimentally. Too low a voltage and too strong an electric field removed all the antiprotons. At too high a voltage no $\bar{p}$ ever left the trap. The optimal parameters used were 3 dBm of drive power and lowering the trapping potential to 0.7 Volts. This technique reproducibly reduced the number of trapped particles to only 1 $\bar{p}$ and 1 H^-.

Exactly why this method ejects the $\bar{p}$ is not clear. The antiprotons leave the trap in a cyclotron orbit well within the ring electrode radius. They do not hit the ring electrode due to a large cyclotron orbit. By some mechanism, the oscillating electric field may also excite the axial motion. This may give the ions enough kinetic energy to escape the weak electrostatic trapping potential. Because this technique removes antiprotons only when the electrostatic potential is weak, the electric field must somehow increase the axial or magnetron orbit.

3.2.3 Removing Heavy Ions

Any heavy ions in the trap prevent accurate cyclotron measurement. An extra ion in the trap center creates an additional electric force on the measured particle and shifts its cyclotron frequency. When two protons are trapped, the proton in the trap center shifts the cyclotron frequency of the proton in the larger cyclotron orbit (Fig. 4.6). When positive ions are in the trap with a proton, the cyclotron frequencies of the proton fit poorly to an exponential just as in Fig. 2.24 where no accurate cyclotron measurements can be made. Similarly for the $\bar{p}$ to H^- comparison it also is important to keep any negative ions from the trap center. Keeping a $\bar{p}$ and an H^- from not influencing each other is possible by allowing only one in the trap center at any time. Any other negative ions need to be removed. It is unlikely that other negative ions remained trapped. As with the H^- they dissociate easily. Certainly negative contaminants ruined some $\bar{p}$ and H^- cyclotron measurements, but most likely these were electrons. Nevertheless, we removed any negative ions with the same method as we used to successfully remove the positive ions.

We removed positive ions by first increasing their axial kinetic energy. We used a combination of filtered noise and axial damping to increase the kinetic energy of

Negative Ions			Positive Ions		
ion	m/e	ν_z(kHz)	ion	m/e	ν_z(kHz)
$\bar{p}$	-1.000	1149	p	1.000	1149
H^-	-1.001	1149	He^{++}	1.986	816
C^-	-11.914	333	N^{5+}	2.780	689

Table 3.2: The axial frequencies of the lightest ions in the trap. The trapping voltage (V_0) is set so that $\nu_z(\bar{p})$ or $\nu_z(p)$ are resonant with the axial RLC tuned circuit.

the ions while keeping the protons in small axial orbits. Initially all the positive ions were damped and the trapping potential was kept at -26 Volts (Fig. 3.12b). We applied broadband white noise to the endcap electrode at frequencies below $\nu_z(p)$. All the positive ions are heavier than the protons and have lower axial frequencies (Table 3.2) since $\nu_z^2 \propto |e/m|$ (Eq. 2.4). The noise increased the axial kinetic energy of the ions (Fig. 3.12b). The trapping voltage placed the ion's resonance frequency well away from the RLC tuned circuit so they were not damped. We found that the ions stayed in large orbits with higher kinetic energy for about 20 minutes. While the noise was on, the trapping voltage placed the protons in resonance with the axial amplifier. This kept the axial energy of the protons low. We also filtered the noise. An elliptic low-pass filter, and two notch filters at $\nu_z(p)$ and $\nu_z(p) - \nu_m(p)$ reduced the noise power at $\nu_z(p)$ and $\nu_z(p) - \nu_m(p)$ by 110 dB. After about 1 minute, the noise was turned off and the size of the trapping potential (V_0) was reduced to -0.7 Volts (Fig. 3.12c). Reducing it any further in practice risked ejecting the protons. This reduced the strength of the electrostatic force and the ions left the trap along the magnetic field axis while the protons remained trapped. Afterwards we restored the trapping potential to -26 Volts (Fig. 3.12d).

The procedure successfully removed positive ions. We first used the field emission point to load 10 protons and ions. Many positive ions such as C^{4+}, N^{5+}, and

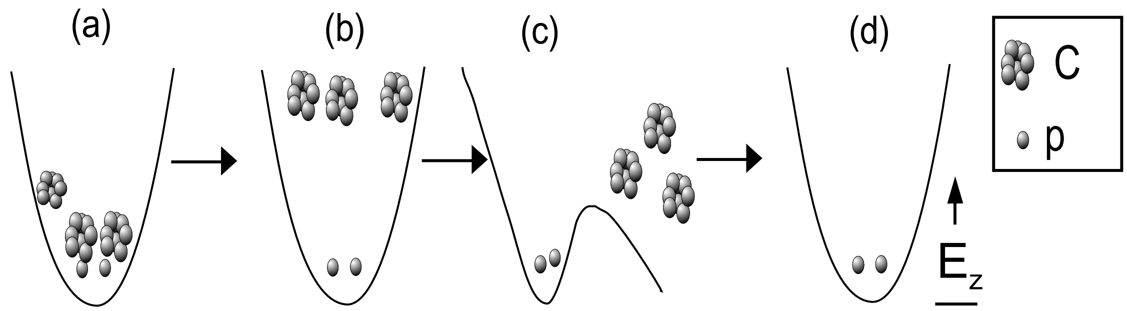

Figure 3.12: Steps to eject ions from the trap. Each figure shows the electrostatic trapping potential and the axial energy (E_z) of the ions. (a) Heavy ions such as C^{4+} and protons all damped together in the trap. (b) Low pass filtered noise increases the axial kinetic energy of only the heavy ions. (c) The size of the trapping potential is lowered to 0.7 Volts and the heavy ions leave. (d) The trapping potential is restored and only the protons remain.

others were loaded as in Fig. 3.10b. Afterwards we repeatedly cycled this cleaning procedure. This removed all contaminant ions and led to accurate cyclotron and axial measurements.

The same procedure should also work for negative ions. The C^-, the next lightest negative ion that we could possibly trap after the H^-, had a much smaller axial frequency than the antiprotons (Table 3.2). This large frequency difference compared with the positive ion case made filtering the noise power at $\nu_z(\bar{p})$ much easier, allowing us to drive the negative ions with 20 dB more noise power. Prior to lowering the trapping potential, the negative ions were driven into bigger axial orbits than the positive ions were.

We expect far fewer negative ions than positive ions. Negative ions are only singly charged, like C^-, O^-, OH^- and F^-. Many more types of positive ions can be loaded, for they often have more than one charge such as C^{4+}. For this reason, more positive ions are initially loaded. Furthermore, the extra electron for all the negative ions easily detaches. We found that in order to keep the H^- trapped for longer than a few hours, its axial energy had to be damped on the RLC tuned circuit. Since the axial motion of the other negative ions was never damped, all the other the negative ions very likely dissociated after a few hours. In contrast the positive ions were much more stable.

We repeated this cleaning procedure for negative ions regularly. After first loading $\bar{p}$, we repeated the cleaning procedure every hour. When the H^- survived past the first day, we repeated the procedure three times a day. This insured that even if the procedure was not perfectly efficient, it still was effective. We never found that we lost an H^- due to a collision with a negative ion. This is unlike the other reasons for H^- loss: the trap vacuum, too many antiprotons, electrons, and a large axial or magnetron H^- orbit.

3.2.4 Eliminating Electrons

The success of the experiment depended on efficient electron removal. Unless most of the electrons loaded to cool the $\bar{p}$ and H^- were removed within a few minutes, no H^- would remain trapped. Even when a few remaining electrons were left in the trap, we found they stripped the H^-. Because electrons do not annihilate $\bar{p}$, electron removal was more important for the $\bar{p}$ to H^- measurement than for earlier measurements that did not use the H^-. Trapped electrons also prevented cyclotron detection of the $\bar{p}$ and the H^-. Even when a few e^- were trapped, we could not measure the cyclotron frequency accurately (Fig. 2.24).

We first reduced the magnetron orbits of the electrons, bringing them into the trap center where the electric field was more predictable. This was critical to removing electrons. The $\bar{p}$ and the H^- were first excited into large cyclotron orbits (Fig. 3.13a) to keep the $\bar{p}$ and the H^- from interfering with the electron measure-

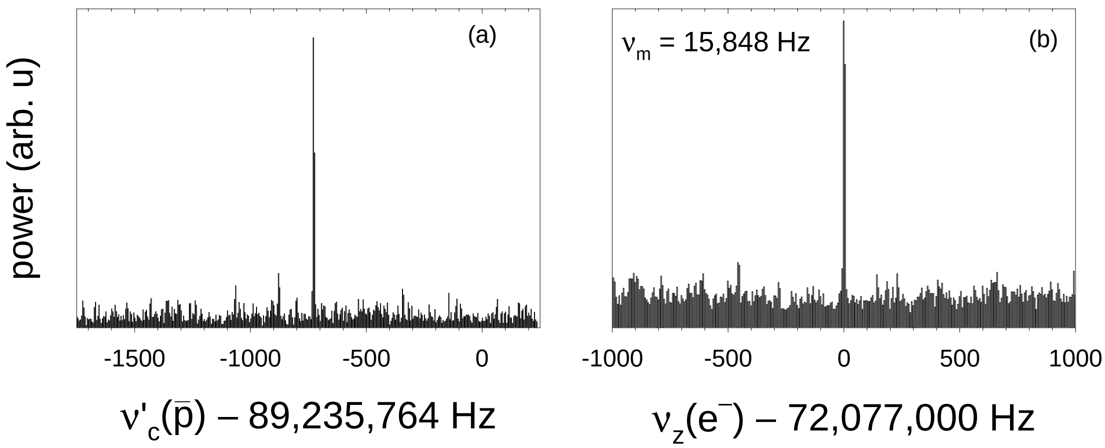

Figure 3.13: An antiproton and a few e^- were in the trap together. (a) The modified cyclotron frequency of an antiproton in a large cyclotron orbit. (b) When a few e^- were trapped, a large signal at $\nu_z(e^-)$ was seen when an oscillating electric field at $\nu_z(e^-) + \nu_m(e^-)$ was resonant. The oscillating field reduced the magnetron orbit of the electrons.

ment. The trapping voltage was raised from 26 V to 43 V to place the axial frequency of the electrons ($\nu_z(e^-)$) in resonance with the electron RLC tuned circuit. The magnetron orbit of the electrons was reduced just as for the fast voltage sweeps (Fig. 2.35). An oscillating electric field "drive" was applied on one of the compensation electrodes at $\nu_z(e^-) + \nu_m(e^-)$ and the trapping potential (V_0) was swept. When electrons were in the trap and the trapping voltage was correct, a large signal at $\nu_z(e^-)$ was seen (Fig. 3.13b). This indicated that the drive was reducing the magnetron orbit of the electrons. The trapping voltage was swept twice over the resonant voltage, the first time at a faster rate (0.25 mV/sec) and the second time at a slower rate (0.10 mV/sec), taking altogether 5 minutes. The e^- sideband cooling signal allowed us to see 10 e^- trapped easily. When we slowed down the sweep and repeated it for about 1 hour, we counted 6 e^- (Fig. 2.8b). We did not sweep the voltage for long enough to detect a single electron.

We found in practice that the H^- could leave the trap during this process. We more likely lost the H^- when its cyclotron orbit was small. When the H^- was in the trap center and the magnetron-cooling drive brought the e^- also into the trap center, the chances of a collision were higher. We kept the H^- cyclotron orbit large to avoid this. This process also heated the magnetron and axial motion of the H^- (Sec. 3.2.5). Slower voltage sweeps would have better reduced the electrons magnetron orbit, but they also would have more likely harmed the H^-.

Next, we removed the electrons while keeping the $\bar{p}$ and the H^- trapped. We reduced the trapping potential. The ring electrode was at 1 Volt, the compensation electrodes were at 0.81 Volts, the upper and lower endcaps were at ground potential (Fig. 3.14a and 3.14b), and we positively biased the longwell electrodes. We opened the trap with a fast pulse applied to the upper endcap (Fig. 3.14c). The electrons accelerated out of the trap first due to their lighter mass. The longwell bias then accelerated the electrons toward the field emission point (FEP). Before the H^- and the $\bar{p}$ moved much, the pulse ended and the upper endcap was restored to ground potential (Fig. 3.14d). The $\bar{p}$ and H^- still remained trapped, and the electrons were transferred to the longwell electrodes.

The pulse was a 4.5 Volt square pulse lasting 150 ns. We used a Stanford Research Systems DS345 function generator to produce the pulse. The pulse traveled down a coaxial cable terminated with a 50 Ω resistor; this preserved the pulse shape. The function generator was connected to the trap with an in-line switch which opened only for 10 ms. The switch prevented the function generator noise from being applied to the trap and from removing the antiprotons and the H^-.

When electrons were magnetron cooled the endcap pulse was effective. First, we loaded and reduced the magnetron orbit of 400,000 electrons. Once their magnetron orbits were small enough, we measured an electron "dip." This determined the

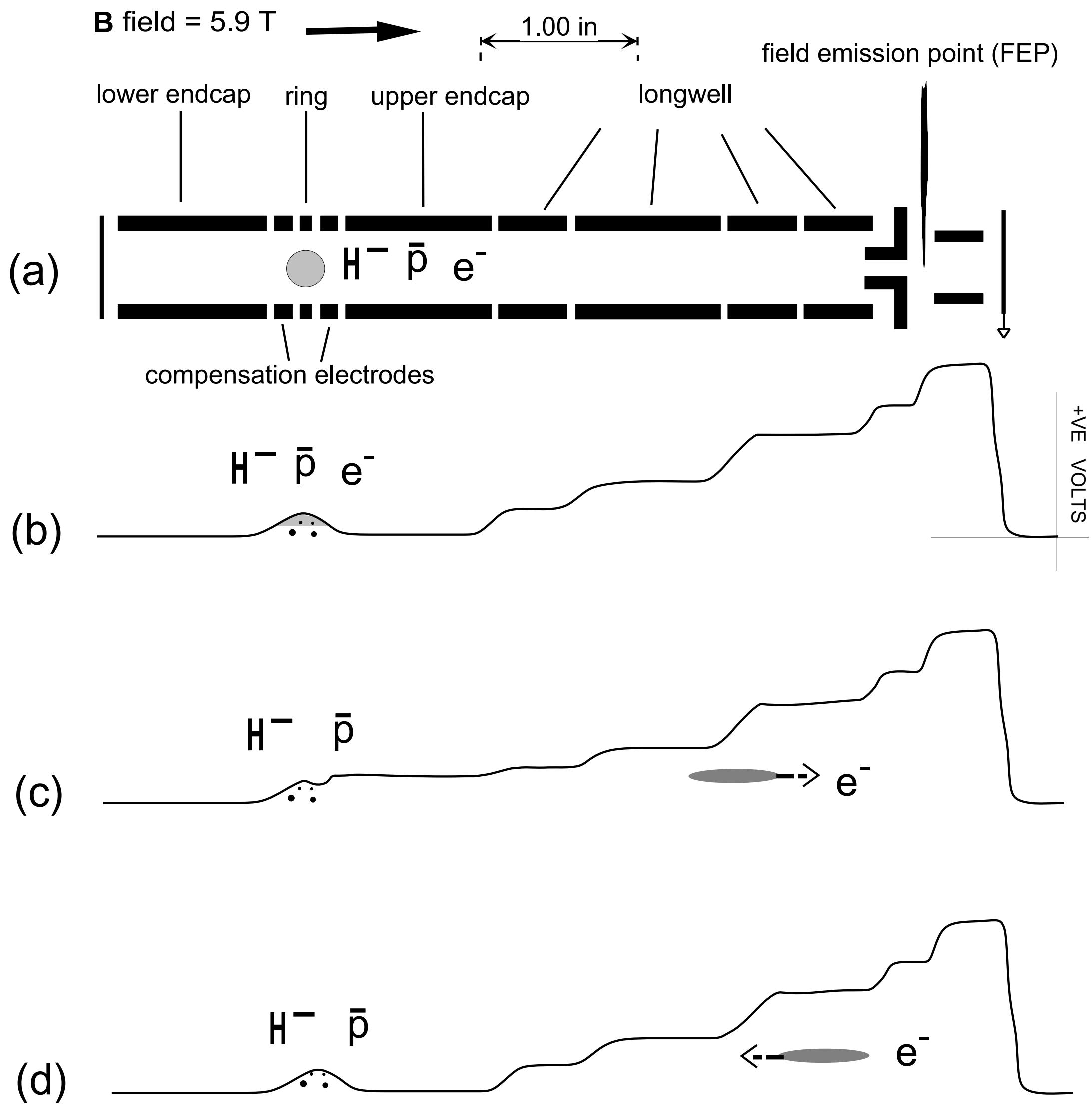

Figure 3.14: We removed the e^- while keeping the $\bar{p}$ and H^- trapped. (a) The trap electrodes with $\bar{p}$, H^- and e^- trapped. (b) The potential along the trap axis. Initially the longwell electrodes were biased to accelerate the electrons. (c) Suddenly the potential on the upper endcap accelerated the charged particles out of the trap. The electrons being the lightest left first. (d) Before the $\bar{p}$ and H^- left, the endcap potential was restored. The $\bar{p}$ and H^- still remained trapped while the e^- were transferred to the longwell.

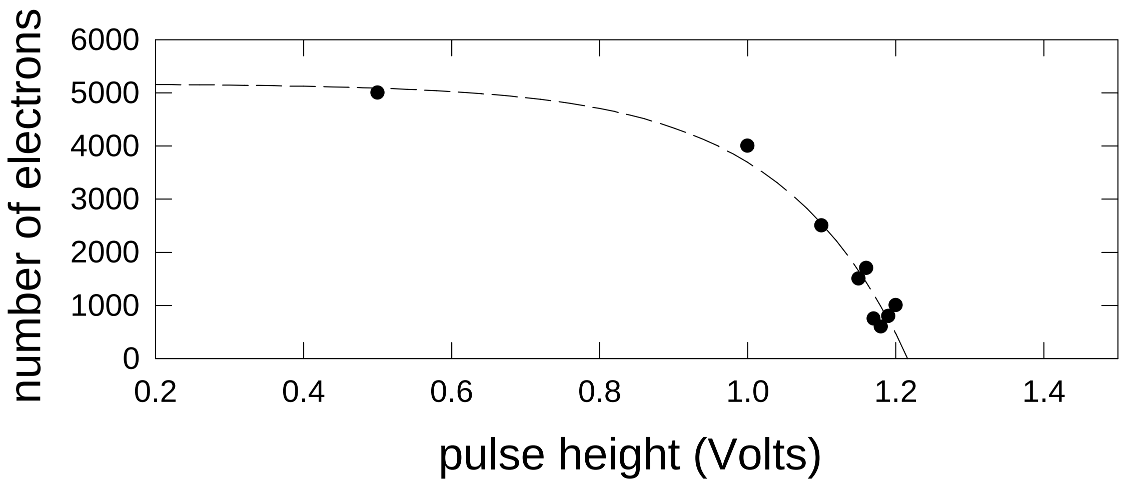

Figure 3.15: The upper endcap pulse removes all electrons for pulse heights greater than 1.3 Volts. We loaded and reduced the magnetron orbit of 400,000 e^-, then applied pulses of different heights to the endcap. Afterwards we counted the remaining e^- by measuring the width of an electron "dip" (Fig. 2.8).

number of trapped e^-. No antiprotons nor H^- were loaded. We lowered the trapping voltage (V_0) and applied pulses of various heights to the upper endcap. Afterwards, we reduced the magnetron orbit of the remaining e^-, and measured again the width of the electron "dip;" this determined the number of electrons in the dip. When the height of the pulse equaled the depth of the trapping potential, 1 Volt, the pulse began removing electrons (Fig. 3.15). In practice we used pulse heights considerably larger than this limit, 4.5 Volts. This accelerated the e^- as much as possible and still kept the $\bar{p}$ and the H^- trapped. This test confirmed that the pulse was of the correct height and the longwell potentials properly biased to efficiently remove electrons.

Repeating the electron removal procedure when e^-, H^- and $\bar{p}$ were trapped removed all the detected electrons. During the first voltage sweeps a large e^- sideband cooling signal was seen (Fig. 3.16a) at a wide range of trapping voltages. The electrons trapped had different magnetron orbits and had different trapping voltages (Fig. 2.34). At this stage many $\bar{p}$ and H$^-$ were also trapped. We then removed the electrons and the extra antiprotons. As we repeated the cooling routine the sideband signal grew smaller (Figures 3.16b and 3.16c), and no signal was seen on the fourth cycle (Fig. 3.16d). Often the slower voltage sweep of the two in each graph cooled the magnetron orbit more efficiently and led to a larger detected signal (Fig. 3.16b). The method needed to be repeated because on each iteration we only partially reduced the magnetron motion of the electrons. Fully reducing it would have taken more time and would have risked losing the H$^-$.

Magnetron cooling was essential to remove the e^-. When we skipped the magnetron cooling procedure, the electrons remained in the trap. Even after applying 7 pulses without magnetron cooling the electrons, we still found electrons in the trap. We still saw a sideband cooling response as seen in Fig. 3.16b. We also tried increasing the axial orbit of the electrons prior to pulsing the upper endcap; this did not improve our rate of removing electrons. Only by first magnetron cooling the electrons could we efficiently remove them. Magnetron cooling was essential perhaps because of the potential on the compensation electrode. When the endcap potential was pulsed, the compensation electrode had a potential which still tended to trap charged particles. Electrons in large magnetron orbits had to overcome this potential prior to being accelerated by the endcap pulse (Fig. 3.14c). This potential kept electrons in large magnetron orbits more strongly trapped and less influenced by the endcap pulse.

Much of the H$^-$ loss was caused by e^-. Prior to developing this technique to remove electrons in June 1995, we were not successful at completing $\bar{p}$ to H$^-$ measurements. We always lost the H$^-$ within a day or two. At some point after loading, we no longer could measure the axial and cyclotron frequencies. During the

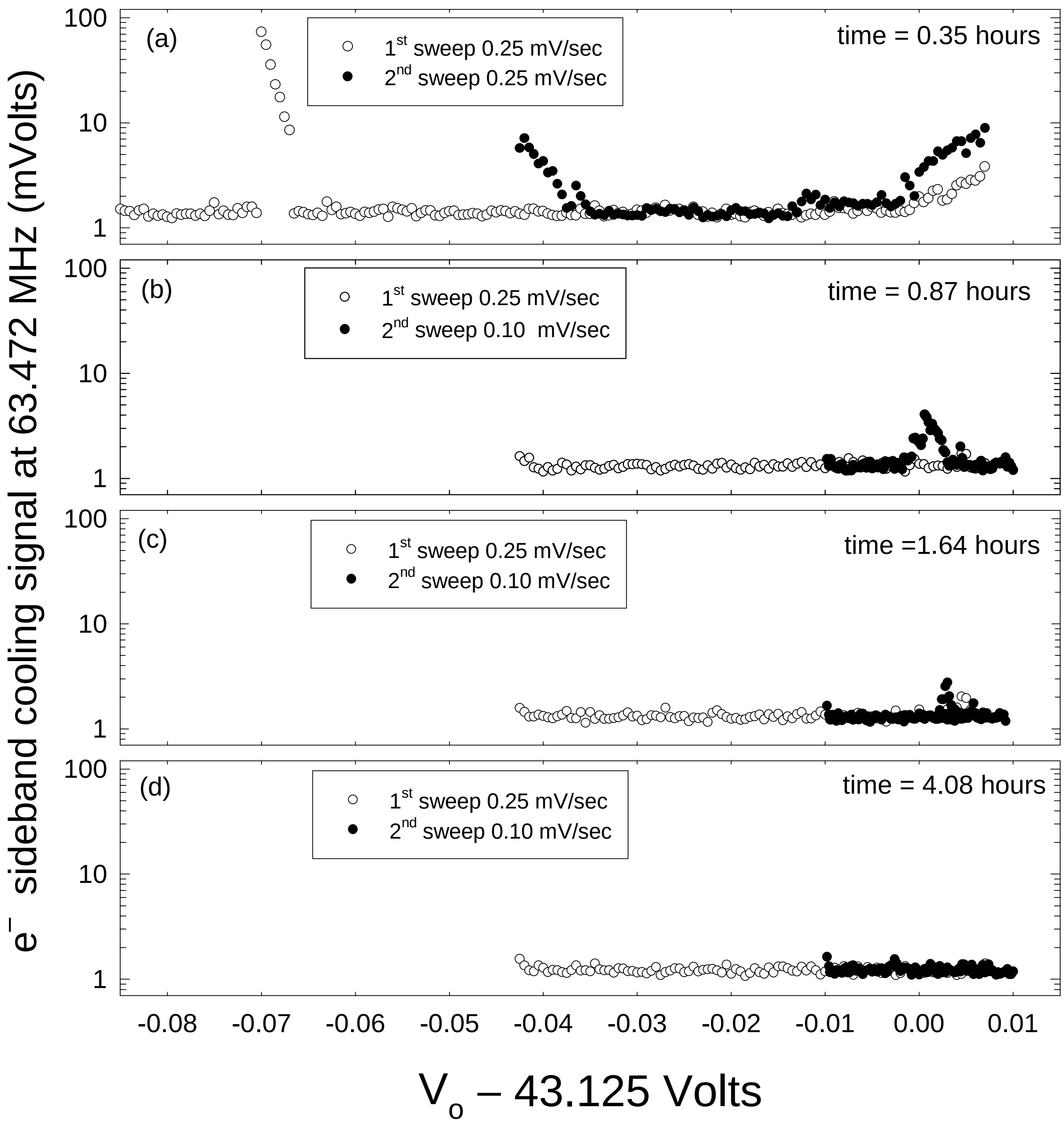

Figure 3.16: We removed the electrons by first sideband cooling the magnetron motion of the electrons, then applying a pulse to the upper endcap electrode. We swept the ring voltage (V_0), and recorded the size of the magnetron cooling response at $\nu_z(e^-)$. (a) Initially many electrons were in the trap and had very different trapping voltages and magnetron orbits. (b) After removing electrons with the electron pulse, fewer electrons were trapped and they produced a smaller signal. (c,d) Repeating the procedure eventually removed all the detected electrons.

frequency sweeps of Fig. 2.30, no axial signal was seen. The cyclotron measurements also no longer fit to an exponential (Fig. 2.24). After removing electrons efficiently, we had much more success. On two occasions we were able to keep a single H^- ion in the trap for 5 days. We also avoided the problems of contaminants by repeating the electron removal procedure 3 times a day. When the procedure was not repeated frequently enough, we lost the H^- ion.

A poor vacuum may have caused electrons to load in the trap. When the vacuum is poor an energetic $\bar{p}$ can strike a background He atom and can ionize it. The liberated electron then most likely remains trapped. In October 1995 when the trap vacuum was worse, we found that hours after first removing all the detected electrons, electrons reappeared in the trap. We first repeated the electron removal procedure three times. Afterwards, no sideband cooling response appeared, indicating that no electrons were present. Eight hours later, we saw a large electron sideband cooling response as in Fig. 3.13b indicating electrons in the trap center. After restoring the good vacuum in 1996, electrons no longer continually loaded. We cycled the electron cleaning routine three times. We never again saw an electron sideband cooling response, indicating that electrons no longer loaded. However, we still repeated the electron cleaning routine daily.

3.2.5 Keeping the H^- Trapped

We still lost the H^-, although our tests indicated that we removed the extra charged particles and improved the vacuum. After having the H^- in a large cyclotron orbit, the cyclotron signal just disappeared, indicating that the H^- was no longer trapped. In a good vacuum with no electrons present we would expect the H^- and $\bar{p}$ to behave the same. At distances further than 10^{-10} m both the H^- and $\bar{p}$ essentially should behave like the same singly charged negative ion. If some procedure ejected the H^- ion, it would also eject the $\bar{p}$. Our experience was contrary to this. We found repeating the procedures to remove the extra charged particles greatly increased the H^- magnetron radius and led to H^- loss.

Repeating the procedure to remove extra charged particles placed the H^- in a very large magnetron orbit. This also increased the antiproton's magnetron orbit (Fig. 2.39), but the effect was larger for the H^-. In a large magnetron orbit, the trapping voltage (V_0) required to keep $\nu_z(H^-)$ fixed on the axial RLC tuned circuit shifted (Fig. 2.34). We swept the trapping voltage (V_0) and applied an oscillating signal at $\nu_z + \nu_m$. This reduced the magnetron orbit in the same way as the fast voltage sweeps (Fig. 2.35). We measured the modified cyclotron frequency (ν_c'). When the trapping voltage (V_0) was correct, magnetron cooling made the cyclotron signal jitter (Fig. 3.17). The H^- in Fig. 3.17 was in such a large magnetron orbit that the ring voltage was shifted by 700 mV. This shift was very much larger than the 20 mV shift in the trapping potential seen in Fig. 2.35. In practice when the magnetron orbit was this large, we never succeeded in reducing it.

We often lost the H^- when it was in such a large magnetron orbit. This occurred at the trapping voltage (V_0) to place the axial frequency ($\nu_z(H^-)$) in resonance with the RLC tuned circuit. We used the modified cyclotron endpoint frequency to estimate the trapping voltage (V_0). The modified cyclotron frequency was measured with no relativistic shift (Fig. 2.13). Based on previous measurements the cyclotron frequency (ν_c) was known. The axial frequency (ν_z) was determined by inverting Eq. 2.8. We then adjusted the trap voltage so that this estimate of $\nu_z(H^-)$ matched the frequency of the RLC tuned circuit. We found this procedure estimated the correct trapping voltage to within 5 mV. At this voltage, first the RLC tuned circuit damped the H^- axial energy, then the H^- left the trap.

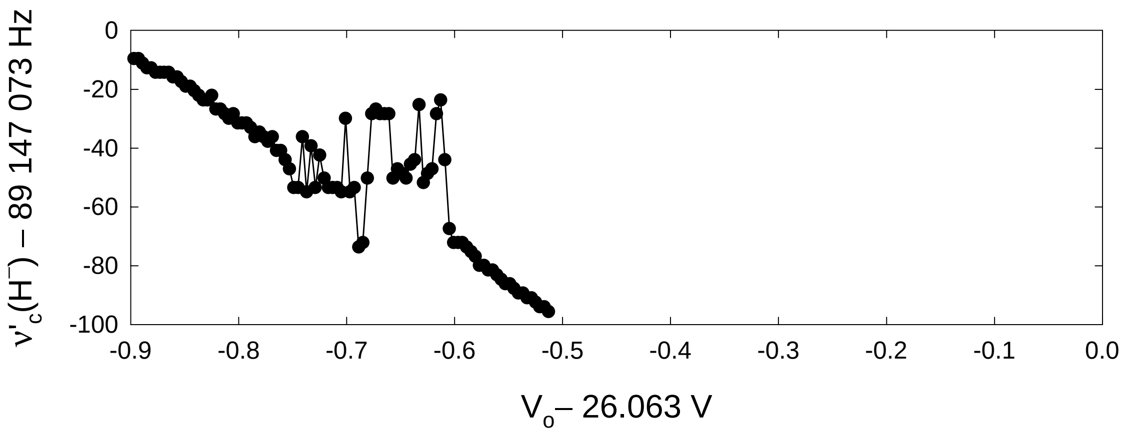

Figure 3.17: Repeating the removal of the extra charged particles increased the magnetron orbit of the H^-. We swept the trapping potential (V_0) and monitored the modified cyclotron frequency (ν_c'). When the trapping voltage placed the H^- in resonance with the magnetron cooling signal, its modified cyclotron frequency jittered. This H^- was in a large enough magnetron orbit to shift its trapping potential by 700 mV.

In four examples the H^- left the trap while simply sweeping the trapping voltage (0.25 mV/s). The H^- was lost minutes after removing the electrons. In these cases we ruled out other reasons for H^- loss. At the time of the loss, no magnetron-cooling signal was being applied. The vacuum was probably about 4×10^{-17} Torr and a mass scan indicated that the He pressure was low (Fig. 3.10b). Before and after losing the H^-, no sideband cooling signals from e^- were seen (Fig. 3.13b), which indicated that no electrons were present. Before losing the H^-, we had ejected the extra antiprotons, and repeated the ion removal procedure at least three times. For these reasons, it was difficult to attribute the loss to a collision with a charged particle or with a He gas atom.

One possibility is that electrons in large magnetron orbits may have collided with the H^-. The method developed to remove electrons was less effective for electrons in large magnetron orbits. Electrons may still have been trapped, but their magnetron orbits were too large to detect and too large to remove effectively. When the RLC circuit damped the H^- axial motion and placed it in the plane with these electrons, the H^- had a higher chance of colliding with them.

To keep the H^- trapped we kept its magnetron orbit small. In between the procedures to remove charged particles, we swept the trapping voltage (V_0) to reduce the magnetron orbit. Over the roughly eight hours taken to remove extra charged particles from the trap, half the time was devoted solely to reducing the magnetron orbit of the H^-. The key to reducing the magnetron orbit was to find the correct voltage to place $\nu_z(H^-)$ on the axial amplifier. The trapping voltage was swept while applying the magnetron-cooling signal.

3.3 Conclusion

We developed a procedure to load and keep a single H^- and $\bar{p}$ trapped. Extra antiprotons, electrons, and possible negative ions had to be removed. Furthermore, the vacuum had to be better than 4×10^{-16} Torr. We developed a sound method for removing all the extra charged particles, but the procedure also tended to increase the H^- magnetron orbit.

While we did not develop a procedure that always keeps a single H^- and $\bar{p}$, we developed good tools to address the problem. First we could load H^- independently of antiprotons, and this would allow us to study how to keep H^- outside of beamtime. Second, we could diagnose and restore the integrity of the trap vacuum. Third, we also could tell when electrons were still trapped. These tools could lead to a more successful loading procedure.

Chapter 4

Comparing the Charge-to-Mass Ratios

This chapter describes the steps followed to compare the proton and antiproton charge-to-mass ratios. The proton charge-to-mass ratio was measured by measuring an H^- cyclotron frequency and by using the known proton to H^- mass ratio. We developed a procedure to keep one particle from disturbing the measurements of the other, which also allowed us to alternate between the antiproton and negative hydrogen ion measurements quickly. The stability of the magnetic field in time limited our accuracy. Although a regulation system stabilized the magnetic field, it still showed small disturbances, drifted with temperature, and occasionally changed abruptly by a tiny amount. A fit determined the ratio of the proton and antiproton charge-to-mass ratios that determined the magnetic field drift; this fit yielded a charge-to-mass ratios result for each night of measurement.

4.1 Measuring the Mass Ratio of the H^- and the Proton

Only the ground state of the H^- ion needs to be considered for the mass ratio of the proton and the H^-. The outer electron experiences no long range Coulomb force, so there is no Rydberg series of excited states. Because of this, only the H^- ground state is stable beyond 1 s. Energy level shifts need to be greater than 0.1 eV in order to affect the mass ratio at 1 part in 10^{10}. The applied electric field (< 50 V/cm) is much too small to cause a large enough Stark shift. Zeeman frequency shifts, even in the 6 T magnetic field, are also negligible.

We deduce the proton cyclotron frequency from the H^- cyclotron frequency that we measure. Three independent measurements determine the mass ratio of the H^- and the proton (M_{H^-}/M_p):

$$M_{\mathrm{H}^-} = M_p(1 + 2\frac{M_{e^-}}{M_p} - \frac{\mathrm{B.E.(H)}}{M_p} - \frac{\mathrm{E.A.(H)}}{M_p}). \tag{4.1}$$

The most important contribution, the proton to electron mass ratio (M_p/M_{e^-}), gives the mass ratio of the separated constituents. The hydrogen binding energy (B.E.(H)) gives the reduction in potential energy when an hydrogen atom is formed in the ground state. The H electron affinity (E.A.(H)) gives the reduction in potential energy when a second electron binds to the H.

The biggest error in the H^- to p mass ratio (M_{H^-}/M_p) is due to uncertainty in the proton to electron mass ratio (M_p/M_{e^-}). Several measurements, including an earlier measurement made in our apparatus [21], are all consistent and measure this ratio to the required accuracy. Recently Farnam et. al. [40] measured the proton-to-electron mass ratio 50 times more precisely than our requirements (Fig. 4.1). They

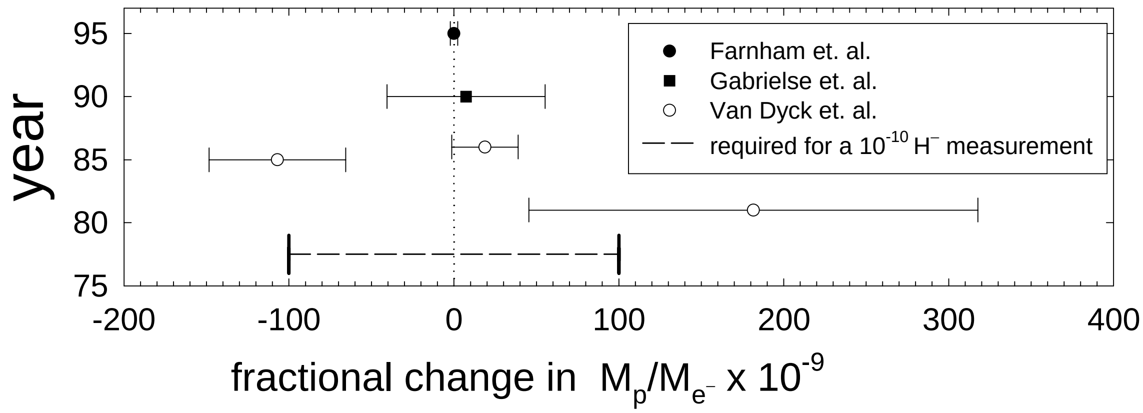

Figure 4.1: The fractional change in the proton to electron (M_p/M_{e^-}) mass ratio relative to the most recent measurement [40]. Measurements after 1986 are precise enough not to contribute to the uncertainty in M_{H^-}/M_p at 1 part in 10^{10}.

compared a small number of electrons with a C^{6+}.

The H binding energy is known so precisely that essentially it does not contribute to the error in M_{H^-}/M_p. Its value relies partly on experiment and partly on theory. The $1S{-}2S$ [41] and the $2S{-}8S$ [42] transitions are both measured to $2{\times}10^{-11}$ cm^{-1}. H energy level calculations [43] which include QED effects, together with these measurements, determine the ionization energy of H to at least 5×10^{-8} cm^{-1}. The hydrogen binding energy (B.E.(H)) is related to M_p by:

$$\frac{\mathrm{B.E.(H)}}{M_p} = \frac{\mathrm{B.E.(H)}}{R_\infty} \frac{M_{e^-}}{M_p} \frac{\alpha^2}{2}, \tag{4.2}$$

where R_∞ is the Rydberg constant and α is the fine structure constant. The hydrogen binding energy in units of the proton mass is limited to greater than 1 part in 10^7 by the fine structure constant (α). Since the hydrogen binding energy is so small, the errors due to the atomic transitions, calculations and the fine structure constant contribute negligibly to the M_{H^-}/M_p uncertainty (Table 4.1).

Measurement	Value	Part of M_{H^-}/M_p	Error $\times 10^{-10}$
M_p/M_{e^-}	1836.1526665(40)	0.001089234047	0.02
binding energy(H)	109678.771(5) cm^{-1}	-0.000000014493	0.00002
electron affinity(H)	6082.99(15) cm^{-1}	-0.000000000804	0.0002
M_{H^-}/M_p		1.001089218750	0.02

Table 4.1: The proton-to-electron mass ratio, the hydrogen binding energy, and the hydrogen electron affinity contribute to the H$^-$-to-p mass ratio (M_{H^-}/M_p). M_{H^-}/M_p is known precisely to 2×10^{-12}, 50 times more precisely than we require for our measurement.

The H electron affinity also does not appreciably contribute to the M_{H^-}/M_p uncertainty. Lykke et. al. [44] measured the minimum energy required to eject the electron from the H$^-$ using threshold-photodetachment spectroscopy and a tunable laser. They used laser beams propagating both parallel and antiparallel to the ion beam to correct to the first order for the Doppler shift. Their result, accurate to 3 parts in 10^5, is based on a fit to a model for the cross section. They left out hyperfine corrections, because they changed the answer by much less than their experimental uncertainty. The H electron affinity also does not add to the M_{H^-}/M_p uncertainty (Table 4.1) at the level of 1 part in 10^{10}.

Measuring the H$^-$ cyclotron frequency is thus equivalent to measuring the p cyclotron frequency. The largest error in the M_{H^-}/M_p measurement, the M_p/M_{e^-} mass ratio was 50 times smaller than we required at our accuracy. We use

$$\begin{aligned} M_{\mathrm{H}^-}/M_p &= 1.001\ 089\ 218\ 750(2) \\ \nu_c(p) &= \nu_c(\mathrm{H}^-) M_{\mathrm{H}^-}/M_p, \end{aligned} \tag{4.3}$$

to convert between the proton and negative hydrogen ion cyclotron frequencies. This adds no uncertainty to our measurement.

4.2 Alternately Measuring an Antiproton and a Negative Hydrogen Ion

While both a single negative hydrogen ion and an antiproton were trapped, their cyclotron frequencies were accurately measured. One particle was measured in a small cyclotron orbit in the trap center while the other particle was kept in a large enough cyclotron orbit to not disturb the measurement. Our method minimized the disturbance to the measured particle. Both particles were kept in small magnetron orbits so that the cyclotron frequency measurements were accurate. Finally, the positions of the particles were exchanged quickly, allowing us to better correct for the large magnetic field drift.

4.2.1 The Measurement Sequence

During the measurement, an applied oscillatory **E** field drive on a ring electrode segment kept the outer particle in a large cyclotron orbit (Fig. 4.2a). When the orbit of the outer particle became too small, this drive increased its energy. Its energy then damped since the motion was coupled to an *RLC* circuit. When the damping reduced the cyclotron orbit too much, the oscillatory field once again increased the cyclotron energy. Fig. 2.13e shows the changes in the cyclotron frequency as the drive increased the particle's energy, and the *RLC* circuit damped it. The outer particle was kept in such a cycle while the axial and modified cyclotron frequencies of the inner particle were measured. This oscillatory field generally did not affect the measured particle, although there were some exceptions (Sec. 4.2.2). Afterwards,

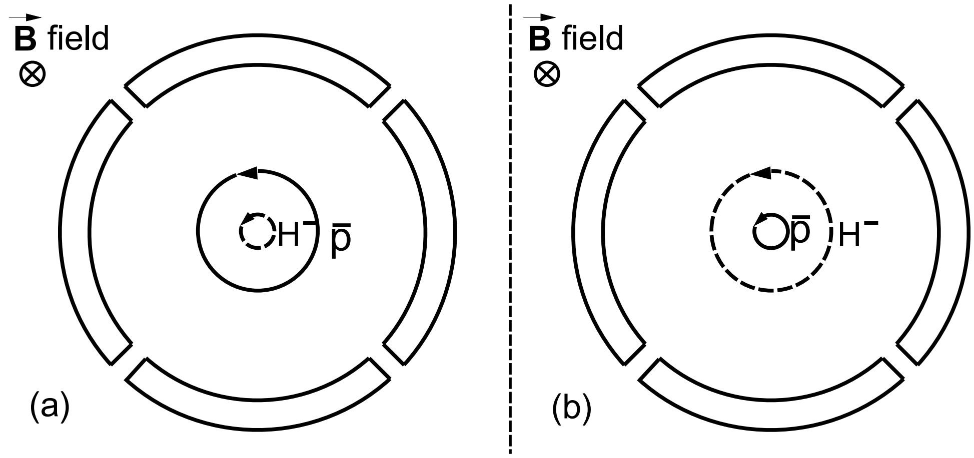

Figure 4.2: (a) First, the axial and modified cyclotron frequencies of the negative hydrogen ion are measured. During this time, the $\bar{p}$ is kept in a large cyclotron orbit. (b) Afterwards, oscillating **E** fields exchange the positions of the two ions, and the $\bar{p}$ is measured. The cycle is repeated 3 to 4 times. The drawing is not to scale.

oscillatory fields exchanged the positions of the two particles and the particle that had been in the outer orbit was measured (Fig. 4.2b). The particles were alternately measured like this, using a computer to control the sequence.

The cyclotron energy of the outer particle was reduced using an oscillatory **E** field at $\nu_c' - \nu_z$. The oscillatory field reduced the cyclotron orbit quickly compared with damping through the *RLC* circuit. Letting the tuned circuit damp the H$^-$ in a large orbit as in Fig. 2.13e would have required 40 minutes before we could have started a measurement (as in Fig. 2.13a). Instead, the oscillatory field reduced the cyclotron orbit in 5 minutes. The oscillatory field was applied to one half of the compensation electrode at the frequency $\nu_c' - \nu_z$. It coupled the axial and cyclotron motions and worked just as the magnetron cooling drive did (Eq. 2.25). The oscillatory field caused the particle to emit a photon by stimulated emission at $\hbar(\omega_c' - \omega_z)$. This reduced the cyclotron energy and increased the axial energy

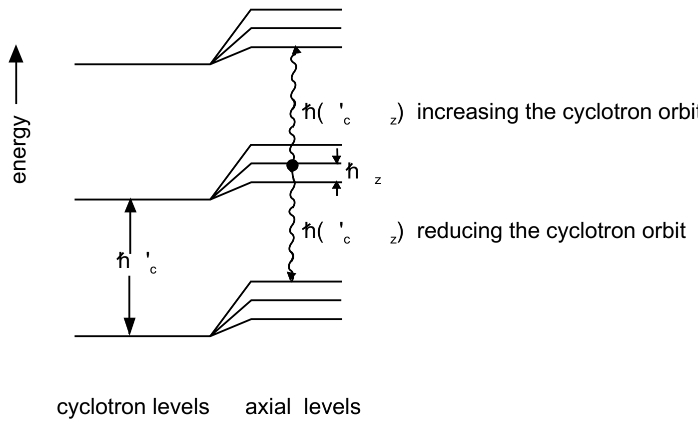

Figure 4.3: Two processes together reduce large cyclotron orbits. More frequently, the oscillating **E** field stimulates emission of a photon at $\hbar(\omega_c' - \omega_z)$. This reduces the cyclotron energy and radius. Less frequently, the particle absorbs a photon of energy $\hbar(\omega_c' - \omega_z)$, and this increases the cyclotron orbit.

(Fig. 4.3). The oscillatory field also caused the particle to absorb a photon at $\hbar(\omega_c' - \omega_z)$; this increased the cyclotron energy. For large cyclotron energies the rate of stimulated emission was larger; therefore, the drive reduced the cyclotron energy. This oscillatory field reduced a large cyclotron orbit (Fig. 2.12a) within minutes, resulting in no detectable signal.

In order for the drive to work, the axial frequency must remain resonant with the axial amplifier. Normally in a large cyclotron orbit, the axial frequency shifts due to the magnetic field bottle (Table 2.1). In practice, we swept the frequency of the oscillatory field and the trapping voltage together. This kept the oscillatory field resonant and kept the axial frequency fixed on the axial RLC circuit even while the cyclotron orbit was decreasing. This oscillatory field reduced the time between alternate cyclotron frequency measurements and sped up the measurement by 50% compared with just letting the particle in the large orbit damp through the RLC circuit.

Keeping one particle in a large cyclotron orbit increased its magnetron orbit. The trapping voltage was set to place the axial frequency of the inner particle, the one being measured, on the axial RLC circuit. This was necessary to measure its frequencies accurately. However, this choice placed the axial frequency of the outer particle very much out of resonance with the axial RLC circuit. This made it impossible to reduce the magnetron orbit with the magnetron cooling drive. The particle's magnetron orbit could then increase if any process dissipates magnetron energy. Keeping a proton in a large cyclotron orbit for 12 hours increased the magnetron orbit so much that the trapping voltage shifted by 100 mV, a large amount. (This is identical to the voltage shift in Fig. 3.17.) In the measurement sequence each particle was kept in a large cyclotron orbit for 1 to 2 hours. This increased the magnetron orbit such that very often its axial frequency could not be measured during an axial frequency sweep (as in Fig. 2.30).

Magnetron cooling with voltage sweeps reduced the magnetron orbit of the outer particle, placing it in resonance with the axial RLC tuned circuit and with the magnetron cooling oscillating $\mathbf{E}$ field. We interrupted the measurement sequence (Fig. 4.4) and swept the trap voltage (V_0) over the outer particle's resonant voltage. This reduced its magnetron orbit. After the particles were exchanged, a slow, more thorough voltage sweep was performed over the particle that had been in the large cyclotron orbit. Following this, we measured its axial and cyclotron frequencies. These voltage sweeps led to more consistent axial measurements. After adding them, we measured the axial frequency nearly every time we performed an axial frequency sweep.

The 12 minutes taken to sweep the voltage kept the magnetron orbit small enough. When the magnetron orbit was so large that no axial frequency measurements could be made, 20 minutes of slow voltage sweeps fully reduced its magnetron

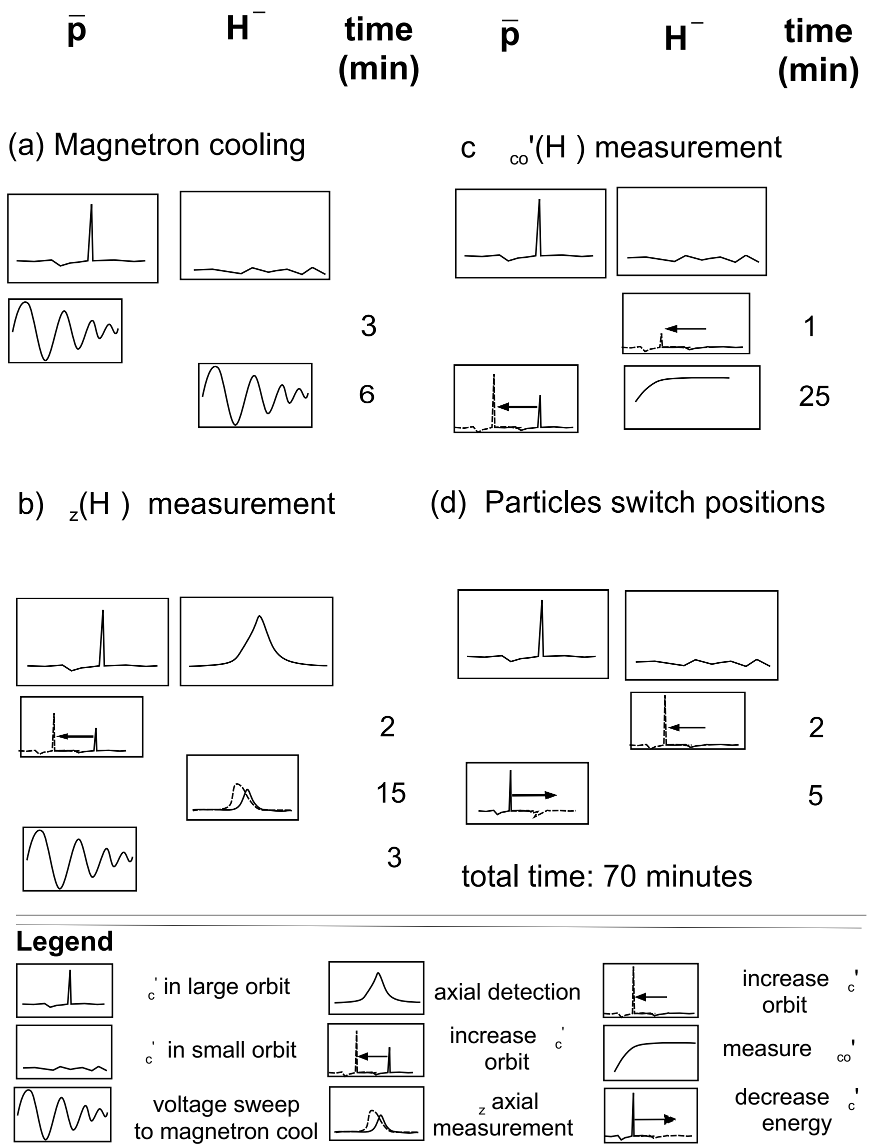

Figure 4.4: The measurement sequence. (a) The voltage is swept to reduce the magnetron orbit of the $\bar{p}$ in a large cyclotron orbit and the H^-. (b) $\nu_z(\mathrm{H}^-)$ is measured while the $\bar{p}$ is kept in a large cyclotron orbit. The voltage is swept over the $\bar{p}$ trapping voltage. (c) The modified cyclotron frequency in a small orbit ($\nu'_{c0}(\mathrm{H}^-)$) is measured while the $\bar{p}$ is kept in a large cyclotron orbit. (d) The particles are exchanged. The $\bar{p}$ cyclotron orbit is reduced, while the H^- cyclotron orbit is increased. Next, the $\bar{p}$ is measured.

Year	Time taken in voltage sweeps(min.)	Time kept in a large orbit (min.)	Cyclotron orbit (mm)
1996	12	70	0.76
1995	12	120	1.6

Table 4.2: Voltage sweeps during the measurement sequence more effectively reduced the magnetron orbit of the outer particle in 1996 than in 1995. In 1996, we kept the outer particle in a smaller cyclotron orbit for a shorter period of time.

orbit (page 78). In our case, the magnetron orbit was not this large. Prior to beginning the sequence, the magnetron orbit had been fully reduced and we had accurately measured the axial frequency. The voltage sweeps then only needed to reverse the effect of keeping the particle in a large cyclotron orbit for up to 2 hours. Taking only 12 minutes both reduced the magnetron orbit enough and saved time.

In 1996, the procedure to reduce the magnetron orbit during the measurement sequence was more effective than in 1995 (Table 4.2). In between exchanges in 1996 each particle spent less time in a large orbit than it did in 1995. The voltage was still swept to reduce its magnetron orbit in the same amount of time. Because of this, the magnetron orbit probably did not increase as much in 1996.

4.2.2 The Effect of the Nonresonant Electric field on the Measurement

The oscillating **E** field drive used to increase the cyclotron orbit of the outer particle was at least 10^5 natural linewidths nonresonant with the inner particle. It thus did not generally affect the inner particle. However, we observed changes in the relativistic shift of the inner particle (Fig. 4.5b) coincident with the drive (Fig. 4.5a) when we set the drive strength at too large a value. We then refitted the cyclotron

No.	Run #	Year	Outer particle $\delta\nu_c'$ (Hz)	radius (mm)	Inner particle change in $\delta\nu_c'$ (Hz)	size
1	T12	95	-625	2.00	-0.340 ± 0.020	< 0
2	T24	95	-625	2.00	-0.130 ± 0.020	< 0
3	T77	95	-525	1.80	-0.320 ± 0.020	< 0
4	T03	95	-595	1.95	-0.090 ± 0.020	< 0
5	T19	95	-330	1.45	-0.110 ± 0.020	< 0
6	T54	96	-90	0.76	-0.251 ± 0.026	< 0
7	T54	96	-90	0.76	-0.092 ± 0.015	< 0
8	T59	96	-90	0.76	-0.015 ± 0.015	$= 0$
9	T63	96	-90	0.76	$+0.047 \pm 0.024$	$= 0$
10	T67	96	-90	0.76	-0.023 ± 0.010	$= 0$
11	T71	96	-90	0.76	-0.015 ± 0.017	$= 0$
12	T75	96	-90	0.76	-0.366 ± 0.031	< 0
13	T79	96	-90	0.76	-0.191 ± 0.023	< 0

Table 4.3: A powerful, nonresonant **E** field increases the cyclotron orbit of the inner particle. The orbit radius and the relativistic shift ($\delta\nu_c'$) of the outer particle before the **E** field turned on and the discrete changes in the relativistic shift ($\delta\nu_c'$) of the inner particle are shown. If the change in $\delta\nu_c'$ were due instead to the proximity of the outer particle, then the change in $\delta\nu_c'$ would be proportional to the orbit of the outer particle. This data shows no correlation, and indicates that the **E** field strength caused the changes in $\delta\nu_c'$.

measurements allowing the relativistic shift of the inner particle to change with this **E** field. This produced better fit residuals which were normally distributed and an improved χ^2_ν (Fig. 4.5d).

In 1995, the drive power was adjusted better than in 1996. The data included in the $\bar{p}$ to H^- measurement taken in 1995 showed no increase in the inner particle's orbit coincident with the nonresonant **E** field. For this reason, we did not allow the relativistic shift to change. In about half of the data taken in 1996, we found the nonresonant **E** field increased the measured particle's orbit. We then allowed the relativistic shift to change with the **E** field in all the 1996 measurements.

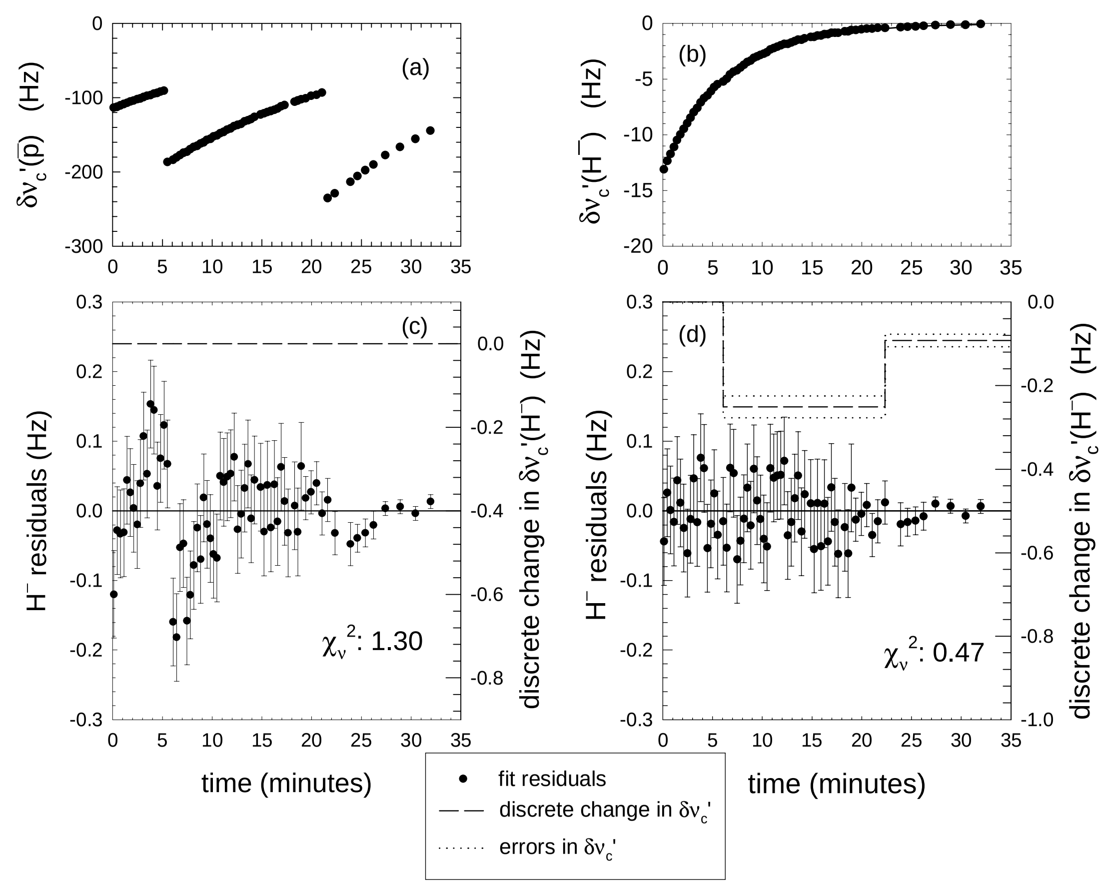

Figure 4.5: The nonresonant **E** field increased the cyclotron orbit of the inner particle. (a) The relativistic shift ($\delta\nu_c'$ of Eq. 2.23) of the outer particle ($\bar{p}$). When the **E** field turned on, $|\delta\nu_c'(\bar{p})|$ increased. (b) $\delta\nu_c'(\mathrm{H}^-)$ of the inner particle is precisely measured. (c) The fit residuals showed $\delta\nu_c'(\mathrm{H}^-)$ changed discretely coincident with the **E** field. (d) When we fit the data, allowing $\delta\nu_c'(\mathrm{H}^-)$ to change discretely, the fit improved. The fit measured two large, significant changes in $\delta\nu_c'(\mathrm{H}^-)$.

Allowing changes in the relativistic shift did not change the fit results very much. When $\delta\nu_c'$ did not significantly shift due to the $\mathbf{E}$ field (examples 8-11 in Table 4.3), the endpoint cyclotron frequency (ν_{c0}' of Eq. 2.23) was the same whether the fit allowed the discrete changes in the relativistic shift ($\delta\nu_c'$) or not. When $\delta\nu_c'$ shifted significantly (other examples in Table 4.3), ν_{c0}' shifted by up to 3 times its error bar.

4.2.3 The Outer Particle's Influence on the Inner One

As the two particles approach each other, the Coulomb potential becomes significant, and their frequencies shift. When the particles are axially damped, the forces and the particles are in the plane perpendicular to the magnetic field. The modified cyclotron frequency is the most important shift. The Coulomb force adds to the radially outward force causing a frequency shift. The axial frequency shift is less important, since the Coulomb force is mostly perpendicular to the motion. The magnetron frequency also shifts, but the shift is less important since the magnetron frequency does not need to be measured precisely.

We expect that the coupling between two protons would be much greater than the coupling between an antiproton and an H^-, since the cyclotron frequencies of the two protons are much closer together. We thus investigated two protons together in a trap. Two protons separated by 160 μm cyclotron orbits noticeably influence each other (Fig. 4.6). We kept one proton in the trap center and measured another proton as it approached the inner particle. Initially, when the separation was large the size of the outer particle's relativistic shift ($\delta\nu_c'$) decreased as expected (Fig. 4.6a). Once the relativistic shift ($\delta\nu_c'$) of the outer particle reached about 4 Hz, its cyclotron frequency began deviating from the exponential fit (Fig. 4.6c). A relativistic shift of 4 Hz corresponds to a separation on the order of 160 μm. To keep the ions from interfering we kept the outer particle greater than 760 μm away, about five times further in radius (Table 4.3).

With an H^- and an antiproton the outer particle in a 0.76 mm orbit caused no measurable frequency shift of the inner particle. If the proximity of the outer particle caused a frequency shift, then each time the outer particle's orbit changed from being in a 0.76 mm orbit to being in a much larger orbit, the inner particle's cyclotron frequency should shift by the same amount. In Table 4.3 we find no consistent shift of the inner particle each time the outer particle's orbit increases. In have the cases in 1996 (Examples 8 through 11 in Table 4.3) as the outer particle increased its orbit no measurable shift occurred in the inner particle. Together these examples indicate that the shift due to the proximity of the outer particle was zero to within 0.007 Hz or 8 parts in 10^{11}.

4.3 The Magnetic Field

The drift of the magnetic field drift in time is the major limitation on our measurement precision. This is also the case with other precise mass spectroscopy measurements [45]. To keep the magnetic field as stable as possible, we kept the pressure stable over each of the four cryogenic dewars that fix the coils of the magnet relative to the trap center. This stabilized the magnetic field enough to complete this measurement. Still the magnetic field changed in time. When one of the accelerator magnets changed its field, the magnetic field in the trap center also changed; however, the magnetic field usually returned to its original value in minutes. We monitored the external changes with two different fluxgate magnetometers. Sometimes, the magnetic field abruptly decreased and remained at the lower value. The size of this effect could be as large as 30 times our accuracy, so it was important

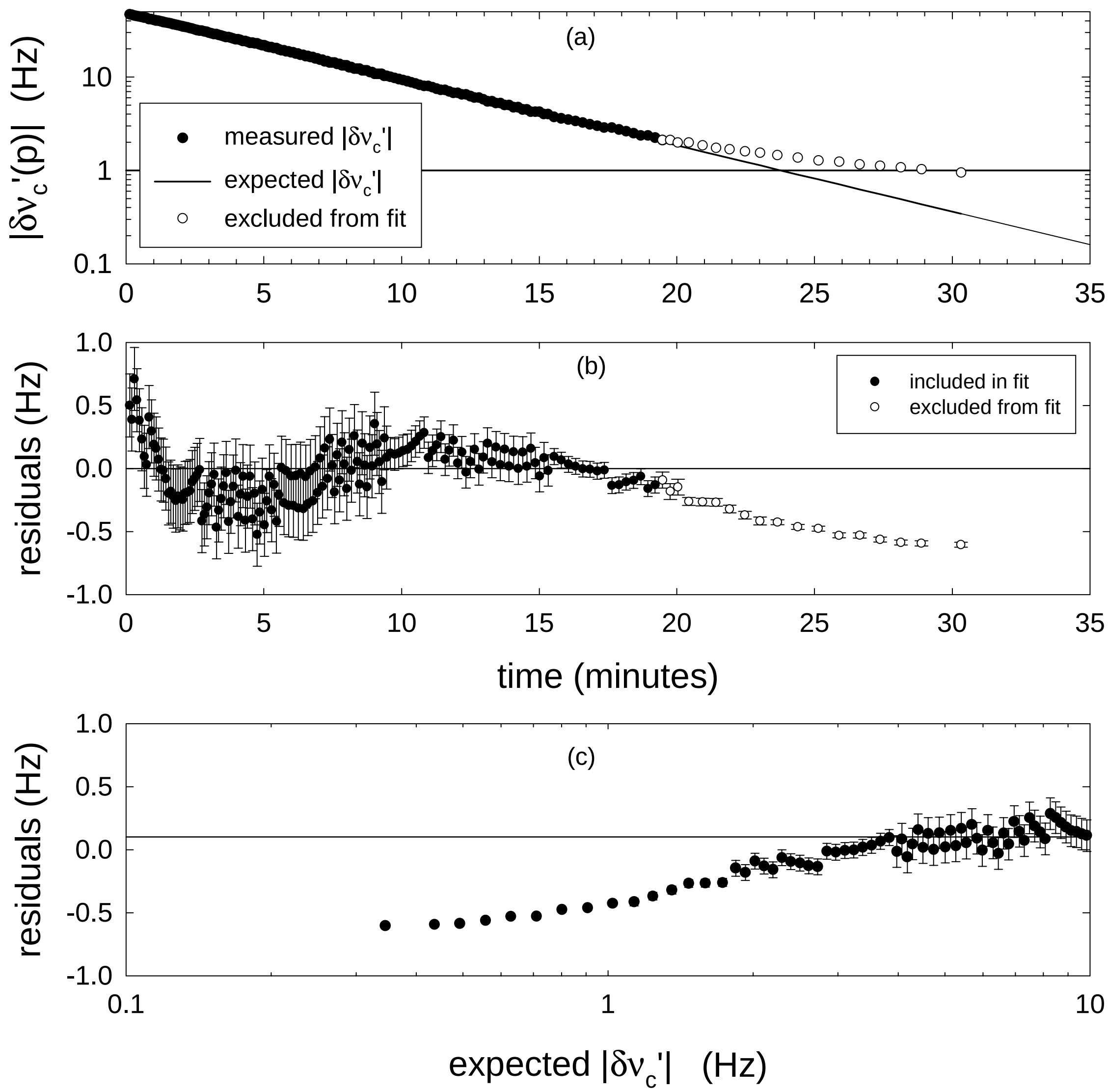

Figure 4.6: Two protons shift each other's cyclotron frequency as they approach each other. The proton measured was in a large cyclotron orbit and the other one was in the trap center. (a) The relativistic shift ($|\delta\nu_c'|$) decreased as expected until about 4 Hz. Afterwards, the inner particle began shifting the frequency of the outer particle. (b) The fit residuals show a significant deviation from the fit at small separations. (c) The expected relativistic shift ($|\delta\nu_c'|$) measured the orbit of the outer particle. Measured ion-ion shifts occurred when the separation was 160 μm, when $|\delta\nu_c'| < 4$ Hz.

to take it into account. In a 24 hour period the magnet temperature changed by 5 °C as sunlight heated the LEAR experimental hall during the day and cooled the hall at night. The slow drift of the magnetic field correlated with the temperature of the magnet. We used the changes in the magnetic field to select data where the magnetic field was stable. Modeling the magnetic field correctly was important for an accurate fit. Here we show how the magnetic field was stabilized, and how the magnetic field changed.

4.3.1 Stabilizing the Magnetic Field

The magnetic field had some gradient (Table 2.1); this made it important that the trap center stay fixed relative to the magnetic field center. A change in the trap location relative to the solenoid of only 3 μm caused a cyclotron frequency shift of 1 part in 10^{10}. The superconducting coils of the magnet were held in position by the helium cryogenic dewar of the magnet (Fig. 4.7). The trap center was held fixed by the helium dewar of the experiment, a support structure made out of an epoxy material called G-10 and the magnet's aluminum neck. When these lengths expanded, the position of the trap center with respect to the magnetic field center changed, shifting the cyclotron frequency. We stabilized the internal magnetic field with a pressure regulation system and a canopy.

The pressure was kept stable above the cryogenic liquids to stabilize the magnetic field. This stabilized the temperature of the liquids and kept the lengths of the dewars stable. Without stabilizing the pressure, the magnetic field drifted too much to complete a charge-to-mass measurement. We compared each dewar's pressure to the pressure of a reference cavity. The temperature stability of this cavity limited the pressure stability of the cavity; this in turn limited the pressure stability of the

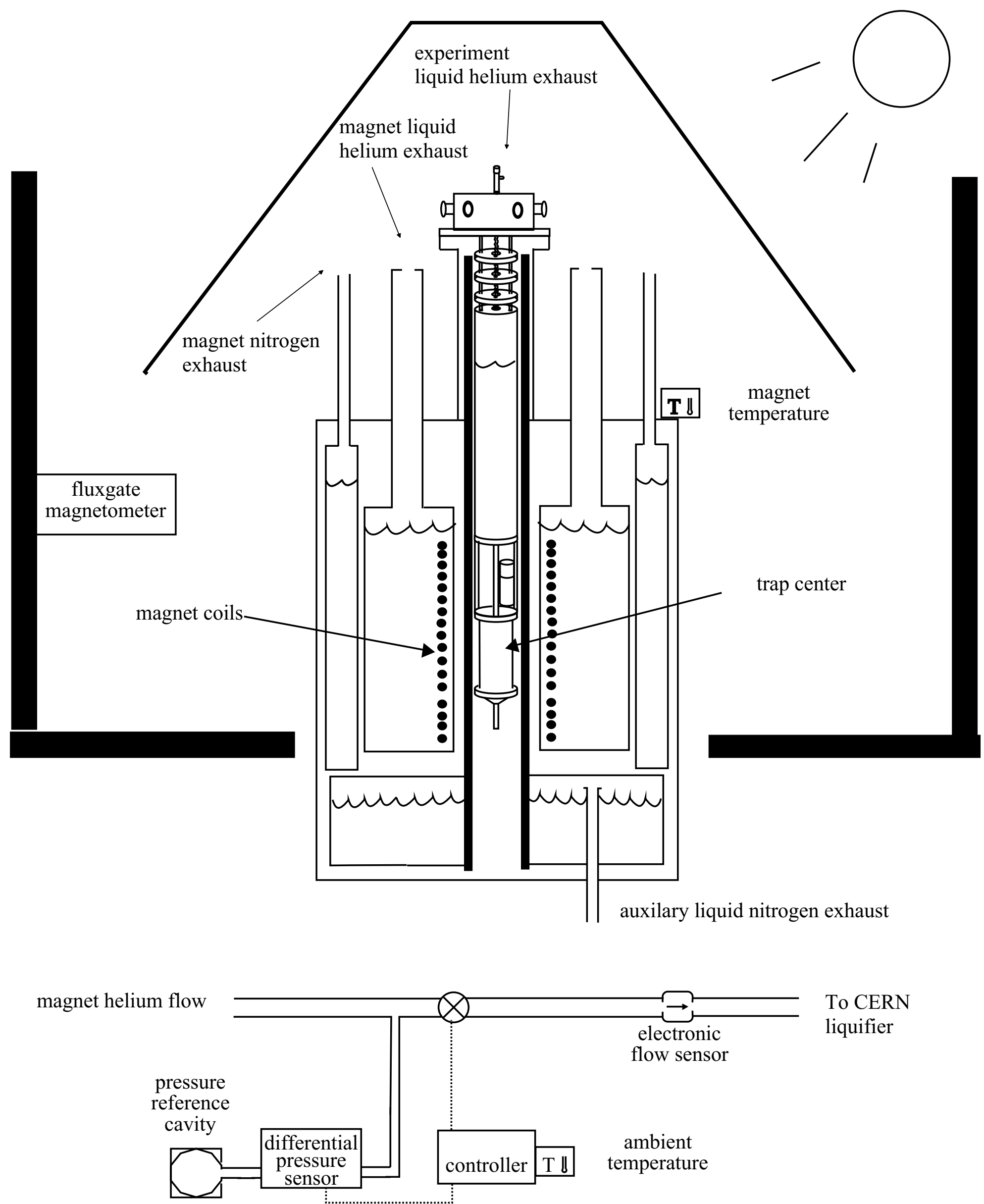

Figure 4.7: The superconducting magnet is shown with the experiment in the center and the regulation system underneath the magnet's floor. The magnet coils sit inside the magnet liquid helium dewar. The trap is fixed below the experiment liquid helium dewar. Both helium dewars are surrounded by surfaces held at the temperature of liquid nitrogen. Underneath the floor a system stabilizes the pressure above the helium and nitrogen dewars. A canopy keeps direct sunlight off the magnet.

dewar. A sophisticated temperature lock loop held the cavity at a fixed temperature to within 3 mK (Fig. 4.8). This temperature stability stabilized the pressure of the magnet helium dewar to within 10 mTorr.

The most important variables that influenced the internal magnetic field stability were monitored (Fig. 4.7). This allowed us to correlate changes in the environment with the changes in the cyclotron frequency measurements. These monitored variables included:

- The ambient magnetic field;
- The magnet temperature;
- The ambient temperature located near the regulation system;
- The pressure of each dewar relative to the reference cavity;
- The temperature of each reference cavity;
- The boil-off rate or flow rate of each cryogenic dewar.

This data was recorded with each cyclotron frequency measurement and showed which variables affect the internal magnetic field on a scale in both minutes and hours.

In 1995, we made the magnetic field more reliable and stable by keeping direct sunlight away from both the regulation system and the magnet. We placed the regulation system underneath the magnet floor. Prior to this, direct sunlight heated the regulation circuits by 5 °C. This caused the temperature stability circuit of the reference cavities no longer to stay locked and caused the magnetic field to drift considerably. It took hours for the temperature of the reference cavity to stabilize again; during this time no charge-to-mass measurements were possible.

After moving the regulator underneath the floor away from the sun, the pressure regulator was much more reliable. No charge-to-mass measurements were lost due to misregulation. The concrete walls underneath the magnet floor kept the environment of the regulation circuitry stable to within 2 ℃, and the regulator stayed locked. We also kept direct sunlight away from the magnet with a canopy (Fig. 4.7); this helped stabilize the magnet's temperature and kept the magnetic field stable (Fig. 4.13).

The regulation circuits were also improved. A Peltier element [1] stabilized the temperature of the pressure reference cavity by heating and cooling it. This stabilized the temperature of the cavity to within 3 mK, an improvement over the previous circuit by a factor of three (Fig. 4.8). The previous circuit turned a resistive nichrome wire on and off to heat the cavity. The Peltier element was in good thermal contact both with the heavily insulated cavity and with a large heat sink. Signal processing was also improved in the regulation circuits. The small milliVolt signals were amplified at the earliest stage possible, and ground loops were removed.

In the following sections we discuss how the variables such as the ambient magnetic field, the ambient magnet temperature, and the helium flow rate affect the internal magnetic field.

4.3.2 Magnetic Field Changes Due to External Changes

The magnetic field occasionally changed its value suddenly when the magnet's environment changed. Correlations were often seen between the ambient magnetic field, the pressure above a magnet dewar and the internal magnetic field. We fit the cyclotron measurements to Eq. 2.23 and used background monitors to identify abrupt changes in the fit residuals.

[1] Christoph Heimann made the Peltier circuit more reliable and stable, and made all the other regulator circuits perform beautifully. Carla Levy first built the Peltier element circuit.

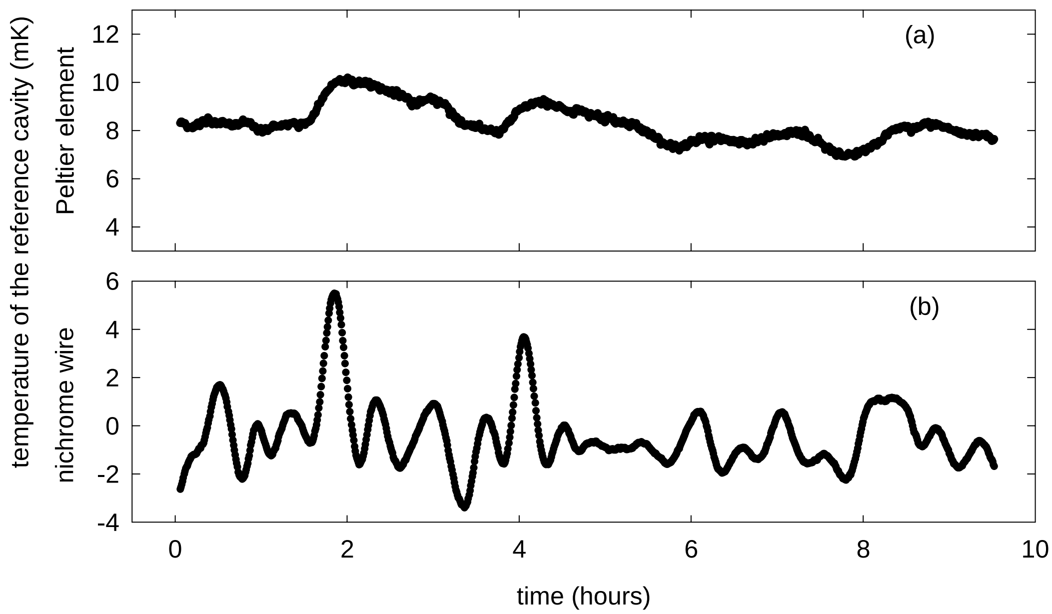

Figure 4.8: A Peltier element improved the temperature stability of the pressure reference cavity. (a) A Peltier element heated and cooled the pressure reference cavity to stabilize its temperature. (b) A nichrome wire heated the pressure reference cavity to a few degrees above room temperature.

External magnetic field changes altered the magnetic field in the trap center. When the ambient magnetic field shifted by -30 mG (Fig. 4.9a), the modified cyclotron frequency fit residuals changed by $+0.3$ Hz (Fig. 4.9b). This corresponded to an internal magnetic field change of 0.2 mG. A self-shielding coil [46, 47, 48] placed inside the magnet screened such disturbances by a factor of -150. The size of the screening factor depended on the proximity of the change to the trap. When the nearest bending magnet used to deliver antiprotons to our experiment remained off, the screening factor varied from -100 to -150 [49]. This coil reduced the effect of the ambient magnetic field changes in this accelerator environment enough to allow us to complete the measurement. We measured a negative screening factor because of the magnetometer orientation. When the ambient magnetic field changed

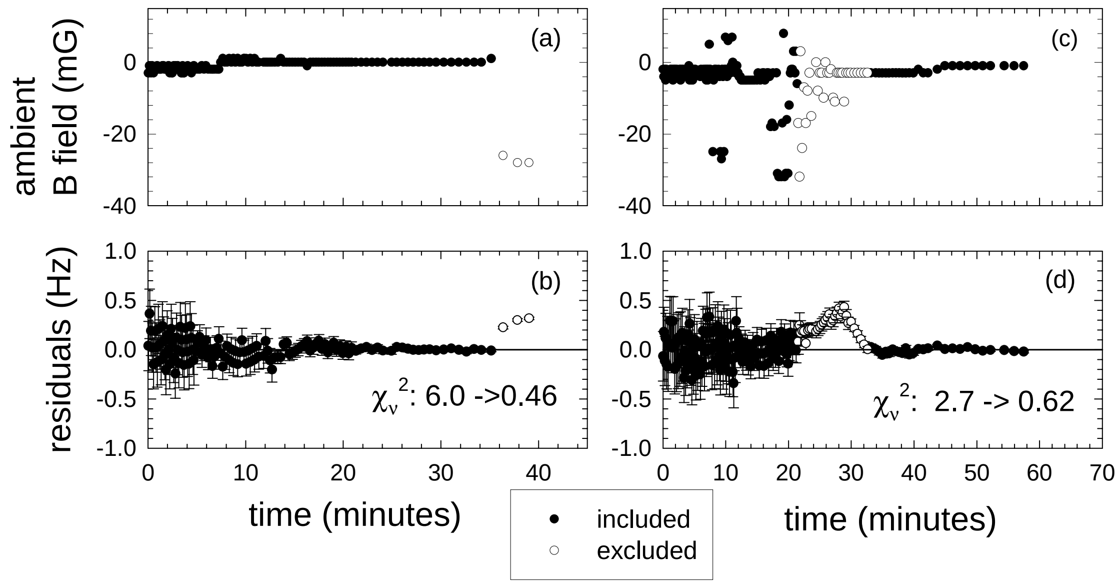

Figure 4.9: The ambient magnetic field changes the cyclotron frequency. (a) The ambient magnetic field changed by -30 mG. (b) The ambient field changed the internal magnetic field by $+0.3$ Hz or $+0.2$ mG. (c) A rapid and oscillating change in the ambient magnetic field. (d) The magnet integrated over the change and the response in the cyclotron residuals was delayed.

quickly (Fig. 4.9c), the fit residuals showed a time-delayed response (Fig. 4.9d). When the ambient magnetic field measurements fluctuated, as in Fig. 4.9d, the ambient magnetic field change was rapid. Changes in the ambient magnetic field mostly affected the latest and most accurate cyclotron measurements. The earlier points had such large error bars that they did not reveal the ambient field changes. We excluded cyclotron measurements affected by these sudden ambient changes. Excluding these points greatly improved the fit to the cyclotron frequency endpoint (ν'_{c0} of Eq. 2.23) and significantly reduced χ^2_ν (Fig. 4.9b and 4.9d).

When the pressure regulation circuit failed, we could no longer measure the cyclotron frequency accurately. When the pressure (Fig. 4.10a) or the flow (Fig. 4.10b) over the magnet helium dewar was no longer stable, the cyclotron measurements

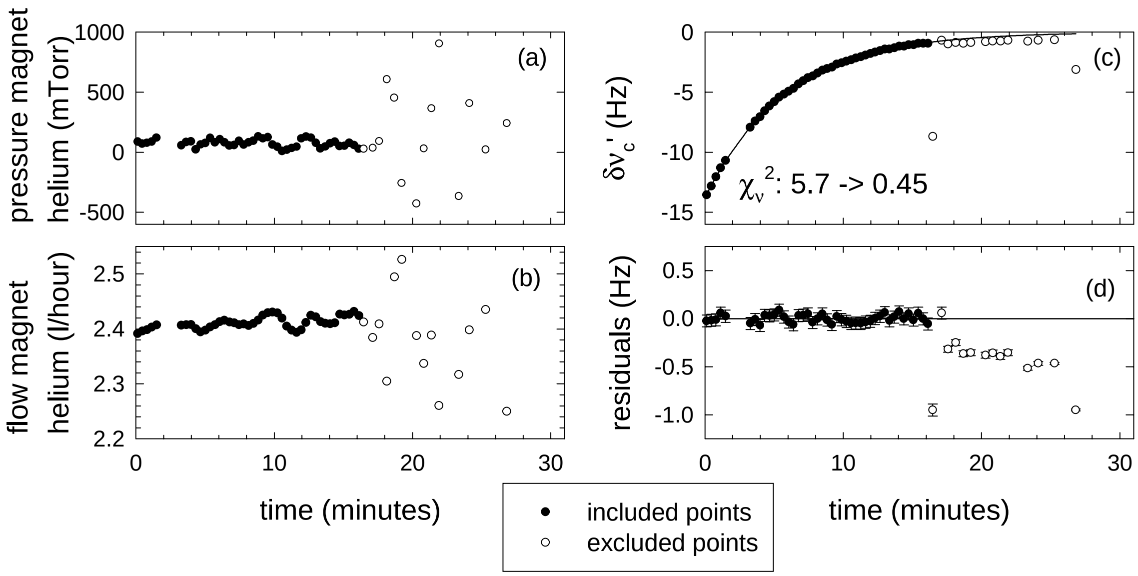

Figure 4.10: A regulation failure ruined the cyclotron measurement. (a) The pressure over the liquid helium dewar of the magnet stopped being stable. (b) The flow of boiling helium showed the change. (c) Cyclotron measurements made after the pressure stopped being stable were no longer accurate. Excluding the bad measurements improved χ^2_ν. (d) The fit residuals show the change in the internal magnetic field.

were no longer accurate (Fig. 4.10c). The residuals (Fig. 4.10d) deviated from the fit by 6 parts in 10^9, a large amount compared with our precision. Cyclotron frequency measurements made when the magnet pressure was not stable were excluded from the measurement. Disturbances like this illustrated the need to regulate the pressure.

4.3.3 Internal Magnetic Field Steps

Perhaps once in 12 hours, the magnetic field at the trap center abruptly decreased and then remained stable. The magnetic field steps ranged in size from -0.1 Hz to -0.3 Hz, at least 10 times our accuracy. These steps were disturbing, since high precision in mass spectroscopy relies on a stable, determined magnetic field.

The origin of these steps is not well understood, but an ambient variable (such as the ambient magnetic field or the flow over the experiment helium dewar) typically changed by a small amount at the time of the step. When such a step took place during a cyclotron decay, the cyclotron fit residuals measured the magnetic field steps.

In rare examples, the residuals of fitting cyclotron data to Eq. 2.23 showed a large step (Fig. 4.11b), many times greater than the cyclotron error bars. These residuals came from a fit which held $\nu'_{c\,0}$ constant. When the step occurred, the relativistic shift was constant ($\delta\nu'_c$ of Eq. 2.23) since drive to increase the orbit of the outer particle remained off. We refit the data and allowed the endpoint cyclotron frequency ($\nu'_{c\,0}$) to change abruptly coincident with the step in the residuals. The resulting fit, with all the cyclotron measurements included, was very good (Fig. 4.11d). The fit residuals were all normally distributed and χ^2_ν greatly improved. Steps in the magnetic field ($\Delta\nu'_{c\,0}$) measured in this way were large, at least 10 times our measurement accuracy. Fitting the data with a step changed the endpoint cyclotron frequency ($\nu'_{c\,0}$) considerably (compare Fig. 4.11d with Fig. 4.11b).

Small disturbances in the ambient channels were seen at the time of the step but were too small and of the wrong duration to cause the large steps in the magnetic field. A small disturbance in the flow (Fig. 4.11a) took place coincident with the step but did not last long enough. The fit residuals still showed a disturbance even after the ν'_c measurements at the time of the flow disturbance were excluded (Fig. 4.11c). The flow change was also just barely larger than the noise and was too small to explain the magnetic field step. A disturbance of the same size as shown in Fig. 4.11a often occurred without causing any change in the fit residuals. In another example, a small ambient magnetic field change occurred at the time of a magnetic field step (Figures 4.12a, 4.12b, and 4.12c). The change in the internal magnetic

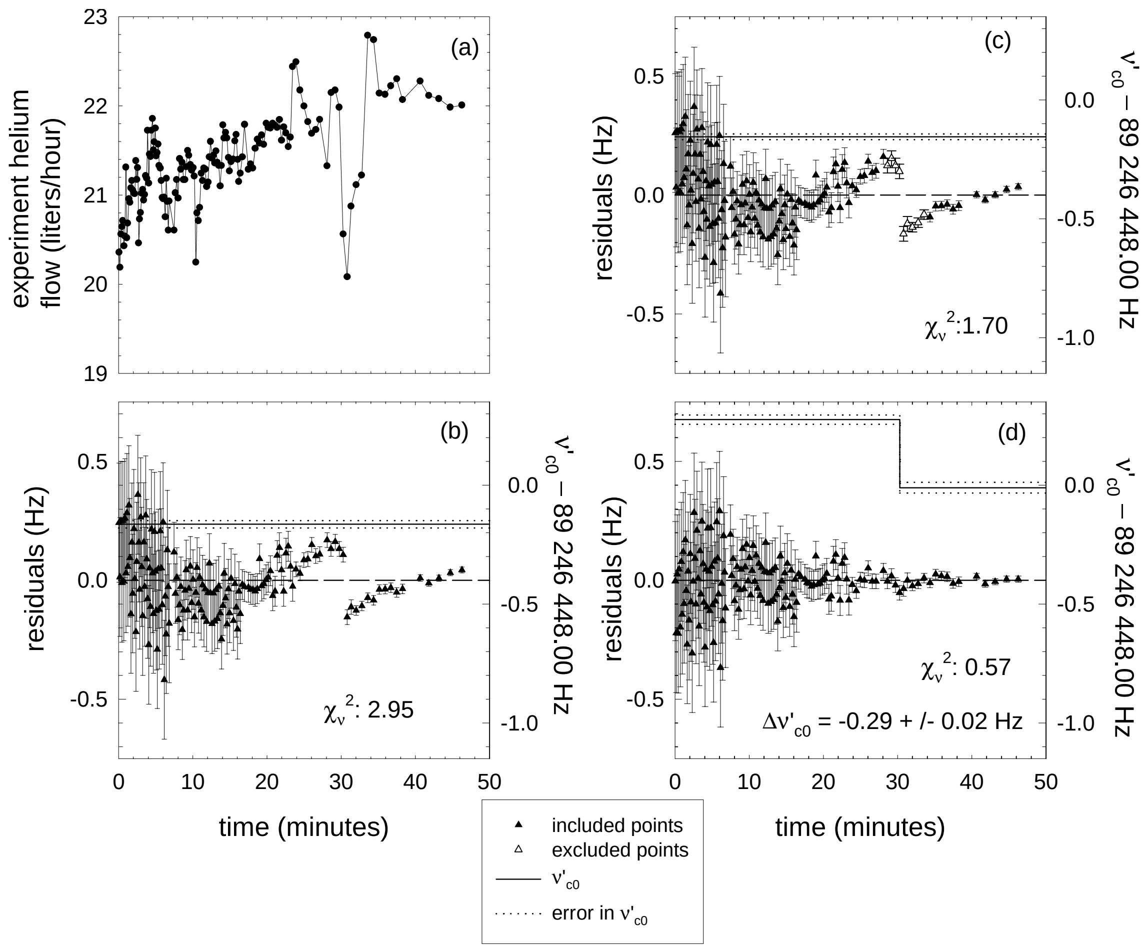

Figure 4.11: The magnetic field at the trap center abruptly decreased. (a) A small change in the flow over the helium dewar of the experiment. (b) The cyclotron fit residuals show a large change coincident with the small variation flow. The change is very much larger than the ν'_c error bars. We fit the ν'_c data to Eq. 2.23, assuming the endpoint cyclotron frequency (ν'_{c0}) is constant. (c) The fit residuals show the step even after excluding the ν'_c measurements at the time of the flow variation. (d) Allowing ν'_{c0} to step to a lower value at the time of the flow variation makes the fit very reasonable. The size of the step is $\Delta\nu'_{c0}$. All the data is included, and it all fits well to the model.

field was also much too large and the wrong sign to be explained by the small change in the ambient magnetic field. An ambient magnetic field change 10 times larger than this in the opposite direction was required to cause this size change in the fit residuals (compare with Fig. 4.9a and 4.9b). Another example shows a step in the internal magnetic field (Fig. 4.12e and 4.12f) coincident with a change in the flow of the experiment helium dewar (Fig. 4.12d). The size of the magnetic field step is not proportional to the change in the flow since in Fig. 4.11 a larger magnetic field step is seen at the time of a much smaller disturbance in the flow.

The magnetic field steps could be due to an abrupt mechanical change between the center of the trap and the internal magnetic field center. Some small disturbances, such as those recorded in one of the ambient variables, could trigger the magnet coils to relax. Given our magnetic field gradient (Table 2.1), a 50 μm mechanical shift between the magnet coils and the trap center would cause this measured effect. After the magnet was first charged, the magnetic field slowly decreased as the magnet coils settled [49]. The decrease may have been in small discrete steps as in Fig. 4.11b. Another possibility is that the flux made by the superconducting coil jumps [50]. This dissipates the energy in the magnetic field resulting in a lower field. Jumps occur when a disturbance locally heats the magnet coils or when the external magnetic field changes. In our case, we observed steps of 1 part in 10^9.

The magnetic field suddenly relaxed by more than 0.1 Hz every 12 hours on average. We observed 6 magnetic field steps of this size after analyzing 75 hours of accurate cyclotron measurements. Most of the cyclotron measurements analyzed were taken overnight, and most of the steps took place between 04:00 hours and 06:00 hours. The steps appeared in the fit residuals and did not occur at the same time as the nonresonant **E** field turned on.

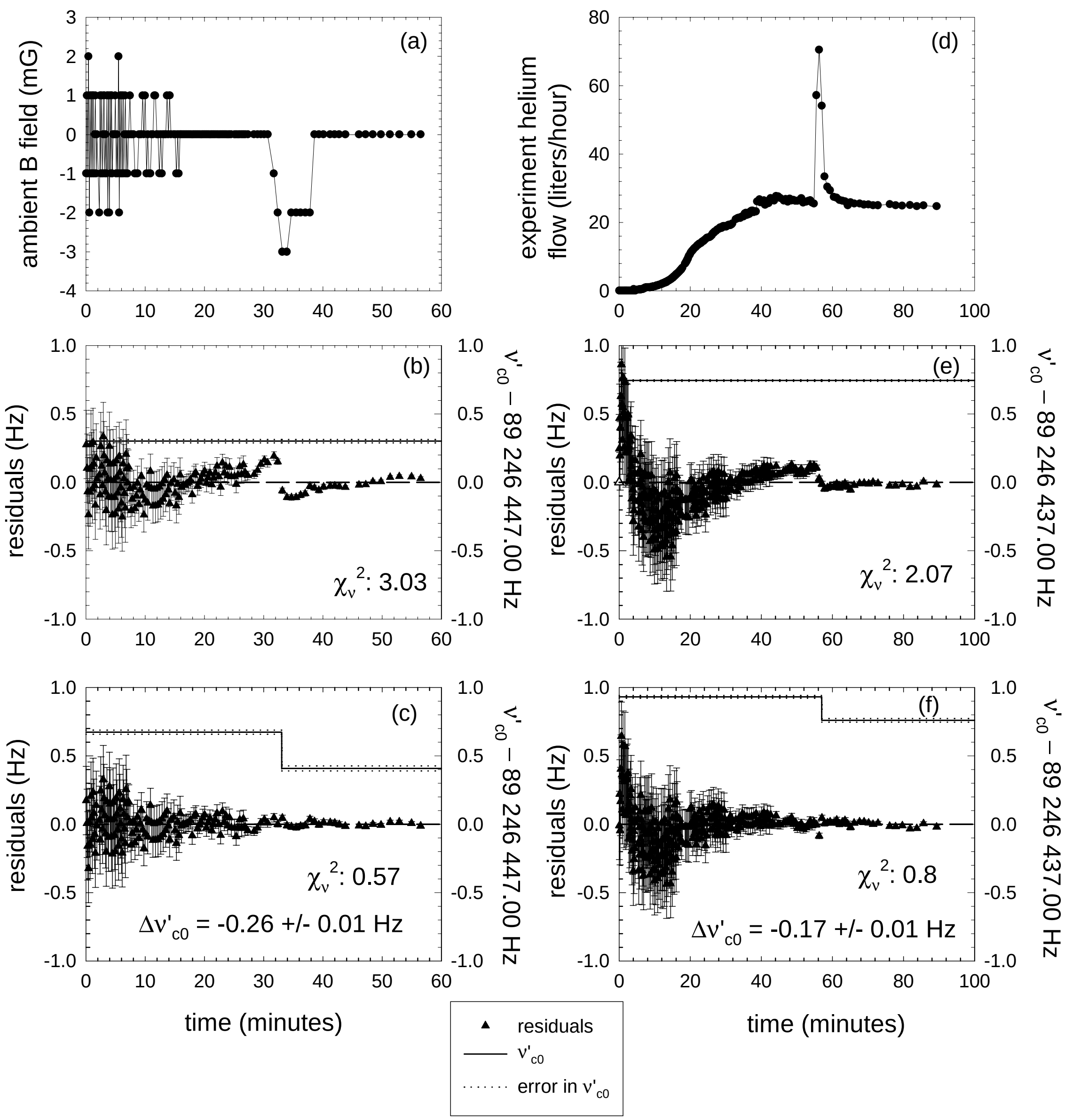

Figure 4.12: Two more examples of magnetic field steps. (a) A small change took place in the ambient magnetic field. (b) The residuals show a discrete jump coincident with the ambient magnetic field change. ν'_{c0} was held constant (Eq. 2.23). (c) The fit was very good when we allowed ν'_{c0} to change coincident with the ambient magnetic field change. (d,e,f) In another example, the experiment helium flow changed at the same time that the magnetic field stepped.

4.3.4 Slow Drifts in the Magnetic Field

The purpose of the pressure regulation was to reduce the magnetic field drift in time, since that drift limited our measurement accuracy. A first step to reducing the magnetic field drift was to identify the most likely causes. When the regulator did not work reliably, many ambient variables changed at the same time; this made finding the cause difficult. Once we made the regulator work well the correlations improved.

The magnetic field drifted with the magnet temperature. The magnet was located in a large, open experimental hall whose temperature increased during the day when the sunlight heated the hall and cooled during the night. The magnet's temperature followed this cycle (Fig. 4.13a). It was highest around 19:00 hours and lowest around 08:00 hours. The modified cyclotron, axial and magnetron measurements were combined to determine the cyclotron frequency (Fig. 4.13b), a measure of the magnetic field. The magnetic field changed directions at the same time as the temperature.

Many examples confirmed a correlation between the magnetic field drift and the temperature (Fig. 4.13). The correlation was clear whether the magnet temperature overnight changed by 4.5 ˚C (Fig. 4.14a) as in the summer, or by 1.5 ˚C (Fig. 4.14d) as in the fall. The four examples in Fig. 4.13 and Fig. 4.14 all have the same slope and determine that the field drifted by -0.38 ± 0.04 Hz/ ˚C. The slope is much different from zero so the correlation is very high. This linear correlation was clear only after the regulation worked reliably. The magnetic field did not correlate well with the other environmental variables such as the helium boil-off rate or the pressure above the dewars.

The drift may be due to an expansion in the aluminum neck of the magnet.

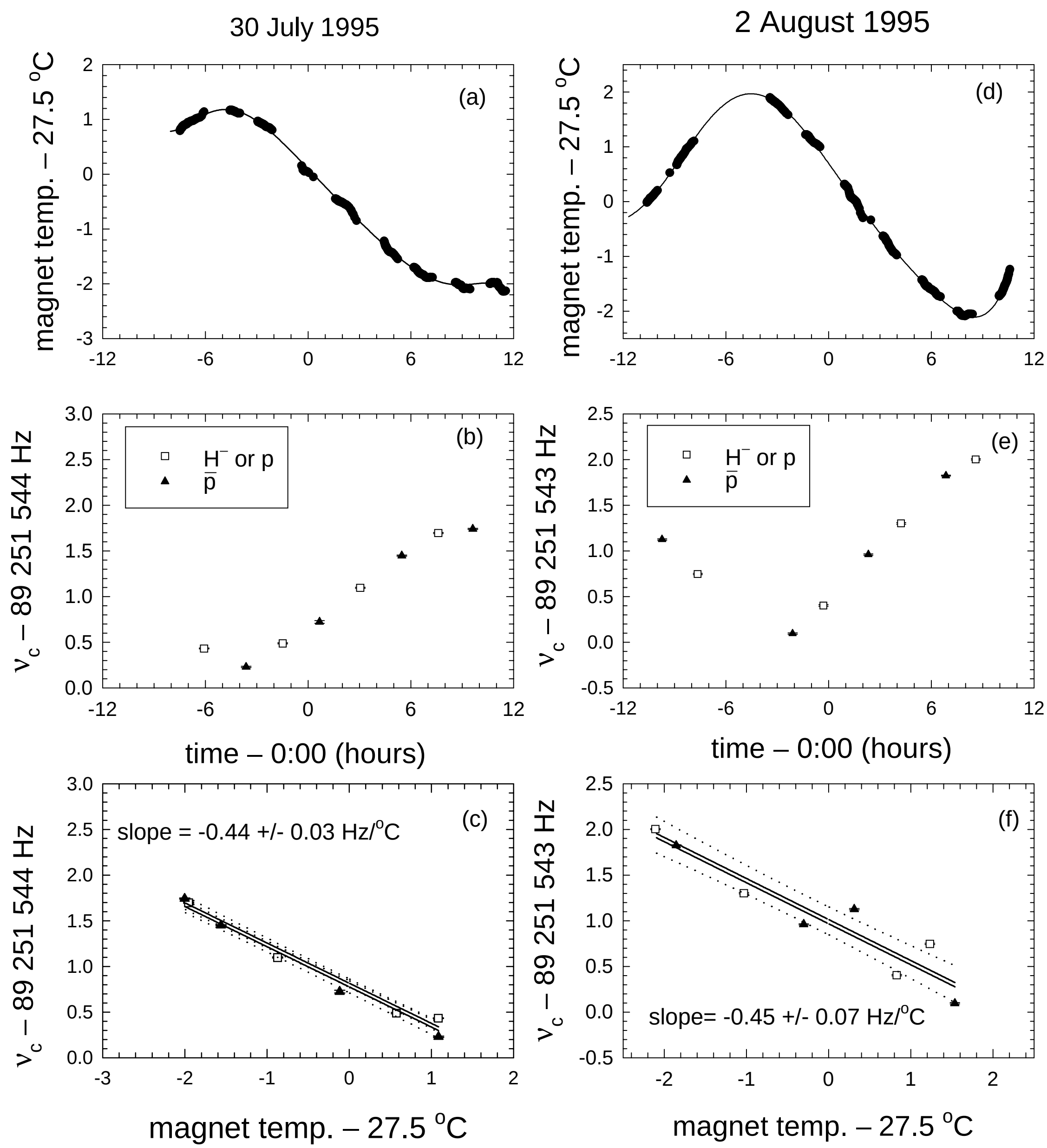

Figure 4.13: The magnetic field drifts with the magnet's temperature. (a) The magnet's temperature changes after sunrise and sunset. Midnight is 00:00 hours. (b) The cyclotron frequency (ν_c), a measure of the magnetic field, increased as the temperature decreased. (c) The magnetic field depends linearly on the magnet temperature. (d,e,f) Another example.

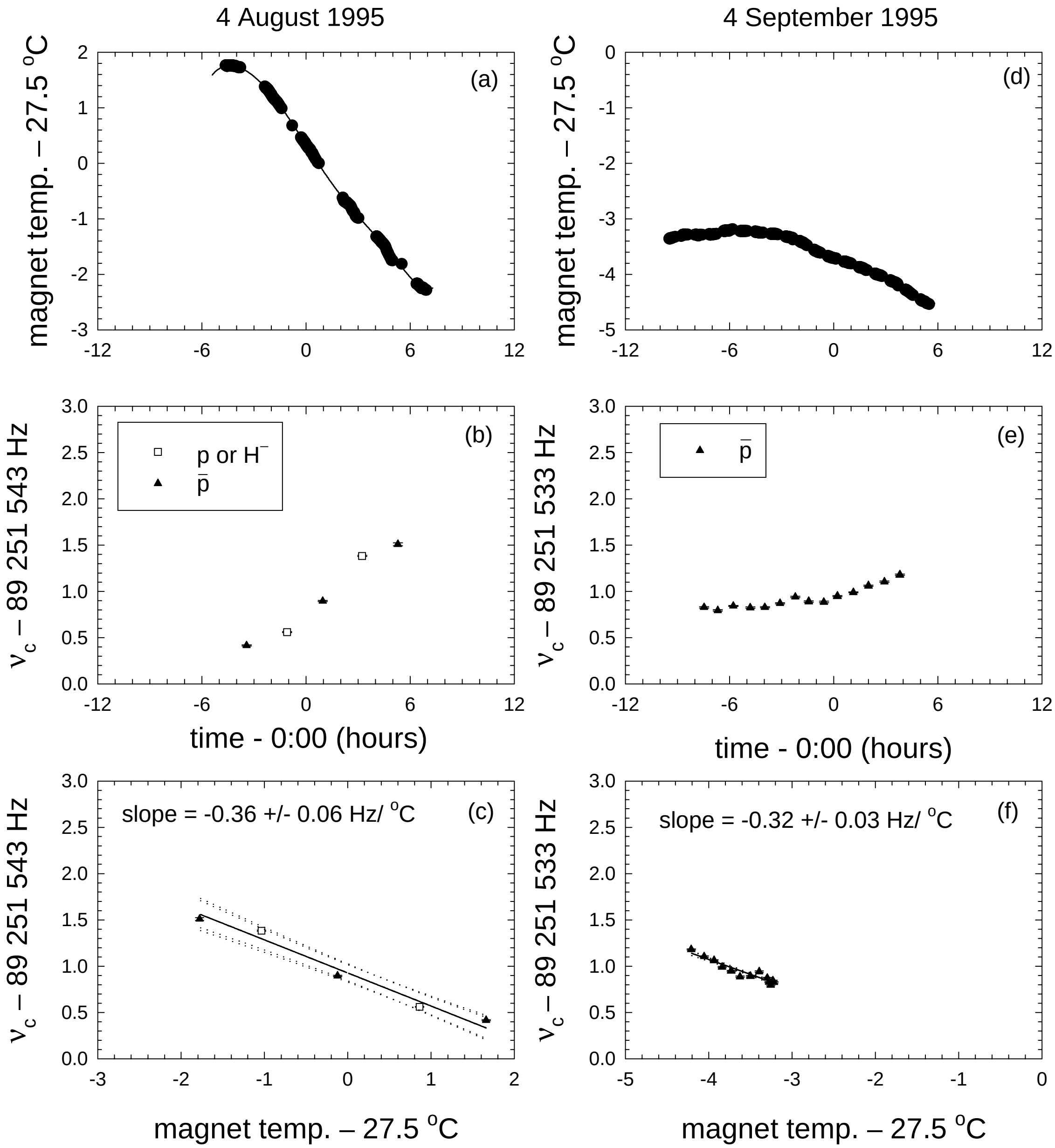

Figure 4.14: The magnetic field drifts linearly with temperature in the same way even when the temperature varies by different amounts. Midnight is 00:00 hours. (a) A large temperature variation measured in the summer. (b) The cyclotron frequency (ν_c) measurements. (c) The cyclotron frequency correlates with temperature. (d,e,f) Another example measured in the fall, showing the same linear drift, even though the temperature variation was smaller.

As the room heats, the neck expands and changes the relative location of the trap center and the coils of the magnet. This causes a cyclotron frequency shift because the magnetic field is not uniform. The 2 m aluminum neck expands by 50 μm/ °C. Using the magnetic field gradient (0.02 Gauss/cm), the cyclotron frequency should drift by 0.2 Hz/ °C. This agrees with the measurement within a factor of 2.

This correlation helped model the slow magnetic field drift. If the temperature measurements had two turning points, then we expected the magnetic field drift also to have two turning points. The magnetic field drift was fitted in time to at least a third order polynomial. The temperature drift accounted for the large changes in the magnetic field drift.

The temperature correlation allowed us to rank the data quality. The magnetic field drifted least during the measurements made in late August and in September when the ambient temperature was most stable between day and night. These were our best data sets. In a 24 hour period the magnetic field drifted least at after sunset when the experimental hall was slowly cooling down. For this reason, we only considered measurements made at night.

Precision mass measurements are very often limited by the stability of the magnetic field. In this case we showed that our field was the most stable when the magnet temperature was stable. Stabilizing the magnet's external temperature would significantly improve the temporal stability of the magnetic field.

4.4 Fitting to Determine the Ratio of Charge-to-Mass Ratios

Every night we alternately measured the cyclotron frequencies of the antiproton ($\nu_c(\bar{p})$) and the proton ($\nu_c(p)$). The $\bar{p}$ was first kept in a large cyclotron orbit and the modified cyclotron frequency, the axial frequency and the magnetron frequency of the H^- were measured. We fitted the data, sometimes allowing the cyclotron orbit of the inner particle to change when the nonresonant **E** field turned on and sometimes allowing the internal magnetic field to step to a lower value. The cyclotron frequency of the H^- was measured by combining the three measured frequencies with the invariance theorem (Eq. 2.9). The H^-cyclotron frequency determined the proton cyclotron frequency since the mass ratio (M_{H^-}/M_p of Eq. 4.3) is known. The particles then switched positions and we measured the cyclotron frequency of the antiproton ($\nu_c(\bar{p})$).

The ratio of cyclotron frequencies determined the ratio of the proton and antiproton charge-to-mass ratios. The difference in the cyclotron frequency ($\omega_c = eB/m$ in Eq. 1.1) is given by:

$$\frac{\Delta\nu_c}{\nu_c} \equiv \frac{\nu_c(p,t) - \nu_c(\bar{p},t)}{\nu_c(p)} = 1 - \left|\frac{e/m(\bar{p})}{e/m(p)}\right|, \tag{4.4}$$

where t is time and $2\pi\nu_c = \omega_c$. Since $\nu_c(p,\mathrm{t})$ drifted by 1 part in 10^8 in 12 hours, it was held constant in the denominator. In the numerator, both $\nu_c(p,\mathrm{t})$ and $\nu_c(\bar{p},\mathrm{t})$ drifted in time because the magnetic field drifted. We fit the ν_c data to drift as a low order polynomial with a constant offset between the $\nu_c(p)$ and $\nu_c(\bar{p})$. This constant offset measured the ratio of the $\bar{p}$ to p charge-to-mass ratios.

The large changes in the magnetic field made the ν_c fit critical to measure the charge-to-mass difference. The measurements were fitted with two complimentary methods. In the first pass fit, we assumed that the magnetic field was constant over the one hour needed for the modified cyclotron measurement. This was the method used in the previous measurement [1, 2]. Individual cyclotron frequency measurements produced in this way were independent and tested the smoothness of the magnetic field drift. However, the assumption of a constant magnetic field drift over the one hour modified cyclotron measurement was inaccurate, since over this time, the magnetic field often drifted by 10 times the cyclotron frequency accuracy. The simultaneous fit which we developed made a more realistic assumption about the magnetic field drift. It assumed that the magnetic field drifted smoothly as a low order polynomial overnight. The simultaneous fit better fit the large magnetic field drift, but it constrained the magnetic field to drift smoothly as a polynomial. When the magnetic field model used for the simultaneous fit was realistic, it produced a more accurate difference frequency ($\Delta\nu_c$).

4.4.1 The First Pass Fit

Each modified cyclotron frequency endpoint (ν'_{c0}) determined one cyclotron measurement (ν_c). The modified cyclotron frequency error bars were adjusted (Fig. 2.20) and the modified cyclotron data was fit to Eq. 2.23, which assumed that the magnetic field was constant. This determined the endpoint modified cyclotron frequency (ν'_{c0}) as already described. The modified cyclotron endpoint (ν'_{c0}) was assigned to the time when the relativistic shift ($\delta\nu'_c$ of Eq. 2.23) was -0.1 Hz. The modified cyclotron frequencies taken overnight are shown in Fig. 4.15. The fit to the night's axial responses (Fig. 2.31) measured the axial frequency and its error bar at that time. The axial and modified cyclotron frequencies were used to determine the mag-

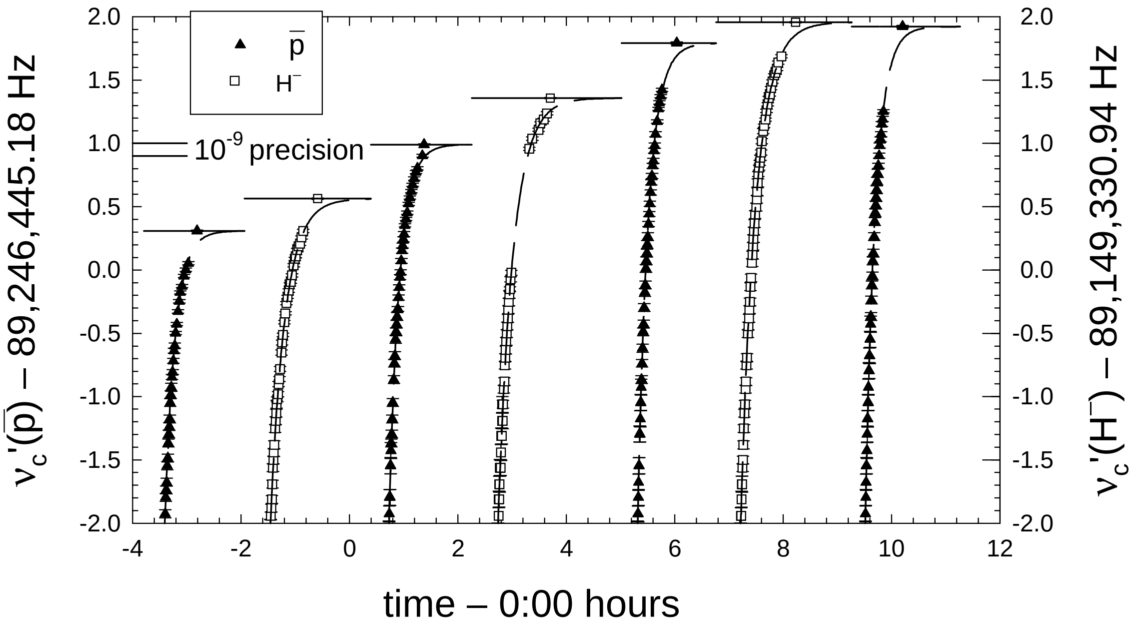

Figure 4.15: A night's modified cyclotron frequency measurements show the magnetic field drift. Midnight is 00:00 hours. Each set of modified cyclotron frequency measurements are fit to Eq. 2.23 to determine the endpoint frequency (ν'_{c0}). The fit assumed that the magnetic field is constant over each measurement set. Since neighboring sets of ν'_{c0} measurements fit to much different endpoint values (ν'_{c0}), this assumption was not correct.

netron frequency using Eq. 2.27. The invariance theorem (Eq. 2.9) and the p to H^- mass ratio (Eq. 4.3) then determined the cyclotron frequency (ν_c).

In the second fitting step, we fit the cyclotron measurements (ν_c) to drift as a polynomial with a constant difference frequency ($\Delta\nu_c$ of Eq. 4.4) between the proton and antiproton. The cyclotron frequencies drifted considerably in the night (Fig. 4.16a). To account for this, the fit allowed the magnetic field to drift. With cause, the magnetic field was sometimes allowed to step abruptly. The cyclotron measurements were fit to all possible polynomial orders while still keeping at least one degree of freedom. We picked the lowest order polynomial that significantly reduced χ^2_ν. In Fig. 4.16b, a third order polynomial was the best order, since the fourth order polynomial did not improve χ^2_ν. We used polynomials of second to fourth order. Generally, the difference frequency ($\Delta\nu_c$) error bar decreased when χ^2_ν did (Fig. 4.16c).

The greatest difficulty with the first pass fit was the assumption that the magnetic field was constant to 1 part in 10^{10} during a cyclotron decay. This was implied in Eq. 2.23, when the fit produced an endpoint cyclotron frequency (ν'_{c0}) accurate to this level. In the time required to complete a cyclotron decay (1 hour), the magnetic field drifted by 20 times this accuracy (Fig. 4.15), about 20 parts in 10^{10}. The poor assumption of a constant magnetic field made the fit's prediction questionable. However, the prediction of the first pass fit did not underestimate the error by 20 times. Since the same method was used to fit proton and antiproton cyclotron measurements, the difference frequency ($\Delta\nu_c$) was not affected to the first order. The assumption of a constant magnetic field seemed to cause an error of about 3 parts in 10^{10} for the large field drift shown in Fig 4.16a. This is the difference between the $\Delta\nu_c$ as predicted by the first pass fit and $\Delta\nu_c$ as predicted by the simultaneous fit (Table 4.4), a fit which never made the poor assumption of a constant magnetic field. When the magnetic field drift was smaller than shown in Fig. 4.16a, the simultaneous and the first pass methods produced much more similar predictions of $\Delta\nu_c$.

The quality of the first pass fit was also not very good. When the polynomial order which minimized χ^2_ν was chosen, the first pass fit had only 1 or 2 degrees of freedom. This caused a great deal of scatter in the error bar of the difference frequency ($\Delta\nu_c$). Different days with about the same magnetic field drift and about the same number of cyclotron measurements had an error bar on $\Delta\nu_c$ which fluctuated by a factor of 4. This was contrary to our expectations that measurements of the same quality should measure the difference frequency to the same accuracy. The

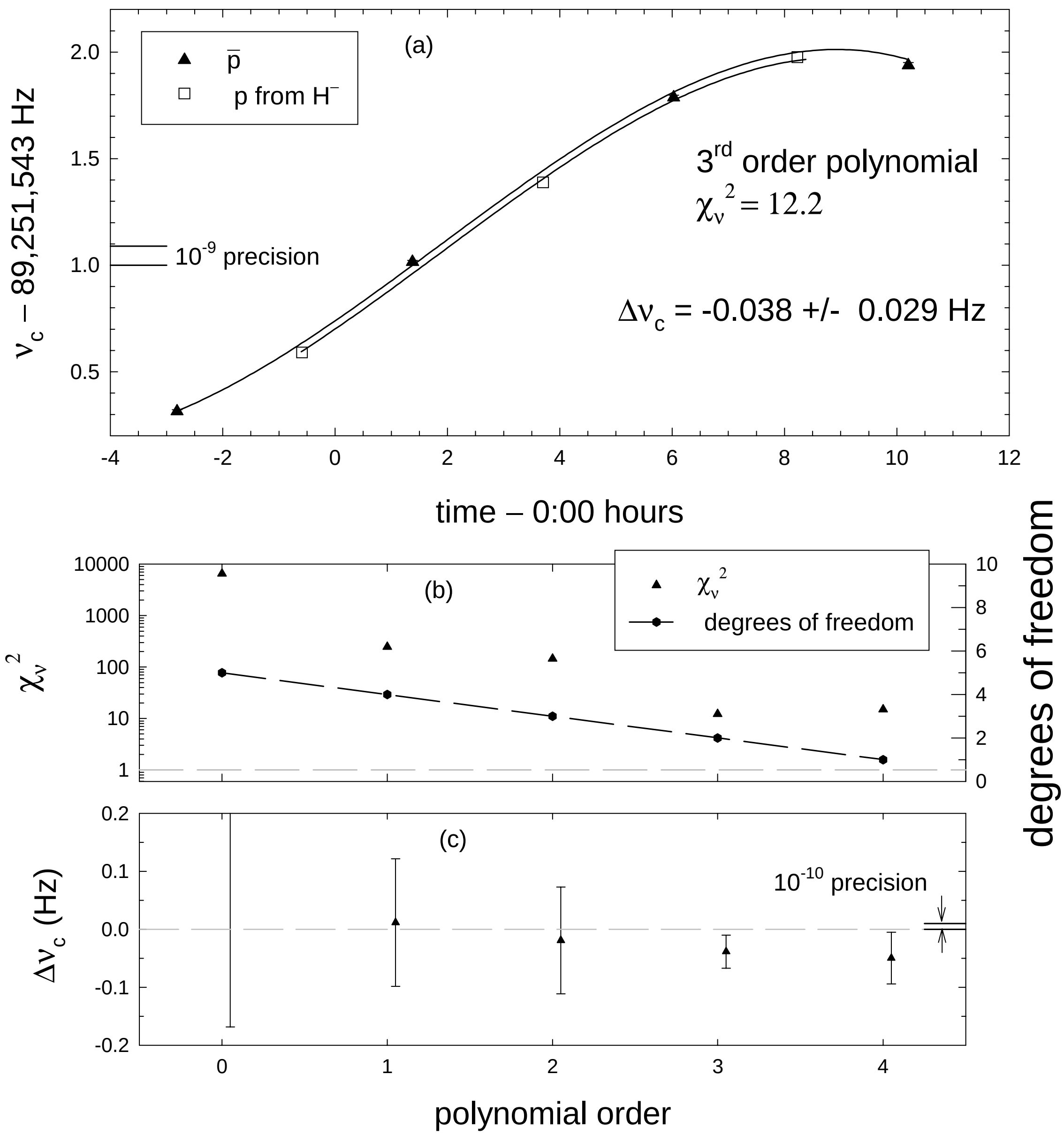

Figure 4.16: A charge-to-mass measurement using the first pass fit. $\Delta\nu_c = \nu_c(p) - \nu_c(\bar{p})$. (a) The cyclotron ($\nu_c$) frequency measurements are fit with the best order polynomial. Midnight is 00:00 hours. The errors on the fit to $\bar{p}$ and p cyclotron frequencies are shown. (b) χ^2_ν and the degrees of freedom change with the polynomial order. The third order polynomial produced the lowest χ^2_ν. The fourth order is the largest possible order. (c) The proton and antiproton cyclotron difference frequency ($\Delta\nu_c$) is smallest for the third order fit.

first pass fit also produced a large χ^2_ν. In Fig. 4.16a χ^2_ν was 12, not 0.7 as expected for a fit with two degrees of freedom like this one. This indicated that the errors originally assigned to each cyclotron endpoint measurement were about 3 times too small.

The first pass fit also had some advantages. Each cyclotron frequency measurement was independent of the others; this independence allowed us to check the magnetic field smoothness. Cyclotron measurements closely spaced as in 1996 allowed us to identify a magnetic field step and helped estimate the best polynomial order with which to fit the data. When the magnetic field drift was small as in 1996, the first pass fit measured the difference frequency ($\Delta\nu_c$) accurately. Finally, it was simple and served as a cross check for the simultaneous fit below.

4.4.2 The Simultaneous Fit for the Charge-to-Mass Difference

The simultaneous fit remedied most of the shortcomings of the first pass fit. It transformed each modified cyclotron frequency measurement into a cyclotron frequency measurement. Each cyclotron frequency was shifted because of the relativistic shift (Eq. 2.21) and the magnetic field drift. The hundreds of cyclotron frequency measurements in a night were fit in one step to determine the magnetic field drift and the difference frequency ($\Delta\nu_c$). The resulting fit produced an χ^2_ν of about 1, and the fit had hundreds of degrees of freedom, making it more satisfactory. Furthermore, the simultaneous fit was more constrained, since it measured the difference frequency ($\Delta\nu_c$) by using fewer fit parameters. It eliminated the need for the endpoint cyclotron frequencies (ν'_{c0}) and only used two time constant parameters, one for all the H^- measurements and another for all the antiproton measurements.

Initially, it was not clear how to fit the modified cyclotron frequency data for a continually drifting magnetic field. Certainly the cyclotron frequency drifted with the magnetic field, but the modified cyclotron drift in time was more complicated. The modified cyclotron frequency not only drifted with the magnetic field but also had a large relativistic shift. The invariance theorem (Eq. 2.9) only related the modified cyclotron frequency with no relativistic shift to the cyclotron frequency, making it unusable by itself. Once we linearized the invariance theorem, we could convert each modified cyclotron frequency that was relativistically shifted into a cyclotron frequency that was relativistically shifted.

The modified cyclotron frequency for a particle with little kinetic energy drifts because the magnetic field drifts and because the electrostatic trapping potential drifts. The magnetic field drift causes the cyclotron frequency to drift in time. The cyclotron frequency can be separated in a large constant part (ν_{c0}) of order 10^8 Hz and a small time varying part ($\delta^d \nu_c(t)$) of order 1 Hz. The time varying cyclotron frequency ($\delta^d \nu_c(t)$) drifts slowly as a polynomial and sometimes has discrete jumps at the time of the magnetic field steps. The fit determines the parameters in $\delta^d \nu_c(t)$ that model the magnetic field drift. The drift in the electrostatic potential is measured by the axial frequency which also has a large constant part (ν_{z0}) and a small time varying part ($\delta \nu_z(t)$). Similarly, the modified cyclotron frequency measured with little kinetic energy has a large constant part (ν'_{c0}) and a small time varying part ($\delta {\nu'_c}_0(t)$). The large constant cyclotron (ν_{c0}), modified cyclotron (ν'_{c0}) and axial (ν_{z0}) frequencies are related by the invariance theorem (Eq. 2.9). The small time varying changes can be related using a linear expansion of the invariance theorem:

$$\delta^d \nu_c(t) = \underbrace{\left(1 - \frac{1}{2}\left(\frac{\nu_{z0}}{\nu'_{c0}}\right)^2\right) \delta {\nu'_c}_0(t)}_{1\ \mathrm{Hz}} + \underbrace{\frac{\nu_{z0}}{\nu'_{c0}} \delta \nu_z(t)}_{10^{-2}\ \mathrm{Hz}} + \cdots \tag{4.5}$$

where t is time, where $\nu_{z0}/\nu'_{c0} \approx 10^{-2}$. The first order expansion is accurate enough to measure the drift in the modified cyclotron frequency $(\delta\nu'_{c\,0}(t))$ to our precision of 0.01 Hz since the expansion converges very rapidly. (The next order term in Eq. 4.5 is of order 10^{-8} Hz.) This expansion simplifies the fit enormously, and allows us to relate the drift in the modified cyclotron frequency to the drift in the cyclotron frequency.

Special relativity causes the modified cyclotron frequency of particles in large orbits to shift (Eq. 2.22). The shift in the modified cyclotron frequency due to special relativity is given by:

$$\delta\nu'_c(t) = -\sum_{i=1}^{n} A_i S_i(t) e^{-(t-t_i)/\tau}, \tag{4.6}$$

where t is time. The start of each cyclotron decay $(t_1, t_2, \ldots)$ is when the modified cyclotron orbit of the measured particle is first increased. The initial relativistic shifts $(A_1, A_2, \ldots)$ are the relativistic shifts just after the oscillatory **E** field drive increases the measured particles orbit. When the drive of the outer particle does not affect the inner one, each initial relativistic shift (A_1 for example) is one fit parameter independent of time. When the nonresonant **E** field drive increases the relativistic shift of the measured particle (Fig. 4.5), each initial relativistic shift (A_1 for example) is really a series of relativistic shifts, a different one for each time the nonresonant **E** field turns on. The step functions $(S_1(t), S_1(t), \ldots)$ make only one value of initial relativistic shift (A_1) nonzero at any one time.

The time constant (τ) was stable overnight. Based on the stability of the cyclotron RLC circuit, the time constant drifted by less than 0.14%/hour which is within the fit uncertainty. We fixed the time constant (τ) in time to take only two values: one for all the antiproton measurements $(\tau_{\bar{p}})$, and another for all H^-

measurements (τ_{H^-}). This better constrained the fit and eliminated unnecessary fit parameters.

The sum of Eq. 4.5 and Eq. 4.6 leads to a time-dependent model for the relativistically shifted cyclotron frequency:

$$\delta\nu_c(t,\bar{p}) = \delta^d\nu_c(t) - \sum_{i=1}^{n} A_i S_i(t) e^{(t-t_i)/\tau_{\bar{p}}} \tag{4.7}$$

$$\delta\nu_c(t,p) = \Delta\nu_c + \delta^d\nu_c(t) - \sum_{i=1}^{n} A_i S_i(t) e^{(t-t_i)/\tau_{\mathrm{H}^-}}. \tag{4.8}$$

The cyclotron frequency is shifted from a constant value (ν_{c0}) both because the magnetic field drifts ($\delta^d\nu_c(t)$) and because of special relativity. The most important fit parameter is $\Delta\nu_c$ which is the constant difference between the proton and antiproton cyclotron frequencies. The constant cyclotron frequency (ν_{c0}) is chosen to be the same for both the proton and the antiproton. This choice insures that $\Delta\nu_c$ determines the difference between the proton and antiproton cyclotron frequencies. The antiproton cyclotron frequency drift ($\delta^d\nu_c(t)$) measures the magnetic field drift. Finally the exponential term determines the shift in the cyclotron frequency due to special relativity as described in Eq. 4.6. Both Eq. 4.8 and Eq. 4.7 depend only on time and on the fit parameters.

The sum of Eq. 4.5 and Eq. 4.6 also lead an expression for measured values of the time-dependent cyclotron frequencies which are relativistically shifted:

$$\delta\nu_c(t,\bar{p}) = \left(1 - \frac{1}{2}\left(\frac{\nu_{z0}}{\nu'_{c0}(\bar{p})}\right)^2\right)\delta^t\nu'_c(t,\bar{p}) + \frac{\nu_{z0}}{\nu'_{c0}(\bar{p})}\delta\nu_z(t,\bar{p}) \tag{4.9}$$

$$\delta\nu_c(t,p) = \frac{M_{\mathrm{H}^-}}{M_p}\left[\left(1 - \frac{1}{2}\left(\frac{\nu_{z0}}{\nu'_{c0}(\mathrm{H}^-)}\right)^2\right)\delta^t\nu'_c(t,\mathrm{H}^-) + \frac{\nu_{z0}}{\nu'_{c0}(\mathrm{H}^-)}\delta\nu_z(t,\mathrm{H}^-)\right]. \tag{4.10}$$

The measured cyclotron frequency shifts from a constant value (ν_{c0}) both because the axial frequency shifts and because the modified cyclotron frequency shifts. The axial frequency of the $\bar{p}$ and the H^- drifts in time as in Eq. 4.5. The axial frequency drift for the H^- ($\delta\nu_z(t, H^-)$) and the antiproton ($\delta\nu_z(t, \bar{p})$) is difference between the full axial frequency and a constant axial frequency (ν_{z0}) which is the same for both the H^- and the $\bar{p}$. A fit to the night's axial frequencies determines the axial frequency drift (Fig. 2.31).

The modified cyclotron frequency is shifted both because of special relativity and because of the drift in the magnetic and the electric fields. Each measured modified cyclotron frequency shift ($\delta^t\nu_c'(t)$) drifts by the sum of the relativistic shift, $\delta\nu_c'$(t), and the drift in the magnetic and electric fields, $\delta\nu_{c\,0}'(t)$. The right hand side of Eq. 4.9 converts each modified cyclotron frequency measurement into a measurement for the relativistically shifted cyclotron frequency. The expression in brackets in Eq. 4.10 converts each H^- modified cyclotron frequency into an H^- cyclotron frequency. The mass ratio (M_{H^-}/M_p) then converts this expression into a measured cyclotron frequency of the proton. Eq. 4.9 and Eq. 4.10 also relate the modified cyclotron frequency errors and the axial frequency errors to the cyclotron frequency errors.

The measured modified cyclotron frequency of the H^- is the sum of the shift in the modified cyclotron frequency ($\delta^t\nu_c'(t, H^-)$) and a large constant value ($\nu_{c0}'(H^-)$). The large constant modified cyclotron frequency ($\nu_{c0}'(H^-)$) is determined by the constant proton cyclotron frequency (ν_{c0}), the proton to H^- mass ratio (M_{H^-}/M_p), the H^- constant axial frequency (ν_{z0}) and the invariance theorem (Eq. 2.9). Similarly the constant offset for the antiproton modified cyclotron frequency ($\nu_{c0}'(\bar{p})$) is determined by the the antiproton cyclotron frequency (ν_{c0}), the antiproton axial frequency (ν_{z0}) and the invariance theorem (Eq. 2.9).

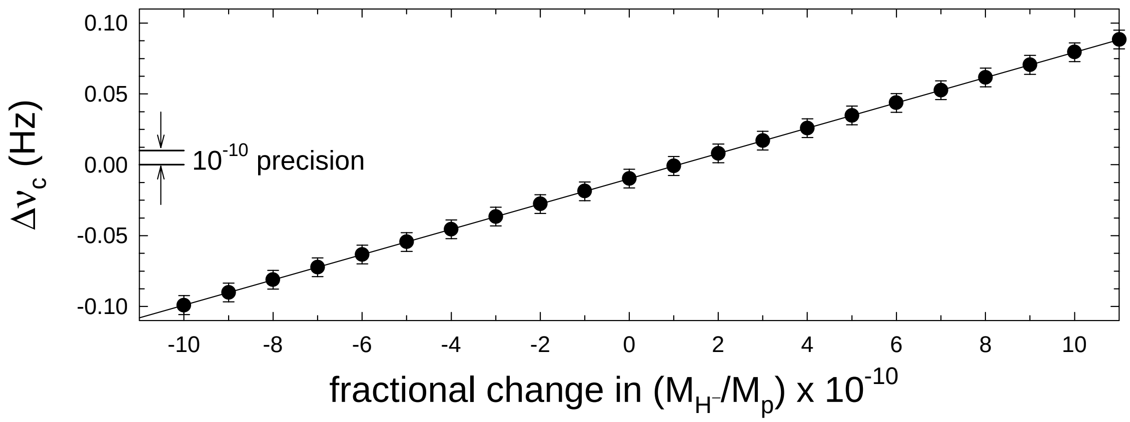

Figure 4.17: To check the simultaneous code, we changed M_{H^-}/M_p and refit the same data for the difference frequency ($\Delta\nu_c = \nu_c(p) - \nu_c(\bar{p})$). $\Delta\nu_c$ increased as expected. The slope equaled ν_{c0} to within 10^{-7} Hz.

The fit was performed by setting the measured proton (Eq. 4.10) and antiproton (Eq. 4.9) cyclotron frequencies equal to the nonlinear model (Eq. 4.8 and Eq. 4.7) for the cyclotron frequencies. Because the large constant frequencies were eliminated from these equations, instead of requiring 10 digits of precision each measured cyclotron frequency only required 4 digits. A reliable way was developed to insure that the complex fit converged. An initial estimate of the fit parameters was made by holding the two time constants (τ_{H^-} and $\tau_{\bar{p}}$) fixed to estimates based on prior fits to Eq. 2.23. Fixing the time constants made the fit linear. Following this initial estimate, the nonlinear fit was performed.

The accuracy of the code which measures the difference frequency ($\Delta\nu_c$) was tested. The mass ratio M_{H^-}/M_p was varied and the data refitted to see that the difference frequency changed as expected. A larger M_{H^-}/M_p mass ratio makes the proton cyclotron frequency and the difference frequency ($\Delta\nu_c$) larger. As we varied the M_{H^-}/M_p ratio, the difference frequency ($\Delta\nu_c$) increased exactly on a line as expected (Fig. 4.17).

The data fit very well to the simultaneous model. When we fit all the data from one night to a third order polynomial magnetic field drift, the model produced χ^2_ν of 1.15 and had 1010 degrees of freedom (Fig. 4.18). $\Delta\nu_c$ was -0.01 ± 0.007 Hz. The low χ^2_ν and the large number of degrees of freedom supported the validity of the model.

The simultaneous fit is an improvement over the first pass fit because it treats the magnetic field drift correctly. The magnetic field prediction is better because it never makes the bad assumption that the magnetic field is constant; instead, it fits for the best magnetic field in a self-consistent manner. For the large field drifts that we have in most of our data, the cyclotron frequency (ν_c) predictions of the first pass fit disagree with the the prediction of the simultaneous fit (Fig. 4.18). These predictions also scatter much more than their error bars. As the size of the magnetic field drift increases, the difference between the first pass fit and the simultaneous fit also increases.

The quality of the simultaneous fit is also better than the first pass fit (Table 4.4). The fit is much more constrained and has fewer parameters. The simultaneous fit uses two independent time constants while the first pass fit uses an independent time constant for each set of modified cyclotron measurements. The simultaneous fit uses parameters for the magnetic field drift and the difference frequency ($\Delta\nu_c$), while the first pass fit uses these parameters and the modified frequency endpoints (ν'_{c0}). Eliminating these unnecessary parameters, as the simultaneous fit does, constrains the fit better. The simultaneous fit also produced a very reasonable χ^2_ν and had many degrees of freedom, enough to produce a good fit. For the simultaneous fit χ^2_ν was reasonably close to 1 (Fig. 4.20), and the error bar of the difference frequency ($\Delta\nu_c$) was always approximately 0.01 Hz, about 1 part in 10^{10}. This was not the case with the first pass fit.

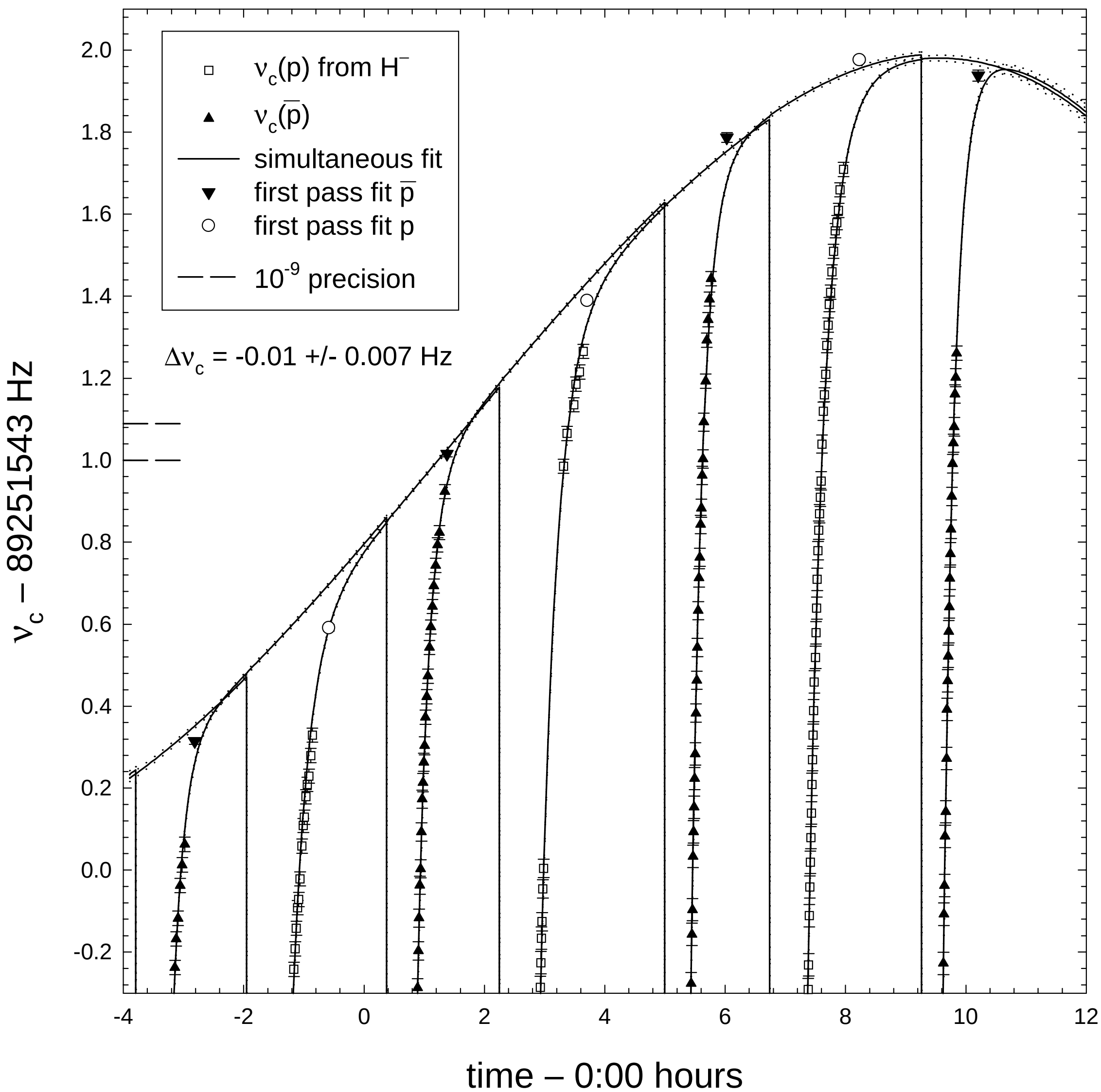

Figure 4.18: The simultaneous fit produces a good fit to the cyclotron data. Midnight is 00:00 hours. The slow drifting magnetic field is modeled as a polynomial of third order. Each cyclotron measurement is shifted from the drifting background because of special relativity. The simultaneous fit determines the best relativistic shifts for each measurement and the magnetic field drift. The cyclotron frequency measurements as determined by the first pass fit are also shown.

Quality indicator	First pass fit	Simultaneous fit
χ^2_ν	12.2	1.15
Degrees of freedom	2	1010
Number of fit parameters	26	14
$\Delta\nu_c = \nu_c(p) - \nu_c(\bar{p})$	-0.04 ± 0.03 Hz	-0.01 ± 0.01 Hz

Table 4.4: The quality of the simultaneous fit was higher than the first pass fit. Shown is a comparison of the fit quality for the same data set that used the same order polynomial.

The simultaneous fit takes into account any axial, magnetron or cyclotron frequency shift which is proportional to the relativistic shift in the modified cyclotron frequency ($\delta\nu_c'$). Due to the magnetic field bottle (Table 2.1), the axial frequency shifts by 2 Hz for every 1 Hz increase in the relativistic shift. Since the relativistic shift exponentially decreases to zero, these shifts do as well. By redefining the fit parameter A_i in Eq. 4.8 and in Eq. 4.7, the fit accounts for them.

When the magnetic field drift was high some of the most important cyclotron measurements deviated from the simultaneous fit. The initial cyclotron measurements in each decay curve, corresponding to large relativistic shifts, had large error bars and fit the model very well (Fig. 4.19a). However, the final cyclotron frequency measurements in a decay, corresponding to small relativistic shifts, sometimes deviated by more than their error bar (σ) (Fig. 4.19d). This was not optimal because the final cyclotron measurements were the most heavily weighted and were the most important for determining the magnetic field drift and the difference frequency ($\Delta\nu_c$). It indicated that the simultaneous fit model still had limitations when the magnetic field drift was large. We shall see that when the magnetic field drift was too large, the simultaneous fit typically underestimated the error bar in $\Delta\nu_c$ (Fig. 5.13).

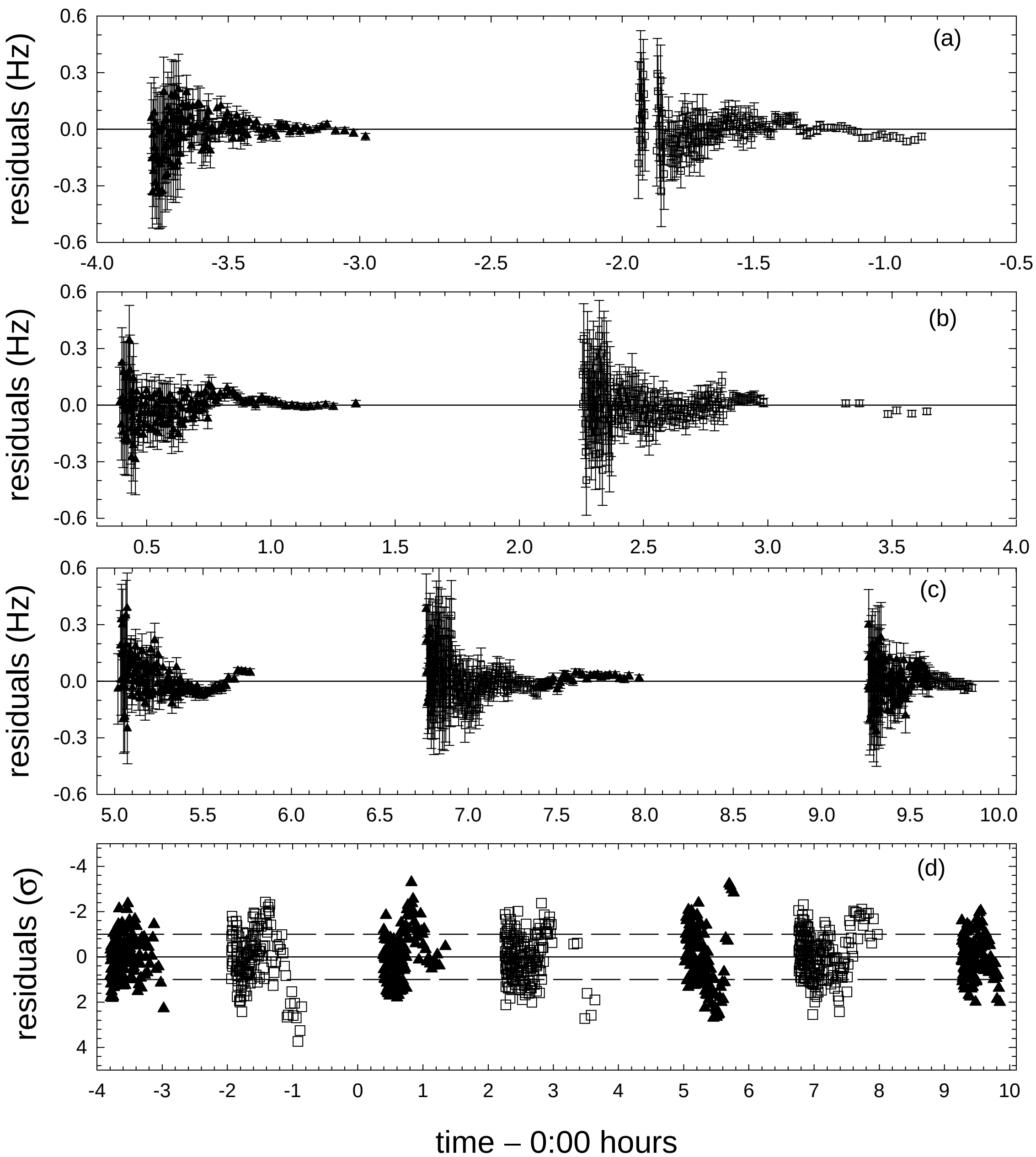

Figure 4.19: The fit residuals of the simultaneous fit show that the most accurate cyclotron measurements deviate from the fit considerably. Midnight is 00:00 hours. Black triangles are the $\bar{p}$ cyclotron measurements, while clear squares are the H^- or proton cyclotron measurements. (a,b,c) The residuals of all the cyclotron measurements in Hertz. (d) The residuals measured in terms of the error bar on each point (σ). They should scatter about the fit within 1 σ. Some of the most important and accurate cyclotron measurements deviate from the fit by more than 3 σ.

Choosing the Polynomial Order to Describe the Magnetic Field

When fitting the data to the simultaneous model, we chose the best order polynomial to fit the data. To make sure the fit result was meaningful, we limited the polynomial order. In 1995, we took cyclotron frequency data during one hour out of every two hours. Only during the last fifteen minutes of that hour did we measure the cyclotron frequency accurately enough to constrain the magnetic field drift. At that time the relativistic shift was within 1 Hz of the endpoint (Fig. 2.25). Because the accurate data was grouped in time, we restricted the polynomial order to prevent the polynomial from making oscillations in the time between measurements of the cyclotron frequency.

Within this limit, we chose the polynomial order that significantly improved the fit. The data was fitted to all orders within this limit and chose the lowest order polynomial that reduced χ^2_ν significantly. Since all the data sets had at least 350 degrees of freedom a 5% change in χ^2_ν was significant. In the 1995 data, the highest possible polynomial order was chosen in six cases. For the day of 1996 data, as well as for two days in 1995, a lower order than the maximum polynomial was sufficient to describe the data. For all data sets, a third or fourth order polynomial was used (Fig. 4.20).

Only low order polynomials accurately fit the data. Simulated cyclotron data with no relativistic shift illustrates this. Fig. 4.21a shows accurate cyclotron data which has the same magnetic field drift and is grouped in time in the same way as the accurate 1995 cyclotron measurements. Fitting this data to a line is accurate, but higher orders are not. The higher order fit depends on the distribution of ν_c points within short time periods and produces an unphysical model of the field. Similarly, two $\bar{p}$ sets and one p set of cyclotron measurements can only be fit to a line

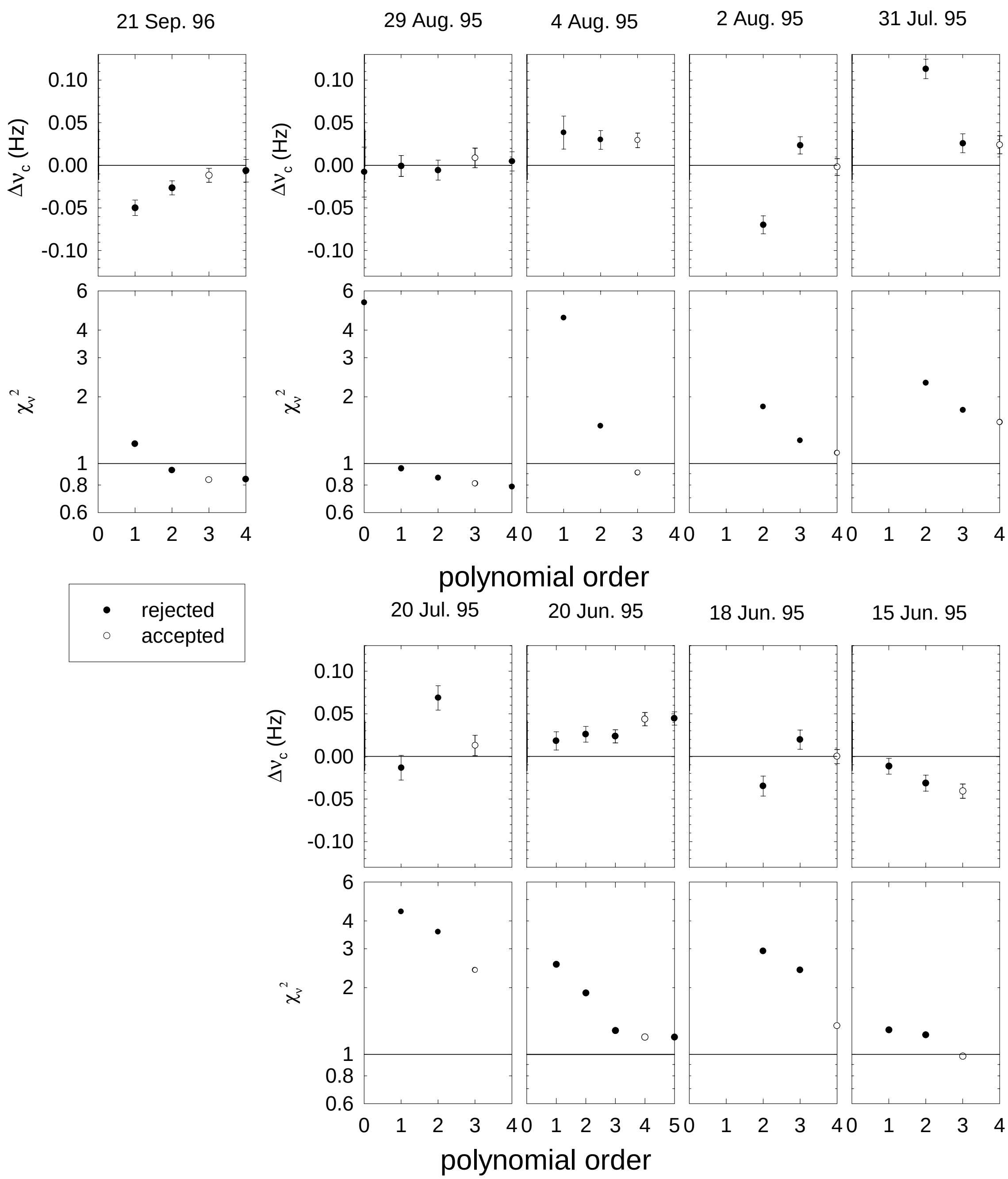

Figure 4.20: The best polynomial order chosen for each data set in the charge-to-mass measurement. The difference frequency ($\Delta\nu_c = \nu_c(p) - \nu_c(\bar{p})$) and χ^2_ν for all the polynomial orders possible is shown. The higher order polynomial was justified when χ^2_ν improved by 5%.

# of separate sets of cyclotron measurements	Maximum polynomial order
3	1
4	2
5	3
6	4
7	5

Table 4.5: The maximum polynomial order used depends on the number of separate sets of cyclotron measurements. Shown here is the maximum polynomial order when no abrupt jump in the magnetic field occurs.

(Fig. 4.21b) and no higher polynomial. When more sets of cyclotron measurements are made, the maximum polynomial order is shown in Table 4.5. This limit restricts the magnetic field model to account only for slow drift that takes place between separate sets of cyclotron measurements. This limit restricts the magnetic field to drift only linearly during a single set of cyclotron measurements.

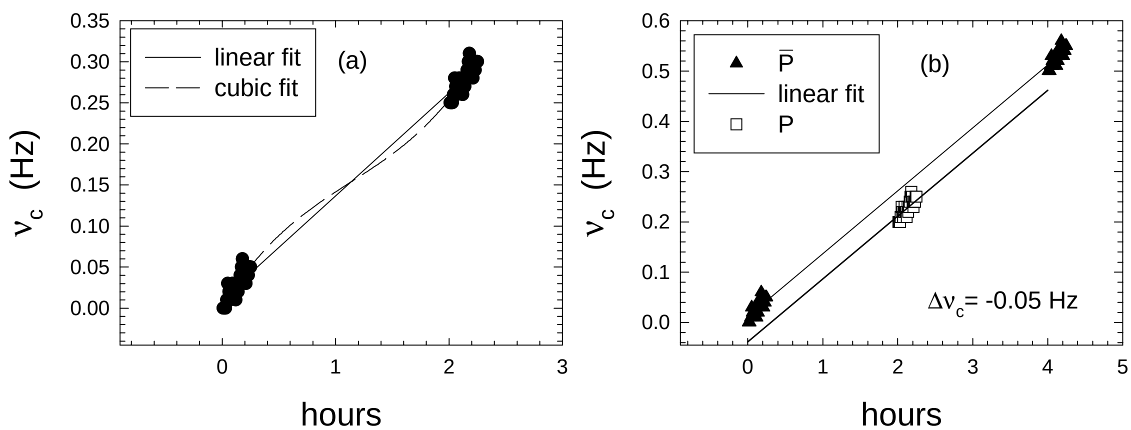

Figure 4.21: Only low order polynomials are accurate. Shown are two simulated data sets which show the real magnetic field drift and time separation of the accurate cyclotron measurements, but show no relativistic shift. (a) Fitting the ν_c data to a line is justified by to a cubic is not. (b) We can fit two $\bar{p}$ measurement sets and one p measurement set to a line.

Chapter 5

$\bar{p}$ to p Charge-to-Mass Ratio Results

Charge-to-mass measurements using the H^- varied in quality over the course of two years from November 1994 to September 1996. During the first six-month period, the procedure used to gather data was developed. We automated the procedure to alternate the antiproton and the H^- measurements; this allowed the data to be taken overnight when the magnetic field drifted less. A procedure was developed to reduce the magnetron orbits of both particles before and during the measurement; this substantially improved the measurement accuracy. Eight good charge-to-mass measurements were performed in the summer of 1995. (Difficulties in keeping the H^- long enough limited the number of measurements made.) The H^- and the antiproton were alternately measured every two hours. In 1996 we improved the apparatus. The detection sensitivity of the most important motion to detect, the cyclotron motion, was doubled, and the trap vacuum restored. We then alternately measured the antiproton and the H^- every hour, minimizing the effect of the magnetic field drift. A measurement made in 1996 was as precise as the measurements made in 1995.

In this chapter, we specify the criteria used to insure the quality of the data. The best data was taken when we alternated between antiproton and H^- measurements quickly when the magnetic field drift was low. Under these circumstances, the simultaneous fit was a good model for the magnetic field drift and accurately predicted the ratio of charge-to-mass ratios.

5.1 The Measurement Data

Since our measurement environment was not completely under control, we used a large number of environment monitors to choose data taken under circumstances which allowed achieving a high precision. Only 9 out of 29 nights were included in the measurement. What constituted an acceptable is discussed below.

The magnetron orbits of both the antiproton and the H^- had to be reduced prior to measuring their cyclotron frequencies. A particle in a large magnetron orbit had a different cyclotron frequency than a particle in a small one (Fig. 2.32) because of a small residual gradients in the magnetic field. Voltage sweeps while magnetron cooling (Table 4.2) within the measurement cycle were critical for keeping the magnetron orbit small. The 8 days of measurement made prior to having these voltage sweeps in the measurement cycle were excluded. Prior to beginning each charge-to-mass measurement, electrons were removed from the trap. We clearly observed that this cycle increased the magnetron orbit of the antiproton and the H^- (Fig. 2.39). Thus the electron cleaning cycle had to be followed by magnetron cooling which included slow voltage sweeps (Sec. 2.5.3) over the resonance voltage of the antiproton and the H^-. In Fig. 5.1 the trapping voltage is swept slowly, the magnetron cooling drive is on and the two axial drives are on just as in Fig. 2.37. The large axial response indicated that each particle had been magnetron cooled

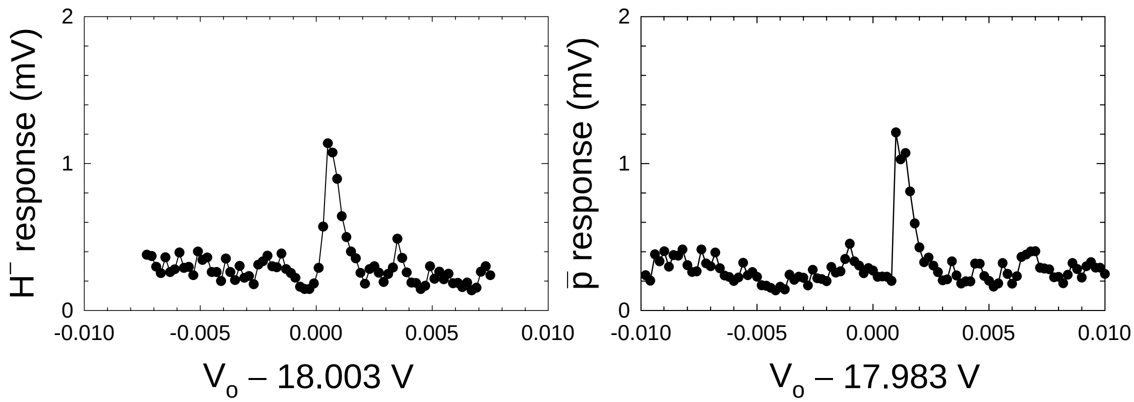

Figure 5.1: Slow voltage sweeps reduce the magnetron prior to measuring the cyclotron frequency. Shown is the axial response for a $\bar{p}$ and an H^- recorded during a slow voltage sweep (Fig. 2.36). The big response indicated that the particles were in a reduced magnetron orbit. Seeing such responses was important prior to accurate cyclotron measurement.

sufficiently. When the sweeps were not performed, the difference frequency ($\Delta\nu_c$) scattered by a large amount (Fig. 2.41) compared with our precision. On 7 of the charge-to-mass measurements, the magnetron orbits of either the H^- or the antiproton were too large prior to measuring. The antiproton or the H^- did not show a large axial signal during a slow voltage sweep as shown in Fig. 5.1. These charge-to-mass measurements were also excluded.

The trap had to be free of contaminant electrons prior to measuring the charge-to-mass ratios. Electrons in the trap caused H^- loss. One charge-to-mass measurement was excluded when we lost the H^- in the middle of it, probably in a collision with electrons. When electrons were present, the modified cyclotron frequency measurements did not fit well to an exponential and χ^2_ν was greater than 2 (Fig. 2.24). Two of the charge-to-mass measurements had some cyclotron measurements with bad fit residuals; these measurements were excluded. When electrons were present, the axial frequency measurement could not be made. In the beginning of another measurement, we first measured an axial signal during a frequency sweep as in Fig. 2.30a, but on all the following frequency sweeps no axial signal was seen. Not being able to measure an axial signal seemed to be the first indication that electrons were present. This measurement was also excluded.

The cyclotron frequency measurements had to be accurate enough to constrain the magnetic field drift accurately. Achieving an accuracy of 1 part in 10^{10} required that we measure cyclotron frequencies with a relativistic shifts less than 1 Hz (Fig. 2.25). We thus excluded measurements which did not meet this criteria (Fig. 5.2a). We also required that a cyclotron decay was measured at least once every two hours (Fig. 5.2b). Both of these criteria led to a magnetic field drift model that was best constrained.

The magnetic field had to be stable. The magnetic field drifted linearly with the magnet temperature (Fig. 4.13) and overnight both the magnet's temperature and the magnetic field were most stable (Fig. 5.2b). One charge-to-mass measurement was eliminated because the cyclotron frequency was not measured enough times successively during the period of low field drift. To keep the magnetic field stable, the pressure over the cryogenic dewars also had to be stable. When the environmental monitors showed that the regulator did not work, in about 2% of the sets of cyclotron measurements, the magnetic field drifted too much (Fig. 4.10). Variations in the ambient magnetic field, detected on external magnetometers, also disturbed the internal magnetic field (Fig. 4.9). These occurred in about 10% of the sets of modified cyclotron measurements, and in these cases the inaccurate measurements were removed.

A few of the 7000 individual modified cyclotron measurements (ν_c') used in the charge-to-mass measurement were inaccurate. As the cyclotron orbit decreased, the signal it induced approached the background noise level. Normally, we reduced

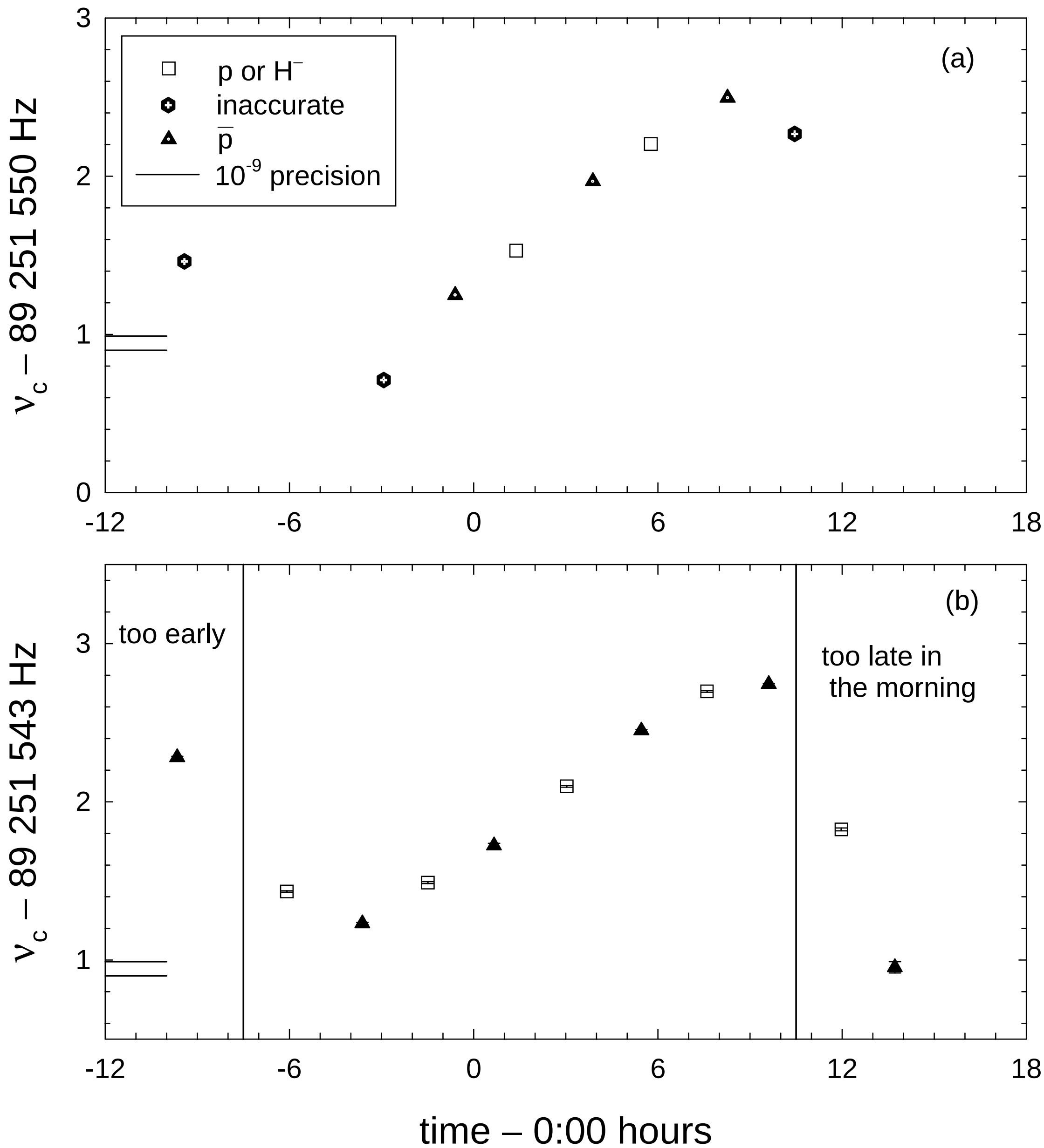

Figure 5.2: Cyclotron frequency measurements used in the first pass fit (page 150). Midnight is 00:00 hours. (a) When the relativistic shift of the most accurate modified cyclotron frequency was larger than 1 Hz, the cyclotron measurement was inaccurate and was not used in the fit. (b) All cyclotron frequencies used in the fit were separated by at most 2 hours. They all took place from the evening up to late in the morning, the time period when the magnetic field was most stable.

the Fourier transform bin width to detect it (Fig. 2.12). Sometimes this happened too late and the signal recorded was a random noise peak (Fig. 5.3a) at a much different frequency. The fit residuals easily identified these errors (Fig. 5.3b). About 20 modified cyclotron measurements like this were excluded from charge-to-mass measurement set. In each case this exclusion improved χ^2_ν and improved the endpoint cyclotron fit ($\nu'_{c\,0}$ of Eq. 2.23). Twice a data acquisition malfunction caused some of the modified cyclotron measurements to be clearly recorded at the wrong time (Fig. 5.3c and 5.3d). Because of this we excluded altogether 12 modified cyclotron measurements. When the cyclotron damping time (τ) was very long, some of the most accurate modified cyclotron measurements were inaccurate (Fig. 5.3e and 5.3f). These measurements had the smallest cyclotron orbits and were the most difficult to measure. In four decay curves a few points were not accurately measured due to a long time constant.

5.2 Determining the Magnetic Field Drift

The magnetic field drifted significantly compared with our precision. For most of our charge-to-mass measurements in 1995, the magnetic field drifted by 20 parts in 10^{10} between successive measurements of the antiproton and the H^- cyclotron frequencies. This drift made the model for the field drift critical for determining the difference frequency ($\Delta\nu_c$) accurately to 1 part in 10^{10} and was the main motivation for the simultaneous fit. When fitting each data set to determine the difference frequency ($\Delta\nu_c$ of Eq. 4.4) two questions should be asked. The first is: how well does the cyclotron data fit the simultaneous model? This is treated in Sec. 5.3. The other question is: based on the size of the magnetic field drift and the accuracy of the cyclotron measurements, how well does the simultaneous fit describe the

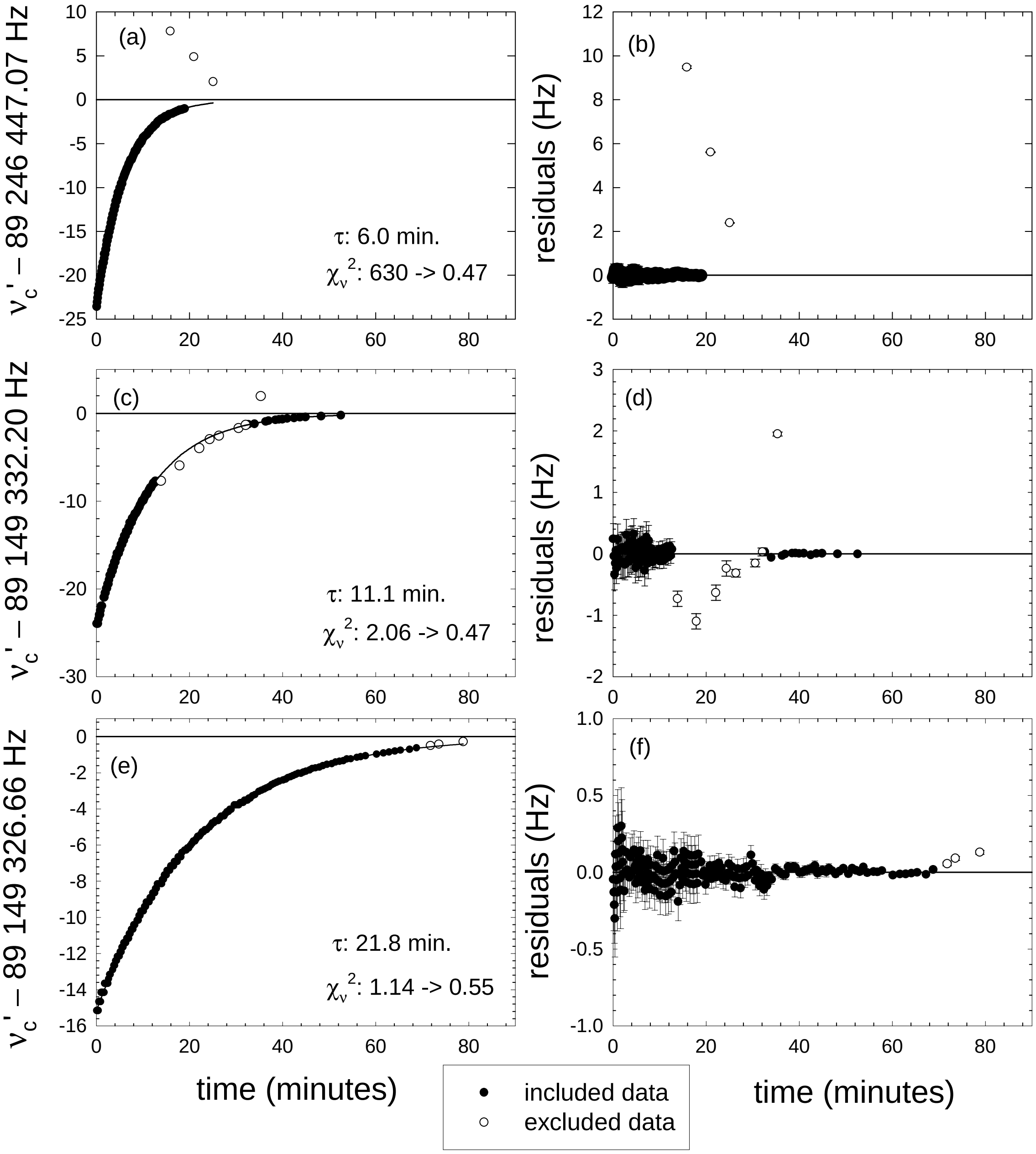

Figure 5.3: Errors in the modified cyclotron frequency. (a) Noise peaks were recorded instead of the modified cyclotron frequency of the particle. (b) The fit residuals show the error. (c,d) Because of a data acquisition error, the wrong time was assigned to some of the cyclotron measurement. (e,f) When the time constant was long, 21 minutes, much longer than in example (a) or (c), the most accurate cyclotron frequencies were poorly measured. The low signal-to-noise ratio caused the error.

magnetic field drift? The magnetic field drift and the difference frequency ($\Delta\nu_c$) is best constrained when the cyclotron damping time (τ) is shortest and the magnetic field drift is lowest.

Fitting the measured cyclotron frequencies under the assumption that the magnetic field is fixed as in Eq. 2.23 illustrates when the cyclotron endpoint frequency is most accurate. The modified cyclotron frequency endpoint (${\nu'_c}_0$ in Eq. 2.23) was determined by extrapolating the fit past the last measurement until the relativistic shift ($\delta\nu'_c$) equaled the fit precision, 0.01 Hz (Fig. 5.4). When the magnetic field was constant over the time required to extrapolate the fit, the modified cyclotron endpoint (${\nu'_c}_0$ in Eq. 2.23) was determined well by the fit (Fig. 2.23). When the magnetic field drifted over this time, the fit underestimated the error. The fit did not know that the magnetic field was drifting and still reported the same error bar, 0.01 Hz. When the magnetic field drift was large, the magnetic field drift during the extrapolation time provided a good estimate of the real modified cyclotron error bar. In 1995, the magnetic field drifted during the extrapolation time by 10 times the fit error bar (Fig. 5.4). This large drift makes the endpoint prediction only accurate to 0.1 Hz, not 0.01 Hz as estimated by the fit. A lower magnetic field drift reduced this error. A shorter time constant (τ) reduced the time required to extrapolate the fit, thus reducing this error.

Describing the drifting magnetic field with a low order polynomial leads to a more accurate magnetic field drift prediction. The low order polynomials used in the simultaneous fit corresponds to a linear field drift during a single cyclotron decay measurement. This linear approximation is a much better than fixing the magnetic field to be constant, but this approximation still has a limit. When the magnetic field drifts during the extrapolation as much as in Fig. 5.4, the simultaneous fit must predict the size of the cyclotron drift correctly to 10% to achieve 0.01 Hz accuracy.

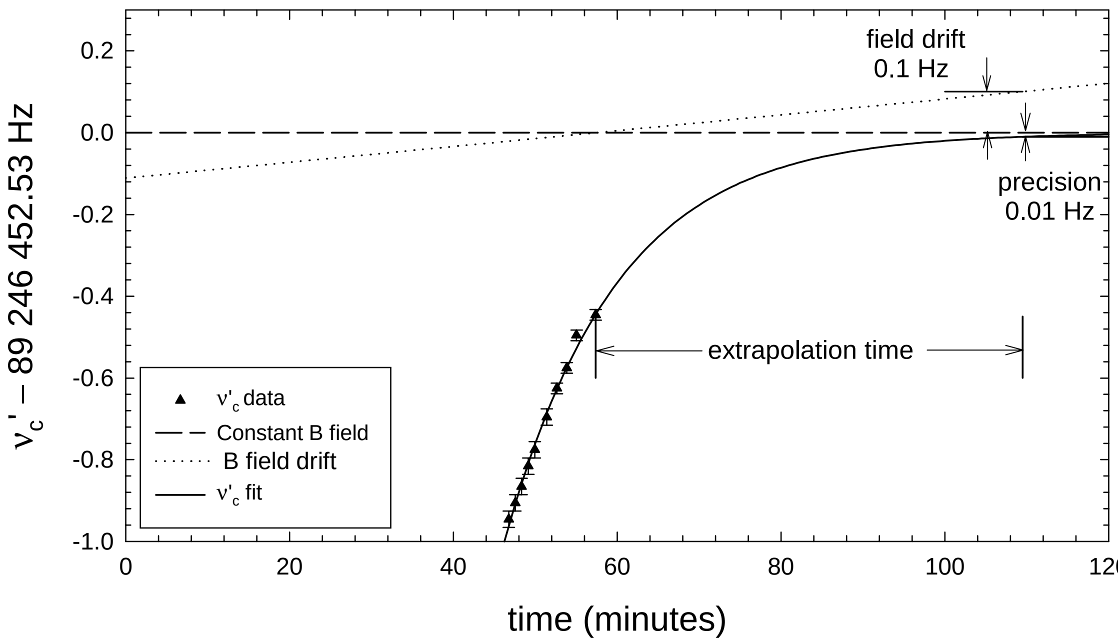

Figure 5.4: The magnetic field drifts, by about 10 times the fit error bar, during the time required to extrapolate the fit to 0.01 Hz. When the magnetic field is held constant, the endpoint is only accurate to 0.1 Hz. When the magnetic field is allowed to drift, the simultaneous fit must predict the size of the magnetic field drift accurately to 10% to measure the cyclotron frequency accurately to 0.01 Hz.

When the magnetic field drifts less during the extrapolation, the simultaneous fit is a much more accurate description.

The 1996 charge-to-mass measurement (Fig. 5.5b) determined the cyclotron frequency drift much more precisely than a typical measurement made in 1995 (Fig. 5.5a). In 1995, the cyclotron frequency drifted by about 0.17 Hz/hour, and the cyclotron damping time (τ) was about 0.27 hours. The long time constant slowed down the measurement; we alternated between H^- and antiproton measurements every two hours. Because of the long time constant, the most accurate cyclotron frequencies had large relativistic shifts, 0.3 Hz on average (Fig. 5.5a). The relativistic shift ($\delta\nu_c$) of each cyclotron measurement is the difference between the measured cyclotron frequency (ν_c) and the fitted background cyclotron drift (exponential term in Eq. 4.7 and Eq. 4.8). In comparison to this measurement, the 1996 charge-to-mass measurement (Fig. 5.5b) had a 4 times lower magnetic field drift and a damping time (τ) less than half as long. The short time constant allowed us to alternate between H^- and antiproton measurements twice as frequently, about every hour. The short time constant also increased the cyclotron signal-to-noise ratio. It allowed more measurements to be made in smaller cyclotron orbits where the relativistic shifts were smaller. The combination of these improvements led to a much better magnetic field drift prediction.

The size of the magnetic field drift during the extrapolation time indicated how well the cyclotron frequency drift was determined. Reducing the time constant, making more cyclotron measurements with small relativistic shifts, and a lower magnetic field drift all contributed to reducing the magnetic field drift during the extrapolation. For each charge-to-mass measurement, we determined the magnetic field drift during the extrapolation for one of the middle cyclotron measurements. We chose one which had a typical cyclotron frequency drift. In the examples in Fig. 5.5a and Fig. 5.5b we chose the antiproton cyclotron measurements at 03:30 hours. In the 1995 measurement of Fig. 5.5a, the magnetic field drifted by 0.16 Hz during the 1 hour extrapolation time (Fig. 5.6a). This drift is large compared to our precision, 0.01 Hz. In order for the cyclotron frequency to be accurate to 0.01 Hz, the simultaneous fit must describe size of this magnetic field drift accurately to 6%. If the simultaneous prediction is in error by more than this, the real cyclotron error bar will be larger than the error bar reported by the fit. In 1995, the fit underestimated the error bar probably for this reason. In 1996, the magnetic field drifted during the 15 minute extrapolation time by only 0.01 Hz (Fig. 5.6b). Even if the size of the magnetic field drift was in error by 50%, the predicted cyclotron drift would

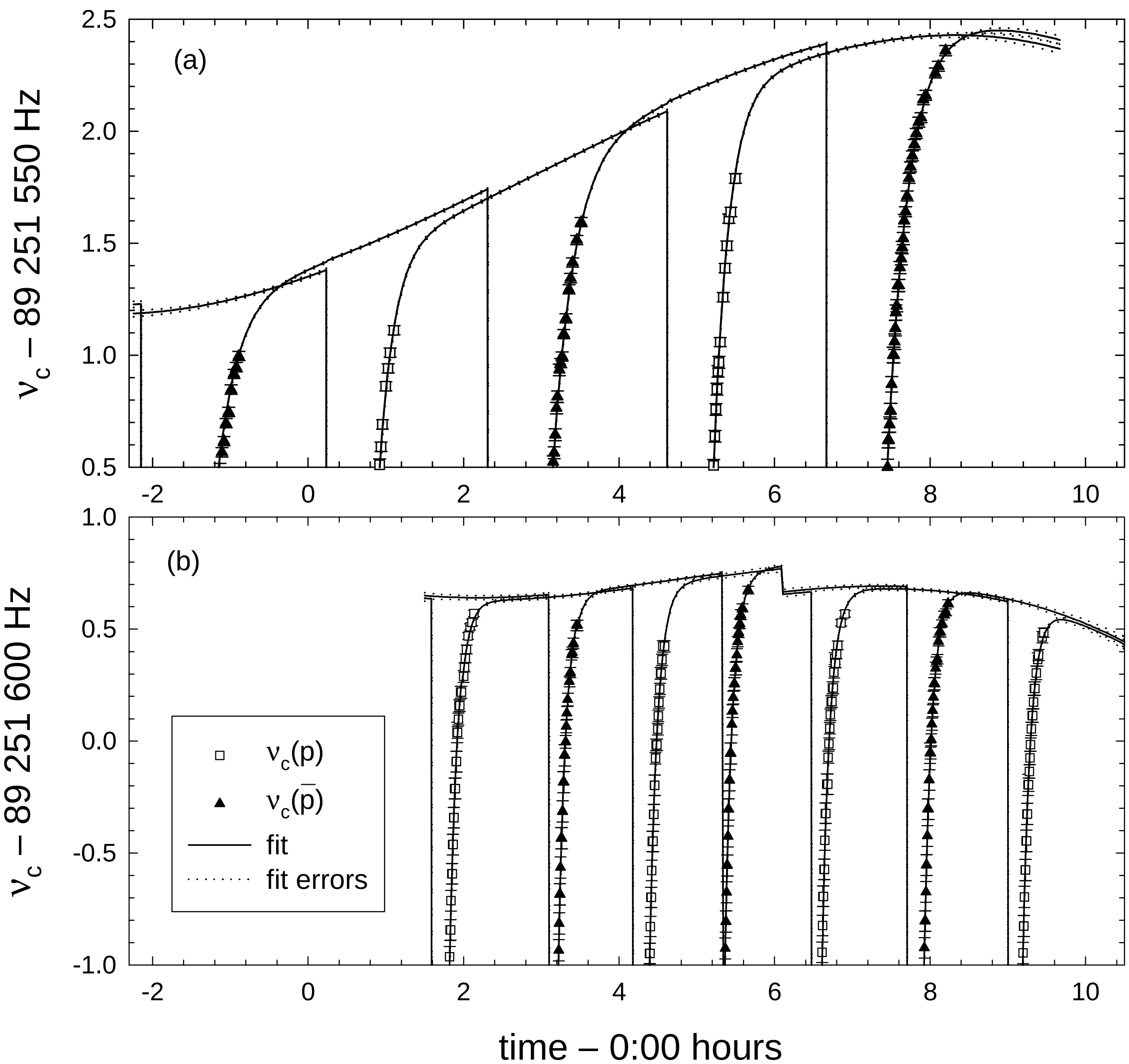

Figure 5.5: The 1996 charge-to-mass measurement best determined the cyclotron frequency (ν_c) drift. Midnight is 00:00 hours. (a) The simultaneous fit of the first charge-to-mass measurement made on 15 June 1995. The cyclotron frequency drift was typically 0.17 Hz/hour. The time between cyclotron measurements was 2 hours, and the most accurate cyclotron measurements had a relativistic shift ($\delta\nu_c$) of 0.3 Hz. (b) The charge-to-mass measurement of 21 September 1996. The cyclotron frequency drift was 4 times lower, and the cyclotron damping time (τ) was half as long. Because of the reduced τ, the time between measurements was 1 hour, and the most accurate cyclotron measurements had a 3 times smaller relativistic shift ($\delta\nu_c = 0.1$ Hz). Because of the reduced τ, many more accurate cyclotron measurements with relativistic shifts ($\delta\nu_c$) less than 1 Hz were made.

No.	date	last point $\delta\nu_c$	τ	extrapo-lation time	field drift during the extrapolation
	d/m/y	(Hz)	(hrs)	(hrs)	(Hz)
1	21/9/96	-0.10	0.10	0.25	0.01
2	29/8/95	-0.20	0.36	1.06	0.04
3	31/7/95	-0.25	0.18	0.57	0.07
4	20/7/95	-0.50	0.22	0.85	0.08
5	18/6/95	-0.45	0.23	0.87	0.10
6	20/6/95	-0.32	0.21	0.72	0.10
7	15/6/95	-0.40	0.27	0.97	0.16
8	4/8/95	-0.32	0.23	0.80	0.17
9	2/8/95	-0.36	0.26	0.92	0.19

Table 5.1: The field drift during the extrapolation to 0.01 Hz. For each day of measurement the relativistic shift ($\delta\nu_c$) of the closest cyclotron measurement, the cyclotron damping time (τ), the time required to extrapolate to 0.01 Hz, and the field drift during the extrapolation are shown.

still be accurate to 0.01 Hz. When the magnetic field drift during the extrapolation was small, as in this case, the simultaneous fit more accurately predicted the cyclotron frequency drift. All the charge-to-mass measurements were ranked by their magnetic field drift during the extrapolation time (Table 5.1).

5.3 The Charge-to-Mass Measurements

When the magnetic field drifted least during the extrapolation time, the cyclotron frequencies fit best to the simultaneous model.

5.3.1 The 1996 Charge-to-Mass Measurement

First, the major improvements over the 1995 measurements and the modified cyclotron and axial frequencies used in the measurement are discussed. Following this,

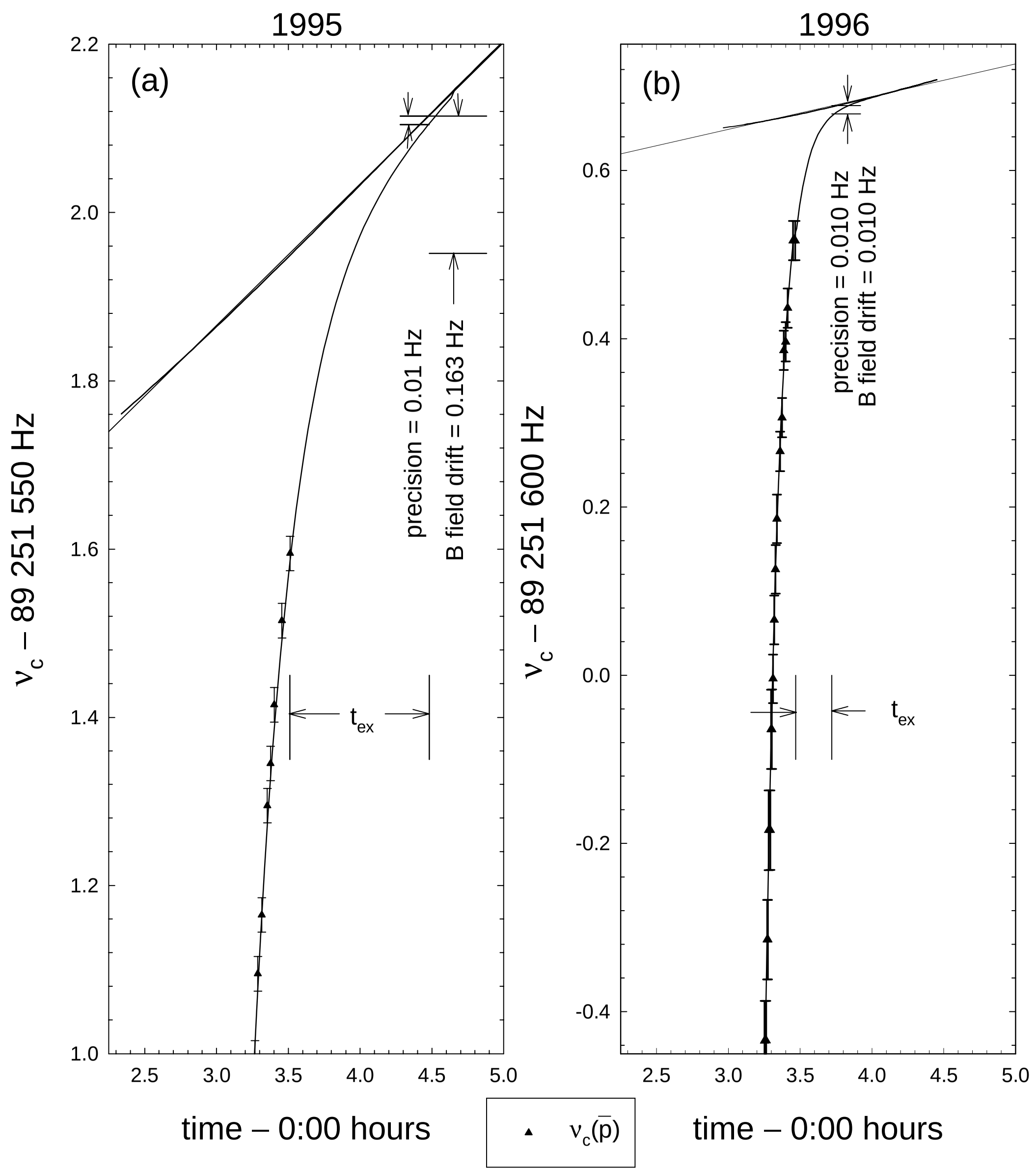

Figure 5.6: In 1996, the magnetic field drifted much less during the extrapolation time than in 1995. Midnight is 00:00 hours. (a) A section of the simultaneous fit for 15 June 1995. The extrapolation time ($t_{ex} = 1$ hour) is the time required for the fit to reach a relativistic shift ($\delta\nu_c$) of 0.01 Hz. During the extrapolation time, the magnetic field drifted by 0.16 Hz, a large amount compared with the fit precision, 0.01 Hz. (b) A section of the simultaneous fit to 21 September 1996. The extrapolation time ($t_{ex} = 0.25$ hours) was shorter because the damping time was shorter and because more accurate measurements were made with smaller relativistic shifts ($\delta\nu_c$). During the extrapolation time, the magnetic field drifted by 0.01 Hz.

the fit used and the measurement errors are discussed.

Major Improvements Made in 1996

The main improvement made in 1996 was reducing the cyclotron damping time (τ); this led to a better determined magnetic field drift.

The measurement took place in a cleaner trap environment than in 1995, as a result of restoring the trap vacuum and more efficiently removing electrons. The vacuum leak found in 1995 was fixed giving us a vacuum probably as low as 5×10^{-17} Torr as determined by earlier measurements [2, 35]. We added the ability to test when electrons were still trapped (Fig. 3.16). This helped diagnose what was effective in removing them and led to a more efficient procedure. Electron magnetron cooling signals were resonant with any trapped electrons for a far longer time; this made electron removal much more efficient (Sec. 3.2.4). Prior to beginning the 1996 measurement, we cycled the electron cleaning routine three times and tested for trapped electrons. None were seen. Even after the measurement, we still saw no indication that electrons were trapped.

The procedure used to reduce the magnetron orbits of both particles was improved over 1995 and caused no systematic shifts at our precision. After the last electron removal cycle, several slow voltage sweeps were performed over the trapping voltage of the H^- and the antiproton. These sweeps were necessary after removing electrons (Fig. 2.39). Many more sweeps were performed in 1996 than we used in 1995, thus they were much more likely to reduce the magnetron orbits of the antiproton and the H^-. When repeated often enough, the sweeps reduced the magnetron orbits to the magnetron cooling limit, enough to cause no systematic effect at our precision (Fig. 2.37). A greater fraction of the measurement cycle was spent reducing the magnetron orbit of both particles (Table 4.2); thus the measurement cycle better kept the magnetron orbits of both particles small. For these reasons we expected even less systematic effect due to magnetron cooling in the 1996 measurement. After the 1995 measurements are presented we will return to this point (Sec. 5.3.3).

The Modified Cyclotron and Axial Measurements

The reduced cyclotron damping time (τ) led to more accurate modified cyclotron (Eq. 2.23) measurements in 1996 than in 1995. The reduced damping time (τ) improved the signal-to-noise ratio, allowing us to measure cyclotron frequencies in smaller orbits. We were able to measure the cyclotron frequency when the size of the relativistic shift ($\delta\nu_c'$) was about 0.1 Hz, three times smaller than we could measure in 1995. Due to an increased signal-to-noise ratio, many more accurate cyclotron measurements were made, measurements with a relativistic shift of less than 1 Hz (Fig. 5.6 and Table 5.3); these measurements best determined the magnetic field drift. The accurate cyclotron measurements also had less scatter about the fit than in 1995 (Fig. 2.19); for this reason they were assigned smaller error bars (Fig. 2.20).

Nearly all the cyclotron measurements taken were used in the charge-to-mass measurement. The pressure over the magnet helium dewar stopped regulating late in the morning; this forced us to exclude the last set of cyclotron measurements (Fig. 4.10). Of the remaining 7 sets, we included all but three individual cyclotron points. Two points excluded were single frequency errors (as in Fig. 5.3a), and one was due to a disturbance in the ambient magnetic field (Fig. 4.9).

The axial frequencies for both particles were measured precisely and regularly throughout the night (Fig. 5.7). The axial frequency of the H^- was measured both when the endcap oscillatory signal swept upward and downward (Fig. 5.7a through 5.7d); this measured it accurately to 1 Hz. Since the H^- axial frequency was stable to 1 Hz, the electric field in the trap was stable and thus the $\bar{p}$ axial frequency was also stable to 1 Hz. The axial frequency of the antiproton was measured consistently when the oscillatory signal was swept upward, but not when it was swept downward (Fig. 5.7e through 5.7h). For this reason the antiproton axial error bars were increased. Sometimes axial driven signals were seen in only one direction when the oscillatory applied signal used was too strong. When the signal power was turned down and no other changes made, an accurate antiproton axial response was seen sweeping both upward and downward (Fig. 5.7i). This measurement, together with the stable electric field in the trap, verified that the initial antiproton axial measurements were accurate. The low electric field drift seen here was typical of other the axial measurements (Fig. 2.31). The axial frequency errors were added to the modified cyclotron frequency errors to determine the cyclotron frequency errors using Eq. 4.9 and Eq. 4.10.

The 1996 Fit with a Magnetic Field Step

The **E** field used to keep the outer particle in a large cyclotron orbit was slightly too strong, causing small changes in the cyclotron orbit of the measured particle (Fig. 4.5 and Table 4.3). To account for this, we allowed the initial relativistic shift parameter (A_i in Eq. 4.6) of the simultaneous fit to have a different value each time the nonresonant **E** field turned on. This improved the fit quality without changing the difference frequency ($\Delta\nu_c$).

A step in the magnetic field occurred at 06:00 hours between cyclotron measurements. Steps occurred every 12 hours on average (Sec. 4.3.3), and in this 9 hour period one was seen. The magnetic field shifted downward by a comparable amount to the other steps seen in Fig. 4.11 and Fig. 4.12. Since there is disagreement about the appropriateness of the step within the TRAP collaboration, I carefully present

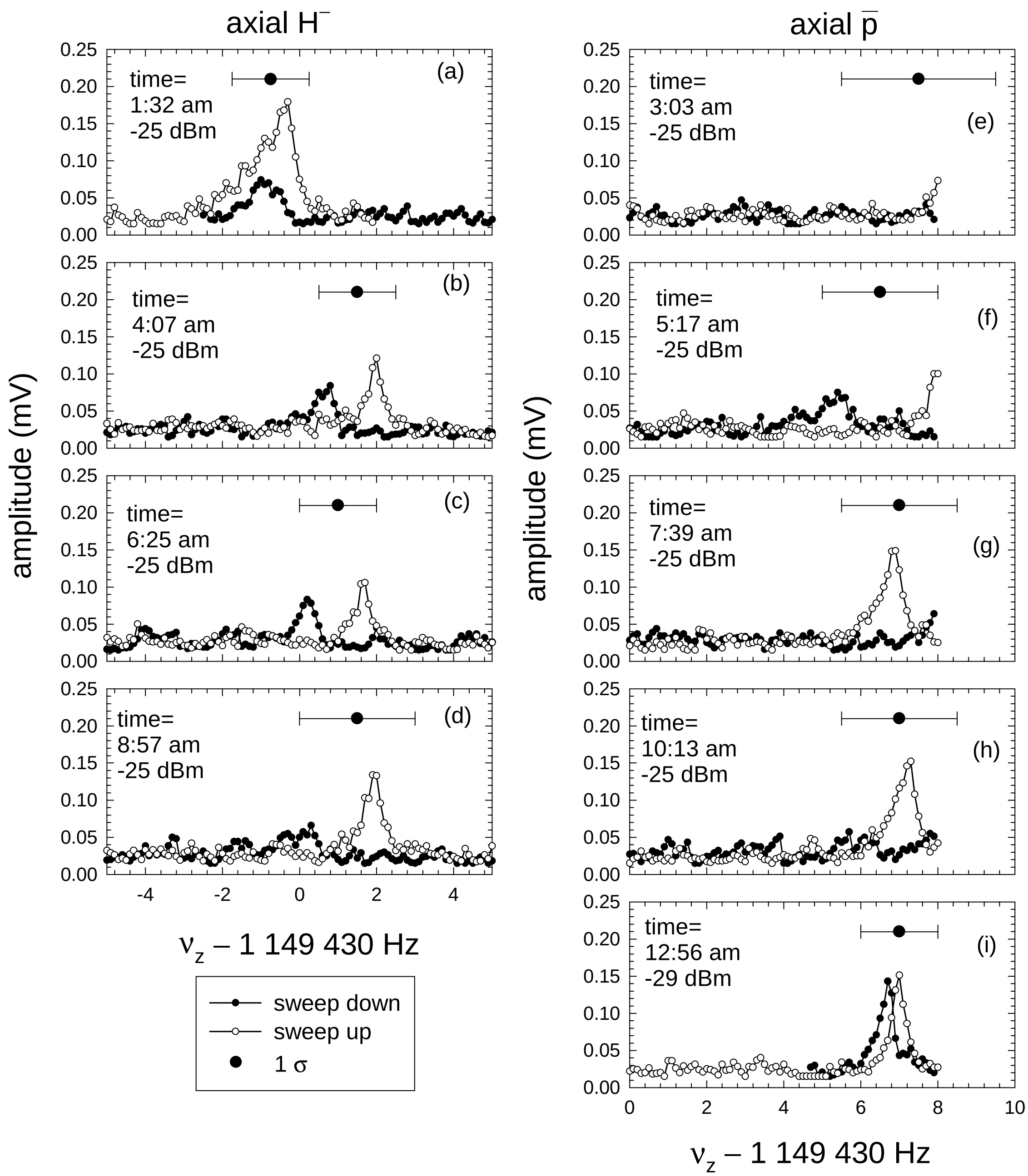

Figure 5.7: The 1996 axial measurements. (a,b,c,d) The axial frequency response for the H$^-$, as the oscillatory endcap signal is swept upward and downward. The power of the oscillatory signal is also shown. (e,f,g,h,i) The axial frequency response of the antiproton. Since the frequency was not consistently measured while sweeping the oscillatory signal in both directions, the axial error bar was increased. In (i) we reduced the oscillatory signal power.

the evidence for the step in the magnetic field.

The fit to the cyclotron frequencies (Fig. 5.8a) shows the step. A combination of the modified cyclotron endpoints (ν'_{c0} in Eq. 2.23) and the axial measurements determined the cyclotron endpoint frequencies (as in Fig. 4.16a). The modified cyclotron fit using Eq. 2.23 assumes that the magnetic field drift is constant over each set of modified cyclotron measurements; in this case the assumption is justified. During the fit extrapolation, the magnetic field only drifts by 0.01 Hz (Fig. 5.6b), making the resulting cyclotron measurements accurate to 0.01 Hz. When the cyclotron measurements are fit to a cubic with no step, the measurements around 06:00 hours deviate from the fit by many times their error bars (Fig. 5.8a). This is a poor model for the magnetic field drift ($\chi^2_\nu = 15$) and is inconsistent with the well estimated cyclotron frequency errors. When the magnetic field drift is allowed to step at 06:00 hours, all the cyclotron measurements fit well to the cubic field drift and χ^2_ν improves considerably ($\chi^2_\nu = 0.64$). The step measured in this way is large and significantly different from zero.

In a different way, the magnetic field drift in time (Fig. 5.8b) also shows the step. The local slope of the magnetic field drift is measured by taking the difference between successive cyclotron measurements and dividing by the time between measurements. If the magnetic field drifts smoothly as a low order polynomial, a cubic for example, then the slope should drift as a lower order polynomial, a quadratic. The measured slope of the drift shows a smooth behavior except at 06:00 hours, the time of the step. Instead of the slope being positive in line with the neighboring slope measurements, the slope is negative, much lower than expected. The measured slope shows that the magnetic field drift cannot be modeled as a low order polynomial because any low order polynomial proposes a slowly changing slope. The simplest way to model the measured cyclotron frequencies is with a quick change in

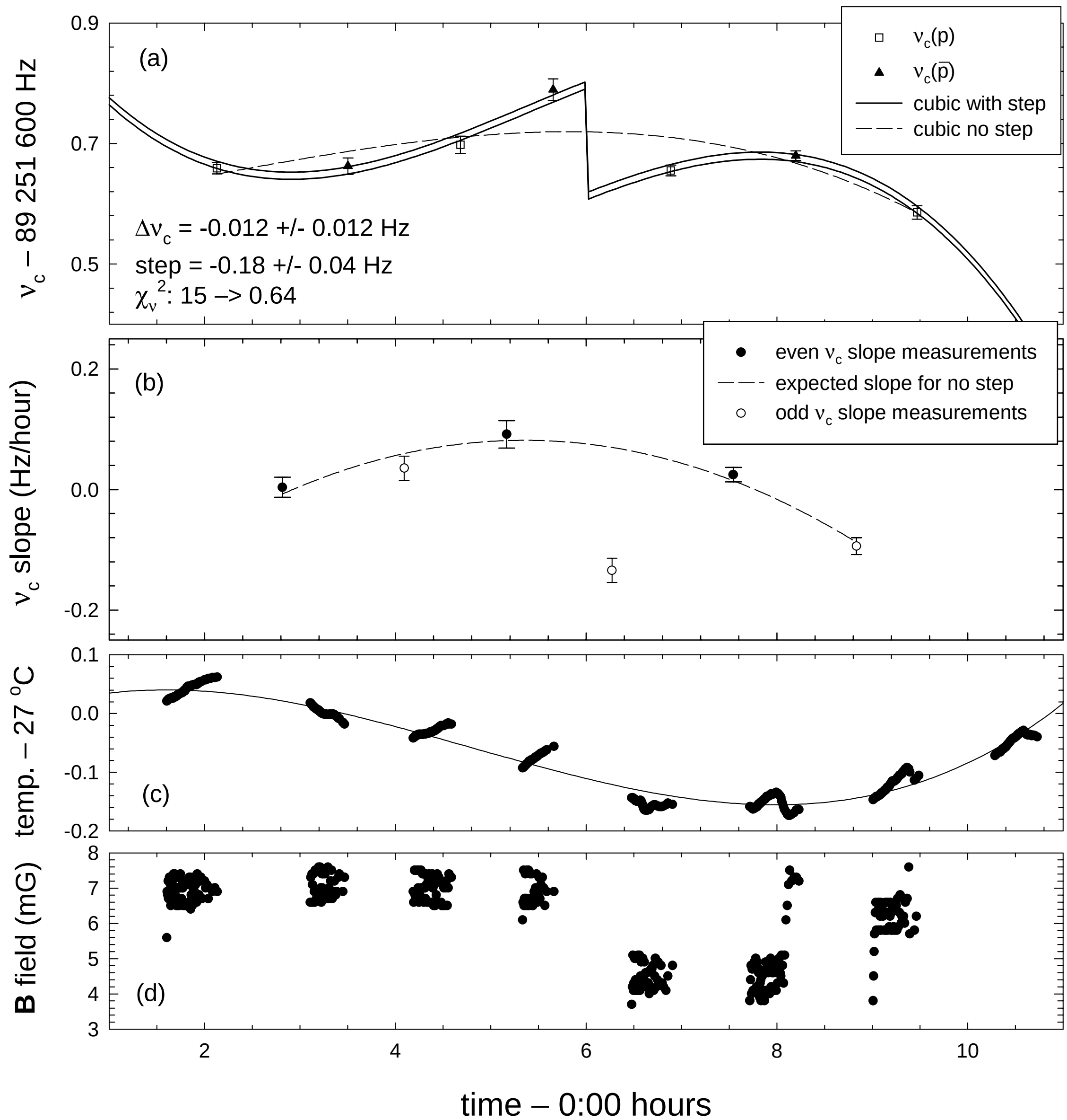

Figure 5.8: A step in the magnetic field took place during the 1996 charge-to-mass measurement. (a) The cyclotron measurements around 06:00 hours do not fit to a smooth cubic polynomial. By allowing the magnetic field to step, the fit improves (χ^2_ν : 15 $\rightarrow$ 0.64). $\Delta\nu_c = \nu_c(p) - \nu_c(\bar{p})$. (b) The slope of the magnetic field drift changes abruptly at 06:00 hours. The slope is measured by taking the difference between adjacent cyclotron measurements and dividing by the time between them. (c) The ambient temperature drift. Both the temperature and the cyclotron frequencies drift fit best to cubic polynomials which have the same turning points. (d) The magnetic field shows a small change at 06:00 hours.

the magnetic field drift at this time.

The cyclotron measurements when assuming that the magnetic field is drifting smoothly are inconsistent with a fixed difference frequency. If the charge-to-mass ratios of the proton and antiproton were different the difference frequency should still be constant. The slope measurements give an experimental way for subtracting out the effect of a smooth magnetic field drift and seeing the difference frequency. If the magnetic field drifts smoothly and there is a constant difference frequency then all the even slope measurements which determine $-(\nu_c(p) - \nu_c(\bar{p}))$ would all be too high by the same amount while odd slope measurements which determine $\nu_c(p) - \nu_c(\bar{p})$ would all be too low (Fig. 5.8b). They are measured with respect to the expected slope for no step. The odd slope measurement at the time of the step (06:00 hours) is inconsistent with the other odd slope measurements. Just as in Fig. 5.8a the measured slope at 06:00 hours is inconsistent with a model for a slowly varying magnetic field drift with a constant difference frequency.

When the magnetic field step is included, the slow magnetic field drift agrees with expectations based on the temperature drift (Fig. 5.8c). We showed that the magnetic field drifts linearly with the magnet temperature (Fig. 4.13 and Fig. 4.14), and this measurement reflects the same trend. The ambient temperature is a measure of the magnet temperature but it drifts about half as much since it is measured underneath the magnet floor (Fig. 4.7). Both the slow drift in the magnetic field (Fig. 5.8a) and the temperature (Fig. 5.8c) fit best to cubic polynomials, and both polynomials have the same turning points: one at 02:00 hours and another at 08:00 hours. The temperature in this example drifts down when the magnetic field drifts up as in Fig. 4.13 and Fig. 4.14. Also the size of the magnetic field drift is as small as expected from the low ambient temperature drift. The stable temperature is one of the main reasons why this charge-to-mass measurement determines the magnetic field drift so well compared to the 1995 measurements. The agreement between the temperature drift and the slow magnetic field drift is good evidence that the magnetic field drift with a step is an accurate description.

It is unlikely that the small change in the ambient magnetic field that occurred at the time of the magnetic field step (Fig. 5.8d) could explain the step seen. As with the other examples (Fig. 4.11 and Fig. 4.12), a small ambient change is seen at the time of the step, but it is too small to cause the step. To cause the step in the magnetic field as seen in Fig. 5.8a, the ambient magnetic field should change by at least 5 times the amount seen in Fig. 5.8d and, furthermore, the ambient magnetic field should increase, not decrease. (Compare this example with Fig. 4.9a and 4.9b.) For the ambient magnetic field change to explain the step instead of a screening factor of -150 as in Fig. 4.9 we would need a screening factor of 25. Screening factors this low were seen only when antiprotons were delivered to our experiment and when the nearest bending magnet to our 6 T magnet turned on. With no people around the experiment, and no antiprotons delivered to us at 06:00 hours, there is no reason to suspect that this bending magnet was turned on. Small changes in the ambient magnetic field also occurred later in the measurement without causing any step in the magnetic field larger than 0.01 Hz. Overnight in every measurement we detected small changes of order 5 mG on our magnetometer as different accelerator magnets turned on and off.

Including the step in the fit at 06:00 hours is equivalent to excluding the frequency difference between the fourth and fifth cyclotron frequencies from the charge-to-mass measurement. This frequency difference is due to a magnetic field step and not to a difference between the charge-to-mass ratios of the proton and antiproton. Including a step would leave the other five pairs of cyclotron measurements to determine the difference between the charge-to-mass ratios of the proton and the antiproton.

The 1996 Ratio of Charge-to-Mass Ratios

The cyclotron measurements fit well to the simultaneous model. The most accurate cyclotron measurements and the simultaneous fit are shown in Fig. 5.9. All the fit residuals scatter about zero within their error bars ($\chi^2_\nu = 0.85$) and are distributed in time in a random fashion (Fig. 5.10). The cyclotron measurements with small relativistic shifts, the most important for determining the magnetic field drift, also fit well. In contrast, when the magnetic field drift was high as in the 1995 measurements, these accurate residuals deviated considerably from the fit (Fig. 5.13). The third order polynomial used for the slow magnetic field drift was well chosen. The cyclotron measurements required at least a third order polynomial since the temperature drifts as a third order polynomial (Fig. 5.8d) and the measured cyclotron gradient (Fig. 5.8b) drifts at least as a quadratic. We varied the order of the simultaneous fit up to the fourth order and found that the third order produced the best χ^2_ν (Fig. 4.20). When we increased the order to the fourth order both χ^2_ν and the difference frequency remained the same as for the third order. Since the fourth order polynomial did not improve the fit, the third order polynomial was well chosen. Polynomials up to the fourth order restrict the slow magnetic field drift to account only for drifts between sets of cyclotron measurements and not for drifts within any one set. The normally distributed fit residuals and the well chosen polynomial order indicate that the magnetic field drift is well modeled.

The simultaneous fit predicted the magnetic field drift accurately to 0.01 Hz. The magnetic field drifted only by 0.01 Hz during the time required to extrapolate the fit (Fig. 5.6b). Because of this low drift, even if the simultaneous fit predicted the slope of the field drift correctly only to 50%, the magnetic field drift would still be accurate

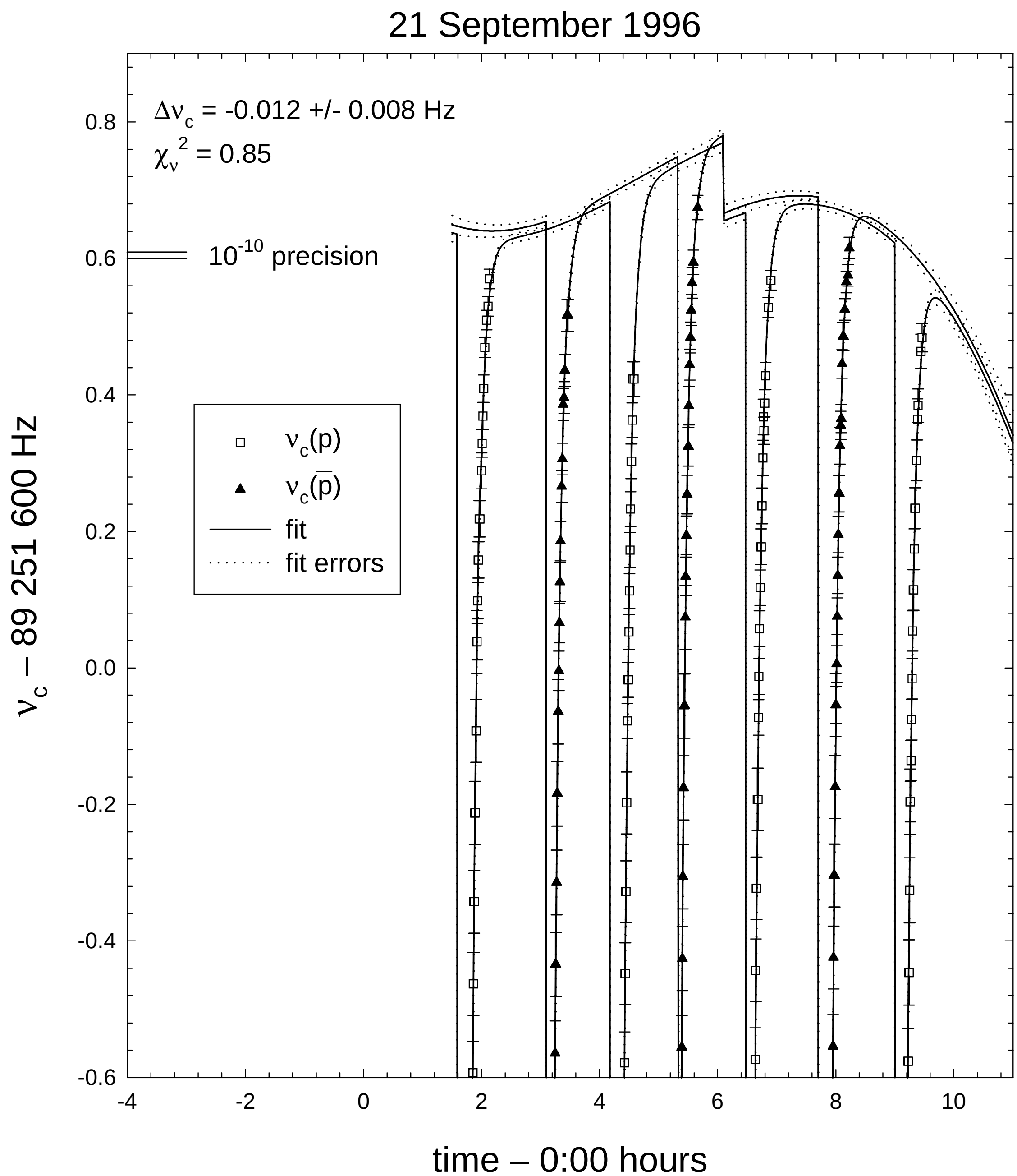

Figure 5.9: Simultaneous fit to the best charge-to-mass measurement, the one made on 21 September 1996. Midnight is 00:00 hours. $\Delta\nu_c = \nu_c(p) - \nu_c(\bar{p})$. An internal magnetic field step took place at 06:00 hours. This was the best measurement mainly because the magnetic field drifted least and the cyclotron damping time was shortest. This one night measured the difference frequency ($\Delta\nu_c$) accurately to 1 part in 10^{10}.

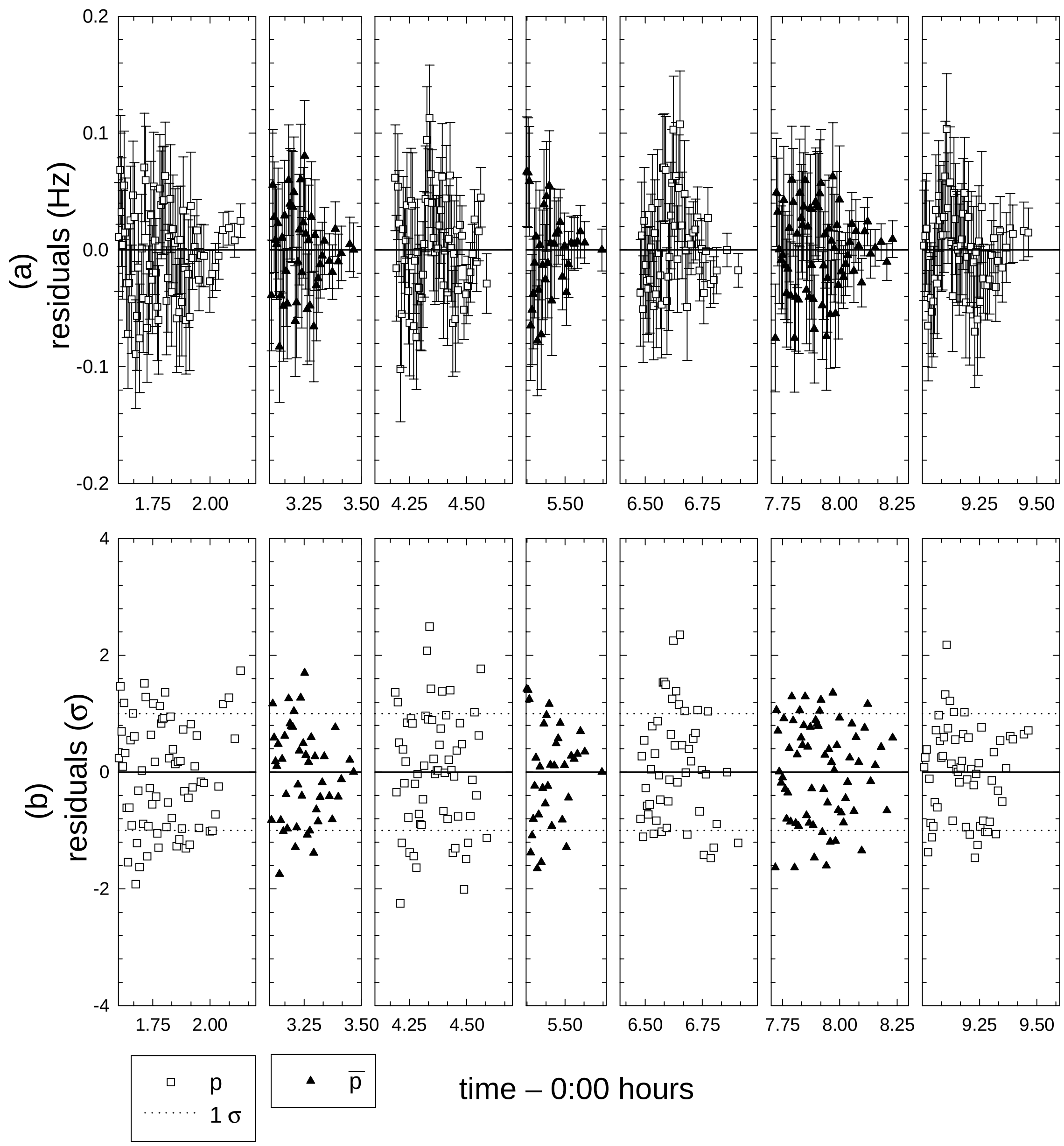

Figure 5.10: The cyclotron fit residuals for the best day of data, 21 September 1996, show that the simultaneous fit is very good. Midnight is 00:00 hours. (a) All the fit residuals, especially the most accurate ones at the end of each set of cyclotron measurements, scatter about zero within their error bars. (b) The fit residuals divided by the error bar per cyclotron measurement (σ). The residuals mostly fall between ± 1 σ of zero as they should, and they are also distributed in time in a random way.

to 0.01 Hz. The magnetic field drift is so low that the first pass prediction (Fig. 5.8a) of both the cyclotron frequencies and the difference frequency ($\Delta\nu_c$ of Eq. 4.4) agrees with the predictions of the simultaneous fit (Fig. 5.9). This shows that the cyclotron frequencies do not change even when assuming a constant magnetic field drift over each set of modified cyclotron frequencies. Thus, we expect the simultaneous fit to describe the cyclotron frequencies and the difference frequency ($\Delta\nu_c$) accurately. No additional error was added to the description of the simultaneous fit due to the drifting magnetic field. In contrast to this, we added an error to the description of the simultaneous fit for the 1995 measurements since the cyclotron measurements did not determine the magnetic field drift well enough (Fig. 5.14). After the errors in the 1995 measurements are presented, this point will be further discussed.

An additional error due to the proximity of the second particle was not larger than 0.004 Hz. When the nonresonant **E** field increased the cyclotron orbit of the outer particle, a shift was seen in the cyclotron frequency of the inner particle. While the cyclotron shifts were mostly due to the nonresonant **E** field itself, we could not rule out a possible shift of 0.007 Hz due to the outer particle being kept in a 0.76 mm (page 132). When the outer particle was close, it always shifted the cyclotron frequency of the inner particle in the same direction, upward. Since this shift was always in the same direction and since an identical measurement procedure was followed for the H^- and the $\bar{p}$, both the $\nu_c(\mathrm{H}^-)$ and $\nu_c(\bar{p})$ should shift in the same direction. The difference frequency ($\Delta\nu_c$) is not affected by the proximity of the outer particle to first order. As a conservative estimate, we added 0.004 Hz to the error bar.

The 1996 charge-to-mass measurement, based on the simultaneous fit with one step in the magnetic field, is:

$$\left|\frac{e/m(\bar{p})}{e/m(p)}\right| - 1 = (1.3 \pm 1.0) \times 10^{-10}. \tag{5.1}$$

The larger field drift during the extrapolation found in the 1995 charge-to-mass measurements will be compared with that found in 1996.

5.3.2 The 1995 Charge-to-Mass Measurements

In 1995, the magnetic field drift was not as well determined as for the 1996 measurement. During the fit extrapolation the magnetic field drifted by about 0.10 Hz, about 10 times the field drift seen in 1996 and about 10 times our desired accuracy of 0.01 Hz (Table 5.1). When the magnetic field drifts this much, the simultaneous fit needs to predict the local slope of the magnetic field drift accurately to 10% in order to predict the difference frequency ($\Delta\nu_c$) accurately to 0.01 Hz. Also the large magnetic field drift made identifying sudden steps in the magnetic field drift such as the one discussed for the 1996 charge-to-mass measurement much more difficult. In between sets of cyclotron measurements, the magnetic field drifted by 2 to 3 times the size of a typical step, making it difficult to identify any steps between sets of cyclotron measurements. We could only identify steps when they occurred toward the end of one set of cyclotron measurements where the individual cyclotron measurements were more accurate. The 1995 charge-to-mass measurement which best determined the magnetic field drift had the highest quality fit; the other measurements which determined the magnetic field drift inaccurately had a poorer quality fit.

The simultaneous fit to the 1995 measurements was straightforward (Table 5.2). Each measurement consisted of 5 to 7 sets of cyclotron measurements where the

No.	Date d/m/y	# of sets	Poly-nomial order	Step identified	χ^2_ν	$\Delta\nu_c$ (Hz)
1	15/6/95	5	3	no	0.98	-0.041 ± 0.008
2	18/6/95	6	4	no	1.35	$+0.000 \pm 0.009$
3	20/6/95	7	4	no	1.20	$+0.044 \pm 0.008$
4	20/7/95	5	3	no	2.40	$+0.013 \pm 0.012$
5	31/7/95	6	4	no	1.53	$+0.024 \pm 0.011$
6	2/8/95	6	4	no	1.11	-0.002 ± 0.010
7	4/8/95	5	3	yes	0.91	$+0.029 \pm 0.009$
8	29/8/95	6	3	no	0.81	$+0.009 \pm 0.011$

Table 5.2: The difference frequencies ($\Delta\nu_c = \nu_c(p) - \nu_c(\bar{p})$) resulting from the simultaneous fit to all the charge-to-mass measurements made in 1995. They are arranged in the order that the measurements were taken. The measurements scatter by more than the fit error bar. Also shown are the number of sets of cyclotron measurements included in the fit, the polynomial order which describes the magnetic field drift, whether a magnetic field step was identified.

antiproton and the H^- were alternately measured. The cyclotron frequency of the inner particle did not shift when the cyclotron orbit of the outer particle increased since the strength of the oscillatory electric field used was finely tuned during these measurements. For this reason, the initial relativistic shift parameter (A_i in Eq. 4.6) of the simultaneous fit was restricted to have only one value for each set of cyclotron measurements. In one cyclotron measurement a step in the magnetic field drift was identified (Figures 4.12a, 4.12b, and 4.12c). It is likely that other steps took place in the data set, but we could not identify them. This charge-to-mass comparison was fit with a step, while the other charge-to-mass comparisons were fit with no step. We fit each set with the best order polynomial possible (Fig. 4.20). The simultaneous fits produced χ^2_ν larger than expected in some cases and the resulting difference frequencies ($\Delta\nu_c$) scattered by more than the fit errors bars (Table 5.2). This large scatter was due to the large magnetic field drift.

The charge-to-mass measurement made on 29 August 1995 had the best determined magnetic field drift of the 1995 measurements (Fig. 5.11). During the extrapolation time, the magnetic field drifted by 0.04 Hz (Table 5.1), about 4 times larger than the measurement in 1996 (Compare Fig. 5.11 with Fig. 5.9), and also about 4 times our measurement precision, 0.01 Hz. The magnetic field drift was about half that of the other measurements made in 1995 (Table 5.1). The magnetic field drifted less than in the other measurements in 1995 mostly because the measurement took place in late August when the temperature in the experimental hall and the temperature of the magnet was most stable.

The simultaneous fit from this day also indicated that the magnetic field drift was well modeled. Just as for the 1996 charge-to-mass measurement, the fit residuals mostly scattered within $\pm 1\ \sigma$ of zero and were distributed in time in a random way (Fig. 5.12). This was the case even for the accurate measurements at the end of each set of cyclotron measurements. The polynomial order was also well chosen (Fig. 4.20). We could increase the polynomial order up to the fourth order and still have a well constrained magnetic field drift (Table 4.5) but we found that the third order polynomial was best. Increasing the order did not change the difference frequency nor reduce χ^2_ν significantly. Based on both the randomly distributed residuals and the well chosen polynomial order, the fit accurately determined the magnetic field drift.

The remaining charge-to-mass measurements with large magnetic field drifts during the extrapolation time had worse fits to the simultaneous model. At the end of some sets of cyclotron measurements, all the accurate fit residuals deviated from zero up to 3 times their error bars (Fig. 5.13a and Fig. 5.13b) and all deviated in the same direction. When the magnetic field drift model is inaccurate, the fit minimizes the deviations from all the sets of cyclotron measurements, but there is no low order

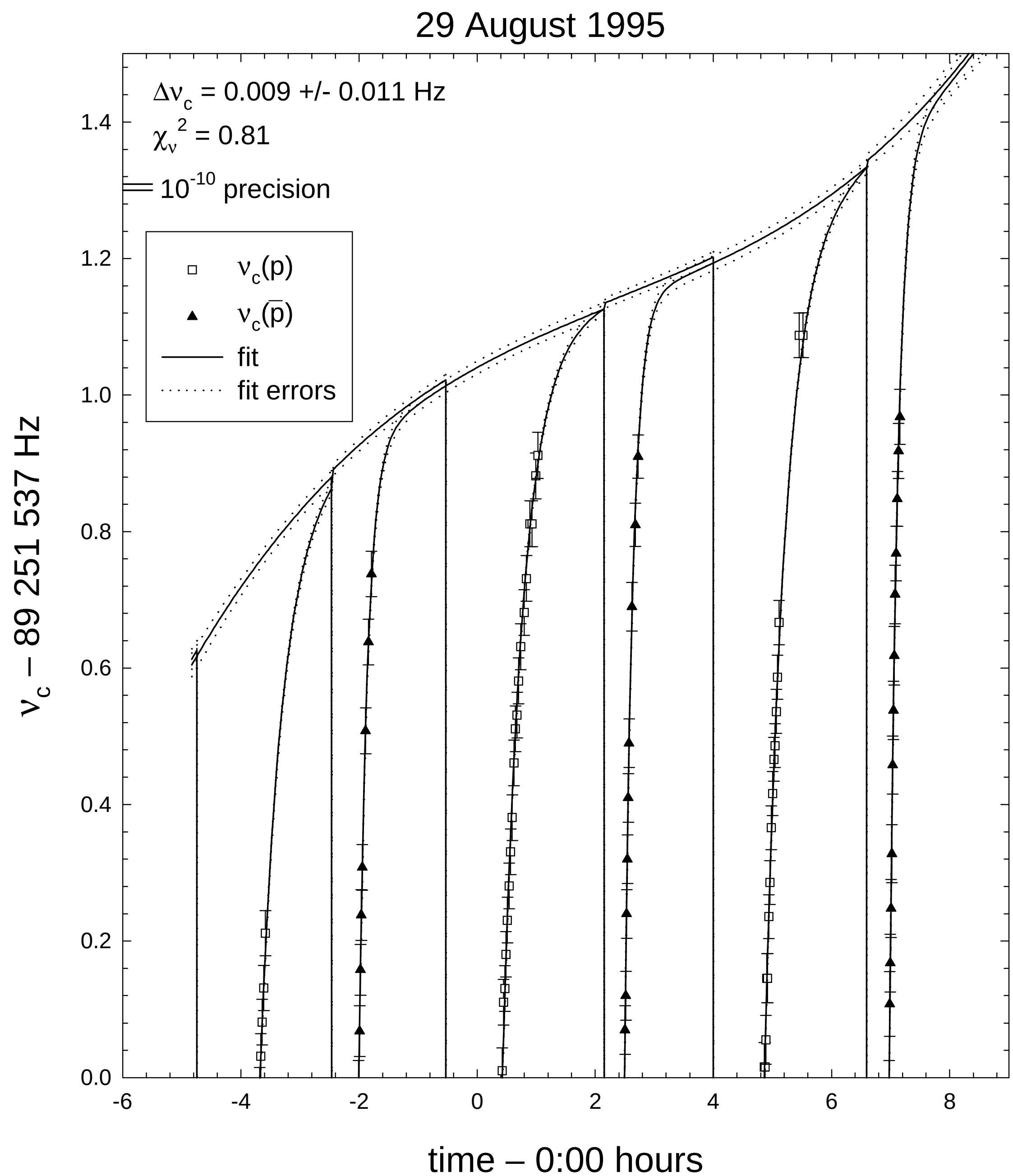

Figure 5.11: The simultaneous fit of the best charge-to-mass comparison made in 1995, that from 29 August 1995. Midnight is 00:00 hours.

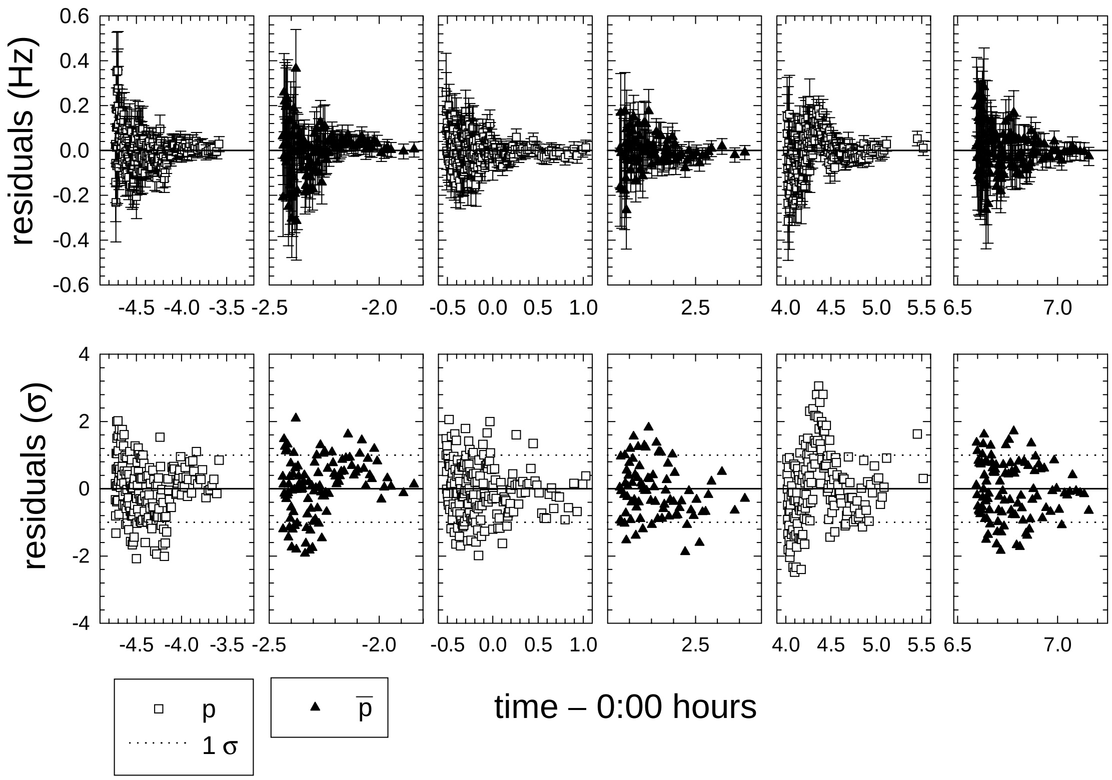

Figure 5.12: The simultaneous fit residuals from 29 August 1995 measured in Hertz and measured in terms of the error bar assigned to each cyclotron measurement (σ). Midnight is 00:00 hours. The residuals, even the most important ones at the end of each cyclotron endpoint measurement, mostly fall within $\pm 1\ \sigma$ of zero as they should. They are also distributed in time in a random way.

polynomial which fits to all of them. The result is that the accurate residuals in some sets are all too high as in Fig. 5.13a, while in other sets the residuals are all too low. Since the cyclotron drift frequency (ν_c) is determined by extrapolating from these accurate cyclotron measurements, the error bar on the cyclotron frequency drift ($\sigma(\nu_c)$) should not be smaller than the average of these deviations. In these cases the fit produced a cyclotron drift error bar ($\sigma(\nu_c)$) that was too small (Fig. 5.13a); the model used for the magnetic field drift did not match well to the real magnetic field drift. Another example of these sorts of residuals is in Fig. 4.19).

A nonideal fit to the simultaneous model is measured by the fit residuals from cyclotron measurements relativistically shifted by less than 1 Hz. When many of these residuals in a row deviate from zero by a few times their error bar (σ) in the same direction, they are distributed in a "nonrandom" way. The fit assumes that the residuals are randomly distributed and that they scatter within their errors; therefore, nonrandom residuals are contrary to the assumptions of the fit. The best way to identify nonrandom residuals is by seeing their distribution. In our case, the total χ^2_ν determined by including all the fit residuals underestimated the effect of these nonrandom residuals. Most of the cyclotron measurements had large relativistic shifts, large error bars, and always fit well to the simultaneous model regardless of the magnetic field drift model. They tend to keep χ^2_ν equal to 1. An approximate way to estimate the size of the nonrandom residuals is by computing an "accurate" χ^2_ν, determined by including only the most accurate fit residuals: the residuals from cyclotron frequency measurements with relativistic shifts less than 1 Hz (Table 5.3). These residuals are the most important for determining the magnetic field drift. When the accurate fit residuals scatter as much as the inaccurate ones, the ratio of the accurate χ^2_ν to the total χ^2_ν should be 1. We found that for the two best charge-to-mass measurements, 29 August 1995 and

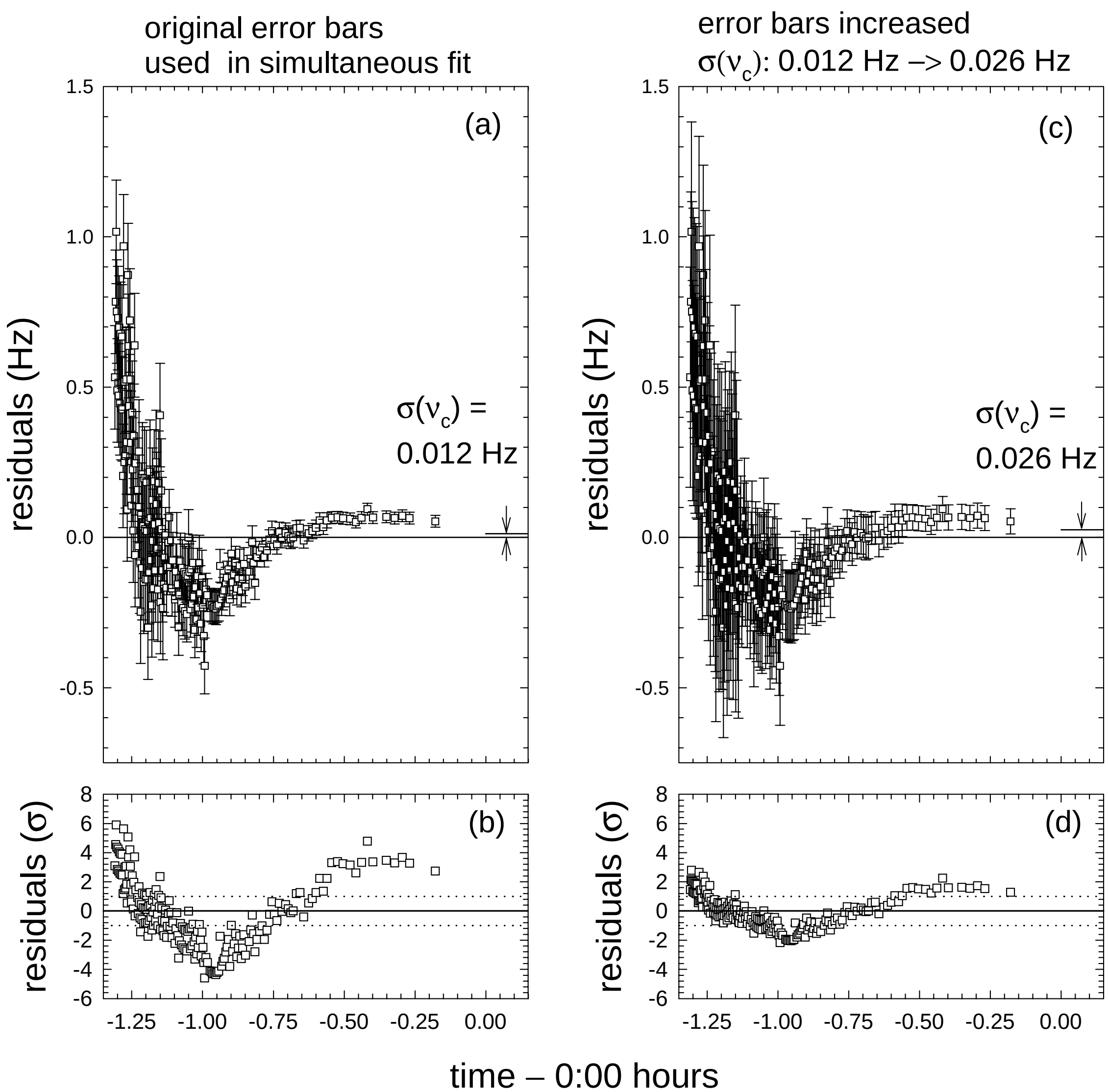

Figure 5.13: When the magnetic field drift during the extrapolation time was large, some of the most accurate residuals deviated from the fit in a nonrandom way. Midnight is 00:00 hours. (a) The most accurate fit residuals all deviate from the fit by 0.05 Hz. The cyclotron frequencies from these residuals cannot be extrapolated to 0.012 Hz, the cyclotron drift error bar ($\sigma(\nu_c)$). (b) The residuals divided by their error bar (σ). They do not fall between $\pm 1\ \sigma$, and are not distributed randomly. (c) When the error bar on the difference frequency ($\Delta\nu_c$) is increased, the accurate fit residuals have larger errors and they can be extrapolated to determine the cyclotron frequency drift to 0.026 Hz. (d) The residuals measured in terms of their increased error bar (σ). They still show the nonrandom pattern, but fall more closely between $\pm 1\ \sigma$.

No.	Date	**B** field drift in extrapolation time (Hz)	# of measurements with $\|\delta\nu_c\| < 1$ Hz	Total χ^2_ν	Accu-rate χ^2_ν	χ^2_ν ratio
1	21/9/96	0.01	133	0.85	0.66	0.78
2	29/8/95	0.04	59	0.81	0.26	0.32
3	31/7/95	0.07	65	1.53	3.74	2.44
4	20/7/95	0.08	54	2.40	8.34	3.48
5	18/6/95	0.10	65	1.35	2.24	1.66
6	20/6/95	0.10	61	1.20	2.04	1.70
7	15/6/95	0.16	49	0.98	1.43	1.46
8	4/8/95	0.17	53	0.91	1.09	1.20
9	2/8/95	0.19	62	1.11	2.18	1.96

Table 5.3: For large field drifts during the extrapolation time, the accurate fit residuals scatter more than the inaccurate ones. The total χ^2_ν includes all the fit residuals. The accurate χ^2_ν includes only the residuals from cyclotron measurements with relativistic shifts ($\delta\nu_c$) less than 1 Hz, the accurate measurements. The χ^2_ν ratio is the ratio of the accurate χ^2_ν to the total χ^2_ν. In the two measurements with the lowest field drift during the extrapolation time, the accurate residuals deviated from the fit less than the inaccurate one, and the χ^2_ν ratio was below 1. In 1996 twice as many accurate cyclotron frequency measurements contributed to the fit compared with the 1995 measurements.

21 September 1996, the accurate fit residuals scattered less than the inaccurate ones, resulting in a ratio of the accurate χ^2_ν to the total χ^2_ν below 1 (Table 5.3). For the measurements with "nonrandom" residuals, the accurate residuals scattered more than the inaccurate ones, resulting in a ratio larger than 1.

In these measurements with a large magnetic field drift during the extrapolation time, the order of the polynomial used to model the magnetic field drift was the maximum possible order. In each case, we limited the polynomial order so that the drift only takes into account the magnetic field drift between adjacent sets of cyclotron measurements and not the drift within any one set (Table 4.5). To have confidence that the polynomial order was well chosen, two adjacent orders of polynomial should produce the same fit, the same χ^2_ν and the same difference frequency ($\Delta\nu_c$). This was the case in the 1996 measurement and in the measurement of 29 August 1995. Then the magnetic field drift was modeled well by the lower order polynomial. In most of the other measurements (6 out of 7) no two polynomial orders gave the same χ^2_ν (Fig. 4.20). For these cases, the field drift would have probably been better modeled to a higher order polynomial, but the limited number of cyclotron measurements could not be fit reliably to any higher order. When the magnetic field drift during the extrapolation time was high, we most often chose the maximum polynomial order possible. This likely did not model the magnetic field drift accurately.

The simultaneous fit underestimated the error bar on each charge-to-mass measurement (Fig. 5.14a). When the points were weighted by their error bars, the fit to one difference frequency produced an χ^2_ν of 9.3. This indicated that the simultaneous fit underestimated each measurements error bar by three times, which is the result of a poor fit to the magnetic field drift.

We estimated the error bar for each measurement by the scatter between measurements. The error bar was determined by equally weighting the individual measurements (Fig. 5.14b); this estimate of the difference frequency agreed with the difference frequency ($\Delta\nu_c$) produced by weighting the measurements by their fit errors (Fig. 5.14a). Based on the scatter between measurements, each individual charge-to-mass measurement was accurate to 0.026 Hz, 3 parts in 10^{10}. Increasing the error bar in this way made the difference frequency ($\Delta\nu_c$) consistent with the large residual deviations of the latest cyclotron measurements (Fig. 5.13c and 5.13d). The 8 charge-to-mass measurements together determine:

$$\left|\frac{e/m(\bar{p})}{e/m(p)}\right| - 1 = (-1.06 \pm 1.01) \times 10^{-10}. \tag{5.2}$$

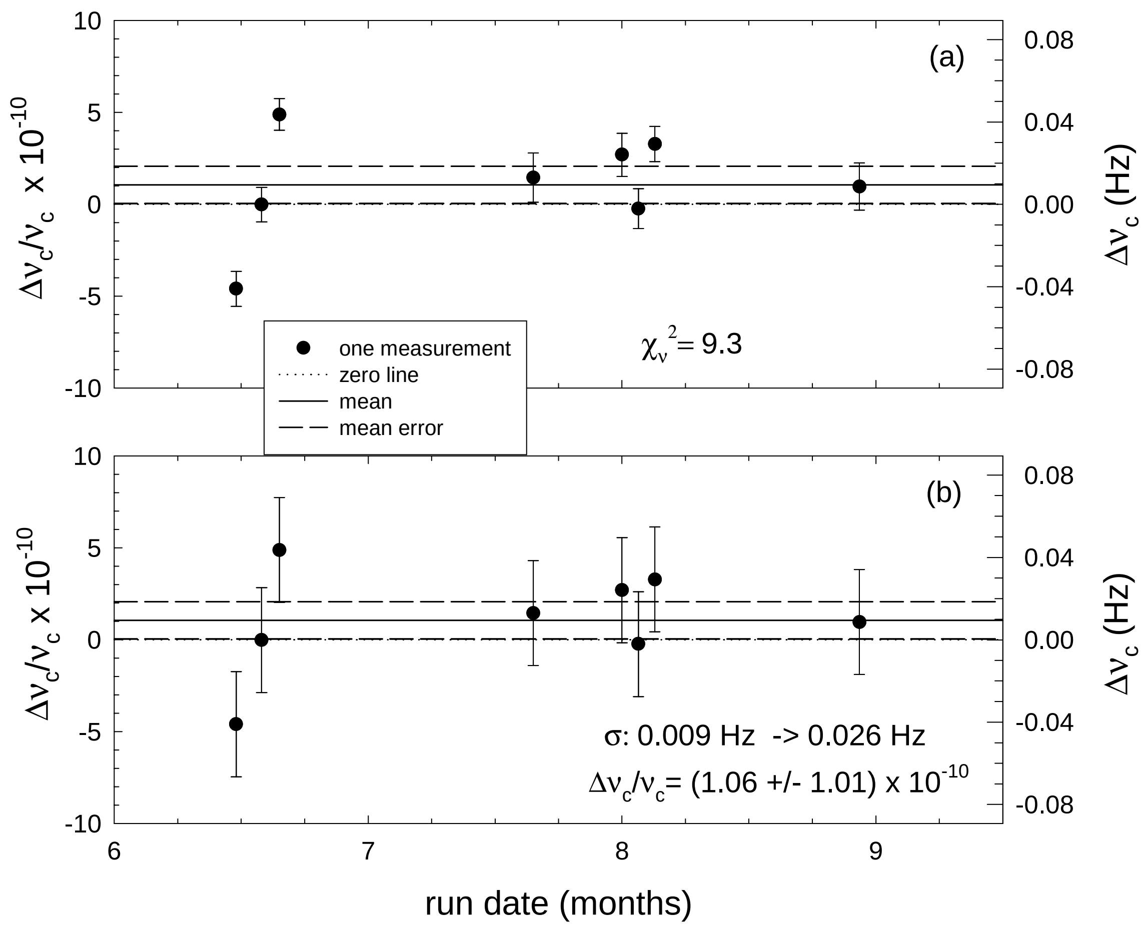

Figure 5.14: The difference frequency ($\Delta\nu_c = \nu_c(p) - \nu_c(\bar{p})$) for every measurement in 1995. (a) The difference frequencies and errors from the simultaneous fit for all the 1995 measurements plotted in time. Weighting the charge-to-mass measurements by their error bars produced a χ^2_ν of 9.3. This indicated that the fit reported an error bar that was 3 times too small. (b) Equally weighting each charge-to-mass measurement, and taking σ of the distribution as the error bar per point lead us to increase the error bar from 0.009 Hz to 0.026 Hz per point. The 1995 charge-to-mass measurement is based on averaging equally weighted individual charge-to-mass measurements. Equally or unequally (a) weighting the measurements produces the same result.

5.3.3 The Combined Charge-to-Mass Result

The magnetic field drift is responsible for most of the error seen in the measurements. The best quality fits also have the smallest magnetic field drift during the fit extrapolation (Fig. 5.15). The difference frequencies ($\Delta\nu_c$) as a function of field drift during the extrapolation time are shown in Fig. 5.15a. The two nights with the lowest magnetic field drift during the extrapolation time are also the only two nights for which the accurate cyclotron residuals are randomly distributed (Fig. 5.15b). The other nights had nonrandom residuals which indicated the magnetic field drift was inaccurately modeled. The χ^2_ν ratio (Table 5.3) is larger than 1 when the accurate residuals have too much scatter. When the magnetic field drift during the extrapolation time was low, the polynomial order was well chosen. Two polynomials of different order produced the same answer; this gave us confidence that the lower order polynomial was correct (Fig. 5.15c). When the magnetic field drift was high, the polynomial order chosen was the maximum possible, not necessarily the optimal one. The quality of the fit correlates well with the magnetic field drift during the extrapolation time. The best fits had well determined magnetic field drifts, and the inaccurate fits had inaccurately determined magnetic field drifts. None of the measurements with high field drifts fit well. The correlation between fit quality and low field drift during the extrapolation time is good evidence that the magnetic field drift was responsible for most of the scatter.

The scatter of the 1995 difference frequencies allowed us to estimate how well the simultaneous fit can describe the magnetic field drift. In 1995, the magnetic field drifted during the extrapolation time on average by 0.10 Hz, and the difference frequencies ($\Delta\nu_c$) and the magnetic field drifts were accurate to 0.026 Hz. Based on this, we expect the simultaneous fit to be able to predict the size of the magnetic

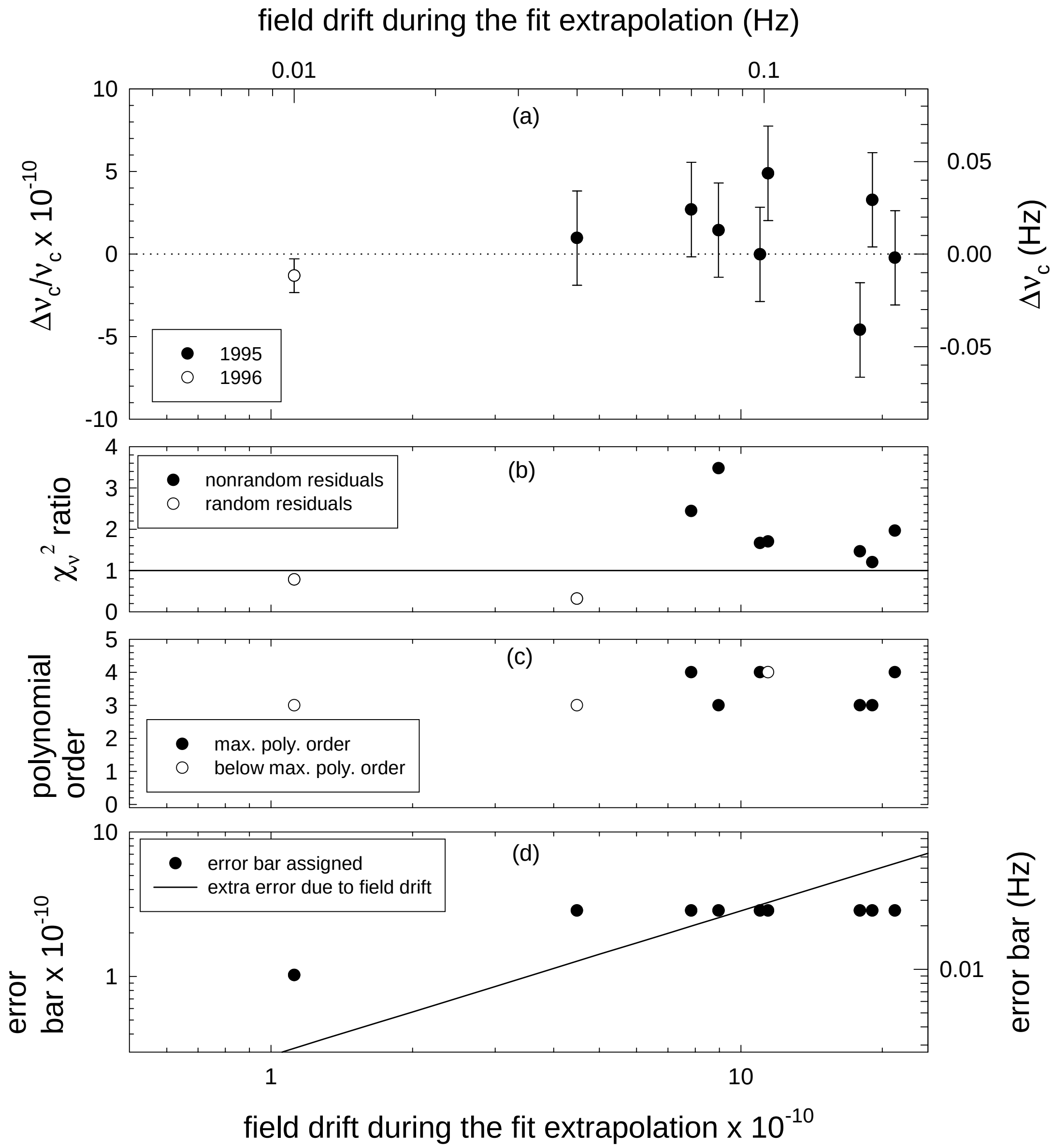

Figure 5.15: The fit quality is higher when the magnetic field drift during the extrapolation is low. (a) $\Delta\nu_c/\nu_c = (\nu_c(p) - \nu_c(\bar{p}))/\nu_c(p)$. All the difference frequency measurements with their error bars. (b) Nonrandom residuals deviate from zero by more than their error bars as in Fig. 5.13a. The χ_ν^2 ratio (Table 5.3) is larger than 1 when the accurate residuals scatter more than the other residuals. (c) The polynomial order. (d) The error bar due to the field drift used for each charge-to-mass measurement. The 1995 error bar came from the scatter between 1995 measurements, and the 1996 error bar came from the fit itself. The line shows how the field drift contributes to the error bar.

field drift during the extrapolation accurately to 25% (Fig. 5.15d). When applied to the 1996 difference frequency, the simultaneous fit was able to describe the difference frequency to 0.0025 Hz, well below the fit error we used. This confirmed our expectations that the 1996 fit well estimated the magnetic field drift. When applied to the next best day, it suggested that we overestimated the error bar. This also suggested that we underestimated the error bar on other 1995 measurements. Since the magnetic field drift during the extrapolation time was an estimate, a more complex error bar assignment than we used so far was not justified.

No large error due to a large magnetron orbit contributed to our measurement. When the magnetron orbit of either particle is larger than 50 μm, a 0.01 Hz shift occurs in the cyclotron frequency (Table 2.6). Since either the antiproton or the H^- could be in the larger magnetron orbit, the difference frequency ($\Delta\nu_c$) could either be positive or negative. This error causes extra scatter between measurements, but no systematic error. Slow voltage sweeps done after the last round electron removal reduced the magnetron motion of both particles (Fig. 2.39) and eliminated the cyclotron frequency shifts. In 1995, when the slow voltage sweeps were not performed, the difference frequency scattered by 0.04 Hz (Fig. 2.41). Those measurements were excluded from the charge-to-mass measurement. For the 1995 measurements included in this result, voltage sweeps were certainly performed but may not always have been performed after the last electron removal cycle. Thus the error bar due to a large magnetron orbit was much less than 0.04 Hz.

The correlation between the large magnetic field drift and the fit quality also indicates that any frequency shift due to inadequately reducing the magnetron orbit is small. When one particle is in a large magnetron orbit compared with the other, the difference frequency ($\Delta\nu_c$) will not be zero but should have a good quality fit. The quality of the fit depends only on the accuracy of the magnetic field drift model.

If the scatter in the 1995 measurements was due to not reducing the magnetron orbit properly, we would have found good quality fits with high magnetic field drift and also large difference frequencies ($\Delta\nu_c$) at low field drifts. Neither of these were seen in the measurements. Thus, most of the 0.026 Hz scatter in the 1995 measurements was due to the large magnetic field drift. Any magnetron cooling error was at most 0.01 Hz and was included in the 0.026 Hz error in 1995. The Bonn analysis [11] expresses a different opinion on this point. In 1996, the proper procedure to reduce the magnetron orbit was followed prior to measuring; furthermore, the magnetron cooling procedure had improved since 1995 (Sec. 5.3.1). Since any error due to a large magnetron orbit was well below 0.026 Hz in 1995, and since the procedure improved in 1996, we made no correction for any magnetron orbit in 1995 or 1996.

Other frequency shifts do not add to our error. When the axial motion is in thermal equilibrium with the tuned circuit, the modified cyclotron frequency shifts by 0.01 Hz due to the finite magnetic field bottle (Table 2.1). Prior to measuring, the particle's axial motion reached thermal equilibrium with the tuned circuit, making this shift is very much the same for both $\nu_c(\bar{p})$ and $\nu_c(\mathrm{H}^-)$. Thus the difference frequency ($\Delta\nu_c$) is unaffected by this shift.

The final charge-to-mass measurement was determined from the weighted average of the 1995 and the 1996 results. The two error bars were about equal. Expressing the measurement in terms of ratios of the charge-to-mass ratio gives:

$$\frac{e/m(\bar{p})}{e/m(p)} = -1.000\ 000\ 000\ 01(7) \tag{5.3}$$

The measurement is accurate to 7 parts in 10^{11}.

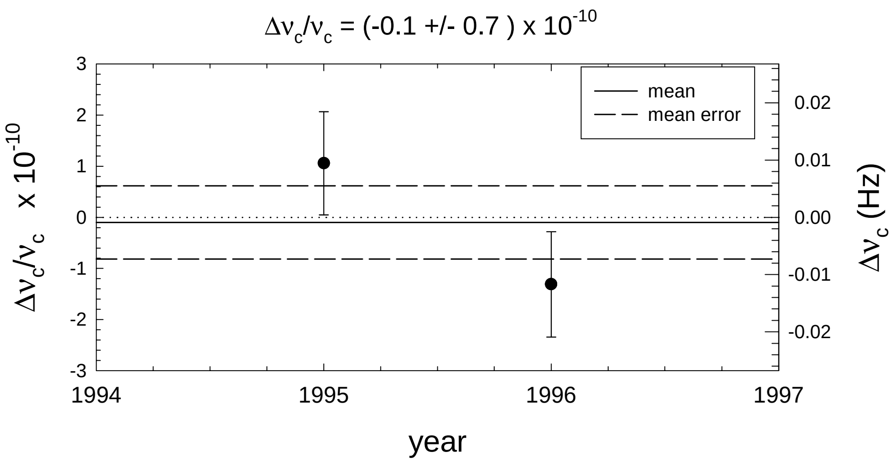

Figure 5.16: $\Delta\nu_c/\nu_c = (\nu_c(p) - \nu_c(\bar{p}))/\nu_c(p)$. The 1995 and 1996 measurements with their proper error bars are shown. The weighted average gives the charge-to-mass measurement reported here.

Chapter 6

Conclusion

We determined that the ratio of the antiproton and the proton charge-to-mass ratios is $-1.000\,000\,000\,01(7)$. This 7 parts in 10^{11} comparison was made by trapping an H^- and a $\bar{p}$ at the same time and alternately measuring them. Trapping two ions of the same charge eliminated the largest systematic error of the previous work [1, 2]. The two ions were measured in the same electric and magnetic fields at separate times. The largest remaining uncertainty comes from the magnetic field drift. Doubling the signal-to-noise ratio for the most important motion, the cyclotron motion, reduced measurement time and hence the uncertainty due to this drift. This allowed us to determine the ratio of charge-to-mass ratios precisely to 1 part in 10^{10} in a single night of measurement. To achieve this result, we developed methods to keep a single H^- ion trapped for days at a time. This measurement is the most accurate test of charge conjugation, parity and time reversal (CPT) invariance for baryons to date.

6.1 Charge-to-Mass Comparison Agreed Within the TRAP Collaboration

In this thesis I argue that we have compared Q/M for the antiproton and proton to an accuracy of 7 parts in 10^{11}. It should be noted that the initial analysis of the same data by our collaborators at the University of Bonn [11] yielded a slightly different conclusion. Their analysis and conclusions differed from what is in this thesis in three ways.

1. Because we only obtained one night of comparison data in 1996, after the improvements in our detection electronics, our collaborators have so far not included our best measurement, the one night of data taken in 1996. More discussion of this point follows.

2. The simultaneous fit of the 1995 data done at Bonn yielded essentially the same statistical error bar but gave individual values which differ slightly within this error bar. There are two reasons. First, each antiproton and proton decay curve was fitted to its own decay constant, whereas we constrained all the antiproton decay curves to have one time constant and all the H^- curves to have the another time constant (Sec. 4.4.2). Second, they often chose a magnetic field polynomial which was only second order whereas we typically chose third or fourth order polynomials to describe the time variation of the magnetic field. We chose the order based on a significantly lower χ^2_ν.

3. The most substantial difference was that our collaborators concluded that a systematic uncertainty of 1.4×10^{-10} should be assigned to account for possible magnetron heating. I argue in Sec. 5.3.3 that magnetron cooling only adds extra scatter to the result and that it is included in the result quoted.

The preliminary Bonn conclusion was to assign a statistical error of 1.0×10^{-10}, and a systematic (magnetron heating error) or 1.4×10^{-10}, leads to a final error of 1.7×10^{-10}.

For the 1996 analysis, I included a discrete step in the magnetic field after the first four measurements (Fig. 5.8). I argued that steps such as we have seen occur every 12 hours occurred during this measurement; the best way to model the magnetic field was with a slow cubic drift with a step. This resulted in including 5 pairs of proton and antiproton cyclotron measurements, but excluding one which took place at the time of the step. The small magnetic field activity seen during this night was incidental to the step. The step contributed to the Bonn decision to discard what otherwise would be our very best night of measurement.

Professor Gabrielse so far prefers a intermediate position in which we include only the first four decay curves during the night in 1996, discarding the last three points which are occurring in the presence of monitored magnetic activity as seen by our external magnetometer. The latter approach would give us a final difference frequency measurement ($\Delta\nu_c = \nu_c(p) - \nu_c(\bar{p})$) of $0.8 \pm 0.9 \times 10^{-10}$ as our result.

This thesis is being submitted before a final decision is made by the TRAP Collaboration. This thesis, and that of Christoph Heimann [11] should thus be regarded as a preliminary analysis that is an input to the final TRAP Collaboration result.

6.2 Future Directions

Making more measurements would improve the accuracy of the comparison. Ten measurements of equal accuracy to our most precise measurement would likely lead to a precision of 3 parts in 10^{11}. Making more measurements in a shorter period of time would also improve the accuracy. An optimized measurement sequence using the same cyclotron damping time could lead to alternate $\bar{p}$ and H^- cyclotron frequency measurements every 45 minutes, an improvement of 25%. To repeat the measurements more frequently, the technique to remove electrons while keeping the H^- trapped will need further development. Fortunately, we demonstrated the possibility to load an H^- in the trap without loading antiprotons, making it much easier to develop a reliable method.

Improving the magnet's temporal stability and spatial homogeneity would also make the measurement much more precise. Controlling the temperature of the magnet would reduce the drift of the magnetic field in time. For a drift as low or lower than that seen in our most precise experiment, the magnet's temperature should drift by less than 0.1 °C/hour. Improving the magnetic field homogeneity will also improve the measurement. It would make any drift between the solenoid coils and the trap center less important and would make the measurement less sensitive to large magnetron orbits.

A smaller trap could possibly lead to a more precise measurement. The trap built prior to leaving for CERN would have determined the **B** field drift much more precisely than what we achieved in this work (Fig. 6.1). This would greatly reduce our largest error: the error due to the large **B** field drift. That trap was 3.6 times smaller, had half the trap capacitance and had nearly twice the Q compared with the trap used for this experiment completed at CERN. These three factors reduced the cyclotron damping time (Eq. 2.14) by over 30 times. Such a trap would greatly reduce the time needed to measure each cyclotron frequency and would lead to a much more precise **B** field drift determination. In this experiment, a 2.4 times reduction in the cyclotron damping time led to a 3 times improved accuracy in each night's charge-to-mass measurement. Based on this, the reduction in cyclotron damping time with the small trap would reduce the error each night due to the **B** field drift to below 1 part in 10^{11}. Another error, perhaps due to not reducing the magnetron orbits sufficiently, would likely dominate the charge-to-mass error. The disadvantage of a smaller trap is that assymetric electric fields affect the particle much more since the trap electrodes are much closer. Based on the previously published direct proton and antiproton comparison [1], this would likely not introduce a systematic error larger than 1 part in 10^{11}. Another possible disadvantage is that it may be more difficult to keep the outer particle in a large enough orbit so as not to influence the measured one.

Before the anti-hydrogen experiments already begun [30] reach the point where anti-hydrogen atoms are precisely measured, the antiproton and H^- charge-to-mass ratios measurement provides the most precise way of testing CPT invariance for baryons.

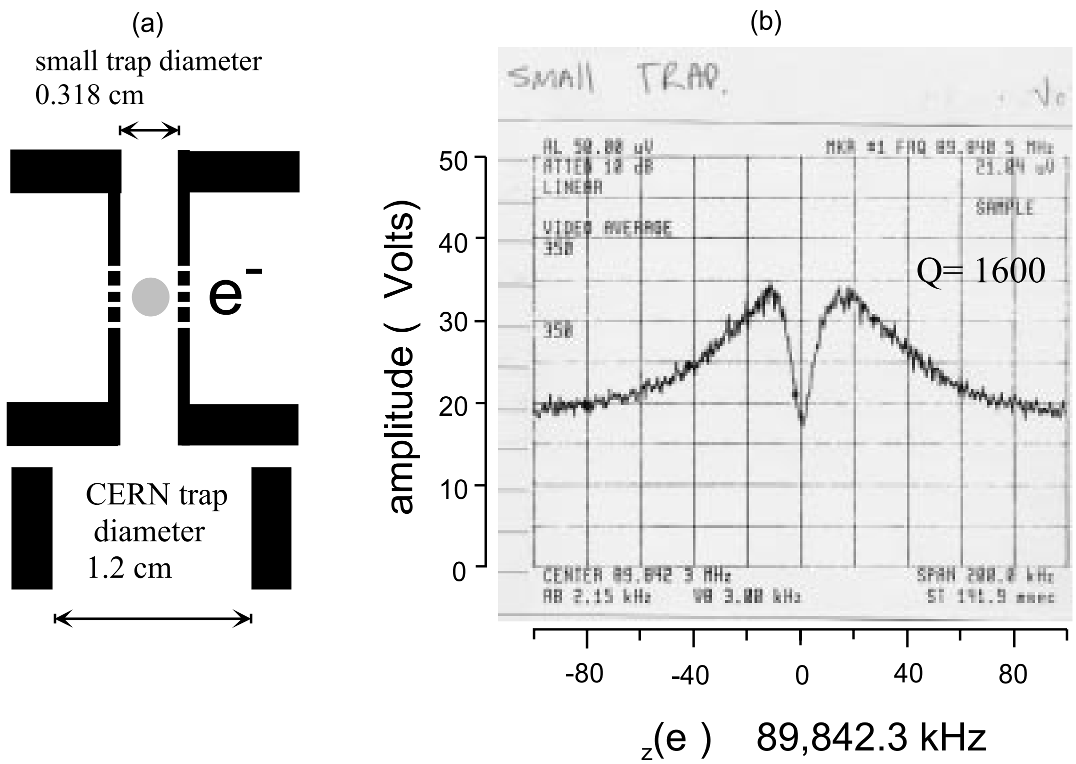

Figure 6.1: The small trap built prior to working at CERN has a 30 times reduced damping time compared with the trap used for this experiment. (a) The small trap was 3.6 times smaller and had half as much trap capacitance compared with the trap used to complete this measurement at CERN. (b) An electron "dip" (compare with Fig. 2.8) with about 500 e^- measured in the small trap. The amplifier Q was 1600.

Bibliography

[1] David Forrest Phillips, Ph.D. thesis, Harvard University, Cambridge, Massachusetts, 1996.

[2] G. Gabrielse, D. Phillips, W. Quint, H. Kalinowsky, G. Rouleau, and W. Jhe, Phys. Rev. Lett. **74**, 3544 (1995).

[3] F. DiFilippo, V. Natarajan, K.R. Boyce, and D.E. Pritchard, Phys. Rev. Lett. **73**, 1481 (1994).

[4] R.F. Streater and A.S. Wightman, *PCT, Spin and Statistics, and All That* (Benjaman, New York, 1964).

[5] D. Colladay and V. A. Kostelecký, Phys. Rev. D **55**, 6760 (1997).

[6] R. J. Hughes and M. H.Holzscheiter, Phys. Rev. Lett. **66**, 854 (1991).

[7] R. Carosi *et al.*, Phys. Lett. B **237**, 303 (1990).

[8] M. Carroll and the CPLEAR Collaboration, Nucl. Phys. A **626**, 157c (1997).

[9] K. Urbanowski, Int. J. Mod. Phys. A **13**, 965 (1998).

[10] Robert S. Van Dyck, Jr., Paul B. Schwinberg, and Hans G. Dehmelt, Phys. Rev. Lett. **59**, 26 (1987).

[11] Christoph Heimann, Ph.D. thesis, University of Bonn, Bonn, Germany, 1998.

[12] O. Chamberlain, E. Segre, C. Wiegand, and T. Ypsilantis, Phys. Rev. **100**, 947 (1955).

[13] A. Bamberger *et al.*, Phys. Lett. **33B**, 233 (1970).

[14] E. Hu, Y. Asano, M.Y. Chen, S.C. Cheng, G. Dugan, L. Lidofsky, W. Patton, C.S. Wu, V. Hughes, and D. Lu, Nucl. Phys. **A254**, 403 (1975).

[15] P. Roberson *et al.*, Phys. Rev. C **16**, 1945 (1977).

[16] B.L. Roberts, Phys. Rev. D **17**, 358 (1978).

[17] D. J. Wineland, P. Ekstrom, and H. G. Dehmelt, Phys. Rev. Lett. **31**, 1279 (1973).

[18] G. Gabrielse, X. Fei, S. L. Rolston, R. Tjoelker, T. A. Trainor, H. Kalinowsky, J. Haas, and W. Kells, Phys. Rev. Lett. **57**, 2504 (1986).

[19] G. Gabrielse, X. Fei, L. A. Orozco, R. L. Tjoelker, J. Haas, H. Kalinowsky, T. A. Trainor, and W. Kells, Phys. Rev. Lett. **63**, 1360 (1989).

[20] G. Gabrielse, X. Fei, L.A. Orozco, S.L. Rolston, R.L. Tjoelker, T.A. Trainor, J. Haas, H. Kalinowsky, and W. Kells, Phys. Rev. A **40**, 481 (1989).

[21] G. Gabrielse, X. Fei, L. A. Orozco, R. L. Tjoelker, J. Haas, H. Kalinowsky, T. A. Trainor, and W. Kells, Phys. Rev. Lett. **65**, 1317 (1990).

[22] F. M. Penning, Physica **3**, 873 (1936).

[23] H. G. Dehmelt, Adv. At. Mol. Phys. **3**, 53 (1967).

[24] L.S. Brown and G. Gabrielse, Phys. Rev. A **25**, 2423 (1982).

[25] L. S. Brown and G. Gabrielse, Rev. Mod. Phys. **58**, 233 (1986).

[26] G. Gabrielse, L. Haarsma, and S. L. Rolston, Int. J. Mass. Spectrom. Ion Proc. **88**, 319 (1989), ibid. **93**, 121 (1989).

[27] Eric A. Cornell, Kevin R. Boyce, Deborah L. K. Fygenson, and David E. Pritchard, Phys. Rev. A **45**, 3049 (1992).

[28] Murray D. Sirkis and Nick Holonyak, Jr., Am. J. Phys. **34**, 943 (1966).

[29] D. J. Wineland and H. G. Dehmelt, J. Appl. Phys. **46**, 919 (1975).

[30] D. S. Hall, Ph.D. thesis, Harvard University, Cambridge, Massachusetts, 1997.

[31] L. D. Landau and E.M. Lifshitz, *Mechanics*, 3rd ed. (Pergamon Press, New York, 1976), p. 154.

[32] A. A. Sokolov and Yu. G. Pavlenko, Opt. Spectrosc. **22**, 1 (1965).

[33] D.J. Wineland and H.G. Dehmelt, Int. J. Mass. Spectrom. Ion Proc. **16**, 338 (1975), ibid. **19** 251E.

[34] S. Baird, J. Bosser, M. Chanel, P. Lefèvre, R. Ley, D. Manglunki, S. Maury, D. Möl, and G. Tranquille, Hyperfine Interact. **76**, 61 (1993).

[35] Xiang Fei, Ph.D. thesis, Harvard University, Cambridge, Massachusetts, 1990.

[36] X. Fei, R. Davisson, and G. Gabrielse, Rev. Sci. Instrum. **58**, 2197 (1986).

[37] *CRC Handbook of Chemistry and Physics*, 74 ed., edited by David R. Lide (Chemical Rubber Publishing Company, Boca Raton, Florida, 1993).

[38] J. P. Gauyacq, J. Phys. B **13**, 4417 (1980).

[39] M. S. Huq, L. D. Doverspike, R. L. Champion, and V. A. Esaulov, J. Phys. B **15**, 951 (1982).

[40] Dean L. Farnham, Robert S. Van Dyck, Jr., and Paul B. Schwinberg, Phys. Rev. Lett. **75**, 3598 (1995).

[41] T. Andrea, W. König, R. Wynands, D. Leibfried, F. Schmidt-Kaler, C. Zimmermann, D. Meschede, and T. W. Hänsch, Phys. Rev. Lett. **69**, 1923 (1992).

[42] F. Nez *et al.*, Phys. Rev. Lett. **69**, 2326 (1992).

[43] J. D. Garcia and J. E. Mack, J. Opt. Soc. Am. **55**, 654 (1965).

[44] K. R. Lykke, K. K. Murray, and W. C. Lineberger, Phys. Rev. A **43**, 6104 (1991).

[45] Eric Allin Cornell, Ph.D. thesis, Massachsetts Institute of Technology, 1990.

[46] G. Gabrielse, J. Tan, L.A. Orozco, S.L. Rolston, C.H. Tseng, and R.L. Tjoelker, J. of Mag. Res. **91**, 564 (1991).

[47] G. Gabrielse and J. Tan, J. Appl. Phys. **63**, 5143 (1988).

[48] Joseph Ngai Tan, Ph.D. thesis, Harvard University, Cambridge, Massachusetts, 1992.

[49] Robert Lee Tjoelker, Ph.D. thesis, Harvard University, Cambridge, Massachusetts, 1990.

[50] Martin N. Wilson, *Superconducting Magnets* (Oxford University Press, New York, 1983).